AD-A174 470 A COLLECTION OF REPRINTS(U) LOUISIANA STATE UNIV BATON ROUGE COASTAL STUDIES INST W J WISEMAN ET AL. JAN 86 TR-398 N00014-83-C-0150 1/3

UNCLASSIFIED F/G 8/10 NL

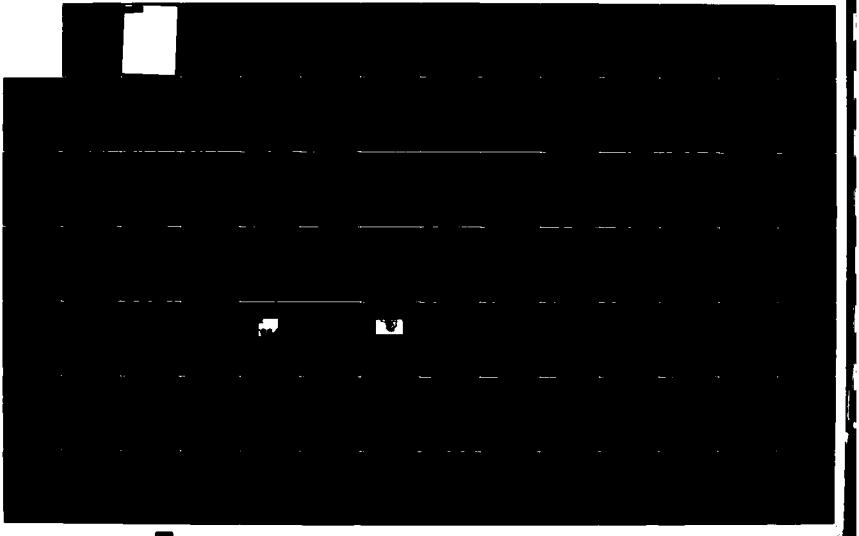

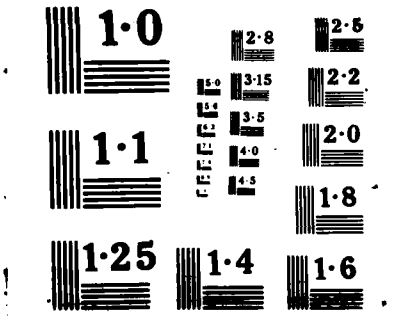
1·0
1·1
1·25
1·4
1·6
1·8
2·0
2·2
2·5
2·8
3·15
3·5
4·0
4·5

Coastal Studies Institute
Louisiana State University
Baton Rouge, LA 70803-7527

Technical Report No. 398

OCEAN CURRENT PROCESSES

Wm. J. Wiseman, Jr., C. N. K. Mooers, and G. Z. Forristall

1983

Reprint from Ocean Science and Engineering, 8(4):367-459, 1983.

Office of Naval Research
Contract No. N00014-83-C-0150
Project NR 388 002

TECHNICAL REPORT NO. 348

OCEAN SCIENCE AND ENGINEERING, 8(4), 367-459 (1983-84)

OCEAN CURRENT PROCESSES

Wm. J. Wiseman, Jr.
Coastal Studies Institute
Louisiana State University
Baton Rouge, LA 70803

C. N. K. Mooers
Naval Postgraduate School
Monterey, CA 93940

G. Z. Forristall
Shell Development Company
Houston, Texas 77001

ABSTRACT

This paper catalogs and discusses the ocean current processes that may impact offshore industrial operations on the continental shelf. The discussion and bibliography are extensive, but not exhaustive. The review is designed to be an introduction for engineers with little or no existing knowledge of physical oceanographic processes.

I. INTRODUCTION

Knowledge of ocean currents is important both as a design criterion for structures and for planning marine construction and operation activities. In addition, the climatology of currents (Beardsley et al., 1976) in the area of interest is an important component of contingency planning for oil spills and the general understanding of the environment. How current measurements in various engineering and environmental studies is summarized, for instance, by Woodward et al. (1978). An excellent review of oil spill modeling is presented by Murray (1982).

The design criteria for offshore structures are usually dominated by storm-generated waves. Thus, the current existing at the time of the peak waves is that which is important for design, and this current is primarily the wind-driven component. It might be thought that the very large velocities and forces in waves over 15 m high might overwhelm the smaller current velocities. However, Morison's equation (Sarpkaya and Isaacson, 1981) is usually used to calculate the force on small members due to combined waves and currents, as well as those due to waves alone. For drag-dominated cases, this equation predicts that the maximum force is nearly proportional to the square of the total velocity. Since the wave particle velocity for a 15-m, 12-second Stokes fifth order wave is about 4.6 m/sec at the surface, a surface current of only 1.04 m/sec will increase the force by 50 percent. Moreover, since, mean currents often decay much more slowly with depth than do wave currents, their contribution often increases in importance with depth.

Wind-driven currents can certainly be large enough to form a substantial contribution to the total flow during

storms. Pertinent measurements are understandably scarce, but Forristall et al. (1977) present useful data collected in tropical storm Delia in 1973. The storm was relatively weak, with a measured maximum wave height of 7.6 m, but the measured maximum current speed was 2.1 m/sec. The current was approximately in the longshore direction and decreased only gradually toward the bottom in 21 m of water. The steady current magnitude was thus as large as the fluctuating velocities due to the waves.

Extrapolation of a few measurements is obviously an unreliable means of determining design criteria. The measurements must be studied within the framework of theories of current generation so that hindcasting can be used. These theories are discussed later in this paper.

Wind-driven currents are not an overly important consideration in most offshore operations, since no work takes place during severe storms. There are many other types of currents, though, that may attain sufficient strength to influence operations and sometimes design in particular circumstances, and the main purpose of this paper is to catalog and discuss the driving mechanisms for these currents.

Tidal currents in the open ocean are weak, but tidal energy can be concentrated by shoreline and bottom configurations so that strong tidal currents exist in many inlets and coastal regions. These current systems are hazards to navigation and can significantly affect the design and operation of structures for petroleum development. In Cook Inlet, Alaska, structures have been successfully designed to withstand tidal currents that regularly exceed 3 m/sec (Goepfert, 1969). The forces from the winter ice cover moving with the current were the most severe criteria for

the design of the structures. Careful planning and attention to the tidal cycles permitted construction activity to proceed with many activities confined to the short slack-water period.

Near the mouths of large rivers, strong currents can be created by the outflow and spreading of fresh water. This type of current is particularly important for petroleum resource development, since many oil fields have been found in the vicinity of river deltas. The strong current is usually concentrated near the surface, where it can cause problems in anchoring drilling rigs and pipelaying and construction barges.

Deepwater drilling and construction activities are particularly influenced by currents, since relatively strong currents can persist deeper than the motions due to surface waves, which die out rather quickly with depth. Shanks et al. (1979) describe the problems that were met and solved while drilling in the South Equatorial Current offshore of Suriname in 1200 m of water. The current velocity was at times over 0.25 m/sec at 300-m depth, which caused large drag forces on the suspended drilling riser.

The details of current variation with depth are particularly important near the bottom, where pipelines must be designed to resist forces that might move them laterally (Jones, 1978). Since a pipeline resting on the bottom is not a symmetrical system, it feels a lift force in addition to a drag force. The structure of the bottom boundary layer of the current can cause a significant variation of current speed over the height of the pipeline.

Many of the topics discussed in this paper may not be familiar to most ocean engineers. It is important for the engineer to be aware of the wide variety of mechanisms that may play a role in driving currents. He will then

be better equipped to deal with problems that may arise in unfamiliar settings. For example, until recently internal waves were thought to be of practical importance only for the study of sound propagation in the ocean. However, Osborne et al. (1978) now report that internal waves with amplitudes over 60 m have affected drilling operations in the Andaman Sea. The currents associated with the waves caused substantial forces on the drilling riser as well as causing repeated surface wave rips due to wave-current interaction.

For design and construction work, only unusually strong currents are important. However, the complete climatology of currents in an area is desirable for oil spill planning and environmental impact statement work. Knowledge of the periods of very weak currents and the direction of prevailing currents is at least as useful as knowledge of peak magnitudes. Specification of the climatology is usually possible only after extensive measurements, but an understanding of the theory is necessary for fullest utilization of the measurements.

In the following pages, after a discussion of the forces due to currents, a catalog of current processes is presented, beginning with tidal phenomena. Models of wind-driven currents due to storms are then described. Internal waves, eddies, plumes, and, finally, currents that are dominated by local topographic variations such as canyons are discussed. The paper ends with a discussion of seasonal variability and the semi-permanent boundary current systems of the oceans.

II. FORCES DUE TO CURRENTS

A. Drag Force

The standard practice used to calculate forces on small cylinders in combined wave and current fields is to add

the currents and wave particle velocities vectorially and apply Morison's equation. However, there exists very little information on which a rational choice of the drag and inertia coefficients for that equation can be based. A large body of knowledge exists showing that the drag force in oscillatory flow is due to complex boundary layer separation and wake encounter effects, which are roughly parameterized in Morison's equation. The presence of a current will affect the physical processes by advecting the wake away from the cylinder and should thus change the coefficients in ways that are impossible to predict without much careful experimental work. Unfortunately, there have been few experiments that combined steady and oscillatory flow. Sarpkaya and Isaacson (1981) review the pertinent literature. The lack of data has no doubt been partly caused by the additional complexity of the experimental apparatus required. Since there is another parameter range to be investigated in addition to the Reynolds and Keulegan-Carpenter numbers, much work remains to be done.

Most of the experimental work that has been done has addressed, not the question of the proper coefficients in Morison's equation, as stated above, but rather the damping of oscillatory flow in the presence of a steady flow. Mercier (1973) oscillated a cylinder in a flume both parallel and transverse to the flow and measured the forces on it. Inertial forces on the sensing element were large but were subtracted out in the analysis of the data. Reynolds numbers were between 4000 and 30,000. Defining the "average drag coefficient" as the coefficient in Morison's equation based on the steady flow velocity alone, he quite naturally found that it increased considerably as the oscillatory flow increased.

The parameter most often used to describe the relative importance of the steady flow and oscillations is the reduced velocity, defined as $\bar{U} = U/fD$, where U is the current, f is the frequency of the oscillations, and D is the diameter of the cylinder. For reduced velocities near 5, the vortex shedding frequency is close to the frequency of oscillation, and the process is poorly described by Morison's equation. However, for reduced velocities greater than 8, Mercier found that the drag coefficient in a Morison's equation based on total velocity was well behaved and slightly higher than that for steady flow. In fact, it was in the range of values found for pure oscillations.

Verley and Moe (1978) performed their experiments using a freely oscillating cylinder in a steady flow, and measured the decay time of the oscillations and thus the damping. Reynolds numbers ranged up to about 10,000. For reduced velocities above 8, the current clearly decreased the drag coefficient and increased the added mass coefficient (C_M). For the parameter ranges investigated, it is possible to form the hypothesis that

$$C_D = \begin{cases} C_O\ (1 - U/V) + C_S\ (U/V) & \text{for } U/V < 1 \\ C_S & \text{for } U/V \geq 1 \end{cases} \qquad (1)$$

where C_O is the drag coefficient for oscillatory flow with the proper Reynolds and Keulegan-Carpenter numbers, C_S is that for steady flow, and V is the maximum velocity of the oscillations. Equation (1) should be taken as a tentative hypothesis in the absence of definitive data.

B. Vortex-Induced Oscillating Forces

Reduced velocities greater than 10 occur in most cases of forces due to combined waves and currents in storms for structural elements near the surface or in shallow water. Situations where current velocities predominate and the reduced velocity attains critical values near 5 are more likely in deep water or simply when the current is strong and the waves are low. Vortices shed at a frequency near the natural frequency of the system can lead to resonant excitation of the member and rapid failure due to fatigue. This process, often called "lock in" or "galloping," is particularly insidious, since it can lead to failure of otherwise well-designed structures. The designer should always be alert to the possibility of resonance, paying particular attention to members that are long and heavy and thus have low natural frequencies, which are more likely to match the vortex shedding frequency.

For the Reynolds number range of most interest for the design of structural members and risers in the ocean, vortices are shed on alternating sides of a cylinder at a frequency given by

$$f_o = SU/D \tag{2}$$

where S is the Strouhal number equal to about 0.2. For a cylindrical member in a steady or quasi-steady flow, the reduced velocity can be defined as

$$\bar{U} = U/f_n D \tag{3}$$

where f_n is the natural frequency of the member. A comparison of equations (2) and (3) shows that resonant excitation

will occur when $\bar{U} = 5$. The remarkable fact is that resonance is observed not only for reduced velocities in the immediate neighborhood of this critical value, but for a wide range of reduced velocities extending from perhaps 4.5 to as high as 10. It appears that the motion of the cylinder influences the frequency of vortex shedding so that this frequency becomes "locked in" to the frequency of cylinder oscillation. The practical importance of this fact is that resonant excitation is much more likely than if precise synchronization of the frequencies were necessary.

Designers should strive to keep the natural frequencies of members far away from possible resonance, where large stresses can quickly lead to fatigue failure. However, in some cases the time of exposure to resonance may be short enough that it is useful to actually calculate stress levels in the design. The simplest estimate can be made by noting the experimental evidence (e.g., Griffin et al., 1975) that the maximum amplitude of the cylinder oscillations is 1.0-1.5 times the diameter of the cylinder. The amplitude depends on $\bar{U}$ and the structural damping but is only a weak function of Reynolds number. The end conditions on the member enter only in the determination of its natural frequency. Once the amplitude is estimated, the stress level can be calculated through elasticity theory.

More sophisticated models of the motion under vortex excitation have been developed. Nakamura (1969) described the system as a cylinder on springs with the wake considered as a compound pendulum. Hartlen and Currie (1970) simulated the system as a van der Pol oscillator and Iwan and Blevens (1974) developed this idea further.

The effect of nonuniform current profiles on "lock in" is poorly understood but of great practical importance.

Construction of the Cognac platform in 300 m of water off the Mississippi Delta (Sterling et al., 1979) required the suspension of long piles beneath a construction barge before they were stabbed and driven. Thorough model testing and theoretical investigations were undertaken before the field activities, and one of the conclusions of the model testing was that currents which varied on a scale of many pile diameters could excite the pile if the reduced velocity was in the critical range over most of the length of the pile.

Since current measurements had indicated that velocities sufficient to oscillate the Cognac piles were quite possible, the pile stabbing procedures were modified to account for the predicted pile motion. During construction only one of the piles was actually oberved to oscillate. This 2.1-m-diameter pile exhibited a peak-to-peak motion of 3.7 m at a reduced velocity of 9.3 (Fischer et al., 1980). The motion stopped when the pile tip contacted the guide. Current magnitudes that were theoretically sufficient to excite oscillations were observed on several other occasions, but the piles did not move. A spiraling of current direction along the length of the pile was noted as a possible cause of this discrepancy. It appears that much more work is needed to define the effect of current shear in speed and direction on vortex-induced oscillations.

Several possibilities exist for the mitigation of vortex effects. In systems such as drilling risers where the member tension is adjustable, it will often be possible to vary the natural frequency of the member until the vibration stops. Rigid splitter plates (flags) attached to the cylinder are very effective in suppressing vibrations but are impractical when the current direction is variable. However, flexible

flags and haired fairings have also been effective. Helical strakes and perforated shrouds are two more possible attachments. Knowledge of these systems is based on empirical evidence, and it would be good practice to undertake model tests unless much experience with a particular system is available.

Sarpkaya (1979) gives a good review of the subject of vortex-induced oscillations. The book by Blevins (1977) is also a good reference.

III. TIDAL PHENOMENA

A. Barotropic Tidal Currents

A transport of water is required to produce the astronomical tides observed as a rise and fall of sea level. Although the range of tidal heights in the open ocean is comparable to that along most coastlines, tidal currents there are negligible, since the transport takes place within a thick water column. Tidal current velocity generally increases with decreasing water depth. Over the continental shelf, tides can be responsible for a substantial portion of the observed currents. In some cases, such as in estuaries with high tide ranges, the tidal current can completely dominate the situation. Except in narrow straits and estuaries, the two components of the horizontal tidal current vector are not in phase. Thus, the current vector will rotate through a more or less elliptical pattern during the course of a tidal cycle.

An engineer should consider himself blessed if tidal currents are an important part of his problem, since the tides are by far the most regular and predictable movement of the ocean. The forcing functions due to the motion of

the astronomical bodies are known with great precision, but as a practical matter the fact that the forces, and thus the tides, are repetitious is more important. This regularity has made the accurate prediction of tidal heights along coastlines a practical reality for a hundred years, and the same empirical methods can be used for tidal current prediction once a suitable data base has been gathered. It is also possible to calculate tidal currents using numerical hydrodynamic models, and these methods serve as a useful introduction to the general problem of numerical current modeling.

The astronomical tide-generating potential consists of a series of sinusoidal terms, and the ocean responds to this forcing in a generally linear, though complicated, fashion. Thus, if the current at a given location has the horizontal vector components (u,v), they can be represented by a Fourier series of the form

$$u(t) = \sum_{k=1}^{K} a_k \cos (2\pi f_k t + \phi_k) \quad , \tag{4}$$

where a_k, f_k, and ϕ_k are respectively the amplitude, frequency, and phase of the k^{th} tidal component given by astronomical theory. From linearity, the frequencies of the tidal current components are the same as the known frequencies of the motions of the sun and moon with respect to the earth. The four most important frequencies are listed in Table 1, and much more extensive tables are available (Doodson and Warburg, 1941).

Equation (4) can be fit to a series of current measurements, and the coefficients thus determined can be used to predict the tidal current at any time in the future.

Table I

Symbol	Name	Frequency f_k (hr^{-1})
M_2	Lunar Semidiurnal	0.080511
S_2	Solar Semidiurnal	0.083333
K_1	Declination Luni-Solar	0.041780
O_1	Lunar Diurnal	0.038730

Periodic data are usually examined through Fourier transform methods, but in the harmonic analysis of tides it is better to take advantage of the fact that the coefficients are needed for relatively few frequencies which are precisely known in advance. If a time series of currents $[u(t_n)$, $n = 1, N]$ has been measured, equation (4) will generate N equations for the unknown amplitudes and phases. The system of equations will generally be overdetermined, i.e., there exist more equations than unknowns, and is solved by a least squares technique. In the solution, the cosines are expanded as the sum of cosine and sine terms, and advantage is taken of their orthogonality.

Reasonably long time series are needed for determination of all but the lowest order coefficients. For example, separation of the M_2 and S_2 constituents requires at least 14 days of data because of their nearly equal frequencies. It is best to use at least one month of data in any harmonic analysis of tides. Longer series are usually required for tidal current analysis than for tidal height analysis, since more signals from other sources generally appear in current data, i.e., the data are noisier. More sophisticated response

methods than the simple least squares solution outlined above have been developed by Munk and Cartwright (1966), among others. These methods are particularly useful when the data include gaps, which is too often the case with current meter records. An excellent review of tidal analysis techniques is available in the recent book by Godin (1972).

Figure 1 gives an example of the harmonic analysis of data from a current meter. The top trace is the east-west component of the near-surface current in 20 m of water near the Texas coast. Periodicities of tidal frequency are noticeable near the beginning and the end of the record, but from day 8 to day 12 a wind-driven event dominates. The least squares solution gave the tidal current shown in the lower half of the figure, which indicates that a substantial portion of the signal was due to tides.

Since the forcing function for the tides is known and the response of the ocean seems to be nearly linear, it is natural to suppose that tidal currents could be calculated without recourse to any observations. The problem has attracted the attention of many famous mathematicians since the 17th century. However, many problems arise with the simple linear equations applied over the global ocean. Only very recently have reasonably accurate solutions been obtained (Schwiderski, 1980), and these include coastal observations in the formulation.

The prediction of tidal currents in any small area, given data from nearby tide gages, is somewhat simpler, and useful models have been available for several years. If the area under consideration has a length scale of less than a few hundred kilometres, the direct attraction of the sun and moon on the area can be neglected, and the solu-

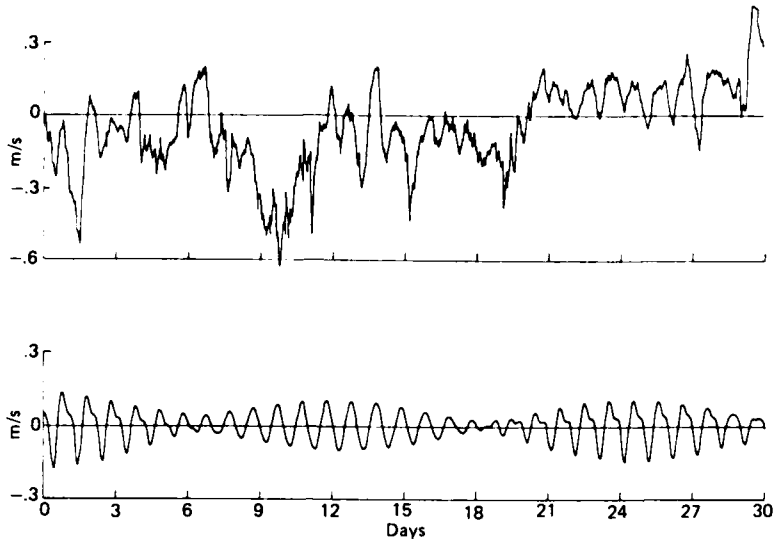

Figure 1. Example of an observed current record from the Texas shelf (upper) and the tidal contribution (lower) as determined from harmonic analysis.

tion depends only on the specified boundary conditions. The simplest equations that retain the relevant physical assumptions are then

$$\frac{\partial U}{\partial t} = fV - gH \frac{\partial \eta}{\partial x} - D_x \tag{5}$$

$$\frac{\partial V}{\partial t} = -fU - gH \frac{\partial \eta}{\partial y} - D_y \tag{6}$$

$$\frac{\partial \eta}{\partial t} = -\left(\frac{\partial U}{\partial x} + \frac{\partial V}{\partial y}\right) \tag{7}$$

where

$$(U, V) = \int_{-H}^{\eta} (u, v)\, dz$$

are the vertically integrated volume transports[1] in the x and y directions, respectively. The currents u, v, being associated with a shallow-water wave, are assumed to be essentially constant with depth and attention is focused on transports. H is the water depth, which is assumed constant; slight modifications allow for a variable depth. η is the sea surface displacement from its mean position, and D_x and D_y are bottom drag terms. The Coriolis parameter is given by $f = z\Omega \sin \phi$, where Ω is the angular rotation rate of the earth and ϕ is the latitude. The effect of the earth's rotation is usually of the same magnitude as the other terms in the momentum equation. This fact is a distinguishing feature of large-scale flows.

Equations (5)-(7) describe waves that propagate under the force of gravity in a rotating coordinate system. A few solutions of the equations are known for simple cases, but numerical methods must be used for the complicated geometries that occur in practical problems. A grid system is laid out for the area of interest, and the equations are made discrete by one of several methods. To complete the specification of the problem, conditions on the lateral boundaries of the grid are imposed. At land boundaries, it is most natural to require that the component of flow normal to the boundary be zero. At open-water boundaries, the tide height is normally specified as a function of time. This condition describes the tide wave as it propagates into the model grid. The tide at the boundaries of bays or inlets can usually be interpolated from coastal stations.

---

[1] Mass transport is normally defined as $\int_{-H}^{\eta} \rho\,(u,v)\,dz$, where ρ is density.

In other cases, it may be necessary to measure the tide at the model boundary using bottom pressure recorders. Regional or global tide models are another possible source of boundary value information.

The specification of the bottom drag terms is one of the more controversial aspects of tidal modeling. This controversy reflects our imperfect understanding of the physical processes involved. The usual formulation relies on the fact that the drag in a turbulent boundary layer is generally proportional to the square of the free stream velocity. Thus

$$D_x = gU\,(U^2 + V^2)^{1/2}/C^2H^2 \quad , \tag{8}$$

where C is the Chezy coefficient. The numerical value of the coefficient depends on the bottom roughness, but in practice C is usually adjusted to tune the model to match observations. A value of $g/C^2 = 0.003$ might be a reasonable starting point if no other information is available.

A large number of schemes have been proposed for the numerical solution of equations (5)-(7). The interested reader could consult Heaps (1969) for a clear description of an explicit finite difference scheme with particular attention given to the boundary conditions. Leendertse (1967) describes a more sophisticated implicit scheme and carefully studies the sources of error. Galerkin methods can be used to set up the implicit discrete equations (Brebbia and Partridge, 1976). Numerical tidal models based on these and other methods have been constructed for many geographical areas, for example the Gulf of Mexico (Mungall et al., 1978) and Cook Inlet (Mungall and Matthews, 1970). Three-

dimensional models are also available, for example Davies and Furnes' (1980) model of the North Sea.

B. Baroclinic (Internal) Tides

If the constant pressure surfaces and constant density surfaces within a fluid do not coincide, the fluid is said to be in a baroclinic state. In such a state, baroclinic flow results.

Baroclinic tides are generated by the interaction of barotropic tides with variable bottom topography and the density stratified water column and modified by the influence of the earth's rotation. The baroclinic tides, deriving from the barotropic tides, wax and wane with the spring-neap tidal cycle of the latter. They are efficiently generated at abrupt changes in bottom topography, such as the shelf break, and where the magnitude of the bottom slope essentially equals $\{(\sigma^2-f^2)/(N^2-\sigma^2)\}^{1/2}$. N is the Brunt-Vaisälä frequency, where $N^2 = -g/\rho\ \partial\rho/\partial z$. σ is the radian tidal frequency. The nature (onshore-offshore versus alongshore propagation, etc.) of the barotropic tides seems to also be a determining factor in the intensity of the baroclinic tides. Because the baroclinic tides depend upon the density stratification for their existence and intensity, they can be quite seasonal. Mathematically, the generation process is a scattering problem, with the variable bottom topography serving to scatter barotropic tidal energy into baroclinic modes in a density-stratified, rotating fluid (Prinsenberg et al., 1974).

The baroclinic tidal energy propagates both shoreward and seaward. Baroclinic tidal motion can produce vertical particle displacements of 10 to 100 m and horizontal velocities

of 0.10 to 1.0 m/sec. By its baroclinic nature, it has large vertical shears which can lead to shear instabilities and thus mixing. Their phase speeds are of the order of 0.10 to 1.0 m/sec; hence, they are very vulnerable to interactions with mean flows (of comparable speeds). Baroclinic tidal motion tends to dissipate and become incoherent over distances of only a few tens or hundreds of kilometres. Petrie (1975) has measured the current structure associated with the M_2 internal tide on the Scotian shelf and slope. He found baroclinic currents as high as 0.17 m/sec over the slope, but much less over the shelf. Baroclinic currents were largest near the surface. Apparently, the internal tidal flows were generated at the shelf break, but damped out through frictional dissipation over the shelf proper with a dissipation length scale of about 15 km.

Occasionally baroclinic tidal motion is so intense that internal tidal bores and short-period internal solitons are formed, which can produce the most intense currents observed in some shelf regions (Halpern, 1971; Lee and Beardsley, 1974). The surface expressions of these motions are readily observable on satellite imagery (Apel et al., 1975). Excellent introductions to the dynamics of baroclinic tidal motion are presented by Mooers (1970), Wunsch (1975), and Chuang (1980).

IV. WIND-DRIVEN CURRENTS

A. Ekman Dynamics

The essential features of wind-driven currents were described in a classical paper by Ekman (1905). He considered the effect of a suddenly imposed, constant wind stress on a horizontally homogeneous, infinitely deep ocean with con-

stant vertical eddy viscosity. The governing equations are:

$$\frac{\partial u}{\partial t} - fv = \frac{1}{\rho} \frac{\partial}{\partial z} \tau_{xz} \tag{9}$$

$$\frac{\partial v}{\partial t} + fu = \frac{1}{\rho} \frac{\partial}{\partial z} \tau_{yz} \tag{10}$$

where τ_{xz} and τ_{yz} are shear stresses. Since the flow is turbulent, the specification of these stresses is the most difficult part of the problem. Ekman made the simplest assumption, that the situation is analogous to laminar shear flow with the molecular viscosity replaced by a much larger eddy viscosity. In that case,

$$\tau_{xz} = \rho K \frac{\partial u}{\partial z} , \tag{11}$$

where K is the kinematic eddy viscosity. Unfortunately, K is not a material property of the fluid, but depends on the flow and the fluid properties in an imperfectly understood fashion. In spite of this problem, models using eddy viscosities that are either constant or defined simply have been reasonably successful.

The wind stress vector (τ_x^w, τ_y^w) enters as a boundary condition through equations of the form

$$\tau_x^w = \rho K \left.\frac{\partial u}{\partial z}\right|_{z=0} . \tag{12}$$

Calculation of the wind stress is a long-standing problem in meteorology. Drag in a turbulent shear flow is expected to be proportional to the square of the speed, so

$$\tau_x^w = \rho_a C_a u_a (u_a^2 + v_a^2)^{1/2} \quad , \tag{13}$$

where subscript a refers to properties of the air and C_a is a drag coefficient. There is now general agreement that C_a increases with wind speed due to the increasing roughness of the sea surface. The formulas

$$\begin{aligned} C_a &= 0.5 \times 10^{-3} w_a^{1/2} \qquad w_a < 15 \text{ m/sec} \\ C_a &= 2.6 \times 10^{-3} \qquad\quad w_a \geq 15 \text{ m/sec} \end{aligned} \tag{14}$$

where $w_a^2 = u_a^2 + v_a^2$

proposed by Wu (1969) have often been used in modeling work.

The stress near the water surface might be expressed by a formula of the same form as (13) rather than by (12). If the wind and current boundary layers are similar, the current speed will be $(\rho_a/\rho)^{1/2}$, or about 3 percent, of the wind speed. This "3 percent rule" has often been used to estimate surface drift currents with reasonable success. However, it should not be expected to give accurate results in all cases, since it neglects the deeper development of the current as well as lateral variations in wind and bathymetry. Still, the ability to predict surface currents from wind measurements only, measurements which soon may be routinely collected by satellite, is so enticing that the problem continues to attract attention. Weber (1981) relates the eddy viscosity to the properties of a fully developed wave field, which depends on the wind, and finds surface Ekman currents to range from 2.1 to 3 percent of the wind speed

and deviate 25 to 36° to the right of the wind direction in the northern hemisphere for moderate winds.

Much insight into the nature of wind-driven currents can be gained by studying simplified cases. If the water depth is infinite, the steady-state solution to equations (9) and (10) with constant eddy viscosity is

$$u = \frac{\tau_y^w}{Ka\sqrt{2}} e^{az} \cos (az + \pi/4)$$
$$v = \frac{\tau_y^w}{Ka\sqrt{2}} e^{az} \sin (az + \pi/4) \qquad (15)$$

where τ_y^w, the wind stress, is applied in the positive y-direction and $a \equiv \sqrt{\rho f/2K}$. Equations (15) represent a velocity vector that lies 45° to the right of the wind stress at the sea surface and that decays exponentially and spirals to the right as depth increases. The net transport, whose magnitude is $\tau_y^w/\rho f$, is directed 90° to the right of the wind stress (in the northern hemisphere). The thickness of this wind-driven boundary layer, known as the Ekman layer, is about π/a. If τ_{xz} and τ_{yz} take a form different from (11), then the resulting velocity profile will also be altered. The fact that the net transport is 90° to the right of the wind stress, though, will not be changed.

The solution of equations (9) and (10) for finite water depths is more complicated, but can still be developed analytically and the development of the current, in time, integrated numerically (Faller and Kaylor, 1969).

Figure 2 illustrates some features of this solution for a 20-m/sec wind blowing over a 100-m-deep ocean with $K = 0.02$ m^2/sec. The bottom boundary condition was zero current rather than a bottom stress law. In each part of

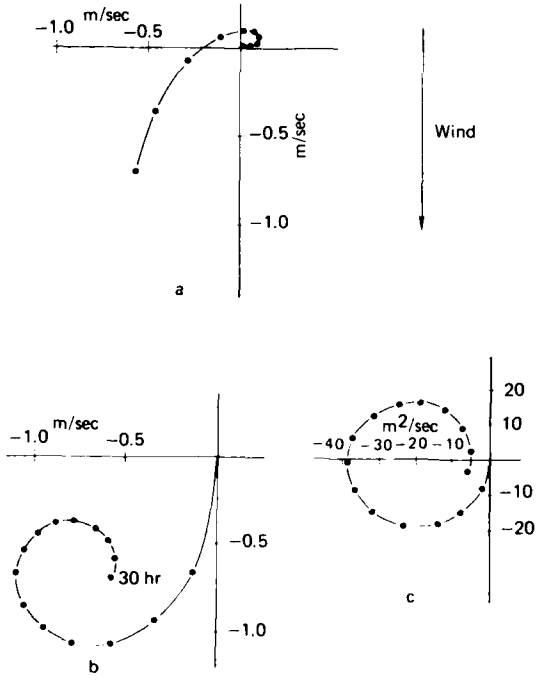

Figure 2. a, Current profile after 30 hours, with dots giving the tips of vectors and 10-m depth intervals. b,c, Development of surface current and transport, with dots representing the tips of vectors at 2-hour intervals. (Forristall, George Z., J. Geophys. Res., 79(18):2724, 1974, copyrighted by the American Geophysical Union).

the figure, the dots represent the tips of vectors whose tails are at the origin. In Figure 2a, the dot farthest from the origin shows the surface current vector, and the other dots show the currents at succeeding levels at 10-m increments. Figures 2b and 2c, respectively, show the surface velocity and the transport at 2-hour intervals. The inertial oscillations (see Sec. IV-E) in the transient response, i.e., oscillations with a period close to $2\pi/f$, decay more slowly than is usually observed in nature. In the computations, this is caused partly by the impulsively started wind stress.

If the water depth is less than π/a, the Ekman depth, then the wind-driven current applies a stress to the seabed. The occurrence of this stress drives a bottom Ekman layer near the seabed which alters the flow in the wind-driven surface Ekman layer. For a constant wind stress, a more or less complex current profile will eventually be obtained depending on the boundary conditions imposed at the seabed, e.g., no slip, linear friction, quadratic friction, etc.

One of the major problems in modeling coastal and shelf circulation is a proper parameterization of the turbulent mixing and dissipative processes. In the present problem, these processes are represented by the right-hand side of equations (9) and (10). Madsen (1977) has reviewed the various suggested parameterizations for this stress term and found them to be inadequate. He suggests that the term be modeled as

$$-\frac{\partial}{\partial z}\left(u_* z \frac{\partial u}{\partial z}\right) \tag{16}$$

where $u_* \equiv \sqrt{|\tau^w|/\rho}$ is the shear velocity and κ is von Karman's

constant, 0.4. This approach is theoretically appealing and furthermore reproduces many of the observed features of wind-driven currents. The surface velocities approach the observed 3 percent of the wind speed, and the turning of the surface current with respect to the wind is only about 10°, much closer to the observed values than the 45° turning required by Ekman. Furthermore, very strong near-surface shear is predicted. On the negative side, inertial oscillations are damped out much more rapidly than is seen in real oceans. (Ekman's original model did not damp them out sufficiently rapidly.) Furthermore, this model for the dissipative process expresses no dependence on density. (The ρ in the definition of u_* is assumed constant.) If the wind is strong, the near-surface shear will become unstable, breaking down into turbulence with increased mixing and a more uniform mean velocity profile resulting. The mixed layer models discussed below may then be more appropriate.

Ekman theory, because of the complex response caused by time-varying winds (Faller and Kaylor, 1969), has been difficult to verify, in detail, from field measurements. Hunkins' (1966) work on the floor under pack ice is a notable exception. Nonetheless, the concepts embodied in the model and the results of the vertically integrated form of the theory have proven to be fundamental to much of our understanding of shelf dynamics (e.g., Csanady, 1981).

B. Storm Surges

Ekman theory must be modified in shallow water and as the shoreline is approached. The restriction that no water may flow across the coastline requires that, when

a wind is blowing parallel to the coast, coastal water level must either rise or fall, thus creating a pressure gradient perpendicular to shore. In the steady-state situation, this pressure gradient may be balanced by the Coriolis force from a current directed parallel to shore (Allen, 1980), although other possibilities also exist. In shallow water, i.e., when the Ekman layer reaches to the bottom, bottom friction will be important and there will be a component of net transport in the downwind direction as well as the cross-wind direction (Groen and Groves, 1963). In such a situation, a cross-shore wind will also cause a rise or lowering of coastal sea level.

The coastal water level rise is called a storm surge. When it reaches heights of up to 8 m above normal high-tide levels, it can be terribly destructive to both shorelines and coastal structures. Strong currents are dynamically linked to high surges, and, inasmuch as the waves that dominate design criteria occur in the same storms, these currents can be important in the design of offshore structures. Few observations of storm currents are available, although the number has increased slowly in recent years (Table II), and their magnitude must thus be estimated through the hindcasting methodology described in previous chapters.

The details of the bathymetry, coastal morphology, and storm meteorology all affect the magnitude of the currents hindcast, and their complexity dictates the use of numerical models. The models used are similar to those described in the section on tidal currents. However, the assumption of a current uniform with depth is much less realistic for wind-driven currents than for tides.

TABLE II

Examples of Observations of Intense Storm-Driven Currents

Max. Speed (m/sec)	Water Depth (m)	Meter Depth (m)	Location	Reference
1.4	465	21	Florida Slope (Hurricane Frederick)	*Shay and Tamul (1981)*
1.6	6.3	5	Florida Shelf (Hurricane Camille)	Murray (1970)
0.8	17	7	Texas Shelf (Hurricane Anita)	Smith (1978)
2.1	20	4	Texas Shelf (Tropical Storm Delia)	Forristall et al. (1977)

To account for the driving force due to the pressure gradient from sea level rise, surface slope terms are added to equations (9) and (10), but baroclinic pressure gradients are still ignored, so that

$$\frac{\partial u}{\partial t} = fv - g\frac{\partial \eta}{\partial x} + \frac{1}{\rho}\frac{\partial}{\partial z}\tau_{xz} \tag{17}$$

$$\frac{\partial v}{\partial t} = -fu - g\frac{\partial \eta}{\partial y} + \frac{1}{\rho}\frac{\partial}{\partial z}\tau_{yz} \tag{18}$$

If equations (17) and (18) are integrated through the depth, they become equations (5) and (6) with the addition of wind stress terms on the right-hand side. The continuity equation is still (7).

The bottom stress is often imposed by simply requiring that the bottom velocity vanish (Ekman, 1905). This was done in deriving the solutions displayed in Figure 2 for an unbounded ocean. The bottom stress drives an Ekman layer near the bottom. The mass transport within this bottom layer is directed opposite to and just balances the Ekman transport in the surface Ekman layer when a coastline is imposed and longshore homogeneity is assumed.

Murray (1975) has suggested that by specifying the stress at the bottom, rather than the velocity, more realistic velocity profiles throughout the water column are obtained.

It is most consistent to take the bottom stress proportional to the square of the near-bottom current. However, there are other possibilities. The oscillations due to waves prevent full development of the turbulent boundary layer, and Forristall et al. (1977) argued that a linear drag relation might be more appropriate in that case. The

question of boundary layers under combined waves and currents has been investigated in much greater detail by Grant and Madsen (1979). It is not presently possible to make a clear choice between the drag formulations since reasonable agreement with the limited data available can be obtained by adjusting the coefficients in the models.

The vertical variation of the currents described by equations (17) and (18) is evidently important, and the surface slope terms in those equations can be found only through combined use of the momentum and continuity equations over the area of interest. The computational demands of a three-dimensional, time-dependent problem are quite large, but numerical models of this sort have been formulated. One approach, taken by Leendertse et al. (1973), is to divide the water into several layers and integrate the equations across each layer. Expressions for the shear stress between layers must then be developed.

Several hybrid numerical schemes have been developed to reduce the computational requirements while retaining vertical resolution. Heaps (1972) described the vertical structure as a series of eigenvectors and solved a momentum equation for each eigenvector. Forristall (1974) solved the integrated equations (5) and (6) on a two-dimensional grid, saving the surface slope history for a later calculation of (17) and (18). Cheng (1976) solved for the vertical structure as the two-dimensional solution was progressing, taking advantage of the fact that long time steps are possible in the solution for the vertical structure. Nihoul et al. (1979) reviewed these models and described a new approach similar to that of Heaps.

Important measurements of currents associated with a storm surge were made by Forristall et al. (1977) during Tropical Storm Delia, which crossed the upper Texas coast early in 1973. Delia was a weak storm compared to severe hurricanes, with a minimum pressure of 987 mb and a peak wind gust measured offshore of 32 m/sec. The 30-minute-average wind speed maximum was 25 m/sec, and the maximum trough-to-crest wave height was 7.6 m. No significant damage was caused by the storm. Nevertheless, Delia produced very strong currents.

The current measurements were made at the Buccaneer oil and gas production platform, located 50 km south of Galveston on the Texas coast. The water depth at the site is 21 m, and the water column is typically well mixed in the late summer. Three electromagnetic current meters were supported on a taut mooring suspended beneath a 60-m-long bridge that connects two pile-supported platforms. The meters were at nominal depths of 4, 10, 18 m below mean water level. The signals from the meters, which have a very fast response time, were continuously recorded, and later filtered at 120 s to remove the oscillations due to waves.

The measurements are shown in Figure 3 as the solid lines. The meters measured vector components of velocity, so there are two traces for each meter. Current meter 1 is the uppermost, the positive x direction is toward the north, and the positive y direction is toward the east. The current speed at the top meter peaked at 2.1 m/s in a west-southwest direction on the afternoon of September 4. Strong currents persisted to the depth of the bottom current meter, where the velocity was about 75 percent of

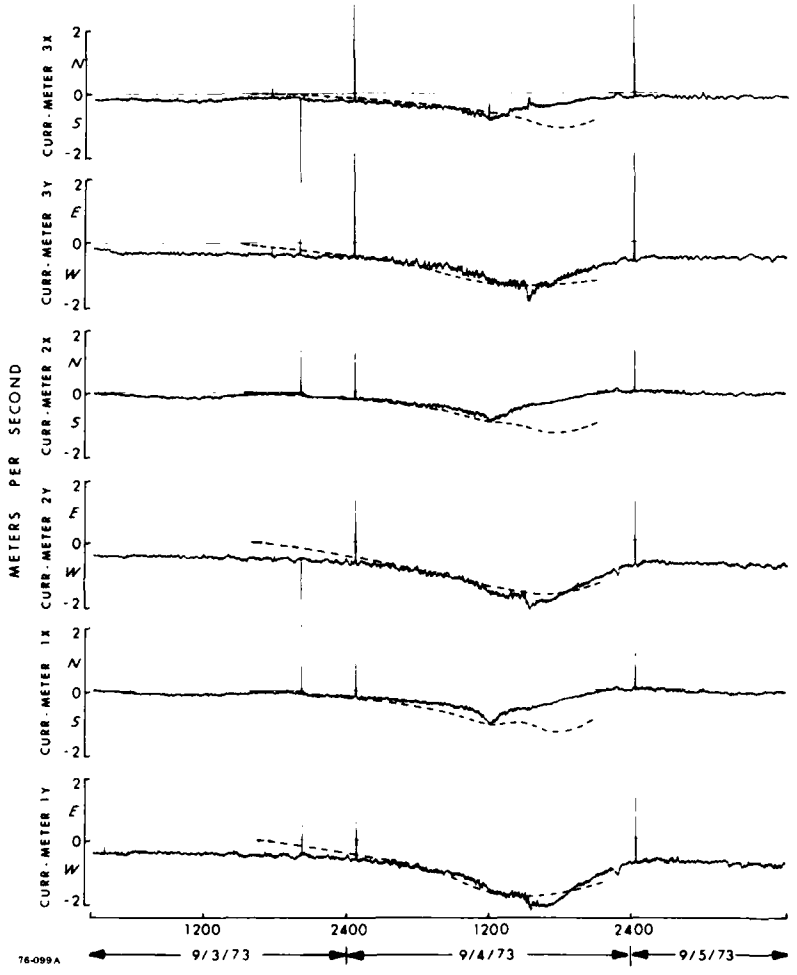

Figure 3. Time-series of currents measured in 21 m of water during Tropical Storm Delia. North-south and east-west components are presented in pairs from top to bottom for the meters at nominal depths of 4, 10, nd 18 m. The dashed lines represent hindcast current estimates. (Forristall, G. Z., et al., J. Phys. Oceanogr., 7(4):537, 1977, copyrighted by the American Meteorological Society).

the velocity at the top meter. The currents were generally directed along trend of the bottom contours near the site.

It is clear that the observed currents were caused by the storm, but they are not related to the local wind in a simple fashion. For example, 3 percent of the sustained wind speed is only 0.75 m/sec. The vertical structure of the currents also does not much resemble the Ekman spiral in Figure 2a. To understand and hindcast currents in this type of situation, a model that includes the details of the bathymetry and spatial structure of the wind field is needed.

Forristall et al. (1977) solved the vertically integrated version of equations (17) and (18) on a 41- by 63-point finite-difference grid with a spacing of 11,592 m. A constant eddy viscosity $K = 0.03\ m^2/sec$ was used, and the bottom friction was taken to be a linear function of the near-bottom velocity, with a drag coefficient of 0.001 m/sec. The near-bottom velocity necessary for this computation was determined through a convolution integral technique. After the surface slopes were calculated using the vertically integrated model, equations (17) and (18) were solved directly for the vertical structure of the currents at Buccaneer.

The results of the computations are shown as the dashed lines in Figure 3. Agreement between the measurements and hindcast is very good for the buildup of the storm, and the proper depth dependence has been achieved. However, the hindcast north-south component is in error after the peak of the storm. The fit was achieved by tuning the bottom drag coefficient and eddy viscosity. More data are needed to determine if the values that gave good results for Delia will also be appropriate in other situations.

It is instructive to study the balance of forces predicted by the model. Although none of the forces was measured directly, the fit between the measured and hindcast currents indicates that these terms are reasonably modeled. Figure 4 shows the forces acting on the vertically integrated current, or transport, at 1200 CDT, September 4, 1973. The dashed line shows the transport in units of square meters per second, and the solid lines show the forces in kinematic units of square meters per second squared.

The transport is 29 m^2/sec toward the southwest, so the average current over the 21-m depth is 1.38 m/sec. The drag force is nearly opposite to the transport direction, with a slight deviation due to the fact that the transport and near-bottom current are not exactly in the same direction. The Coriolis force is directed 90° to the right of the transport, and the pressure gradient force, or slope force, points roughly offshore. The "inertia force" points in the opposite direction to that in which the flow is being accelerated. At the time for which the figure is drawn, the wind is accelerating the flow against the bottom drag, while the pressure gradient force partly balances the Coriolis force perpendicular to the flow. This balance of forces should not be taken as a general rule, since it depends on the details of the bathymetry and storm track. The most important fact about the diagram is that all the terms are of comparable magnitude, and it is thus unlikely that a simpler model which neglects any of the terms could give reliable results.

Cooper and Pearce (1980) also modeled the Delia measurements using a Galerkin numerical technique but parameters similar to those used by Forristall et al. (1977). The

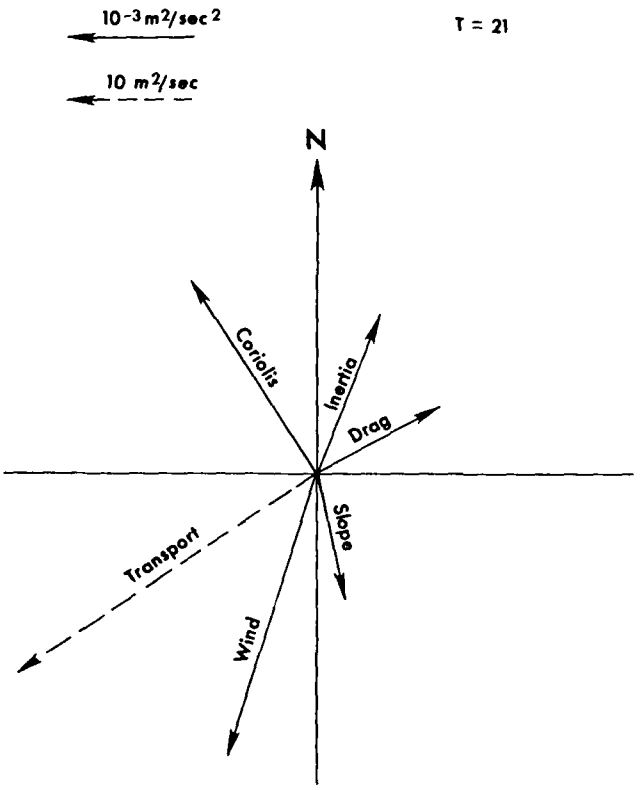

Figure 4. Vertically integrated force balance at Bucaneer Platform during Tropical Storm Delia (1200 CDT, 4 September 1973).

fit of their results is slightly better, which is apparently due to differences in the wind field used.

C. Mixed Layer Models

There is good observational evidence that the wind stress can mix a surface layer well enough for the current to be nearly uniform through the depth of the layer with thin shear layers occurring at the surface and near the large density gradient at the base of the mixed layer. Over the inner shelf the surface mixed layer may be only 10 m thick or less. It usually thickens seaward and may be 50 m or more thick at the shelf break. It often constitutes a large portion of the water column over the shelf.

Horizontally homogeneous models of this surface mixed layer have been used with varying degrees of success in the open ocean. These models offer certain insights into the important dynamical balances. Energy for mixing within the layer is supplied at the sea surface either by the wind stress or the buoyancy flux, i.e., heating, cooling, evaporation, precipitation, brine rejection by freezing ice, or fresh water input by melting ice or river flow. If a buoyancy flux causes the surface waters to become more dense, then overturning and turbulence generation will result. If the surface waters become less dense, then the water column becomes more stable and the mixed layer can deepen only if energy is supplied from some other source. The wind stress can supply energy directly to the turbulence in the mixed layer. This turbulence maintains the well-mixed nature of the layer and also erodes the base of the layer, causing it to deepen through turbulent entrainment of lower layer water. Figure 5 shows the time history of

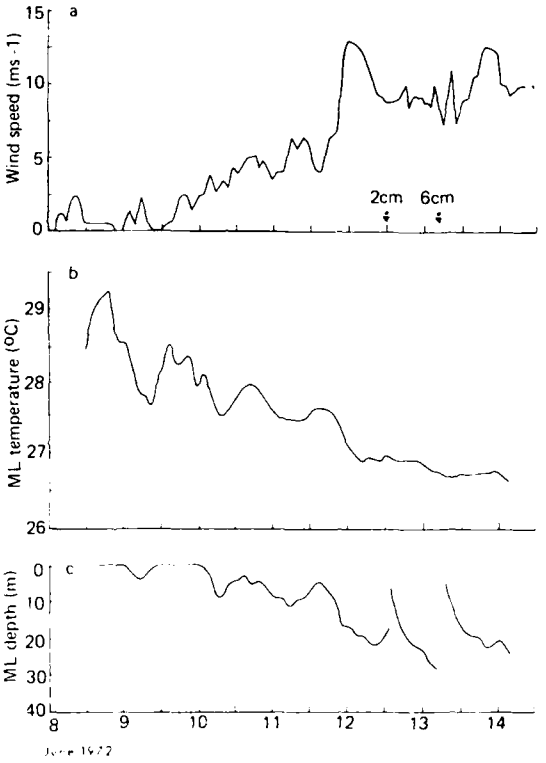

Figure 5. Time histories of a) wind speed, b) mixed layer temperature, and c) mixed layer thickness from the West Florida shelf. The abrupt changes in mixed layer thickness at the end of the record are due to rainfall (arrows), which reduced the near-surface density and generated a shallow mixed layer. (Redrawn from Price et al., 1978.)

a wind-stress event over the West Florida Shelf and its effect on mixed-layer temperature and depth. As the stress increases, the mixed layer deepens and cools because colder water is entrained across the pycnocline. Two rainfall events of 0.02 and 0.06 m are noted on the upper diagram. The thin mixed layers of lighter water caused by these rainfalls are rapidly deepened by the strong winds at the end of the record. The wind also drives the mean motion in the mixed layer, creating a shear across the base of this layer. This shear results in turbulent entrainment of water from below the base of the mixed layer. Niiler (1975) and Niiler and Kraus (1977) describe how the balance between the dominant source terms mentioned above and the sinks for turbulent energy, background dissipation and entrainment vary during the course of a storm. Entrainment, driven by shear instability of the mean flow at the base of the mixed layer (Pollard et al., 1973), is by far the most impressive stage of the mixed layer deepening caused by storm passage. This occurs during a period $T = \pi/f$ after the onset of the storm, and during this time the depth of the mixed layer rapidly deepens to a depth

$$h_{ml} = 2 \left(\frac{\tau^w}{\rho N f}\right)^{1/2} \tag{19}$$

where N is the Brunt-Vaisälä frequency immediately below the mixed layer and τ^w is the magnitude of the applied wind stress. The transport within the mixed layer is the Ekman transport, so, ignoring the transient inertial oscillations, the velocity should be of the order of

$$u_{ml} = 0.5 \left(\frac{\tau N}{\rho f}\right)^{1/2} \tag{20}$$

On longer time scales, though, the weaker winds between wind events may supply enough energy to the turbulence in the surface layer to slowly, but continually, erode the base of the mixed layer (Denman and Miyake, 1973).

The depth of the mixed layer is important in current modeling because mixing processes strongly affect the vertical profile of wind-driven currents. In the mixed layer, the vertical exchange of momentum is so rapid that it is possible to consider a slab model in which the current is constant with depth in that layer. In a model that uses an eddy viscosity to parameterize the exchange of momentum, the value of this coefficient would be taken to be much higher in the mixed layer than below it. Gordon (1982) discusses the measurements needed to distinguish which approach is more realistic.

During Hurricane Eloise, some measurements were made which have helped to motivate and verify mixed-layer current models. The storm passed close to two environmental buoys in the Gulf of Mexico in September 1975 on its way to a landfall near Fort Walton Beach, Florida. The minimum central pressure near landfall was 955 mb. Forristall (1980) measured currents from an oil production platform located in 100-m water depth near the Mississippi Delta, which was on the fringe of the storm. The current speed was nearly the same at 5- and 23-m depths, reaching a maximum of 0.70 m/sec. The current at 46-m depth was much less. Measurements of the density structure before and after the storm indicated that the mixed layer depth increased from virtually zero to between 30 and 45 m.

Forristall attempted to model these results using a constant mixed-layer depth of 30 m, with the eddy viscosity

$K = 0.03\ m^2/sec$ in the mixed layer and $K = 0.003\ m^2/sec$ below it. The model was reasonably successful while the current speed was increasing, but the hindcast current continued to increase after the measurements reached their peak.

Current measurements in Eloise were also made by the NOAA Data Buoy Office (Withee and Johnson, 1975) in deep water with a current meter suspended at 50-m depth. The measured current speed reached 0.90 m/sec almost a day after the center of the storm passed the buoy. This strong current was due to inertial oscillations set up by the storm rather than to direct wind forcing. Surface and 50-m temperature and salinity measurements were interpreted by Martin (1982) as implying a maximum mixed-layer depth of 55 m.

Martin (1982) hindcast the buoy observations using a one-dimensional mixed-layer model. He used the level 2 turbulence closure of Mellor and Yamada (1974) in which the eddy viscosity is specified as a function of the local vertical velocity shear and the stability of the density structure. Despite the presence of a mixed layer, the parameters used permit considerable variation of current with depth. At the peak of the storm, the current varies smoothly from 1.50 m/sec at the surface to an assumed initial value of 0.30 m/sec at a depth of 60 m. The hindcast results at 50-m depth agree well with the measurements, but the current at that depth was strong only in the oscillations after the storm. There are no data for the direct verification of the near-surface currents at the peak of the storm.

Price (1981) also hindcast Eloise and compared the results to the data buoy measurements. His model was two-dimensional, with three layers representing the mixed layer,

a shear zone, and a deep interior. The velocity in the mixed layer was taken to be constant. The results presented showed that the mixed layer grew to a depth of 82 m under the storm and the velocity within the layer was 1.13 m/sec. The total transport in the mixed layer is thus considerably greater than that implied by Martin's results. The difference is likely due to the inclusion of the curvature of the moving wind field in Price's model. It would seem both practical and useful to now construct a model that includes the two-dimensional structure of the wind and bathymetry, permits a vertically variable velocity, and has a dynamically controlled mixed-layer depth.

As mentioned earlier, when a current that extends to the bottom is flowing on the shelf, it will apply a snear stress on the bottom. This shear stress will generate a bottom mixed layer, often referred to as the benthic boundary layer, similar to the surface mixed layer. Many of the concepts appropriate to the surface layer can be carried over to the benthic boundary layer. There are differences, though, as well. The sea surface is a free surface, while the seabed is often rigid. (An elastic seabed has proven to be a useful model in certain nearshore wave modeling, e.g., Tubman and Suhayda, 1976.) This implies a different set of boundary conditions to be imposed on the respective mixed layers. Also, sediment erosion and transport by the benthic boundary layer may directly influence its dynamics. Progress in modeling the benthic boundary layer (e.g., Adams and Weatherly, 1981) is paralleling similar efforts in the surface mixed layer. A major observational program to investigate the properties of such a bottom boundary layer, HEBBLE (Hollister, 1981), is presently in progress.

D. Upwelling (Event Scale)

Atmospheric synoptic disturbances (cyclones, anticyclones, and frontal passages) can produce transient coastal upwelling if a favorable alongshore wind stress is imposed for at least several inertial periods (a few days in mid-latitudes). Thus transient upwelling typically occurs with a repetition rate of several days to several weeks, depending on season and latitude (Kundu and Allen, 1976).

When a wind blows over stratified water in the northern (southern) hemisphere, with the coast to its left (right), an Ekman transport of water away from the coast develops. The divergence of water at the coast is partially balanced by a vertical flux of water from below. If this vertical velocity persists long enough, the pycnocline, the region of maximum density gradient, will be brought to the surface and outcrop, causing a density front in the surface layers. Associated with the resultant horizontal density gradients are horizontal pressure gradients. To a first approximation, these drive geostrophic currents over the shelf.

If frictional dissipaiton is negligible and the time scales of interest are sufficiently long that mean vertical accelerations are small compared to gravity, i.e., we ignore gravity waves, then the vertical momentum balance is hydrostatic

$$\frac{1}{\rho}\frac{\partial p}{\partial z} = g \tag{21}$$

where p is pressure, g is the acceleration due to gravity, and z is the vertical coordinate. If, furthermore, the field acceleration terms in the horizontal equations of motion are negligible, then

$$\frac{1}{\rho}\frac{\partial p}{\partial x} = fv \tag{22}$$

$$\frac{1}{\rho}\frac{\partial p}{\partial y} = -fu \tag{23}$$

Equations (21)-(23) describe a geostrophic current. These equations may be combined to yield a description of the vertical shear of the horizontal current structure, the thermal wind equations

$$\frac{g}{\rho f}\frac{\partial}{\partial x} \approx \frac{\partial v}{\partial z}$$

$$\frac{g}{\rho f}\frac{\partial}{\partial y} \approx -\frac{\partial u}{\partial z} \tag{24}$$

It is readily seen that the geostrophic currents are strongly sheared.

Significant upwelling events are known to occur in many regions, e.g., off the Oregon coast, the Peru coast, the northwest African coast, and the west South African coast (Smith, 1968). Major investigations of the upwelling regimes have been carried out along the Oregon, Peruvian, and northwest African coasts. While similarities exist between the regions, there are also local differences (Allen and Smith, 1981).

Smith (1974) describes a series of current meter measurements from the Oregon shelf during the summer upselling season of 1972. The meters were moored in 100 m of water. The mean wind stress was southerly, but variable. The 20- and 40-m current meters showed a mean southerly drift, while the meters at 60 and 80 m showed a mean northerly flow.

Numerous events occurred in which the wind increased to greater than 7 m/sec in the southerly direction. These events were associated with a drop in coastal sea level, an increase in the southerly flow (it measured near 0.5 m/sec at 20 m during such an event on July 15), and development of a surface density front. The vertical shear was at times as high as 0.4 m/sec/60 m. The presence of the surface density front is important not only because of its effect on the geostrophic flow but also because of the convergences associated with such a front (Mooers et al., 1976) (see Sec. V-C).

E. Near-Inertial Motions

Near-inertial motions are caused both by time-varying winds (Pollard and Millard, 1970) and the geostrophic adjustment of unbalanced currents (Blumen, 1972); sometimes these are related processes. The inertial motion resulting from a suddenly imposed wind stress has already been shown in Figure 2. Pure inertial motions are horizontal motions in circles with a radius of $|u|f^{-1}$, where $|u|$ is the magnitude of the horizontal velocity. They rotate with a period equal to the inertial period, $2\pi f^{-1}$. They result from the local acceleration being balanced by the Coriolis force,

$$\frac{\partial u}{\partial t} = fv$$

$$\frac{\partial v}{\partial t} = -fu \qquad (25)$$

The period of near-inertial motions is a few percent greater than the inertial period. Near-inertial motions over the shelf are observed to contain appreciable energy.

If vertical density stratification is present, near-inertial motions propagate vertically (Johnson et al., 1976). Near-inertial motion may be generated by an impulsively applied wind stress of finite horizontal scale and amplified if the wind vector rotates clockwise (anticlockwise), in the northern (southern) hemisphere, with an inertial period. Typically, the velocity amplitude of these motions is a few tenths of a meter per second, the vertical scale is about 10 m, the horizontal scale is about 10 km, and they persist for several cycles. Because of its relative intensity and short vertical scales, near-inertial motion often produces sufficient vertical shear to cause mixing through shear instability, both at the base of the surface mixed layer and in the interior of the water column. Over the continental shelf, it can also reach the bottom boundary layer, where it may contribute to mixing or modulate the strength of the boundary layer flow (Johnson et al., 1976).

During strong, impulsive wind events, near-inertial oscillations may be the strongest flows generated. Daddio et al. (1978) found inertial oscillations of 0.5 m/sec amplitude over the Louisiana inner shelf following normal winter frontal passages. Hurricane Frederick generated inertial motion with an amplitude of 1.1 m/sec over the Florida slope (Shay and Tamul, 1981) at 21-m depth in 550 m of water. As mentioned above, Martin's (1982) hindcast of mixed-layer currents driven by Hurricane Eloise show inertial currents approaching 0.5 m/sec.

F. Coastal Boundary Layer

Strong currents flowing parallel to shore are often observed within the highly stratified inner shelf waters

near the coast. This coastal boundary layer is typically about 10 km wide and responds rapidly to an imposed wind stress. Nearshore waters are often so highly stratified that the situation must be approximated as two-layered, a light (warm and/or fresh) surface layer overlying a heavier (colder and/or saltier) bottom layer. The simplest set of equations for the transports in the two layers are:

$$\frac{\partial U}{\partial t} - fV = -\frac{\partial p}{\partial x}$$

$$\frac{\partial V}{\partial t} + fU = -\frac{\partial p}{\partial y} + F$$

$$\frac{\partial U}{\partial x} + \frac{\partial V}{\partial y} = -\frac{\partial}{\partial t}(\eta - \eta') \qquad (26)$$

$$\frac{\partial U'}{\partial t} - fV' = -\frac{\partial p'}{\partial x}$$

$$\frac{\partial V'}{\partial t} + fU' = -\frac{\partial p'}{\partial y}$$

$$\frac{\partial U'}{\partial x} + \frac{\partial V'}{\partial y} = -\frac{\partial \eta'}{\partial t}$$

where U(U'), V(V') are the transports perpendicular to shore and parallel to shore, respectively, p(p') is the integrated pressure across the layer, $\eta(\eta')$ is the free surface (interface) displacement from its equilibrium position, and F is an applied shore-parallel force. Primed quantities refer to the lower layer. These equations are to be solved under the condition of no normal flow at the coast. If F, which is treated as a body force in the above equations, results from a wind stress abruptly applied at t = 0, both a periodic motion (see section on near-inertial motion) and an aperiodic motion result. Csanady (1976) has solved these equations for the aperiodic motion under the assumptions

of an infinitely-long, flat shelf or a sloping shelf terminated by a vertical wall at the point where the pycnocline intersects the bottom when no motion is present. In the flat shelf case, the alongshore velocities are of the form of an exponentially decaying, shore-bound jet in the upper layer and a much slower flow in the lower layer. The offshore scale length is

$$R = \frac{c}{f} \tag{27}$$

and c, the internal wave phase speed, such that

$$c^2 = g' \frac{HH'}{H + H'} \tag{28}$$

where g' is reduced gravity

$$g' = g \frac{\rho' - \rho}{\rho} \tag{29}$$

and H and H' are the equilibrium layer depths. The equations suitable to the more realistic case of a sloping bottom must, in general, be solved numerically. The resulting flow structure is again jetlike, but the velocity maximum is now displaced offshore rather than being at the shoreline itself. This is indeed what is observed in nature (e.g., Csanady, 1972; Crout and Murray, 1979). Figure 6 illustrates the density and current structure within such a boundary layer along the Nicaraguan shelf. A wedge of fresher water against the coast is separated from deeper, saltier, and therefore denser offshore water by a strong density gradient. The current structure is a southerly jet displaced 10 km offshore and essentially confined to the upper 5 to 10 m. A slight reverse flow in the bottom layer near shore is

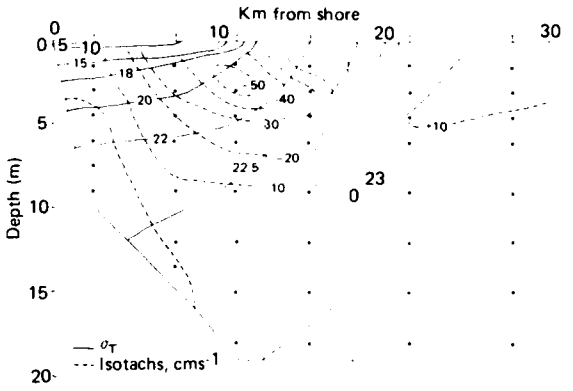

Figure 6. Cross-section of density and alongshore current on the Nicaraguan shelf.

observed. The peaks in alongshore speed are observed to be approximately 0.50 m/sec. The on-offshore velocities within the coastal boundary layer are much smaller in magnitude.

Since frictional forces are absent from equations (26), the solutions to these equations will be valid only for the initial period following onset of a forcing event. Furthermore, with neither friction nor alongshore pressure gradients, the lower layer flow within the coastal boundary layer will be very small. With the addition of an alongshore pressure gradient, significant lower layer flow may develop. An alongshore pressure gradient will produce a cross-shelf geostrophic flow which, when constrained by a no-flux condition at the shore, requires a longshore flow. The importance of longshore pressure gradients to continental shelf flow is becoming more apparent (e.g., Csanady and Scott, 1974), and the development of lower layer transports within the coastal boundary layer due to a time-varying longshore pressure

gradient has been observed (Csanady and Scott, 1974). A realistic solution to equations (26) would require their numerical solution with realistic bottom topography and the addition of frictional dissipation terms on the right-hand side of the four momentum equations, at least near shore. Observations indicate the existence of an inner frictional layer near shore which is distinct from an outer inertial boundary layer where friction is not important but inertial oscillations must adjust to the presence of a boundary (Murthy and Dunbar, 1981). Successful numerical solutions of similar sets of equations have been made by numerous authors, particularly in the context of coastal upwelling (e.g., Hurlburt and Thompson, 1973).

In the presence of realistic bottom topography, the coastal boundary layer structure described above may be significantly modified by the presence of topographic waves (see Sec. IV-G). The presence of such waves within the coastal boundary layer has been observed by Csanady (1976) significantly modified by the presence of topographic waves (see Sec. IV-G). The presence of such waves within the coastal boundary layer has been observed by Csanady (1976) in Lake Ontario. Crout and Murray (1979) also observed a meandering jetlike current within the coastal boundary layer on the Nicaraguan shelf. They were further able to estimate the importance of the various terms in the equations of motion and thus give the best available basic equation set for the coastal boundary layer:

$$fv - \frac{1}{\rho}\frac{\partial p}{\partial x} - \frac{1}{\rho}\frac{\partial \tau_x}{\partial z} = u\frac{\partial u}{\partial x}$$

$$fu + \frac{1}{\rho}\frac{\partial p}{\partial y} + \frac{1}{\rho}\frac{\partial \tau_y}{\partial z} = 0 \qquad (30)$$

where the x-axis is perpendicular to shore. The authors further determined that in the second of equations (30) only the barotropic pressure gradient, i.e., that due to the slope of the sea surface, was important. In the first equation the contribution to the pressure gradient due to the spatially varying density distribution is also important. Furthermore, the stress-gradient term in the first equation was found to be important only in the near-surface waters. Equations (30) have not yet been solved for the coastal boundary layer, either analytically or numerically.

G. Shelf Waves (Free and Forced)

Continental shelf waves are topographically trapped long waves. Their alongshore wavelength typically ranges from 100 to 1000 km. The waves are trapped over the continental margin by the sloping bottom and are strongly influenced by the earth's rotation. (They are only negligibly influenced by gravity.) They have alongshore phase speeds of a few meters per second or less, while their associated alongshore particle velocities can be as large as several tenths of a meter per second. Continental shelf waves propagate with the continent on the right-hand (left-hand) side in the northern (southern) hemisphere.

Shelf waves are primarily manifested as current oscillations; they can be viewed as vorticity waves. (However, corresponding coastal sea level perturbations may be as large as severals tenths of a meter.)

Shelf waves are dispersive with a high frequency cutoff that is less than the inertial frequency. The energy propagation of long waves is in the same direction as the phase propagation; for short waves, the energy propagation is

opposite. At the wavelength and frequency where the alongshore group velocity changes sign, wave energy can accumulate on the shelf (Buchwald and Adams, 1968). If the water column is density stratified, the situation is further complicated by the presence of vertically structured eigenmodes. Mean alongshore currents also add complexity. Since the phase speeds of the waves are generally of the same order of magnitude as the mean currents on a shelf, strong interactions between the shelf wave and mean motion may occur.

Atmospheric synoptic disturbances are usually, though not always, the source of shelf waves. Thus, they can be generated as part of the transient coastal upwelling or downwelling response, or the relaxation from a storm surge. Free waves exist in the far field of their atmospheric forcing and propagate at their eigenvelocity. Forced waves exist in the near field of their atmospheric forcing and propagate at the velocity of the forcing, which can oppose the direction of free waves. Resonance can also occur between free waves and the forcing. A rather comprehensive review of the complex topic of shelf waves has recently been presented by Mysak (1980).

Shelf waves are particularly important since we tend usually to think only of local forcing of shelf dynamics. Through the medium of these waves, information about a disturbance at one location can be transmitted along the shelf to another location (Gill and Clarke, 1974). Strong, rapid reversals of current structure that are apparently totally unrelated to the local wind have been recorded. During a coastal upwelling study over the Oregon shelf in 1973 the flow field was observed to change from a highly sheared southward flow to a nearly barotropic northward flow within

a period of about a day. The maximum change in current speed during the event was about 0.5 m/sec (Kundu et al., 1975). This event was later shown to have propagated northward along the shelf with a speed of about 120 km/day (Kundu and Allen, 1976). Not only current signals are transmitted by waves, but also water level signals. If the arrival of such a peak in water level coincides with high tide, abnormal and unexpected water level rises may occur with significant resulting damage (Groen and Groves, 1963). Finally, tidal currents may be strongly amplified if the shelf is resonant at the tidal frequency. Such a situation appears to occur over Rockall Bank (Huthnance, 1974), where diurnal currents as large as the semi-diurnal currents were observed in a region where the diurnal flows are expected to be only one-tenth the size of the semi-diurnal.

V. MOTIONS NOT DIRECTLY DRIVEN BY THE WIND

A. Internal Gravity Waves

Internal gravity waves are flow perturbations governed by the restoring force due to buoyancy, which is proportional to the product of the density gradient and the acceleration due to gravity. They may be generated by winds, tides, and unbalanced currents, among other mechanisms. Their horizontal phase speeds are of the order of a few hundredths of a meter per second to a few meters per second. For the lower frequency, longer wavelength internal waves, the Coriolis force also acts as a restoring mechanism. In general, free internal waves can exist for frequencies, σ, such that $f < \sigma < N$. Typically, wave periods range between a few minutes and a day, depending on the density stratification and the latitude. Internal waves are ubiquitous in the ocean, and

especially vigorous on continental shelves. (In fact, they are often of finite amplitude over shelves, taking the form of short wave trains of internal solitons.) They can propagate upward and downward as well as horizontally. Because they have strong vertical shear in the horizontal velocity, internal gravity waves can produce mixing due to shear instabilities. Roberts (1973) presents a comprehensive bibliography of earlier work on internal waves. She has also written a general introduction to the topic of internal waves (Roberts, 1975).

There have been at least two reported instances where internal waves with periods of a few minutes affected deepwater drilling operations.

During drilling operations in the Andaman Sea in 1976, Osborne et al. (1978) measured very large internal waves in 600 to 1000 m of water. The largest waves had heights over 60 m in the sharp thermocline, which lay at a depth of 50-150 m. The maximum currents caused by these waves had a speed of 1.8 m/sec. The passage of the waves was made evident at the water surface by surface rips. These bands of steep waves are caused by the convergence and divergence of the surface currents associated with internal waves. In fact, rips and the intervening slicks are visible in satellite photographs.

Osborne and Birch (1980) have interpreted the Andaman Sea waves as internal solitons. Calculations of the internal wave particle velocities based on this model agree well with the observations. The current velocity can thus be calculated from measurements of the wave height and period, which can be made with water temperature sensors.

Another set of measurements of large internal waves was made by Hodgins and Westergard (1981) in the Davis Strait in 1979. Waves of 20-45 m amplitude were measured in 350 m water depth. Currents up to 0.80 m/sec were associated with the waves. To give warning of an approaching packet of waves to the drilling vessel, a string of current meters with a surface buoy for radio telemetry was placed upwave of the vessel.

In both the Andaman Sea and Davis Strait, the packets of waves arrived at a specific time in the tidal cycle, and it has been possible to trace the source of the waves back to likely sites where tidal currents flowing over a sill could generate the waves.

The question of how the deep-ocean internal wave spectrum is modified as it impinges on the continental shelf and slope is important. Qualitatively, the concept of bottom intensification of internal wave energy on a slope is easily understood. For an inviscid fluid with constant N and small-amplitude internal waves whose properties, e.g., velocities, displacements, are proportional to

$$\exp i\,(k_x x + k_z z - \sigma t)$$

where k_x and k_z are wave numbers in the x and z direction, then

$$\sigma = N \cos \theta \tag{31}$$

where θ is the angle between the horizontal and the wave-number vector, $\vec{k}$, and σ is the wave frequency (Turner, 1973). Because the frequency of a wave must be conserved during

reflection from the bottom, or the ("rigid") sea surface, two situations, depending on the slope of the bottom, result when deep-ocean internal waves approach the continental slope and shelf. If the slope of the bottom is greater than the critical slope, θ_{cr} = arc cos (σ/N), for the wave in question, then the internal wave energy will be reflected back into the deep ocean. If the bottom slope is less than the critical angle, then the wave energy will be reflected toward the shore and concentrated within the nearshore wedge (Fig. 7). Internal wave energy density will increase landward. Furthermore, if one considers, in the subcritical case, two wave rays, before and after reflection from the bottom, it is apparent that the distance between the rays has decreased during reflection. Since energy cannot cross rays within the linear hypothesis, the wave energy near the bottom increases, giving rise to larger near-bottom velocities and shears. Other interesting phenomena such as an increase in k_x upon reflection also occur (Wunsch, 1969). The oceans are not inviscid, and some mixing and dissipation obviously must take place. The form that this dissipation assumes is still open to conjecture. Laboratory experiments (Cacchione and Wunsch, 1974) show good agreement with the theoretical predictions of linear wave theory and clearly demonstrate the importance of boundary-layer mixing. Field measurements are less conclusive. Data from the continental slope south of Massachusetts (Wunsch and Hendry, 1972) agree well with theory near the semi-diurnal tidal frequency, but are inconclusive at higher frequencies. Near-bottom amplification at the higher internal wave frequencies can be shown to be associated with turbulence in the bottom boundary layer. Data from Hudson submarine canyon

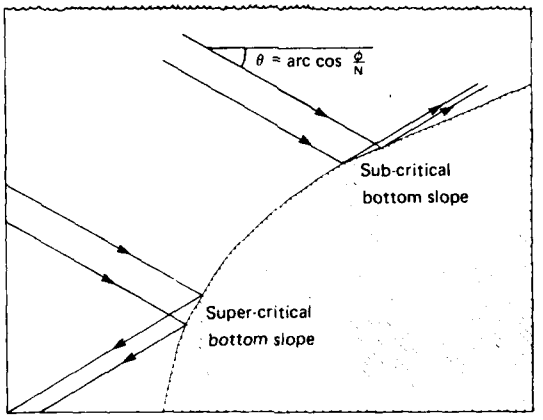

Figure 7. Schematic of subcritical and supercritical bottom reflection of internal wave in a fluid with constant Brunt-Vaisälä frequency, N.

also lend some credence to the predictions of linear theory (Hotchkiss, 1980). The complicating factors of a significantly three-dimensional topography make interpretation of the results difficult. Near-bottom intensification of internal wave energy, a shoreward energy flux, and a shoreward decrease in wavelength are all apparent in the data, though. The important, and as yet unresolved, problem is how the near-bottom internal wave field, which is amplified by the slope, interacts with the bottom boundary layer.

B. Eddies

Eddies are probably one of the most prevalent phenomena on continental shelves, yet they have not been much studied due to observational difficulties. Many data sets exhibit perturbations attributable to eddies, e.g., Niiler (1976), but few data sets provide a complete and convincing description of them; i.e., three-dimensional maps of anomalous

density structure or a set of velocity measurements indicating an essentially closed circulation. However, from basic dynamical considerations, and consistent with some available data, baroclinic eddies can be expected to be common in stratified shelf waters (Mooers et al., 1979). These eddies have a horizontal scale of the order of tens of kilometres to hundreds of kilometres. Horizontal velocities of 1 m/sec or greater and lifetimes of weeks to months can be anticipated.

Eddies can be generated on the shelf or offshore, and then propagate onto and along the shelf. They may be generated by baroclinically unstable boundary currents, by direct atmospheric forcing, or by flow over bathymetric anomalies. Open ocean eddies which "go aground" over the continental margin tend to be topographically controlled or guided (e.g., Elliott, 1979). As they advect or propagate along isobaths, they interact with ambient offshore and shelf waters. For example, they can entrain shelf water, form "streamers" of it, and inject it into the open ocean; hence, such eddies provide an enhancement of the oceanic transfer processes, particularly at the shelf break. Such a situation, south of Cape Cod, can be seen in the satellite image reproduced in Figure 8. Due to locally intense mixing and topographic control over submarine banks and canyons, and around coastal capes and embayments, standing eddies can be encountered in such environments (see Sec. VI-C).

Eddies can be particularly important where a strong oceanic current approaches a shelf. One such well-studied situation is the region north of Miami where the Florida Current interacts with a very narrow shelf. Spinoff eddies (Lee, 1975), with a cross-shelf scale of 10 km and an along-

Figure 8. Daytime thermal infrared image of the shelf and slope region south of Cape Cod, 1 July 1978. The image, from the NASA Heat Capacity Mapping Mission, was provided by NASA Goddard Space Flight Center. Two warm (lighter tones) eddies are seen at the north side of the Gulf Stream. They are interacting with shelf and slope waters, entraining filaments of cold (darker tones) shelf waters.

shelf scale two or three times this, occur with a periodicity of approximately 2 days. Major current reversals are associated with the passage of these eddies as well as a significant transport of heat and salt. Peak-to-peak velocity changes of approximately 1 m/sec have been observed to occur during the passage of an eddy.

C. Plumes

When low-density fresh or brackish water from a river mouth flows onto the shelf, a thin effluent plume with sharp

frontal boundaries often occurs (e.g., Fig. 9). This effluent plume may persist for large distances from the river mouth. At the base of the plume, a strong vertical density gradient exists. This restricts vertical mixing of both mass and momentum and efficiently isolates the deeper water from the direct influence of the atmosphere. In particular, it acts as a false bottom during short-lived wind events concentrating the wind-driven flow to the thin plume, which may move at extremely rapid speeds. One of us (GZF) has observed speeds of 1.2 m/sec in a layer only 2 m thick. Strong shear across the base of the plume may be caused by changes in both current speed and direction within distances of the order of a meter (Garvine, 1977). Plumes may well represent a hazard to navigation, not only because of strong currents and shear found within them, but also because the power from a ship's engines may preferentially generate internal waves on the density interface at the base of the plume, causing a loss of steerage (Coleman and McIntire, 1971).

Three distinct regions of the plume are of interest: the near field, the far field, and the frontal boundaries. The near field is a restricted region close to the river mouth, generally within ten river mouth widths. Within this region, initial conditions of the flow at the river mouth, i.e., inertia and initial hydrostatic head, strongly influence the flow and mixing with ambient shelf waters. Numerous models for the near-field dynamics have been suggested, each meeting with some degree of success in describing observed features. Bates (1953) considers the effluent to be a two-dimensional jet with lateral mixing. Similarity solutions for such flow exist. Takano (1954) presents a

Figure 9. Earth Resource Technology Satellite image (band 5) of the Mississippi River delta, 17 November 1973. Note the large number of interacting plumes and fronts, delineated by suspended sediment concentration (lighter tones).

solution for the horizontal transport assuming a balance between the pressure gradient force and momentum diffusion. Bondar (1969) models the plume as an immiscible fluid buoyantly spreading over ambient water. Each of these models reproduces plume morphology qualitatively. None allows for the dynamic effects of mixing of salt with the ambient waters. Wright and Coleman (1971) use a modified version of Bondar's model to describe Mississippi River effluent. In their model, they ignore lateral mixing and assume vertical entrainment in order to increase the density of and decelerate the effluent plume. They still allow buoyant spreading. This approach reproduces both the plume morphology and velocity structure successfully. The assumption of vertical entrainment may be erroneous, though, as strong mixing at the lateral fronts combined with a cross-stream secondary circulation

within the plume could also have been responsible for the observed distributions (McClimans, 1979).

The far-field region of the flow may extend tens of kilometres downstream from the river mouth. Because of the large length scales involved, the far-field trajectory will be strongly influenced by Coriolis force. Inertial forces associated with the initial momentum of the effluent will be less important, as will buoyant spreading. The lateral fronts and vertical density gradient, though, will still isolate the plume waters from the shelf waters and wind effects on the plume path may be significant (Bowman, 1978). Currents on the shelf, both tidal (Garvine, 1974a) and those of longer period (Conomos and Gross, 1968; Wiseman et al., 1976) will also have a strong effect in guiding the flow and controlling the mixing with the ambient waters. Models for this far-field region are generally lacking, although Bowman (1978) has had some success in describing the Hudson River effluent utilizing a modified version of Takano's model.

Clearly, the large number of processes that contribute to the spreading and deceleration of a buoyant effluent plume preclude the development of a simple analytical model for either the near field or the far field. Recourse to a numerical model is necessary. Waldrop and Farmer (1974) developed such a model utilizing the full Navier-Stokes equations, conservation of salt and heat equations, and a linear equation of state. Variable bottom topography and cross-stream flows were permitted, but surface shear stress was not considered. Attention was focused on the near-field plume, and results were encouraging. The general flow patterns produced by the model strongly resembled those

observed in nature, but the model was unable to maintain a well-developed frontal boundary. This appears to be due to a combination of causes. The model utilized constant eddy diffusivities with all the incumbent problems (see secs. IV-A and IV-B). A better parameterization of the turbulent mixing properties, especially in the presence of strong vertical density gradients, is necessary. Also, the model, being of the multi-level type, tended artificially to spread the gradients, since cost prohibited the large number of grid points required to adequately resolve the front. Windward differencing was utilized in an attempt to reduce these effects, but was only partially successful. Before significant further progress can be made, a proper parameterization of the mixing processes at the frontal boundaries is needed. Mixing across the pycnocline within the frontal region has generally been assumed to be due to vertical entrainment from the deep waters into the effluent plume. Garvine (1974b), though, points out that the relative levels of turbulence above and below the pycnocline determine the direction of entrainment. Both upward and downward entrainment are presumably possible, depending on the wind stress and the temporal variation of the ambient currents, McClimans (1978) has identified a series of vertically oriented vortices generated at the front as possible locations of intense local mixing.

The fronts formed where the plumes intersect the sea surface are regions of strong horizontal convergence and downwelling. This is normally evidenced by foam lines and the accumulation of other flotsam. During oil spills in the vicinity of river mouths, these convergence zones at frontal boundaries may act as natural booms protecting the

shoreline from the deleterious effects of crude oil. Numerous examples of this phenomenon from a major oil spill in the vicinity of the Mississippi River delta in early 1970 are presented by Murray (1982).

VI. TOPOGRAPHIC INFLUENCES

A. Submarine Canyons

Submarine canyons are common on continental margins, but their circulation has not been much studied. The heads of some submarine canyons are at the shoreline; for others, the heads are at the shelf break. Scripps and La Jolla canyons, on the California shelf, approach to within a few hundred meters of the shoreline, and the sediment carried down the canyons is predominantly sand. A variety of forcing mechanisms are proposed for flow within the canyons, including astronomical tides, internal waves, spin-off eddies, gravity waves and swell, edge waves, and meteorological tides (Inman et al., 1976).

Neglecting bottom stress, the elevation of the wind-driven setup at the head of a canyon is expected to be less than that over the adjacent shelf, and a pressure gradient will result that will tend to drive water from the shelf into the canyon. A similar result, although for other reasons, is caused by incoming gravity waves. Waves refract away from canyons, so that wave energy over the adjacent shelf will be higher than over the canyon. Thus breaker height will be greater there. To a first approximation, the shoreline setup resulting from the radiation stress of an incoming wave field is proportional to the breaker wave height. Therefore, a sea-surface gradient will develop, due to the breaking waves, which will again drive water along the shelf

toward the canyon head. Edge waves provide a further mechanism for transporting sediment to and down a canyon. These waves are shore-trapped long gravity waves. They can be preferentially trapped by headland topography, which provides simple boundary conditions of no longshore flow and undisturbed on-offshore flow at antinodes. Submarine canyons can act in the same fashion. Field observations are consistent with long trapped edge waves having antinodes at the heads of both Scripps and La Jolla canyons, where strong periodic oscillations in on-offshore flow are observed. It is only farther offshore, in the deeper regions of the West Coast canyons, that the influences of tides and internal waves become felt, although internal surges have been recorded running up the shelf close to shore (Winant, 1974).

Because the water at the heads of the East Coast canyons is so much deeper than waters on the West Coast, the processes that have been identified as triggering downslope transport on the West Coast are probably not applicable to the East Coast. Those processes that are responsible have yet to be clearly identified. Most of the East Coast work to date has been in Hudson Canyon, which may be somewhat anomalous, since it extends much closer to the shore and has a channel connecting its head with Hudson River. Its head lies at approximately the 100-m depth, which is sufficiently deep that it is not severely influenced by any but the strongest storm waves.

The most comprehensive review of current velocity measurements within submarine canyons is that of Shepard et al. (1979). Many years of current measurements in canyons around the world have been summarized. These records were generally of short duration, but a number of interesting

phenomena are clear. Periods of strong up-canyon and down-canyon flow are apparent in most records. There is a tendency for down-canyon flow to predominate. The periodicity of reversals of these flows varies with depth, approaching the tidal frequency as depth increases. The approach to tidal periodicity is more rapid where the oceanic tidal signal is stronger. Clear periodicities at higher frequencies are often apparent and appear to be related to internal waves which propagate up the canyon. Pulses of strong down-canyon flow with speeds on the order of 0.3 to 1 m/sec are also often seen. The authors attribute these downslope flows to turbidity flows, not the catastrophic sort that has occasionally been invoked to explain the Grand Banks cable breaks (Heezen and Ewing, 1952), but a much slower and more common variety, referred to as slow turbidity currents. In a more recent study, Hotchkiss (1980) discusses a major wind-driven event she observed in Hudson Canyon, with up-canyon flows of 1.12 m/sec, followed by down-canyon flows of 0.6 m/sec. This storm-induced event was the most dramatic current perturbation during the 15-week study.

The continual loss of instruments during major events (and consequent loss of data) has discouraged investigators from implanting meters in canyons where turbidity currents are expected. The data base from which to develop models of canyon flow regimes is therefore sparse, but constantly augmenting. Two diagnostic models of shelf circulation have recently been applied to the flow over the section of shelf containing the valley connecting the Hudson River with the Hudson Canyon (Hsueh, 1980; Han et al., 1980). Both models clearly indicate the importance of topographic steering of shelf currents by such a bottom feature. They

also suggest that the canyon may act as a "pulley" in response to wind forcing, with an up-canyon wind resulting in a down-canyon surface flow, and vice-versa. Eddies may also preferentially intrude up canyons onto the shelf.

Although few data are available, certain characteristics of canyon flow can still be identified. Submarine canyons serve to focus and amplify tidal and internal gravity wave currents. These fluctuating currents may be as strong as a few tenths of a meter per second near bottom with the net near-bottom flow being generally down-canyon and a few hundredths of a meter per second. Due to the high intensity of tidal and internal gravity currents generated and refracted in submarine canyons, relatively intense mixing occurs near their heads, yielding local horizontal pressure gradients that drive an up-canyon mean flow at mid-depths, akin to estuarine circulation. In coastal upwelling situations, upwelling is generally most intense, and the water coldest, at canyon heads.

B. Shelf Break

The shelf break is where coastal and oceanic waters generally meet, often in a distinct oceanic front. Some of the surface tidal energy is scattered into internal (baroclinic) modes there. The sharp change in bottom slope causes the shelf break to serve as a wave guide for waves trapped along the coast. Synoptic-scale oceanic eddies become topographically trapped on the continental slope and then are guided along depth contours, frequently entraining coastal waters from near the shelf break (Mooers et al., 1979). Often, baroclinic undercurrents are bound to the upper slope and outer shelf, thus straddling the shelf break. Ocean

swell and long, oceanic internal waves transform to shallow-water waves near the shelf break. Hence, there are several indications that the shelf break region is, from a physical oceanographic standpoint, extraordinarly variable and thus functions as a turbulent boundary layer between oceanic and coastal waters (Voorhis et al., 1976; Halliwell and Mooers, 1979).

C. Shoreline Variations and Other Topographic Perturbations

Mesoscale variations in both the shoreline and the shelf bathymetry have been observed to cause similar perturbations in the shelf flow regime. It has been suggested that the vorticity generated by a cape or headland may result in downstream upwelling. The resultant alteration of the density field would then cause a stationary eddylike feature to occur (Arthur, 1965). Others imply that the headland itself is not the dominant cause of the flow perturbations observed downstream of the headland, but rather the bathymetric perturbations associated with the headland (Peffley and O'Brien, 1976). Large embayments in the coastline may also support mesoscale circulation patterns which can be independent of or interact with the adjacent shelf circulation (Hsueh and Peng, 1973).

Bathymetric highs and lows may also cause mesoscale perturbations to the flow. Lowest order vorticity dynamics theoretically support the importance of these features to shelf dynamics. The Charleston "Bump" has been observed to be associated with major perturbations to the Gulf Stream, wavelike flow patterns being observed downstream of the bump. A large, relatively consistent and stationary eddy associated with a topographic high on the northern section

of the East Greenland shelf has been observed numerous times in satellite imagery of ice flow within the East Greenland Drift. Similar situations also occur in shallow water. Murray et al. (1981) observed a trapped circulation pattern associated with a shallow-water ridge extending offshore near the Damietta mouth of the Nile River.

While the dynamics are not sufficiently well understood to allow prediction of such features, they can often be explained after being observed. Satellite imagery offers an excellent tool for observing at least the surface expression of these features (e.g., Beal et al., 1981).

VII. SEASONAL CIRCULATION

A. Seasonal Currents

The currents on continental shelves vary seasonally in response to seasonal variations in atmospheric forcing. Thus, the intensity of seasonal variations in shelf curents can generally be expected to increase with latitude. A notable counter example, though, is the monsoon-driven circulation of the Somali coast, where currents can reach 3.5 m/sec (Swallow and Bruce, 1966).

Poleward of about 25° latitude there is a seasonal alongshore wind reversal off west coasts. The summertime shelf circulation is dominated by an equatorward baroclinic surface jet with a poleward undercurrent over the outer shelf and upper slope (Smith, 1974), while the wintertime shelf circulation is dominated by a surfacing of the undercurrent or countercurrent (e.g., Hurlburt and Thompson, 1973).

Off east coasts, spring runoff is followed by summer heating and evaporation and then intense winter cooling

and precipitation, accompanied by strong wind stirring. Thus, there is strong vertical thermal stratification across the shelf in summer and not much in winter. (There may be substantial vertical salinity stratification in winter due to runoff, especially in the nearshore (5-to 10-km) coastal boundary layer.) Conversely, there is strong horizontal thermal stratification in winter, but it is weak in summer. Good success has been obtained in modeling shelf currents as geostrophically balanced with appropriate frictional boundary layers at the surface and bottom (Hsueh, 1980; Galt, 1980). The processes that alter the density distribution over the shelf, and thus the geostrophic flows will cause significant seasonal variability.

B. The Seasonal Sea Ice Zone (SSIZ)

The ice cover and inaccessibility of polar shelves have greatly restricted the collection of field data from these regions. Thus, we have only the most rudimentary knowledge of the magnitude and variability of shelf currents within the SSIZ. We expect the physics operative within the SSIZ to be similar to those operative on more temperate shelves. Because of the interest the SSIZ holds for the petroleum industry, we will qualitatively mention several dynamical modifications caused by the presence of a time-varying ice cover. Quantitative discussion of the pertinent dynamical balances is presented elsewhere within this chapter.

One immediate consequence of an ice cover is that the wind no longer acts directly on the water surface, but rather on the ice, which transmits a filtered stress signal to the water. If the ice is in a divergent state so that individual small floes may move freely, the wind stress is trans-

mitted to the water essentially unmodified by the internal stresses. If the ice is convergent, so that extremely large areas of ice are forced to move coherently, then only the largest scales of motion in the wind field applied to the upper surface of the ice are directly transmitted to the water. Smaller scales are filtered out. Shorefast ice, which is frozen to the shore and therefore not free to move at all, eliminates completely the direct driving of coastal waters by the local wind.

Because of the significant effect that an ice cover may have on the applied surface stress, there exists the possibility that a significant curl of the applied stress can develop at the ice edge, i.e., in the Marginal Sea Ice Zone (MSIZ). The existence of such a curl can result in upwelling or downwelling at this site (Buckley et al., 1979). Other mechanisms, though, may also explain the observed upwelling (McPhee, 1980).

The temporal variations in the extent of the ice cover cause changes in the density structure of the shelf waters. Rejection of brine during freezing and melting represents sources of salt and fresh water, respectively, which are added to the surface layers. The former causes convective mixing, the latter generates vertical density gradients which reduce the vertical mixing of mass and momentum (see Sec. IV-C).

The alterations to the density field caused by freezing may subsequently affect the velocity field over the shelf (Neshyba and Badan-Dangon, 1974). In the shallowest regions, brine rejected by the ice does not have a large vertical column of water beneath it with which it can mix. Therefore, a dense bottom layer is formed by the brine rejection process.

This dense water will subsequently flow downslope and into the deeper parts of the ocean, and is thought to be an important mechanism for flushing waters from the arctic shelves (Aagaard, 1979). A shoreward flow immediately beneath the ice maintains continuity (Matthews, 1981).

During summer months, sea ice melting results in the formation of an intense vertical stratification, which is often nearly two-layered: light, fresh water overlying dense, salty water. A salinity front may develop seaward of the ice edge (Paquette and Bourke, 1979). The resultant structure strongly resembles that of the coastal boundary layer (see Sec. IV-F). Computations of the geostrophic current in such a frontal region suggest the existence of a thin, narrow stream aligned parallel to the ice edge, with velocities of about 0.5 m/sec. Fixed observation sites established on ice floes near the ice edge have also been tracked and observed to move rapidly parallel to the ice edge, at times against the wind stress. Although these observations are suggestive of the pertinent dynamics, further observations are required before a reliable model can be developed.

VIII. SEMI-PERMANENT CURRENTS

As petroleum exploration activities extend farther and farther offshore, they encroach on the regions of the swift, semi-permanent ocean boundary currents. These currents are to a large extent in geostrophic balance. They tend to flow along the outer shelf and slope regions. They are often very swift, and because of their spatial extent, they are responsible for massive transports of water.

Figure 10 presents a schematic representation of some of these currents. Such figures, often showing the difference

between the circulation during northern hemisphere summer and northern hemisphere winter, are found in most general texts on physical oceanography. Neumann and Pierson (1966) present such a set of figures taken from Defant's earlier work (Defant, 1961). Some care must be taken when utilizing such figures, as they often involve significant spatial and temporal averaging as well as a certain amount of artistic license. Detailed descriptions of particular areas are found in texts on regional oceanography.

The swiftest of these current systems are the western boundary currents. Probably the best known and most studied of these are the Gulf Stream system of the North Atlantic (Stommel, 1966) and the Kuroshio system of the North Pacific (Stommel and Yoshida, 1972). Less well studied, but of equal local importance, are the Agulhas Current, the Brazil Current, the East Greenland Current, the Somali Current, and the Oyashio Current. Eastern boundary currents such as the California Current, the Norwegian Coastal Current, and the Canary Current are, in general, less swift, although they are also extremely important locally.

Being strongly baroclinic, these currents are highly sheared in the vertical. A characteristic shear in the Gulf Stream in the upper 100 m is of the order 10^{-2} s^{-1}. Similarly, there is often strong cross-stream shear, particularly in the western boundary currents. At times this shear can approach or exceed the Coriolis parameter. Although to a first approximation these currents are often geostrophic, with such large lateral shears present, a complete description of their dynamics must include consideration of the inertial terms in the equations of motion.

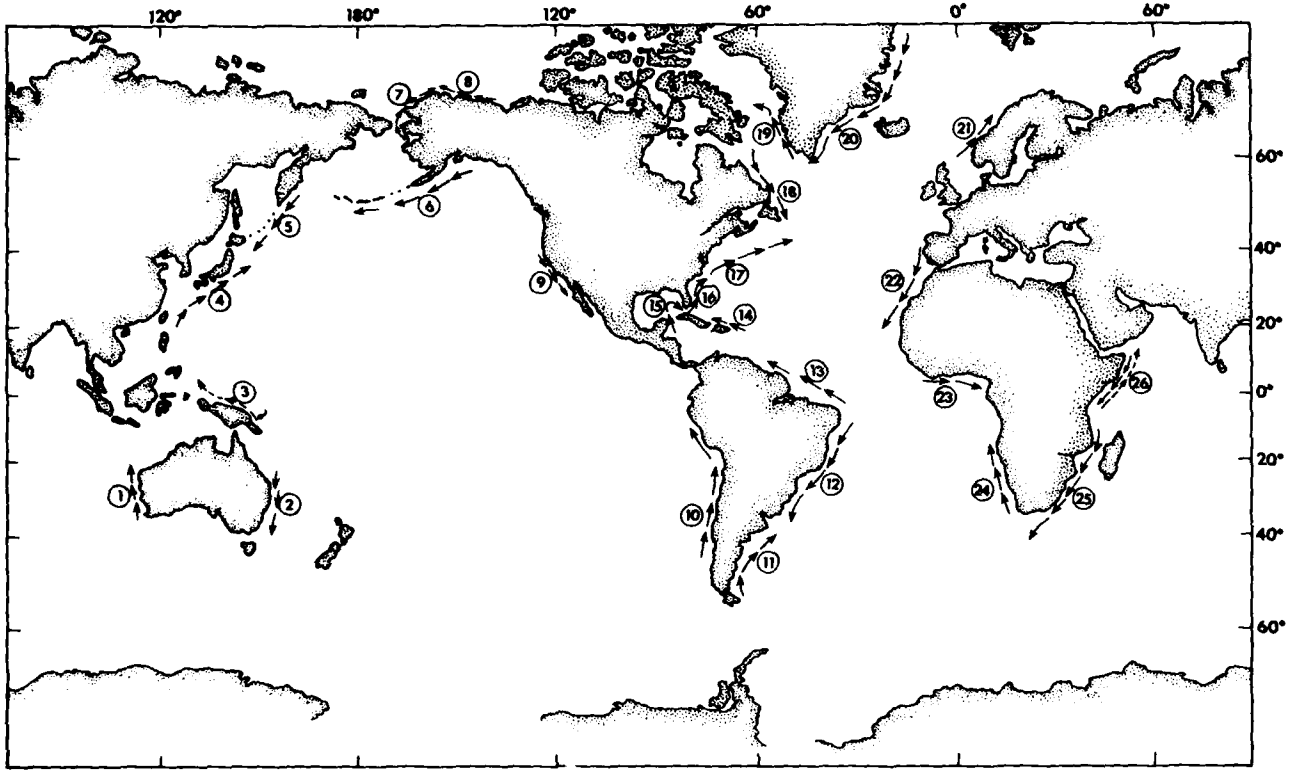
120°
180°
120°
60°
0°
60°
60°
40°
20°
0°
20°
40°
60°
1
2
3
4
5
6
7
8
9
10
11
12
13
14
15
16
17
18
19
20
21
22
23
24
24
25

Figure 10. Schematic chart of the major semi-permanent oceanic boundary currents.

1) West Australian Current
2) East Australian Current
3) Unnamed
4) Kuroshio
5) Dyashio
6) Aleutian Current
7) North Alaskan Coastal Current
8) Barrow Current
9) California Current
10) Peru-Chile Current
11) Falkland Current
12) Brazil Current
13) Guiana Current
14) Antilles Current
15) Loop Current
16) Florida Current
17) Gulf Stream
18) Labrador Current
19) West Greenland Current
20) East Greenland Current
21) Norwegian Coastal Current
22) Canary Current
23) Guinea Current
24) Benguela Current
25) Agulhas Current
26) Somali Current

Dashed arrows represent currents (3 and 26) that flow only during the northern hemisphere summer.

On the largest time and space scales these currents are part of the permanent circulation of the oceans. On smaller scales, they are variable. Any operational planning in a region of a semi-permanent current must account for this variability. A few examples will illustrate the extent of this variability.

The section of the Gulf Stream system within the Gulf of Mexico is referred to as the Loop Current. It carries warm, salty water from the Yucatan Straits to the Florida Straits. At certain times it hugs the shelf near Cuba, while at other times it extends far northward into the Gulf. It was initially thought that this intrusion into the Gulf was seasonal (Leipper, 1970), but it is now believed that this is not the case (e.g., Behringer et al., 1977). After an intrusion reaches its maximum extent, an eddy or warm core ring appears to break off from the northern part of the current and migrate into the western Gulf (Elliott, 1979). During its northward intrusion, the current affects processes on the west Florida shelf (Niiler, 1976). The eddies that migrate westward influence the circulation of the western Gulf.

Both northern hemisphere subtropical western boundary current systems exhibit meandering. Downstream of Cape Hatteras, the Gulf Stream meanders strongly (Hansen, 1970). These meanders often break off to form rings that migrate either into the Sargasso Sea or along the shelf (Lai and Richardson, 1977) before merging again with the Gulf Stream. The Kuroshio system also exhibits meanders downstream of the Izu-Bonin Ridge. In the case of the Kuroshio, there are indications that the system assumes two major modes of circulation in the region of the Izu-Bonin Ridge and

the current switches between circulation modes on an aperiodic time scale (Shoji, 1972). At times meandering and eddies may be the dominant characteristic of a current. Such appears to be the case for the East Australian Current (Boland and Hamon, 1970; Godfrey et al., 1980).

Seasonal variations of currents have already been mentioned. The coastal jet associated with an upwelling regime waxes and wanes seasonally in response to a varying wind field. The strength of the current generated during this process, though, is usually less than 0.5 m/sec. A striking example of a strong seasonal current is provided by the Somali Current. Southwest monsoon winds affect the Indian Ocean during the northern hemisphere summer. At this time, a strong current develops off the west coast of Africa. The normal southerly flow reverses, and the current flows northward across the equator at very rapid speeds. Speeds attaining 3.5 m/sec have been observed. Nearshore flows of 2 m/sec are consistently observed (e.g., Leetma, 1973).

IX. CONCLUSION

From the preceding information, it should be clear that there exists a wealth of circulation modes over the continental shelf. These cover a broad spectrum of time and space scales. The dynamics of some are well understood; others are only qualitatively described. All are important for one or more of the problems an engineer will be called on to solve. Analytical and numerical models of the different flow regimes are often available, but these are no substitute for direct observation. On the other hand, with an understanding of the types of motion that are potentially present in a given region, and historical information con-

cerning bathymetry, runoff, tides, and meteorology, a good estimate of the important modes of circulation may often be made.

Clearly, in an overview this short, all topics of interest to all people could not be broached. Many excellent reviews of the general topic of shelf dynamics have appeared in recent years. Three that we would recommend to anyone interested in the field are those by Allen (1980), Csanady (1981), and Winant (1980). We have not discussed shelf fronts as a separate topic, although they were mentioned at many places when a front occurred in conjunction with some other dynamical feature of interest. The proceedings of a recent meeting (Bowman and Esaias, 1978) devoted to this subject, though, should provide a starting point for anyone interested in the topic. In the introduction we mentioned the need for current information in oil spill contingency planning. Again, the topic was only briefly dealt with in the following pages because a comprehensive review (Murray, 1982) has recently appeared and it seemed redundant to elaborate further on this subject.

A word of caution is in order concerning the models that have been discussed in the preceding pages. The accuracy of each is highly variable. For example, the numerical models for tidal circulation may be tuned to give excellent predictions of water level, but may be much less accurate in their representation of currents. Some of the difficulties associated with the prediction of wind-driven currents, particularly those associated with parameterization of the turbulent fluxes, have already been mentioned. A model may be good only to the proper order of magnitude unless it is tuned to observations in the appropriate regime.

Yet even such coarse models can be invaluable for understanding the causes of observed currents and isolating the most important driving forces in a regime. If enough data and a model that incorporates the basic physics are available, it can be possible to hindcast currents to within 10-20 percent.

The interaction between different modes of motion has been only briefly mentioned, but for an engineer interested in the total loading or net drift of an object these interactions must be of paramount importance. Unfortunately, since the currents of interest are strong, the usual assumption of linear dynamics, with the various motions simply additive, is probably not applicable. For example, in cases where two baroclinic modes interact, such as when the internal tide is important in an upwelling region, the distortion of the stratification by one mode will necessarily affect the first-order dynamics of the other. Similarly, when a wave motion is involved and the wave's phase velocity approaches the mean flow velocity on the shelf, there is the potential for significant interaction, as is also the case when strong shear is present. Lateral shear may be particularly important on low-latitude shelves, where the shear can approach the magnitude of the Coriolis parameter. The nonlinearity of these interactions makes their treatment, though, difficult numerically and often intractable analytically.

Acknowledgments

WJWJR was supported under a contract between the Coastal Sciences Program and the Arctic Program of the Office of Naval Research and the Coastal Studies Institute, Louisiana

State University. R. J. Crout supplied the data in Figure 6. The LSU Remote Sensing and Image Processing Laboratory brought the image in Figure 8 to our attention.

REFERENCES

Aagaard, K., 1979, STD measurements in possible dispersion regions of the Beaufort Sea. In Environmental Assessment of the Alaskan Continental Shelf, Annual Reports of the Principal Investigators for the Year Ending March 1978, vol. IX, Transport.

Adams, C. E., and G. L. Weatherly, 1981, Some efects of suspended sediment on an oceanic bottom boundary layer. J. Geophys. Res., 86:4161-4172.

Allen, J. S., 1980, Models of wind-driven currents on the continental shelf. In (M. van Dyke, J. V. Wehausen, and J. L. Lumley, eds.) Annual Review of Fluid Mechanics, 12:389-433.

Allen, J. S., and R. L. Smith, 1981, On the dynamics of wind-driven shelf currents. Phil. Trans. Roy. Soc. London, sec. A, #302:617-634.

Apel, J. R., H. M. Byrne, J. R. Proni, and R. L. Charnell, 1975, Observations of oceanic internal and surface waves from the Earth Resources Technology Satellite. J. Geophys. Res., 80(6):865-881.

Arthur, R. S., 1965, On the calculation of vertical motion in eastern boundary currents from determinations of horizontal motion. J. Geophys. Res., 70:2799-2803.

Bates, C. C., 1953, Rational theory of delta formation. Bull. Am. Assoc. Petrol. Geologists, 37(9):2119-2161.

Beal, R. C., P. S. DeLeonibus, and I. Katz, 1981, Spaceborne Synthetic Aperture Radar for oceanography. The Johns Hopkins University Press, Baltimore, Md., 215 pp.

Beardsley, R. C., 1975, A numerical investigation of a laboratory analogy of the wind-driven ocean circulation. In Numerical Models of Ocean Circulation, National Acad. Sci., pp. 311-326.

Beardsley, R. C., W. C. Boicourt, and D. V. Hansen, 1976, Physical oceanography of the Middle Atlantic Bight. Spec. Symp. Amer. Soc. Limnol. Oceanogr., 2:20-34.

Behringer, D. W., R. L. Molinari, and J. F. Festa, 1977, The variability of anticyclonic current patterns in the Gulf of Mexico. J. Geophys. Res., 82(34):5469-5476.

Blevins, R. D., 1977, Flow-induced vibrations. Van Nostrand Reinhold, New York.

Blumen, William, 1972, Geostrophic Adjustment. Rev. Geophys. and Space Phys., 10(2):485-528.

Boland, F. M., and B. V. Hamon, 1970, The East Australian Current. Deep-Sea Res., 17(4):777-794.

Bondar, C., 1969, Theoretical study on the spreading of a light-liquid current in a basin with a heavier liquid. Symposium on Hydrology of Deltas, UNESCO, Bucharest, Romania.

Bowman, M. J., and W. E. Esaias (eds.), 1978, Oceanic fronts in coastal processes. Springer-Verlag, Berlin, 114 pp.

Bowman, M. J., 1978, Spreading and mixing of the Hudson River effluent into the New York Bight. In (J. C. J. Nihoul, ed.), Hydrodynamics of Estuaries and Fjords Elsevier Oceanography Series.

Brebbia, C. A. and P. Partridge, 1976, Finite element simulation of water circulation in the North Sea. J. Appl. Math. Modeling, 1:101-107.

Buckley, J. R., T. Gammelsrøed, J. A. Johaannessen, O. M. Joohannessen, and L. P. Røed, 1979, Upwelling, oceanic structure at the edge of the Arctic ice pack in winter. Science, 203:165-167.

Buchwald, V. T. and J. K. Adams, 1968, The propagation of continental shelf waves. Proc. Roy. Soc., London, ser. A, 305:235-250.

Cacchione, D. A. and C. Wunsch, 1974, Experimental study of internal waves over a slope. J. Fluid Mech., 66(2): 223-239.

Cheng, R. T., 1976, Transient three-dimensional circulation of lakes. ASCE Nat. Water Res. Conv., San Diego, Paper Number 2692.

Chuang, Wen-Snn, 1980, Propagation and generation of internal tides on the continental margin. Ph.D. dissertation, The Johns Hopkins Univ., Baltimore, Md.

Coleman, J. M., and W. G. McIntire, 1971, Transiting coastal river channels. Internat. Hydrogr. Rev., 48(1):11-43.

Collipp, B. G., R. C. Hamilton, J. VanLear, and C. Abbott, 1979, Currents and current meters for the Cognac platform installation. Marine Tech. Conf., New Orleans.

Conomos, T. J., and M. G. Gross, 1968, Mixing of Columbia River and ocean waters in summer. Proc. ASCE, J. San. Engr. Div., 94(SA5):979-994.

Cooper, C., and B. Pearce, 1980, On the forcing mechanisms affecting the bottom shear stress in coastal waters. J. Phys. Oceanogr., 10:1870-1876.

Crout, R. L. and S. P. Murray, 1979, Shelf and coastal boundary layer currents, Miskito Bank of Nicaragua. 16th Coastal Engr. Conf., ASCE, Aug. 27-Sept. 3, 1978, Hamburg, Germany, III:2715-2729.

Csanady, G. T., 1972, The coastal boundary layer in Lake Ontario, Part I: The spring regime. J. Phys. Oceanogr., 2(1):41-53.

Csanady, G. T., and J. T. Scott, 1974, Baroclinic coastal jets in Lake Ontario during IFYGL. J. Phys. Oceanogr., 4(4):524-541.

Csanady, G. T., 1976, The coastal jet conceptual model in the dynamics of shallow seas. In (E. D. Goldberg, I. N. McCave, J. J. O'Brien, and J. H. Steele, eds.) The Sea, VI:117-144. Wiley Interscience, New York.

Csanady, G. T., 1981, Circulation in the coastal ocean. In (Barry Saltzman, ed.) Advances in Geophysics. Academic Press, New York, pp. 101-183.

Daddio, E., Wm. J. Wiseman, Jr., and S. P. Murray, 1978, Inertial currents over the inner shelf near 30°N. J. Phys. Oceanogr., 8(4):728 733.

Davies, A. M., and G. K. Furnes, 1980, Observed and computed M_2 tidal currents in the North Sea. J. Phys. Oceanogr., 10(2):237-257.

Defant, A., 1961, Physical oceanography, vols. I and II. Pergamon Press, New York.

Denman, K. L., and M. Miyake, 1973, Upper layer modifications at Ocean Station PAPA: observations and simulation. J. Phys. Oceanogr., 3:185-196.

Doodson, A. T. and H. D. Warburg, 1941, Admiralty manual of tides. Her Majesty's Stationery Office, London, 270 pages.

Ekman, V. A., 1905, On the influence of earth's rotation on ocean currents. Arkiv Mat. Astron. Fysik., 2:1-53.

Elliott, B. A., 1979, Anticyclonic rings and the energetics of the circulation of the Gulf of Mexico. Ph.D. Dissertation, Texas A and M Univ., College Station, 188 pp.

Faller, A. J., and R. Kaylor, 1969, Oscillatory and transitory Ekman boundary layers. Deep-Sea Res., Supp. to Vol. 16, pp. 45-58.

Fischer, F. J., W. T. Jones, and R. King, 1980, Current-induced oscillations of Cognac piles during installation--prediction and measurement. Proc. IAHR/IUTAM Symposium on Practical Experience with Flow-Induced Vibrations. Springer-Verlag, Berlin, pp. 570-581.

Forristall, G. Z., 1974, Three-dimensional structure of storm generated currents. J. Geophys. Res., 79(18):2721-2729.

Forristall, G. Z., 1980, A two-layer model for hurricane driven currents on an irregular grid. J. Phys. Oceanogr., 10(9):1417-1438.

Forristall, G. Z., R. C. Hamilton, and V. J. Cardone, 1977, Continental shelf currents in tropical storm Delia: observations and theory. J. Phys. Oceanogr., 7:532-546.

Galt, J., 1980, A finite-element solution procedure for the interpolation of current data in complex regions. J. Phys. Oceanogr., 10(12):1984-1997.

Garvine, R. W., 1974a, Physical features of the Connecticut River outflow during high discharge. J. Geophys. Res., 79(6):831-846.

Garvine, R. W., 1974b, Dynamics of small scale oceanic fronts. J. Phys. Oceanogr., 4(4):557-569.

Garvine, R. W., 1977, River plumes and estuary fronts. In Estuaries, Geophysics, and the Environment, National Academy of Sciences, Washington, D. C.

Gill, A. E., and A. J. Clarke, 1974, Wind-induced upwelling, coastal currents and sea-level changes. Deep-Sea Res., 21(4):325-345.

Godfrey, J. S., G. R. Cresswell, T. J. Golding, and A. F. Pearce, 1980, The separation of the East Australian Current. J. Phys. Oceanogr., 10(3):430-440.

Godin, Grabriel, 1972, The analysis of tides. Univ. Toronto Press, 264 pp.

Goepfert, B. L., 1969, An engineering challenge - Cook Inlet, Alaska. Offshore Technology Conference Paper 1048, New Orleans.

Grant, W. D. and O. S. Madsen, 1979, Combined wave and current interaction with a rough bottom. J. Geophys. Res., 84:1797-1808.

Greenspan, H. P., 1969, The theory of rotating fluids. Cambridge Univ. Press, 328 pp.

Griffin, O. M., R. A. Skop, and S. E. Ramberg, 1975, The resonant, vortex-excited vibrations of structures and cable systems. Offshore Technology Conference Paper 2319, Houston.

Groen, P., and G. W. Groves, 1963, Surges. In (M. N. Hill, ed.) The Sea, Vol. I, pp. 611-646. Interscience.

Halliwell, G. T., Jr., and C. N. K. Mooers, 1979, The space-time structure of the shelf water-slope and Gulf Stream surface temperature fronts and associated warm-core eddies. J. Geophys. Res., 84:7707-7725.

Halpern, D., 1971, Observations of short period internal waves in Massachusetts Bay. J. Mar. Res., 29(2):116-132.

Han, G., D. V. Hansen, and J. Galt, 1980, Steady-state diagnostic model of the New York Bight. J. Phys. Oceanogr., 10(12):1998-2020.

Hansen, D. V., 1970, Gulf Stream meanders between Cape Hatteras and the Grand Banks. Deep-Sea Res., 17(3):495-511.

Hartlen, R. T., and I. G. Currie, 1970, Lift-oscillator model of vortex-induced vibration. J. Engr. Mech., ASCE, 96:577-591.

Heaps, N. S., 1969, A two-dimensional numerical sea model. Phil. Trans. Roy. Soc. London, ser. A, 265:93-137.

Heaps, N. S., 1972, On the numerical solution of the three-dimensional hydrodynamical equations for tides and storm surges. Mem. Soc. Roy. Sci. Liege, ser. 6, 2:143-180.

Heezen, B. C., and M. Ewing, 1952, Turbidity currents and submarine slumps and the 1929 Grand Banks earthquake. Amer. J. Sci., 250:849-873.

Hodgins, D. O., and H. G. Westergard, 1981, Internal waves in Davis Strait and their measurement with a real time system. Proc., POAC, Quebec City, pp. 423-432.

Hollister, C. D., 1981, The high energy benthic boundary layer experiment: a program overview. EOS, 62(45):891-892 (abstract only published).

Hotchkiss, F. L. S., 1980, Internal gravity waves and sediment transport in Hudson Submarine Canyon. Masters Essay, Mass. Inst. Tech., 115 pp.

Hsueh, Y., 1980, On the theory of deep flow in the Hudson Shelf Valley. J. Geophys. Res., 85(C9):4913-4918.

Hsueh, Y. and C.-Y. Peng., 1973, A numerical study of the steady circulation in an open bay. J. Phys. Oceanogr., 3(2):220-225.

Hunkins, Kenneth, 1966, Ekman drift currents in the Arctic Ocean. Deep-Sea Res., 13:607-620.

Hurlburt, H. E. and J. Dana Thompson, 1973, Coastal upwelling on a beta-plane. J. Phys. Oceanogr., 3(1):16-32.

Huthnance, J. M., 1974, On the diurnal currents over Rockall Bank. Deep-Sea Res., 21(1):23-35.

Inman, D. L., C. E. Nordstrom, and R. E. Flick, 1976, Currents in submarine canyons, an air-sea-land interaction. In (M. van Dyke, W. G. Vincenti, and J. V. Wehausen, eds.) Annual Review of Fluid Mechanics, 8:275-310.

Iwan, W. D., and Blevins, R. D., 1974, A model for vortex-induced oscillations of structures. J. Appl. Mech., 41:581-586.

Jones, W. T., 1978, On-bottom pipeline stability in steady water currents. J. Petro. Tech., 30:475-484.

Johnson, W. R., J. C. Van Leer, and C. N. K. Mooers, 1976, A cyclesonde view of coastal upwelling. J. Phys. Oceanogr., 6:556-574.

Kundu, P. K., and J. S. Allen, 1976, Some three-dimensional characteristics of low-frequency current fluctuations near the Oregon coast. J. Phys. Oceanogr., 6:181-199.

Kundu, P. K., J. S. Allen, and R. L. Smith, 1975, Modal decomposition of the velocity field near the Orgin coast. J. Phys. Oceanogr., 5(4):683-704.

Lai, D. Y., and P. L. Richardson, 1977, Distribution and movement of Gulf Stream rings. J. Phys. Oceanogr., 7(5):670-683.

Lee, C.-Y. and R. C. Beardsley, 1974, The generation of long non-linear internal waves in a weakly stratified shear flow. J. Geophys. Res., 79(3):453-462.

Lee, T. N., 1975, Florida Current spin-off eddies. Deep-Sea Res., 22(11):753-765.

Leendertse, J. J., 1967, Aspects of a computational model for long-period water wave propagation. Memo. RM 5294-PR, Rand Corp., Santa Monica.

Leendertse, J. J., R. C. Alexander, and S. K. Liu, 1973, A three-dimensional model for esutaries and coastal seas, Vol. I - Principles of Computation, Memo. R-1417-OWRR, Rand Corp., December.

Leipper, D. F., 1970, A sequence of current patterns in the Gulf of Mexico. J. Geophys. Res., 75:637-657.

Madsen, O. S., 1977, A realistic model of the wind-induced Ekman boundary layer. J. Phys. Oceanogr., 7(2):248-255.

Martin, P. J., 1982, Mixed-layer simulation of buoy observations taken during Hurricane Eloise. J. Geophys. Res., 87:409-427.

Matthews, J. B., 1981, Observations of under-ice circulation in a shallow lagoon in the Alaskan Beaufort Sea. Ocean Management, 6:223-234.

McClimans, T. A., 1978, Fronts in fjords. Geophys. Astrophys. Fluid Dynamics, 11:23-34.

McClimans, T. A., 1979, On the energetics of river plume entrainment. Geophys. Astrophys. Fluid Dynamics, 13:67-81.

McPhee, M. G., 1980, Physical oceanography of the seasonal sea ice zone. In (B. G. Anderson, W. F. Weeks, and J. L. Newton, eds.) The Seasonal Sea Ice Zone, Cold Regions Sci. and Tech., Vol. 2.

Mellor, G. L., and T. Yamada, 1974, A hierarchy of turbulence closure models for planetary boundary layers. J. Atmos. Sci., 31:1791-1806.

Mercier, J. A., 1973, Large amplitude oscillations of a circular cylinder in a low speed stream. Ph.D. thesis, Stevens Inst. Tech., Hoboken, NJ.

Mooers, C., 1970, The interaction of an internal tide with the frontal zone of a coastal upwelling region. Ph.D. dissertation, Oregon State Univ., Corvallis, 480 pp.

Mooers, C. N. K., C. A. Collins, and R. L. Smith, 1976, The dynamic structure of the frontal zone in the coastal upwelling region off Oregon. J. Phys. Oceanogr., 6(1):3-21.

Mooers, C. N. K., R. W. Garvine, and W. W. Martin, 1979, Summertime synoptic variability of the Middle Atlantic Shelf water/slope water front. J. Geophys. Res., 84: 4837-4854.

Mungall, J. C. H., and J. B. Matthews, 1970, A variable-boundary numerical tidal model. Tech. Rept. No. R70-4, Inst. Mar. Sci., Univ. Alaska, Fairbanks, 160 pp.

Mungall, J. C. H., C. E. Abel, and C. R. Olling, 1978, Hydrodynamical model estimates of the M_2 and K_1 currents of the Gulf of Mexico. Tech. Rept. Ref. 78-9-T, Texas A and M Res. Fdn., Texas A and M Univ., 109 pp.

Munk, W. H. and D. E. Cartwright, 1966, Tidal spectroscopy and prediction. Phil. Trans. Roy. Soc. London, ser. A, 259:533-556.

Murray, S. P., 1970, Bottom currents near the coast during Hurricane Camille. J. Geophys. Res., 75(24):4579-4582.

Murray, S. P., 1975, Trajectories and speeds of wind-driven currents near the coast. J. Phys. Oceanogr., 5:347-360.

Murray, S. P., 1982, The effects of weather systems, currents, and coastal processes on major oil spills at sea. In (G. Kullenberg, ed.) Pollutant Transfer and Transport in the Sea, Vol. II, pp. 169-227. CRC Press, Boca Raton, Fl.

Murray, S. P., J. M. Coleman, H. H. Roberts, and M. Salama, 1981, Accelerated currents and sediment transport off the Damietta Nile promontory. Nature, 293(5827):51-54.

Murthy, C. R., and D. S. Dunbar, 1981, Structure of flow within the coastal boundary layer of the Great Lakes. J. Phys. Oceanogr., 8(4):728-733.

Mysak, L. A., 1980, Topographically trapped waves. In (M. van Dyke, J. V. Wehausen, and J. L. Lumley, eds.) Annual Review of Fluid Mechanics, 12:45-76.

Nakamura, Y., 1969, Vortex excitation of a circular cylinder treated as a binary flutter. Reports of Research Inst. for Appl. Mech., 27:217-234.

Neshyba, S., and A. Badan-Dangon, 1974, On ocean current induced by a prograding ice-pack. Geophys. Res. Letters, 1(8):351-354.

Neumann, G., and W. J. Pierson, Jr., 1966, Principles of physical oceanography. Prentice-Hall, New York, 545 pp.

Nihoul, J. C. J., Y. Runfola, and B. Roisin, 1979, Nonlinear three-dimensional modeling of mesoscale circulation in seas and lakes. In (J. C. J. Nihoul, ed.) Marine Forecasting. Elsevier, pp. 235-259.

Niiler, P. P., 1975, Deepening of the wind-mixed layer. J. Mar. Res., 33(3):405-422.

Niiler, P. P., 1976, Observations of low-frequency currents on the western Florida continental shelf. Mem. Soc. Roy. Sci. Liege, X:331-358.

Niiler, P. P. and E. B. Kraus, 1977, One-dimensional models of the upper ocean. In (E. B. Kraus, ed.) Modeling and Prediction of the Upper Layers of the Ocean, Pergamon Press, New York.

Osborne, A. R., and T. L. Burch, 1980, Internal solitons in the Andaman sea. Science, 208:451-460.

Osborne, A. R., T. L. Burch, and R. I. Scarlet, 1978, The influence of internal waves on deep-water drilling. J. Petro. Tech., 30:1497-1504.

Paquette, R. G. and R. H. Bourke, 1979, Fine structure in the vicinity of the Arctic Sea ice margin. J. Geophys. Res., 84(C3):1115-1164.

Peffley, M. B. and J. J. O'Brien, 1976, A three-dimensional simulation of coastal upwelling off Oregon. J. Phys. Oceanogr., 6(2):164-180.

Petrie, Brian, 1975, M_2 surface and internal tides on the Scotian shelf and slope. J. Mar. Res., 33(3):303-323.

Pollard, R. T., and R. C. Millard, Jr., 1970, Comparison between observed and simulated wind-generated inertial oscillations. Deep-Sea Res., 17(4):813-821.

Pollard, R. T., P. B. Rhines, and R. O. R. Y. Thompson, 1973, The deepening of the wind-mixed layer. J. Geophys. Fluid Dyn., 3:381-404.

Price, J. F., 1981, Upper ocean response to a hurricane. J. Phys. Oceanogr., 11:153-175.

Price, J. E., C. N. K. Mooers, and J. C. Van Leer, 1978, Observation and simulation of storm-induced mixed-layer deepening. J. Phys. Oceanogr., 8(4):582-599.

Prinsenberg, S. J., W. L. Wilmott, M. Rattray, Jr., 1974, Generation and dissipation of coastal internal tides. Deep-Sea Res., 21:263-281.

Roberts, Jo, 1973, Internal gravity waves in the ocean: bibliography and key word index. Tech. Rept. No. R73-4, Inst. Mar. Sci., Univ. Alaska, Fairbanks, 430 pp.

Roberts, Jo, 1975, Internal gravity waves in the ocean. Marcel Dekker, New York, 274 pp.

Sarpkaya, T., 1979, Vortex-induced oscillations--a selective review. J. Appl. Mech., 46:241-258.

Sarpkaya, T., and M. Isaacson, 1981, Mechanics of wave forces on offshore structures. Van Nostrand Reinhold, New York.

Schwiderski, E. W., 1980, On charting global ocean tides. Rev. Geophys. Space Phys., 18:243-268.

Shanks, F. E., D. S. Hammett, and H. L. Zinkgraf, 1979, Experience drilling in deepwater high current areas. Offshore Technology Conference Paper 3582, Houston.

Shay, L. K., and J. J. Tamul, 1981, Current observations during the passage of Hurricane Frederick. Unpublished manuscript, U.S. Naval Oceanographic Office, Bay St. Louis, MS.

Shepard, F. P., N. G. Marshall, P. A. McLoughlin, and G. G. Sullivan, 1979, Currents in submarine canyons and other sea valleys. Amer. Assoc Petrol. Geologists, Tulsa, Okla., 173 pp.

Shoji, D., 1972, Time variation of the Kuroshio south of Japan In (H. Stommel and K. Yoshida, eds.) Kuroshio, Physical Aspects of the Japan Current. Univ. Washington Press, pp. 217-234.

Smith, N. P., 1978, Longshore currents on the fringe of Hurricane Anita. J. Geophys. Res., 83:6047-6051.

Smith, R. L., 1968, Upwelling. In (H. Barnes, ed.) Oceanogr. Mar. Biol. Ann. Rev., 6:11-46.

Smith, R. L., 1974, A description of current, wind, and sea-level variations during coastal upwelling off the Oregon coast, July-August, 1972. J. Geophys. Res., 79:435-443.

Sterling G. H., A. O. P. Casbarian, N. L. Dodge, and D. G. Godfrey, 1979, Construction of the Cognac platform, 1025 feet of water, Gulf of Mexico. Offshore Technology Conference Paper 3493, Houston.

Stommel, Henry, 1966, The Gulf Stream, a physical and dynamical description. Univ. California Press and Cambridge Univ. Press, 248 pp.

Stommel, Henry, and Kozo Yoshida (eds.), 1972, Kuroshio: physical aspects of the Japan Current. Univ. Washington Press, 517 pp.

Swallow, J. C., and J. G. Bruce, 1966, Current measurements off the Somali coast during the southwest monsoon of 1964. Deep-Sea Res., 13(5):861-888.

Takano, K., 1954, On the salinity and velocity distributions off the mouth of a river. J. Oceanogr. Soc. Japan, 10(3):92-98.

Tubman, M. W., and J. N. Suhayda, 1976, Wave-action and bottom movements in fine sediments. Proc. 15th Conf. Coastal Engr., ASCE, Honolulu, 2:1168-1183.

Turner, J. S., 1973, Buoyancy effects in fluids. Cambridge Univ. Press, 367 pp.

Verley, R. L. P. and G. Moe, 1978, The effect of cylinder vibration on the drag force and the resultant hydro-

dynamic damping. Symposium on Mechanics of Wave-Induced Forces on Cylinders, Univ. of Bristol, U.K. Internat. Assoc. for Hydraulics Res.

Voorhis, A. D., D. C. Webb, and R. C. Millard, 1976, Current structure and mixing in the shelf/slope water front south of New England. J. Geophys. Res., 81:3695-3708.

Waldrop, W. R., and R. C. Farmer, 1974, Three-dimensional computation of buoyant plumes. J. Geophys. Res., 79(9):1269-1276.

Weber, J. E., 1981, Ekman currents and mixing due to surface gravity waves. J. Phys. Oceanogr., 11(10):1431-1435.

Winant, C. D., 1974, Internal surges in coastal water. J. Geophys. Res., 79(3):4523-4526.

Winant, C. D., 1980, Coastal circulation and wind-induced currents. In (M. van Dye, J. V. Wehausen, and J. L. Lumley, eds.) Annual Review of Fluid Mechanics, 12:271-301.

Wiseman, Wm. J., Jr., S. P. Murray, J. M. Bane, and M. W. Tubman, 1976, Offshore physical oceanography. Appendix III in (J. G. Gosselink, R. R. Miller, M. Hood, and L. M. Bahr, Jr., eds.) Louisiana Offshore Oil Port and Environmental Baseline Study. Center for Wetland Resources, Louisiana State Univ., Baton Rouge.

Withee, G. W., and A. Johnson, 1975, Data report: buoy observations during Hurricane Eloise. NOAA Data Buoy Office, Bay St. Louis, MS, 21 pp.

Woodward, W., C. N. K. Mooers, and K. Jensen (Eds.), 1978, Proc. of Working Conference on Current Measurement, Tech. Report DEL-SG-3-78, College of Marine Studies, Univ. of Delaware, Newark, DE.

Wright, L. D. and J. M. Coleman, 1971, Effluent expansion and interfacial mixing in the presence of a salt wedge, Mississippi River delta. J. Geophys. Res., 76(36):8649-8661.

Wu, J., 1969, Wind stress and surface roughness at air-sea interface. J. Geophys. Res., 74:444-455.

Wunsch, Carl, 1969, Progressive internal waves on slopes. J. Fluid Mech., 35(1):131-144.

Wunsch, Carl, 1975, Internal tides in the ocean. Rev. Geophys. and Space Phys., 13(1):167-182.

Wunsch, Carl and R. Hendry, 1972, Array measurements of the bottom boundary layer and the internal wave field on the continental slope. Geophys. Fluid Dyn., 4:101-145.

UNCLASSIFIED
SECURITY CLASSIFICATION OF THIS PAGE

REPORT DOCUMENTATION PAGE

1a. REPORT SECURITY CLASSIFICATION Unclassified	1b. RESTRICTIVE MARKINGS
2a. SECURITY CLASSIFICATION AUTHORITY	3. DISTRIBUTION / AVAILABILITY OF REPORT Approved for public release; distribution unlimited.
2b. DECLASSIFICATION / DOWNGRADING SCHEDULE	
4. PERFORMING ORGANIZATION REPORT NUMBER(S) Technical Report No. 398	5. MONITORING ORGANIZATION REPORT NUMBER(S)
6a. NAME OF PERFORMING ORGANIZATION Coastal Studies Institute 6b. OFFICE SYMBOL (If applicable)	7a. NAME OF MONITORING ORGANIZATION
6c. ADDRESS (City, State, and ZIP Code) Louisiana State University Baton Rouge, LA 70803-7527	7b. ADDRESS (City, State, and ZIP Code)
8a. NAME OF FUNDING / SPONSORING ORGANIZATION ONR, Coastal Sciences Program 8b. OFFICE SYMBOL (If applicable)	9. PROCUREMENT INSTRUMENT IDENTIFICATION NUMBER
8c. ADDRESS (City, State, and ZIP Code) Code 422 CS 800 North Quincy Street Arlington, VA 22217	10. SOURCE OF FUNDING NUMBERS PROGRAM ELEMENT NO. / PROJECT NO. NR 388 002 / TASK NO. 4.A / WORK UNIT ACCESSION NO. 18

11. TITLE (Include Security Classification)
OCEAN CURRENT PROCESSES (Unclassified)

12. PERSONAL AUTHOR(S)
Wiseman, Wm. J., Jr., Mooers, C. N. K. (Naval Postgraduate School), Forristall, G. Z. (Shell) (Devel.)

13a. TYPE OF REPORT	13b. TIME COVERED	14. DATE OF REPORT (Year, Month, Day)	15. PAGE COUNT
	FROM 1/1/83 TO 12/31/83	1983	93

16. SUPPLEMENTARY NOTATION
Reprint from Ocean Science and Engineering, 8(4):367-459, 1983.

17. COSATI CODES		
FIELD	GROUP	SUB-GROUP
08	03	

18. SUBJECT TERMS (Continue on reverse if necessary and identify by block number)
ocean current, processes, continental shelf

19. ABSTRACT (Continue on reverse if necessary and identify by block number)

This paper catalogs and discusses the ocean current processes that may impact offshore industrial operations on the continental shelf. The discussion and bibliography are extensive, but not exhaustive. The review is designed to be an introduction for engineers with little or no existing knowledge of physical oceanographic processes.

20. DISTRIBUTION / AVAILABILITY OF ABSTRACT ☒ UNCLASSIFIED/UNLIMITED ☐ SAME AS RPT. ☐ DTIC USERS	21. ABSTRACT SECURITY CLASSIFICATION UNCLASSIFIED
22a. NAME OF RESPONSIBLE INDIVIDUAL Cheri Marquette	22b. TELEPHONE (Include Area Code) 504-388-2395 / 22c. OFFICE SYMBOL

DD FORM 1473, 84 MAR 83 APR edition may be used until exhausted. All other editions are obsolete.

SECURITY CLASSIFICATION OF THIS PAGE
UNCLASSIFIED

AD-A174 470 A COLLECTION OF REPRINTS(U) LOUISIANA STATE UNIV BATON ROUGE COASTAL STUDIES INST W J WISEMAN JR ET AL. JAN 86 2/2
TR-398 N00014-83-C-0150

UNCLASSIFIED F/G 8/10 NL

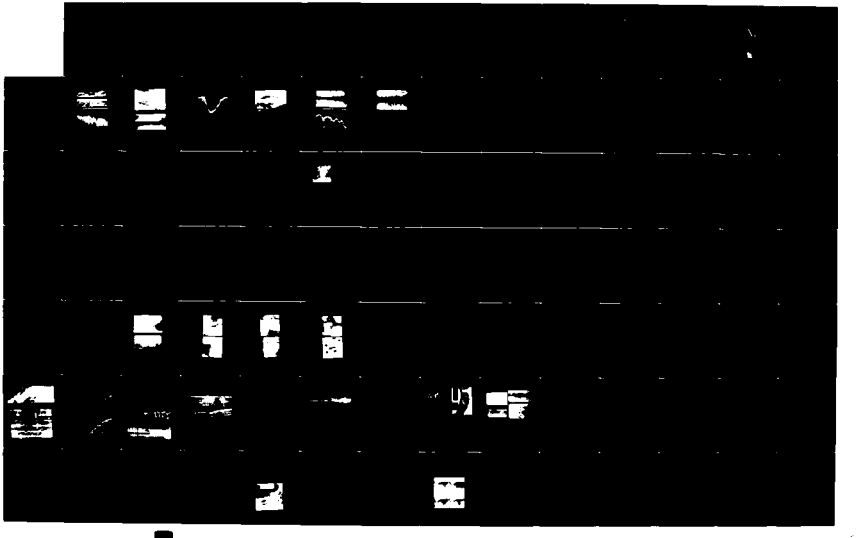

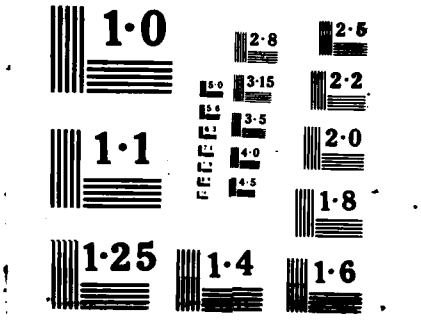
1·0
2·8
2·5
3·15
2·2
3·5
1·1
2·0
4·0
4·5
1·8
1·25
1·4
1·6

Coastal Studies Institute
Louisiana State University
Baton Rouge, LA 70803-7527

Technical Report No. 399

DEVELOPING CARBONATE PLATFORMS: SOUTHERN GULF OF SUEZ, NORTHERN RED SEA

Harry H. Roberts and Stephen P. Murray

1984

Reprint from Marine Geology,
59:165-185, 1984.

Office of Naval Research
Contract N00014-83-C-0150
Project NR 388 002

Marine Geology, 59 (1984) 165—185
Elsevier Science Publishers B.V., Amsterdam — Printed in The Netherlands

DEVELOPING CARBONATE PLATFORMS: SOUTHERN GULF OF SUEZ, NORTHERN RED SEA

HARRY H. ROBERTS and STEPHEN P. MURRAY
Coastal Studies Institute, Louisiana State University, Baton Rouge, LA 70803 (U.S.A.)

(Received August 15, 1983; revised and accepted November 3, 1983)

ABSTRACT

Roberts, H.H. and Murray, S.P., 1984. Developing carbonate platforms: southern Gulf of Suez, northern Red Sea. Mar. Geol., 59: 165—185.

The Ashrafi reef complex represents two small (~8—10 × ~2 km) carbonate platforms and associated shoals located along the western side of the Jubal Strait at the Gulf of Suez's southern end. These features are developing in an active marine environment that is operating within the geologic constraints of a tectonic trough characterized by mountainous fault-controlled margins. Origin of the platforms is uncertain, but the present morphology appears to be a product of the dynamic marine setting in which they are developing. Tidal flow between the Red Sea and the Gulf results in strong rectilinear currents (commonly >50 cm s^{-1}). Of the current velocities, 5—10 cm s^{-1} can be attributed to surface currents driven by a regional, unidirectional wind that blows from north to south down the axis of the Gulf throughout the year.

Side-scan sonar data, coupled with echo-sounder profiles, direct observations via Scuba, and bottom sampling indicate that the Ashrafi platforms are actively building northward by windward reef accretion and extending to the south by sediment transport and accumulation. The drumstick shape is a product of wave-induced reef development along the northern margin and sediment distribution forced by strong tidal currents, which, coupled with unidirectional wind drift, favors net transport to the south. Small reefs and hardgrounds along the downdrift platform flanks assume a linearity consistent with the long axis of the platform. The intensely mounded sediment of the platform flanks suggests that bioejection of particles in the mound-building process, together with a strong flow field, is a downdrift sediment transport agent.

Although the ambient salinity of surrounding Gulf water is ~41‰, platform-top water masses were measured at >47‰. A lack of significant coral growth on the shallow platform top and the almost total exclusion of sediment-producing calcareous green algae may be related to these hypersaline conditions. Sediments for the platform flanks are largely provided by the breakdown of platform margin reef communities and in-situ organisms (largely foraminifera).

INTRODUCTION

In June—July 1981 the Coastal Studies Institute of Louisiana State University conducted a marine geology/physical oceanography field study of the Strait of Jubal at the southern end of the Gulf of Suez, northern Red Sea (Fig.1). Objectives of the project were twofold: (1) to develop an understanding of the dynamical forces that control flow in the Jubal Strait by observation

0025-3227/84/$03.00

and analysis of important physical agents (primarily wind, currents, tides and density gradients); and (2) to determine the sea floor boundary characteristics (form and response to driving forces) of the strait through indirect (side-scan sonar and high-resolution seismic) and direct (bottom sampling, photography, and Scuba) observations. Results presented in this paper deal with the marine geology and physical process environment of the western Jubal Strait area, the Ashrafi Reef complex (Fig.1).

The Ashrafi carbonate platforms (Fig.2) occur in a narrow embryonic sea (Gulf of Suez) that has developed, along with the Gulf of Aqaba (Elat), as a product of rifting associated with opening of the Red Sea. The Gulf of Suez has formed primarily by block faulting, which was underway by Oligocene—Early Miocene (Garfunkel and Bartov, 1977), whereas transform faulting, as well as normal faulting, controls the geometry of the Aqaba (Elat) Gulf (Ben Avraham et al., 1979; Garfunkel, 1981). As a consequence of this early to middle Tertiary faulting, quite different sea floor morphologies and sedimentary fill sequences have developed within the two gulfs.

As compared to the Gulf of Aqaba (Elat), the Gulf of Suez is shallower (averages <100 m as compared to >1000 m), has more sediment fill (in excess of 4.5 km compared to slightly over 3.0 km thus far proven from the Gulf of Aqaba), and has a much wider and more complicated strait connecting it with the Red Sea. Flanks of the Suez Gulf are characterized by rugged mountains (~ 2000 m) of igneous and metamorphic basement rocks that rise abruptly from narrow coastal plains formed from interfingering alluvial fans composed of poorly sorted terrigenous debris. An arid climate promotes aperiodic transport of this siliciclastic sediment to the Gulf during flash-flood events. In low-relief coastal areas at the distal ends of alluvial fans or in interfan zones, high rates of evaporation, coupled with tidal activity, promote the development of narrow coastal sabkhas. Within this tectonic and sedimentologic framework, numerous small-scale carbonate platforms are forming at the southern end of the Suez Gulf. Some of these features, such as the Shoab Ali complex along the eastern margin of the strait (Fig.1), have obviously accreted over a controlling subsurface structure, as confirmed by drilling data (Glen Steen, Gulf of Suez Petroleum Company, pers. commun., 1981). Other platforms, such as the Ashrafi system (Fig.2), are not so easily linked to subsurface control. Although positions of these platforms are generally thought to be associated with structures created by the complicated tectonic heritage of the area, surface and near-surface platform characteristics appear to be controlled by combined physical and sedimentological processes. In this paper the present sea floor expression of the Ashrafi reef complex is explored and the physical process climate in which these platforms are developing is examined.

METHODS

A 22-m fishing boat, the "Karam El Suez", out of Port Suez, was chartered to serve as a research vessel. Hurghada (Fig.1), the site of the Egyptian

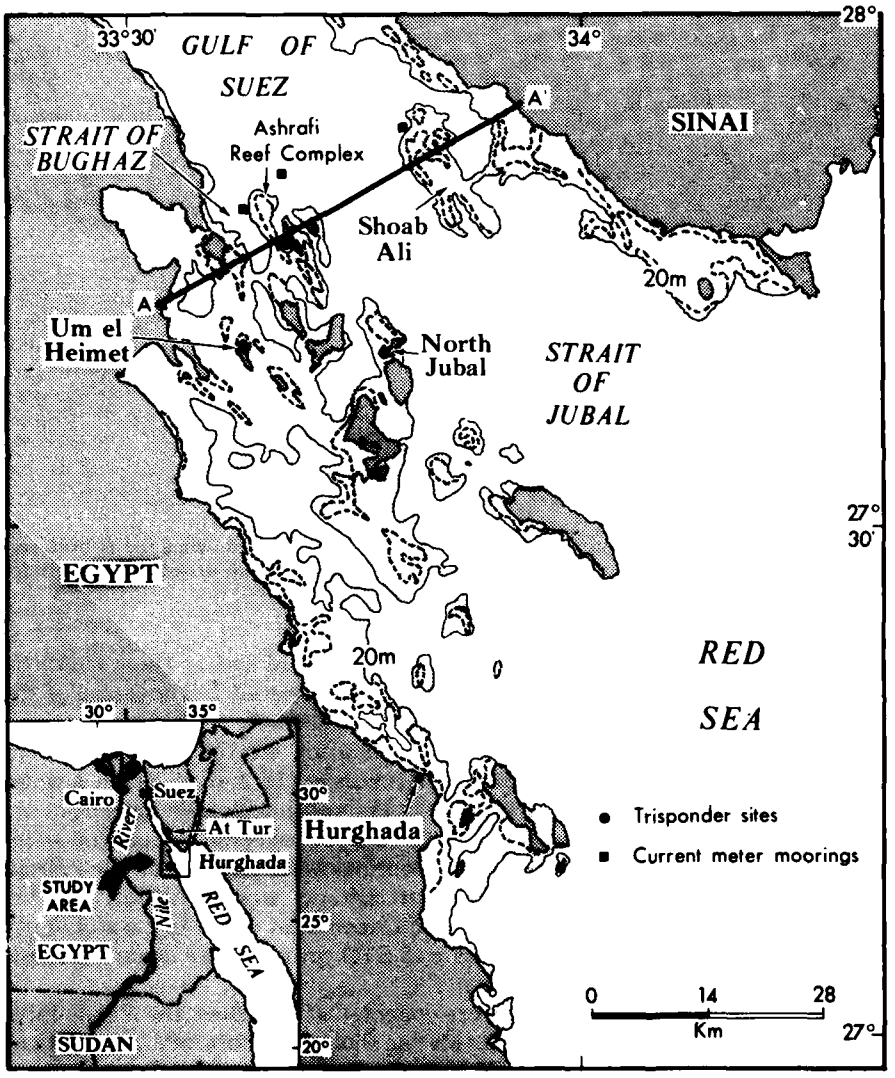

Fig.1. Location map of the study area at the southern end of the Suez Gulf showing the Jubal Strait and Ashrafi reef complex. Field operations were staged from the small town of Hurghada. In-situ instrumentation sites are shown.

Academy of Sciences' Red Sea Laboratory, served as a base of operations. From Hurghada it was a 4—5 h run north to the study area.

Marine geology data and the locations of current meters, as well as other geologic/physical oceanographic sample positions, were fixed by a Decca Del Norte electronic range-range locating system. Trisponder navigation stations

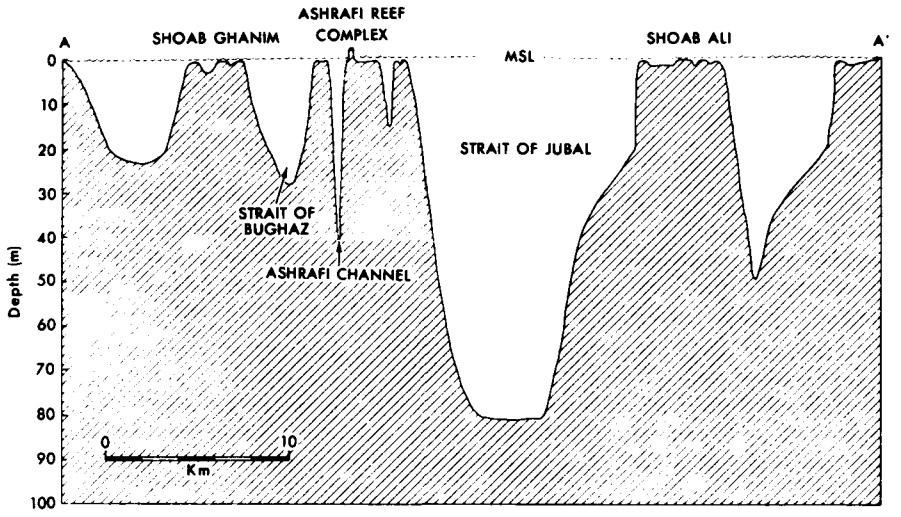

Fig.2. Cross-section of the southern Gulf of Suez (looking north) showing the Ashrafi reef complex and other carbonate platforms associated with the Strait of Jubal (see Fig.1 for location of section).

were set up by small boat on Umm El Heimet Island and on the western tip of North Jubal Island (Fig.1). This deployment allowed full coverage of the strait study area.

In-situ current meter data were collected using six Endeco 174 current meters. Two meters were deployed on a mooring (18 and 58 m) in a water depth of 61 m in West Jubal Strait (Fig.1). Another double current-meter mooring (12 and 52 m) was placed in the East Jubal Strait, where the water depth was 56 m (Fig.1). Single-meter moorings were made near the Ashrafi reef complex in the Bughaz Strait, a short distance west of Ashrafi (at 12 m in a water depth of 26 m), and in Ashrafi Channel (at 4.5 m in a water depth of 26 m). Additional anchor stations and STD profiles were made on a traverse across the strait.

Wind speed and direction data were collected at two sites, the North Jubal Island trisponder site (Fig.1) and the Marine Biology Laboratory in Hurghada. Water levels were also continuously monitored at the Red Sea Laboratory as well as North Jubal Island.

Marine geology data were collected using a variety of methods, including bottom sampling (Shipek sampler), side-scan sonar (Klein system with 3.5 kHz subbottom profiler), bathymetric profiling (Raytheon Model 231 echo-sounder), and Scuba diving for direct observations and sampling. Locations of survey lines and sample sites were tightly controlled by using the Trisponder system with position updates at 1 min intervals.

DYNAMICAL CONDITIONS

Constraints imposed on the study area by geologic framework and climate have led to some interesting dynamical conditions. For example, the elongate shape of the Gulf of Suez and the abrupt mountain fronts that parallel its perimeter produce strong axial winds by channeling regional wind as well as generating local winds by heating and cooling of the mountain slopes. Regional wind data from the Red Sea area show that winds in the northern Red Sea, above 20°N lat., are persistently from the north throughout the year with maximum speeds between June and October at the latitude of our study area, 27°—28°N (Patzert, 1974). South of 19°N the unidirectional nature of the surface winds breaks down. Long-term records from Hurghada (U.S. Naval Oceanographic Office, Sailing Directions, 1965) indicate that 79% of the winds are north-northwest, while southerly winds account for only 3%. Our data collection stations at both Hurghada and North Jubal Island (Fig.1) confirm their strong speeds (10—15 m s^{-1}) and steady directional properties (Fig.3).

Although the Gulf of Suez is a fetch-limited system, strong local winds, coupled with a directionality that nearly always coincides with the long axis

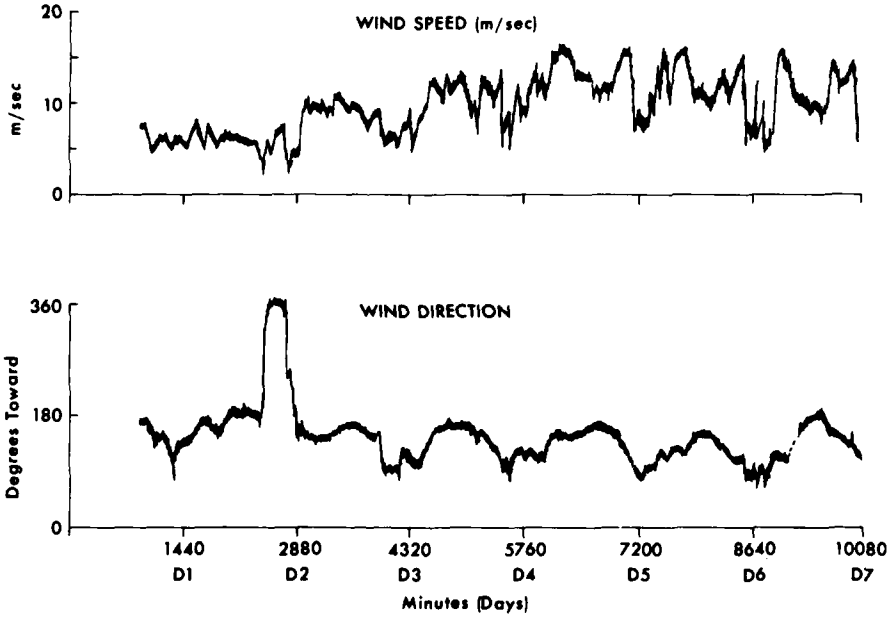

Fig.3. Wind speed and direction data collected over a period of approximately 7 days at the North Jubal Island instrument station (Fig.1). The sample interval was 10 minutes. Start time was 1457 h on 5 July 1981. Note the nearly unidirectional nature of the wind field and the normally high speeds during the period 8—11 July. The axis of the gulf is approximately 150°.

of the Gulf, creates an unexpectedly strong wave field. The maximum effect of the Gulf's fetch (~250 km) is focused on the islands and carbonate platforms of the study area (Strait of Jubal), creating high-energy conditions on the northern ends of the platforms. In response, densely populated reef communities that have adjusted to strong waves fringe the northern ends of these submarine relief features.

Morcos (1970) indicates that the tidal range (~0.3—1.5 m) in the Gulf of Suez (average depth of 36 m) decreases from the southern entrance toward a nodal point (At Tur, ~60 km north of the study area) and then increases again to approximately 1.5 m at the northern end. High water in the north is one-half cycle out of phase with high water in the strait, indicating the existence of a first mode (one-half wavelength) standing wave. Amplitude of the semidiurnal tide measured at both North Jubal Island and Hurghada was approximately 30—50 cm during the period of our studies. These tidal oscillations are extremely important in our area of study because they drive strong tidal currents capable of moving bottom sediment and stimulating viable reef development, both of which affect bottom topography. As summarized by Morcos (1970), Vercelli (1931), who apparently has published the only prior current observations in the Gulf of Suez basin, reports tidal currents reaching velocities of about 75 cm s^{-1} at springs and 25 cm s^{-1} at neaps along the central axis of the Gulf. In the Strait of Jubal, current amplitudes were reported to reach 100 cm s^{-1}.

The six current meters deployed across the Gulf in this study (Fig.1) produced data that substantiate basic observations of Vercelli (1931). That is, a well-developed tidal oscillation dominates all current data sets (Murray and Babcock, 1982). In contrast to his measurements, our tidal current oscillations were generally of lower velocities, 30—40 cm s^{-1} (Fig.4). However, meters in this study were actually deployed on the flanks of the major channel, which is commonly referred to as the Strait of Jubal (the deep channel was a military restricted area for moorings at the time of our project). A general profile (Fig.2) of the sea floor across the area of investigation, with its flanking islands, carbonate platforms, and relatively deep central channel, shows that Ashrafi Channel (the site of one current meter mooring) is small in comparison with the main Strait of Jubal and might be significantly affected by frictional retardation. However, a record from the Ashrafi reef complex current meter (Fig.4) illustrates a strong and nearly rectilinear flow through this relatively small channel.

Because of the unusually high yearly evaporation rate in the northern Red Sea region, estimates ranging from 100 to 365 cm yr^{-1} (Neumann, 1952; Morcos, 1970; Grashof, 1975; Assaf and Kessler, 1976), density-driven flows could be expected. Morcos (1970) shows from inclinations of isotherms and isohalines that there is generally a surface inflow of warmer, less saline Red Sea water and a bottom layer outflow of colder, saltier Gulf of Suez water through the Strait of Jubal. Despite strong and persistent north winds directed to drive water out of the Gulf to the Red Sea, current data collected during this project indicate that a mean surface flow (3-day low pass) directed into

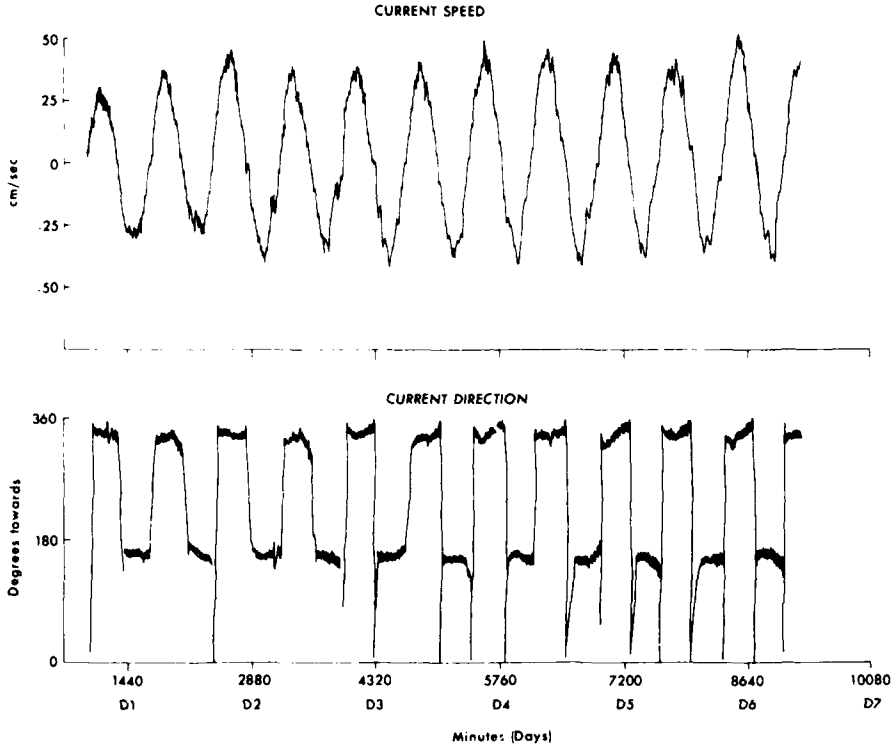

Fig.4. Current speed and direction data from an ENDECO current meter moored at 4.5 m in Ashrafi Channel (water depth 26 m). Data are from the time period 15 July 1981 (1342 h)—21 July 1981 (1120 h) using a 2-min sample interval. The speed trace represents the resultant flow along the principal axis of the tidal current ellipse ($U = 336°$, essentially the orientation of the channel), which clearly shows the semidiurnal tidal forcing. Note the rectilinear nature of the direction data. Cross-channel components of the current are insignificant.

the Gulf is characteristic of only the eastern side of the strait (Murray and Babcock, 1982). Two-layered flow, however, is confined to the deep central part of the Jubal Strait. Along the topographically complicated western flank of the deep strait, where the Ashrafi carbonate platforms are located, wind stress has more impact on the local current field than density differences. Although tidally driven currents are by far the most important, wind forcing can account for 5—10 cm s^{-1} (~20%) of the total current velocity. Because of the unidirectional nature of the wind field, flow to the south is augmented. This asymmetry in the current field interfacing with the Ashrafi platforms is clearly evident in the wind stress and resultant wind-driven current component (Fig.5) from the Bughaz Strait, which borders the western flank of the study area.

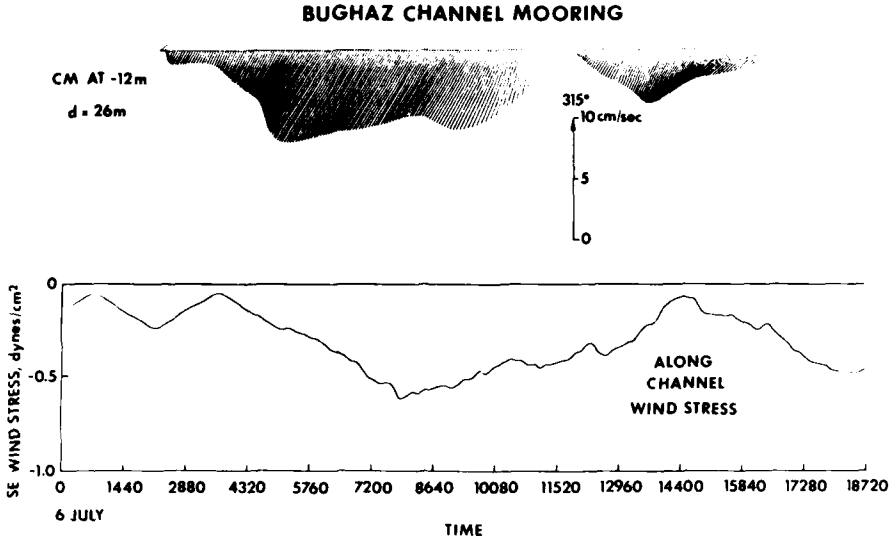

Fig.5. The along-channel wind stress is plotted for a 13-day period and compared to the wind drift component of the current from the Bughaz Channel mooring west of the Ashrafi platform. The meter was located 12 m below the surface in a total water depth of 26 m. For current meter location, see Fig.1. These data indicate that currents in shallow channels on the western side of the Jubal Strait are greatly influenced by wind stress.

ASHRAFI PLATFORMS

Subsurface data are not available to determine a substrate for the Ashrafi carbonate platforms. Because of recent drilling activity associated with the search for and production of hydrocarbons (Hargras et al., 1983), more data are being generated from which an understanding of the formative stages in carbonate platform growth can be developed. Shoab Ali reef platform, on the eastern side of the Jubal Strait (Fig.1), for example, is known to have started on a structural high associated with a shallow (~1500 m below the sea floor) block of igneous basement (Glen Steen, Gulf of Suez Petroleum Company, pers. commun., 1981). Other platforms like those in the Ashrafi complex are not so clearly linked to a structural beginning.

It is known, however, that after opening of the Gulf of Suez Graben, Miocene and later deposition was controlled by fault-bounded margins, with the Sinai Massif providing the eastern boundary and the igneous-metamorphic Red Sea Hills forming the western margin. Within this tectonic framework, recent drilling has confirmed that approximately 4.5 km of Early Miocene and younger sediments have accumulated in the Gulf of Suez Graben, including a thick (>1 km) unit of evaporites (Glen Steen, Gulf of Suez Petroleum Company, pers. commun., 1981). Although the excessive thickness of Miocene and younger salt has caused exploration problems (Kanes and Abdine, 1983), mobilization of these sediments has produced elongate Gulf-parallel

structures with which carbonate platforms such as Ashrafi may be associated. Alternatively, the Ashrafi platforms may have had a fault-related beginning. Garfunkel and Bartov (1977) indicate that numerous Gulf-parallel normal faults cut the Pliocene—Recent alluvium flanking the present Gulf. A slight offset on the Gulf floor associated with this faulting may have provided the initial sea floor relief that commonly promotes reef and hardground development. Drilling data from the Ashrafi area suggests shallow faulting of the carbonates (Stan Slocki, geologist for the Gulf of Suez Petroleum Company, pers. commun., 1981) as well as possible association with a deep salt ridge. Regardless of the mode of origin, there can be little doubt that the present elongate configuration of Ashrafi carbonate platforms and shoals is primarily related to the dynamic marine setting in which they are forming.

Figure 6 illustrates the streamlined morphology of the Ashrafi platforms and shoals. Strong tidal currents as measured in Ashrafi Channel (Fig.4) and the adjacent Strait of Bughas, augmented by southerly directed wind stress, produce a net sediment transport to the south. This dynamical setting promotes a wave-dominated northern end to the platforms, with a downdrift or southerly end characterized by an accumulation of sediment that decreases in width and increases in water depth.

A side-scan sonar track map, Fig.7, illustrates the variability of bottom features around the easternmost drumstick-shaped platform in the Ashrafi reef complex (Fig.6).

Windward margin

The northern end of this carbonate platform has very rough bottom topography related to irregular patterns of reef growth. Some reef elements have relief of up to 6 m (Fig.8), but most are less than 3 m. Progressing from the northern wave-stressed end of the platform to the lower energy flanks, the sizes of reef masses seaward of the shallow crest diminish systematically, and they appear to become less organized than the ridges and channels of the northern margin. As is illustrated on both the side-scan sonar track map (Fig.7) and the side-scan sonograph (Fig.8), rough-textured living reefs are separated by smooth, sediment-floored channels. Unlike the windward margins of most modern coral reefs (Roberts, 1974), these channels tend to be oriented subparallel to the reef crest rather than at a high angle to it. Although preliminary calculations (Roberts and Murray, 1983) indicate that wind conditions in the Gulf of Suez can produce waves of the same order of magnitude as experienced by central Caribbean reefs, side-scan data indicate that well-organized spur and groove topography has not developed in the Ashrafi reefs. Perhaps strong tidal flow, augmented by wind-driven currents and mass flux contributed by waves, provides the most important physical inputs to this part of the platform, thus tending to streamline the reef elements around the platform perimeter.

Unlike the typical gulf-margin reefs that fringe the perimeters of both the Gulfs of Suez and Elat (Friedman, 1968; Loya and Slobodkin, 1971; Erez

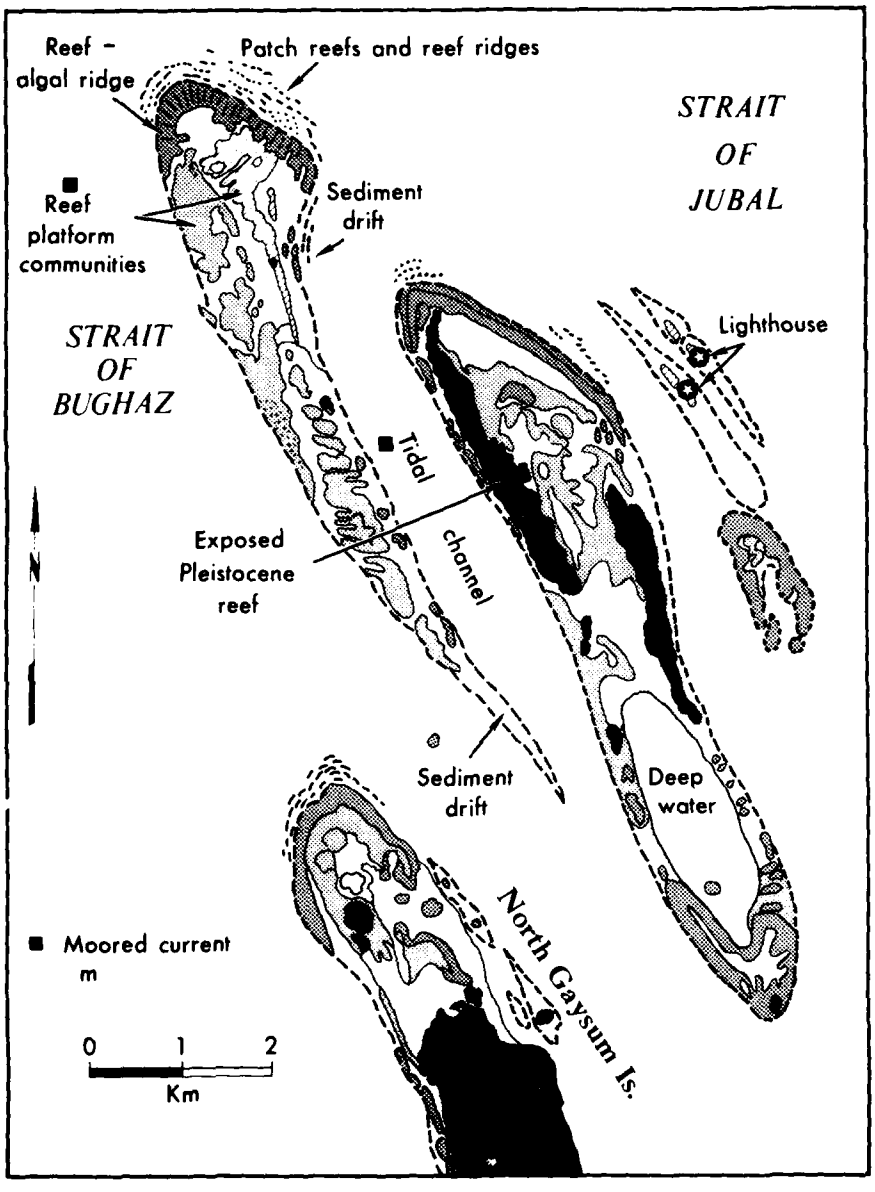

Fig.6. A plan-view map of the "streamlined" Ashrafi carbonate platforms showing the areal extent of reef and other platform communities (mapped from air photographs with major subdivisions confirmed by "ground truth" observations).

and Gill, 1977; Gvirtzman et al., 1977), the Ashrafi platform reef does not have an extremely level reef flat followed by a very steep reef wall on the seaward side. The Ashrafi reef has a coral-covered reef crest and flat that slopes gently into the forereef area (Fig.9). Abundant coral growth is characteristic of the shallow reef and offshore patch-like reef development observed on side-scan sonographs (Fig.8). Commonly occurring corals include *Acropora*, *Porites*, *Platygyra*, *Pocillopora*, *Alcyonium*, *Stylophora*, and others. In addition, coralline algae are abundant as both encrusting and free living forms. These carbonate producers appear to be very significant in the reef-building process in shallow windward parts of the platform. In this wave-stressed part of the reef, the bottom is covered with a thick plant growth tentatively identified as *Cymodocea*. This plant is an important part of the bottom community to a depth of 15—20 m, where *Halophila*, another non-calcareous marine plant, becomes dominant.

Platform flanks and tidal channels

Shallow flanks of the Ashrafi platform are characteristically hardgrounds with patchy coral growth broken by well-defined channels. These linear topographic lows are oriented roughly normal to the platform margins and function as routes for off-platform sediment transport (Fig.10). Hardgrounds and areas of patchy reef growth appear to be seated on an erosional Pleistocene (?) surface, two small remnants of which still exist with relief of 2—4 m above MSL (Fig.6). At some locations along the platform flanks where sedimentation has not created a smooth slope between the platform top and its flanks, this transition can be quite abrupt, as is shown in Fig.10. In contrast, toward the southeast (downdrift) end of the northern platform margin high-energy reef is a wide and very well defined area of sediment accumulation. This sediment drift, as indicated on Fig.6, has resulted from sediment derived from biological and mechanical breakdown of the reef framework and subsequent transport of this material toward the backreef. Initial sediment transport appears to take place as a product of wave-breaking on the reef crest. As described by Roberts and Suhayda (1983), this process creates strong reef-normal surge currents that transport sediments to the immediate backreef. Once in this setting, other mechanisms such as off-platform flow driven by tidal activity provide the forces necessary to further distribute the sedimentary material.

Adjacent to the platform are tidal channels (Fig.11) that vary in depth from ~30 to 60 m. The flanks of these channels are mantled with sediments that are highly mounded and colonized by a thick community of the marine plant *Halophila* (Fig.12). In areas where mounding is most intense, the bioturbation of an organism, which is believed to be *Callianassa*, appears to exclude the colonization of benthic plant communities. In addition to this relationship, Roberts et al. (1981) found that the mound-building process can be a very important sediment transport agent, even in the presence of low-velocity currents. As the organism ejects sediment into the water column,

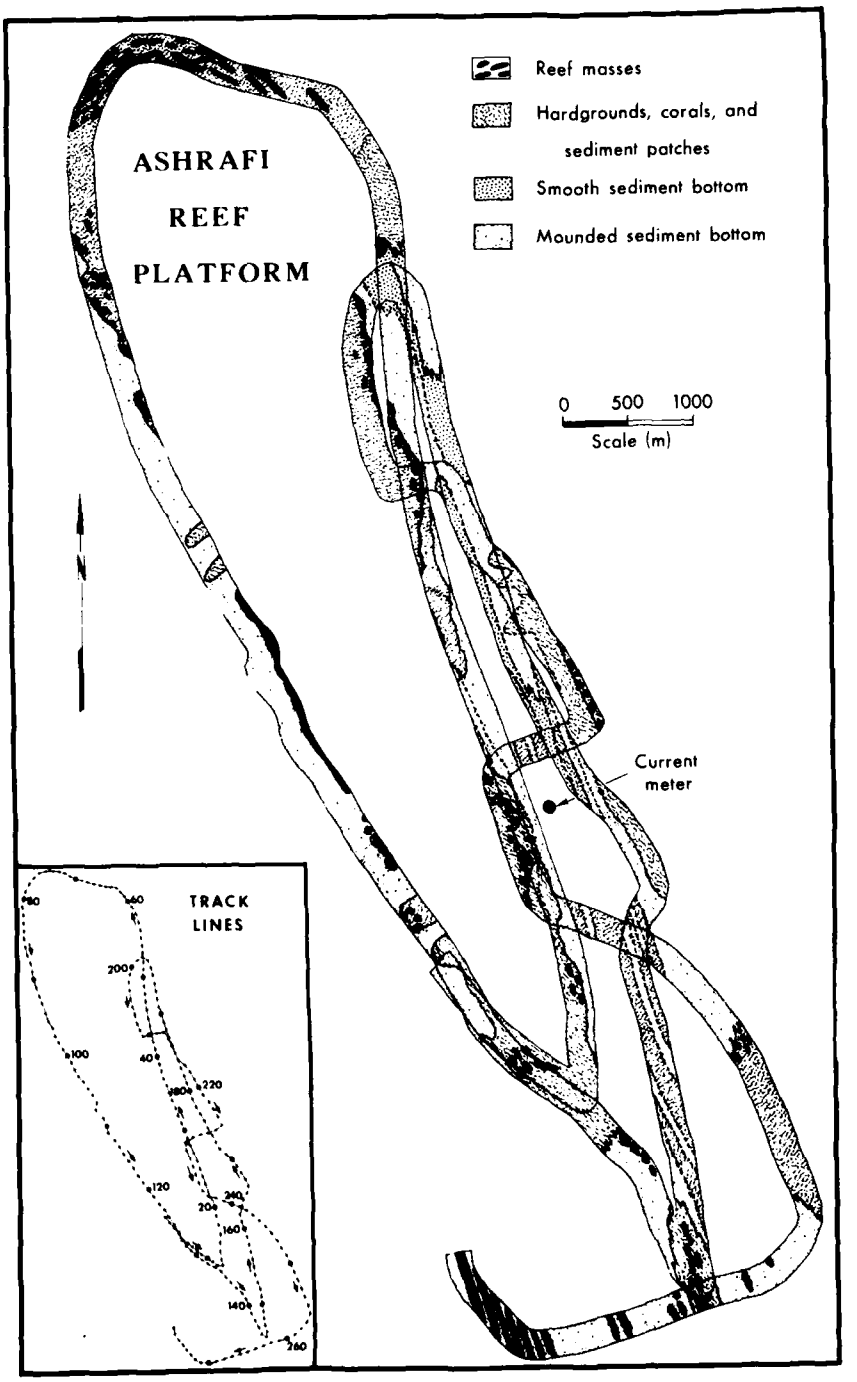
ASHRAFI
REEF
PLATFORM
Reef masses
Hardgrounds, corals, and sediment patches
Smooth sediment bottom
Mounded sediment bottom
0 500 1000
Scale (m)
N
Current meter
TRACK LINES

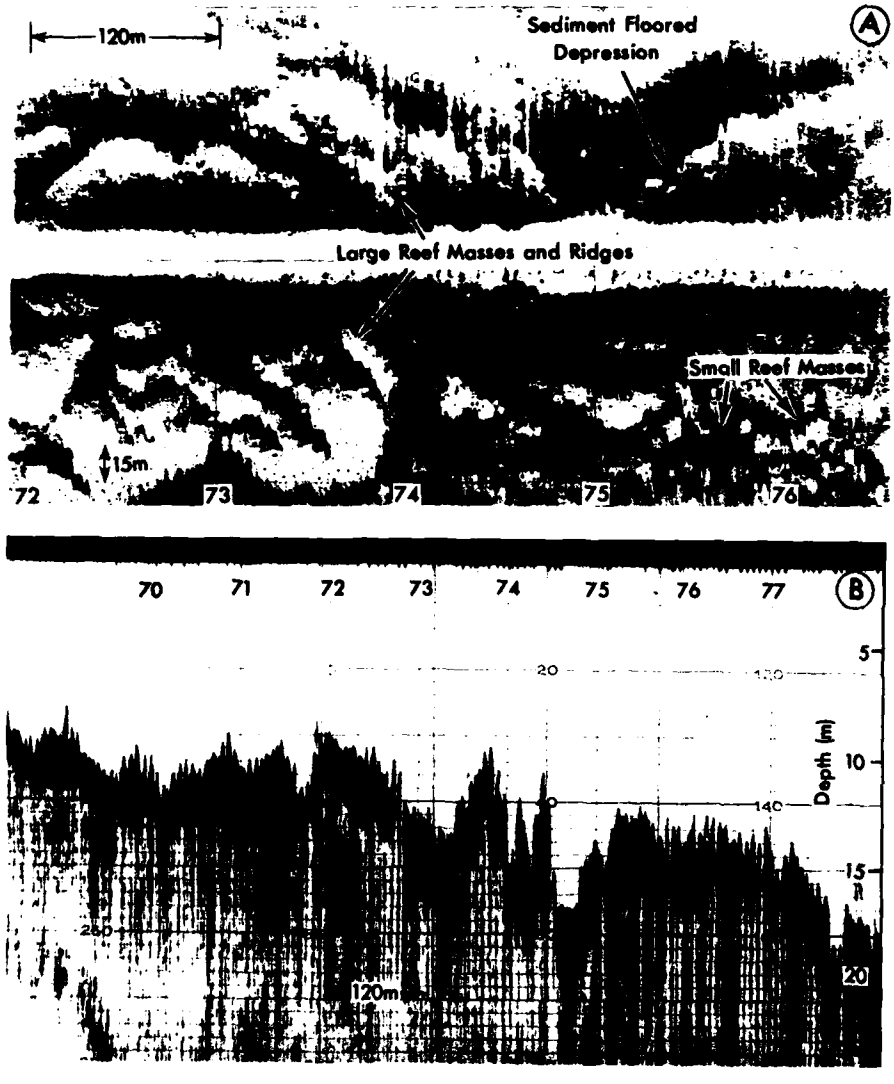

Fig.8. (A) Side-scan sonograph and (B, accompanying echo-sounder trace of the high-energy northern end of Ashrafi Reef shown on the track map (Fig.6). Note the highly irregular bottom topography and the lack of distinct spur and groove morphology. Refer to the track-line map (Fig.7) for exact locations of the side-scan sonograph and bottom profile (position fixes 70-77).

Fig.7. A side-scan sonar track map compiled from data taken around the westernmost platform in the Ashrafi reef complex (see Fig.5). The inset illustrates survey track lines showing location fix points. Fix points on side-scan sonographs used in this paper can be referred to these track lines for location.

Fig.9. Windward reef crest area of Ashrafi platform. Water deepens to forereef toward the right (water depth approximately 1.5 m in the central part of the photo).

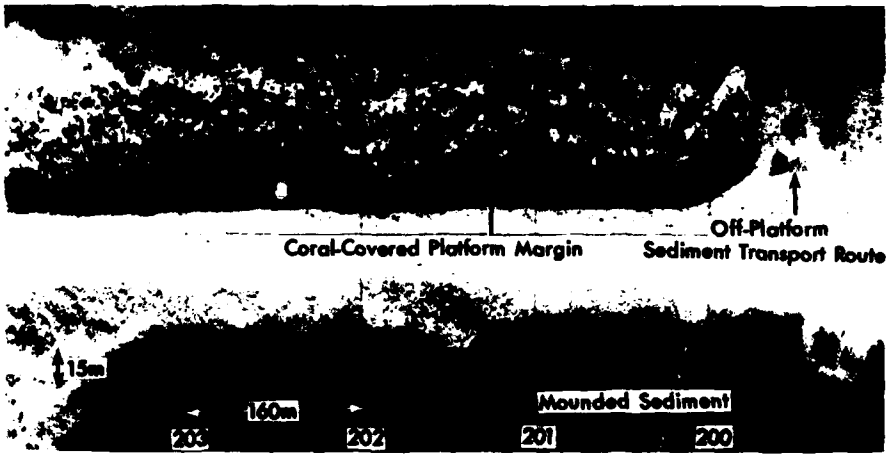

Fig.10. Side-scan sonograph showing the shallow coral-covered edge of the Ashrafi platform with a well-developed sediment-floored channel at the right (northern) end of the figure. Abundant sediment collects downslope of the shallow hardgrounds (position fixes 200–205, Fig. 7).

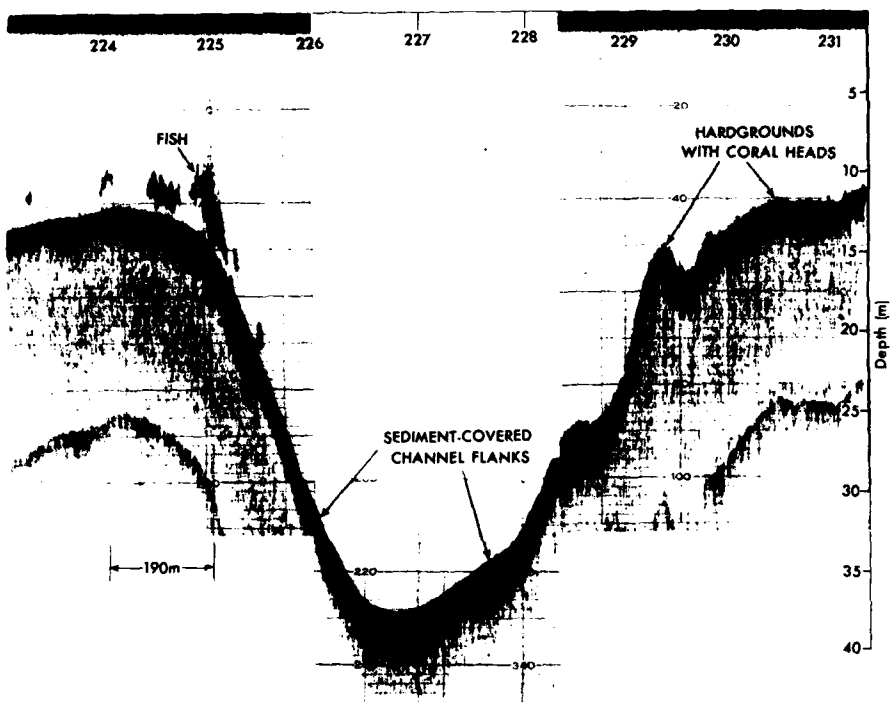

Fig.11. An echo-sounder profile across the Ashrafi tidal channel (position fixes 225-230 on Fig.7) showing the generally smooth bottom representing a covering of unconsolidated Holocene sediment.

it is advected downdrift by the mean flow regime, while the particles settle from suspension. In the Ashrafi platform flank environment, strong tidal currents (Fig.4) work the sediment back and forth. Augmented by wind-driven currents (Fig.5), the net flow is to the south, creating a process that favors southerly progradation of the platform flanks.

Downdrift end

The drumstick shape of the westernmost Ashrafi platform (Fig.6) suggests a high-energy northern part with a streamlined southern downdrift "tail". North Gaysum Island shelters the Ashrafi platforms from direct access to energy from the south (Figs.1 and 6). This sheltering creates a lower energy setting for the southern parts of the Ashrafi platforms, which are characterized by a minimum of wave activity but exposed to strong tidal exchanges.

The side-scan sonar track-line map (Fig.7) illustrates some interesting sea floor features that are apparent toward the platform's southern end. Although sediments clearly mantle the platform flanks and the Ashrafi tidal channel floor along the northern two-thirds of the platform, long, linear hardgrounds

Fig.12. Highly bioturbated carbonate sediments on the flank of Ashrafi tidal channel (depth 36 m). The extremely mounded surface appears to be related to the burrowing activity of the shrimp *Callianassa*. A benthic plant community dominated by *Halophila* occupies areas of least intense mounding.

develop at the southern end (Fig.13). These features parallel the long dimension of the platform and may be related to a variety of possible process-form interactions, including shoreline development during the last Holocene rise in sea level, tidally induced ridges, or a product of the combined effects of marine processes and tectonic activity. The bathymetric profile of Fig.13B is suggestive of a mechanism that favors constant sediment movement in the topographic lows, thus eliminating substrate areas for sedentary organisms. The ridges then become sites of accretion by a variety of carbonate-secreting organisms. A detailed analysis of the process-form relationships associated with these features is beyond the scope of data collected during this project. The same basic morphology, however, is reflected in smaller and very actively growing reef ridges near the crest of the narrow southern extremity of the platform (Fig.14). Like the broader and longer features that occur on the flanks of Ashrafi tidal channel (Fig.7), these shorter but higher relief reef ridges are actively growing with an orientation that parallels the platform's long axis. Certainly, the strong rectilinear tidal currents in Ashrafi channel promote lineations parallel to the channel axis.

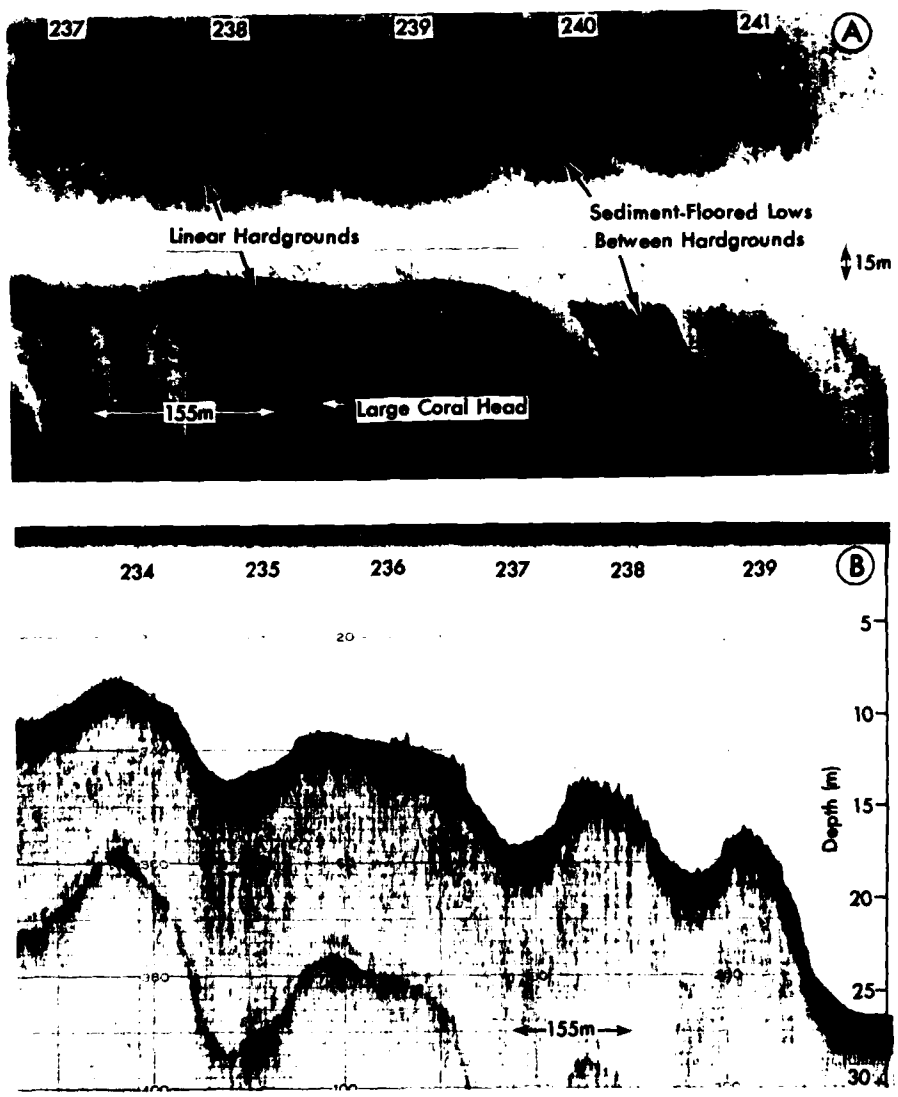

Fig.13. *A*. A side-scan sonograph illustrating downdrift flank of Ashrafi platform (position fixes 237-241 on Fig.7). Note the linear hardground ridges separated by depressions containing only a thin sediment veneer. *B*. The accompanying echo-sounder trace shows the morphology of these ridges that roughly parallel the platform's long dimension.

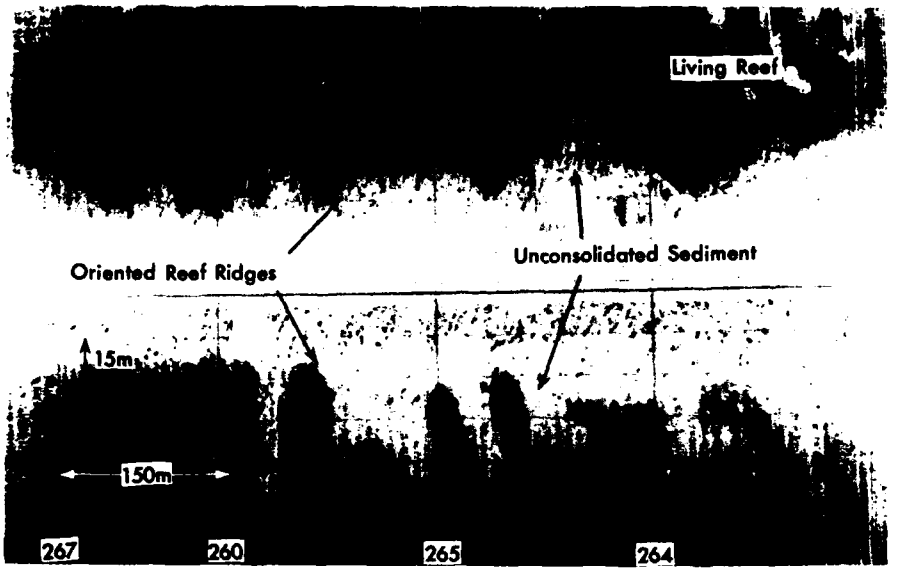

Fig.14. Side-scan sonograph across the crest of downdrift end of Ashrafi platform. Note the linear reefs that are aligned with the long axis of the platform. Sediments fill the topographic lows between these linear relief features (position fixes 263-267, Fig.7).

Platform top

As previously stated, the platform top is shallow (at least half of the platform is <1.5 m at mean tide) and with very little relief. The presence of two small islands of former platform carbonates presumably of Pleistocene age suggests that the present surface is one of marine planation. Various communities of non-calcareous marine plants inhabit most of this surface. Corals and viable reef structures are restricted to the platform margins except at the downdrift end, where water depths increase substantially. Two observations were interesting to the authors concerning these shallow platform environments. Firstly, there was very little coral growth on the platform top. Secondly, calcareous algae were conspicuous by their absence. Routine collection of physical oceanographic data adjacent to the platform may have provided some insight into the reasons for a scarcity of both corals and calcareous green algae from the platform tops. Water masses from this environment were measured as having 47‰ salinities, while average Gulf salinities are approximately 41‰. Although Kinsman (1964) observed coral growth in the Persian Gulf at 48‰, salinities of this magnitude may exclude most common coral species and forms of calcareous green algae.

SUMMARY

The present marine setting of the southern Gulf of Suez is dominated by strong tidal exchanges with the Red Sea. These rectilinear currents regularly reach magnitudes of greater than 60 cm s^{-1} in the complicated region of islands, platforms, and shoals characteristic of the western side of the southern Gulf. Previous investigators (Vercelli, 1931) have reported current speeds of up to 100 cm s^{-1} in the main Strait of Jubal just east of the Ashrafi reefs. Augmenting the tidal currents is a persistent wind-driven component from the north. Tidal forcing is by far the most important contributor to the flow field within the southwestern part of the gulf. Wind-driven currents account for 5—10 cm s^{-1} to the total velocity. Because of the unidirectional nature of the regional wind field (north to south down the gulf axis), southerly flowing ebb-tide currents are augmented by wind drift. The net drift, and therefore the long-term sediment transport direction, is to the south. This dynamic setting, in conjunction with a moderate wave field from the north, has had a streamlining effect on the carbonate platforms and shoals that are developing in the southern Gulf of Suez.

The Ashrafi carbonate platform that is the subject of this investigation has a shallow, coral-algal reef-dominated northern end with a narrowing and deepening extension to the south. The platform top is shallow and flat, with two small subaerial remnants of probable Pleistocene platform limestone, suggesting that the present platform top communities are seated on an erosional surface. These communities are primarily marine plants, brown and green algae, which do not produce calcareous sediment. However, large foraminifera (*Amphistegina*) live in these habitats and are abundant in the platform top sediments.

Active coral growth is concentrated around the platform margins, with the best developed reefs on the wave-impacted northern end. Individual reef ridges in this area have maximum relief of 7 m at the most northerly part of the platform. The relief of reef elements decreases down both flanks away from this point. Typical spur and groove topography is not well developed along the windward margin of the Ashrafi platform. In contrast, reef ridges tend to be oriented subparallel to the shallow reef crest rather than at a high angle to it, suggesting that strong currents encountering the northern end and sweeping around the platform have a greater impact on reef morphology than waves.

Side-scan sonar data suggest that the reefs supply sediment to the platform flanks down well-defined pathways. The high degree of mounding of off-platform sediments suggests that sediment transport may be augmented by the ejection of sediment into the water column by burrowing organisms (*Callianassa*). Net transport direction is to the south. Linear hardgrounds separated by sediment-floored depressions are apparent along the southerly flanks of the platform, with similar but higher relief reefs at the narrow southern platform limit.

In conclusion, marine survey data, coupled with physical oceanographic measurements, suggest that the shape of the Ashrafi platforms is a product

of their dynamic marine environment. Platforms are building by reef progradation to the north, primarily in response to the wave field, and southern transport of sediment along the platform flanks is responding to strong tidal currents that are biased toward southerly flow by wind effects. Research is continuing on the subject of carbonate platform development in straits areas of narrow and relatively young seaways of the northern Red Sea. Future studies will focus on their possible long-term effects with regard to regulating flow and to some extent sedimentation in the gulf.

ACKNOWLEDGEMENTS

We gratefully acknowledge support of this study by the Coastal Sciences Program, Office of Naval Research, Arlington, VA 22217. Technical support prior to as well as during field data collection phase of the project was provided by Norwood Rector and Walker Winans. Mrs. Gerry Dunn prepared the illustrations, and Mr. Kerry Lyle is cited for photographic assistance. The authors are very grateful to Glen Steen, Stan Slocki, Tim Russell, Tom Semerad, and others at the Gulf of Suez Petroleum Company (GUPCO) for their helpful discussions concerning the geology of our study area. The project coordinator for the Egyptian effort was Dr. Gerges F. Soliman, a physical oceanographer, now acting as director of the Institute of Physical Oceanography, Alexandria.

REFERENCES

Assaf, G. and Kessler, J., 1976. Climate and energy exchange in the Gulf of Aqaba. Mon. Weather Rev., 104: 381—385.

Ben-Avraham, Z., Garfunkel, Z., Almagor, G. and Hall, J.K., 1979. Continental breakup by a leaky transform: The Gulf of Elat (Aqaba). Science, 206: 214—216.

Erez, J. and Gill, D., 1977. Multivariate analysis of biogenic constituents in Recent sediments off Ras Burka, Gulf of Elat, Red Sea. Math. Geol., 9: 77—98.

Friedman, G.M., 1968. Geology and geochemistry of reefs, carbonate sediments, and waters, Gulf of Aqaba (Elat), Red Sea. J. Sediment. Petrol., 38: 895—919.

Garfunkel, Z., 1981. Internal structure of the Dead Sea leaky transform (rift) in relation to plate kinematics. Technophysics, 80: 81—108.

Garfunkel, Z. and Bartov, Y., 1977. The tectonics of the Suez Rift. Geol. Surv. Israel, Bull., 71.

Grashof, K., 1975. The hydrochemistry of landlocked basins and fjords. In: J.P. Riley and G. Skirrow (Editors), Chemical Oceanography, vol. 2. Academic Press, New York, N.Y., pp.456—597.

Gvirtzman, G., Buchbinder, B., Sneh, A., Nir, Y. and Friedman, B., 1977. Morphology of Red Sea fringing reefs: a result of the erosional pattern of the last glacial low-stand sea level and the following Holocene recolonization. Mém. Bur. Rech. Géol. Min., 89: 480—491.

Hargras, M., Hunter, G. and Nairan, A.E.M., 1983. Oil potential of western Gulf of Suez. Am. Assoc. Pet. Geol., Annual Convention, Dallas, April 17—20, 1983, Book of Abstracts, p.91.

Kanes, W.H. and Abdine, S., 1983. Egyptian exploration: backgrounds, models, and future potential. Am. Assoc. Pet. Geol., Annual Convention, Dallas, April 17—20, 1983, Book of Abstracts, p.104.

Kinsman, D.J.J., 1964. Reef coral tolerance of high temperatures and salinities. Nature, 202: 1280–1282.

Loya, Y. and Slobodkin, L.B., 1971. The coral reefs of Eilat (Gulf of Eilat, Red Sea). Symp. Zool. Soc. London, 28: 117–139.

Morcos, S.A., 1970. Physical and chemical oceanography of the Red Sea. Oceanogr. Mar. Biol. Ann. Rev., Allen and Unwin, London, 8: 73–202.

Murray, S.P. and Babcock, A.L., 1982. Observations of two-layered circulation in the Gulf of Suez. Am. Geophys. Union, Annual Meeting, San Francisco, Calif., December 7–15, 1982 (abstract).

Neumann, J., 1952. Evaporation from the Red Sea. Israel Explor. J., 2: 153–162.

Patzert, W.C., 1974. Wind induced reversals in Red Sea circulation. Deep-Sea Res., 21: 109–121.

Roberts, H.H., 1974. Variability of reefs with regard to changes in wave power around an island. Proc., 2nd Int. Coral Reef Symp., v. 2, Great Barrier Reef Committee, pp.497–512.

Roberts, H.H. and Murray, S.P., 1983. Gulfs of northern Red: depositional settings of distinct siliciclastic–carbonate interfaces. Am. Assoc. Pet. Geol., Annual Convention, April 17–20, Dallas, Texas, Book of Abstracts, p.541.

Roberts, H.H. and Suhayda, J.N., 1983. Wave-current interactions on a shallow reef (Nicaragua, Central America). Coral Reefs, 1: 209–214.

Roberts, H.H., Wiseman Jr., W.J. and Suchanek, T.H., 1981. Lagoon sediment transport: the significant effect of *Callianassa* bioturbation. Proc. 4th Int. Coral Reef Symp., Manila, 1: 459–465.

U.S. Naval Oceanographic Office, 1965. Sailing directions for the Red Sea and Gulf of Aden. Publ. 61, 375 pp.

Vercelli, F., 1931. Nuove recherche sulli correnti marine del Mar Rosso. Ann. Idrogr. Genova, 12: 1–74.

REPORT DOCUMENTATION PAGE

1a REPORT SECURITY CLASSIFICATION Unclassified	1b. RESTRICTIVE MARKINGS
2a SECURITY CLASSIFICATION AUTHORITY	3. DISTRIBUTION/AVAILABILITY OF REPORT Approved for public release; distribution unlimited.
2b DECLASSIFICATION/DOWNGRADING SCHEDULE	
4 PERFORMING ORGANIZATION REPORT NUMBER(S) Technical Report No. 399	5. MONITORING ORGANIZATION REPORT NUMBER(S)
6a NAME OF PERFORMING ORGANIZATION Coastal Studies Institute 6b OFFICE SYMBOL (If applicable)	7a. NAME OF MONITORING ORGANIZATION
6c. ADDRESS (City, State, and ZIP Code) Louisiana State University Baton Rouge, LA 70803-7527	7b. ADDRESS (City, State, and ZIP Code)
8a NAME OF FUNDING/SPONSORING ORGANIZATION Coastal Sciences Program/ONR 8b. OFFICE SYMBOL (If applicable)	9. PROCUREMENT INSTRUMENT IDENTIFICATION NUMBER N00014-83-C-0150
8c ADDRESS (City, State, and ZIP Code) Code 422 CS 800 North Quincy Street Arlington, VA 22217	10. SOURCE OF FUNDING NUMBERS PROGRAM ELEMENT NO: PROJECT NO.: NR 388 002 TASK NO.: 1A & 2A WORK UNIT ACCESSION NO: 15

11 TITLE (Include Security Classification)

DEVELOPING CARBONATE PLATFORMS: SOUTHER GULF OF SUEZ, NORTHERN RED SEA (Unclassified)

12 PERSONAL AUTHOR(S)
Roberts, Harry H. and Murray, Stephen P.

13a TYPE OF REPORT	13b. TIME COVERED	14. DATE OF REPORT (Year, Month, Day)	15. PAGE COUNT
	FROM 1/1/83 TO 12/31/83	1984	21

16 SUPPLEMENTARY NOTATION
Reprint from Marine Geology, 59:186-185, 1984.

17 COSATI CODES			18. SUBJECT TERMS (Continue on reverse if necessary and identify by block number)
FIELD	GROUP	SUB-GROUP	AShrafi reef, carbonate platforms, Jubal Strait, Red Sea Gulf of Suez, reef accretion, sediment transport
08	08		
08	10		

19. ABSTRACT (Continue on reverse if necessary and identify by block number)

The Ashrafi reef complex represents two small (~8-10 x ~2 km) carbonate platforms and associated shoals located along the western side of the Jubal Strait at the Gulf of Suez's southern end. These features are developing in an active marine environment that is operating within the geologic constraints of a tectonic trough characterized by mountainous fault-controlled margins. Origin of the platforms is uncertain, but the present morphology appears to be a product of the dynamic marine setting in which they are developing. Tidal flow between the Red Sea and the Gulf results in strong rectilinear currents (commonly >50 cm s^{-1}). Of the current velocities, 5-10 cm s^{-1} can be attributed to surface currents driven by a regional, unidirectional wind that blows from north to south down the axis of the Gulf throughout the year.

Side-scan sonar data, coupled with echo-sounder profiles, direct observations via Scuba, and bottom sampling indicate that the Ashrafe platforms are actively building northward by windward reef accretion and extending to the south by sediment transport and accumulation.

20. DISTRIBUTION/AVAILABILITY OF ABSTRACT	21. ABSTRACT SECURITY CLASSIFICATION
☒ UNCLASSIFIED/UNLIMITED ☐ SAME AS RPT. ☐ DTIC USERS	Unclassified
22a. NAME OF RESPONSIBLE INDIVIDUAL Cheri Marquette	22b. TELEPHONE (Include Area Code) 504-388-2395 / 22c. OFFICE SYMBOL

The drumstick shape is a product of wave-induced reef development along the northern margin and sediment distribution forced by strong tidal currents, which, coupled with unidirectional wind drift, favors net transport to the south. Small reefs and hardgrounds along the downdrift platform flanks assume a linearity consistent with the long axis of the platform. The intensely mounded sediment of the platform flanks suggests that bioejection of particles in the mound-building process, together with a strong flow field, is a downdrift sediment transport agent.

Although the ambient salinity of surrounding Gulf water is ~41°/oo, platform-top water masses were measured at >47°/oo. A lack of significant coral growth on the shallow platform top and the almost total exclusion of sediment-producing calcareous green algae may be related to these hypersaline conditions. Sediments for the platform flanks are largely provided by the breakdown of platform margin reef communities and in-situ organisms (largely foraminifera).

Coastal Studies Institute
Louisiana State University
Baton Rouge, LA 70803-7527

Technical Report No. 400

FALL-SEASON PATTERNS OF TURBIDITY AND SEDIMENT TRANSPORT IN THE KOREA STRAIT AND SOUTHEASTERN YELLOW SEA

J. T. Wells and O. K. Huh

1984

Reprint from Ocean Hydrodynamics of the Japan and East China Seas, pp. 387-397, 1984.

Office of Naval Research
Contract N00014-83-C-0150
Project NR 388 002

Reprinted from *Ocean Hydrodynamics of the Japan and East China Seas*, pp. 387–397
1984 Elsevier Science Publishers B.V., Amsterdam — Printed in The Netherlands

FALL-SEASON PATTERNS OF TURBIDITY AND SEDIMENT TRANSPORT IN THE KOREA STRAIT AND SOUTHEASTERN YELLOW SEA

J. T. WELLS and O. K. HUH
Coastal Studies Institute, Louisiana State University, Baton Rouge, Louisiana 70803 (U.S.A.)

ABSTRACT

Suspended-sediment data collected in mid-November of 1980 and 1981 and current meter moorings deployed in September and early October of 1982 suggest an early-fall entrainment and subsequent transport of suspended sediment into the Korea Strait by the South Korean Coastal Current. During transition from summer to winter conditions, suspended-sediment concentrations in the southeastern Yellow Sea range from 5 to 100 mg/l at the surface and 15 to 250 mg/l at the bottom in waters that are 20-80 m deep. These concentrations, 1 to 3 orders of magnitude higher than "typical" shelf-depth waters in most other parts of the world, provide the opportunity for enormous sediment transport rates within this coastal mudstream, even under relatively weak currents. The abrupt termination of this inshore band of cold, turbid water as a turbidity front some 25-50 km offshore marks the seaward boundary of the high-transport zone. Landward of the turbidity front, surface waves associated with strong cold-air outbreaks every 7-10 days may destratify the coastal mudstream and entrain additional bottom sediment. Suspended sediments transported into the Korea Strait may accumulate in south-coast embayments, reside in the deep strait, or be carried into the Sea of Japan.

INTRODUCTION

The Korea Strait serves as a conduit for the transport of sediment-laden waters from the Yellow Sea and East China Sea to the Sea of Japan. Characterized by mesoscale eddies and meandering fronts, the waters of the strait, particularly those close to the Korean Peninsula, have been shown from oceanographic data to be consistently turbid and highly complex (Huh et al., 1981). The characteristics and distribution of suspended sediment in the Korea Strait and vicinity, the subject of this paper, may provide important clues to the hydrodynamic processes that operate in this part of northeast Asia.

Several features of the Yellow Sea-East China Sea-Korea Strait region promote the usefulness of suspended-sediment data in oceanographic problems. First, the dominance of fine-grained sediment from large rivers such as the Yangtze and Hwangho in China, and smaller rivers such as the Han, Kum, and Yeongsan in Korea, provide an enormous source of silt and clay for entrainment into the water column. Second, the mineralogy and geochemistry of sediments, complex yet distinct within drainage basins, may provide an opportunity to differentiate source areas. Finally, the high-energy conditions of late-fall and winter associated with cold-air outbreaks provide a detectable perturbation in particulate material that may aid in determining transport pathways. The purpose of this paper is to use suspended sediment and current meter data, collected during field seasons 1980-1982, to 1) characterize the suspended-sediment distribution during the fall-season onset of winter monsoon winds, 2) identify the nature and extent of turbidity fronts first noted in satellite imagery, and 3) support a hypothesis for transport of suspended sediment from the southeastern Yellow Sea into the Korea Strait.

DATA ACQUISITION

The collection of 557 water samples for suspended solids analysis was undertaken as part of KEYRSEX I and II (Korea, East China Sea, Yellow Sea Remote Sensing Experiment), conducted jointly with Korean university and government scientists. Three to five depths were sampled at each of 154 stations during mid-November 1980 and 1981. As a minimum, samples were taken from the surface, mid-depth, and bottom along transect lines given letter designations in Figure 1. Sample spacing was typically 10 km.

To determine concentration of particulate material, samples of 200-400 ml were filtered through preweighed 0.45-μm Millipore membrane filters following standard techniques (Wells and Coleman, 1977). In samples where sufficient particulate material was available (85 samples), size determinations were made using a model TA electronic Coulter Counter with a 100-μm aperture tube. Identification of clay minerals was made from X-ray diffraction analysis using a Norelco wide-angle diffractometer on random bulk-sample mounts. Because of space constraints, presentation of sediment data will be restricted to that collected in 1981 and from line H in 1980.

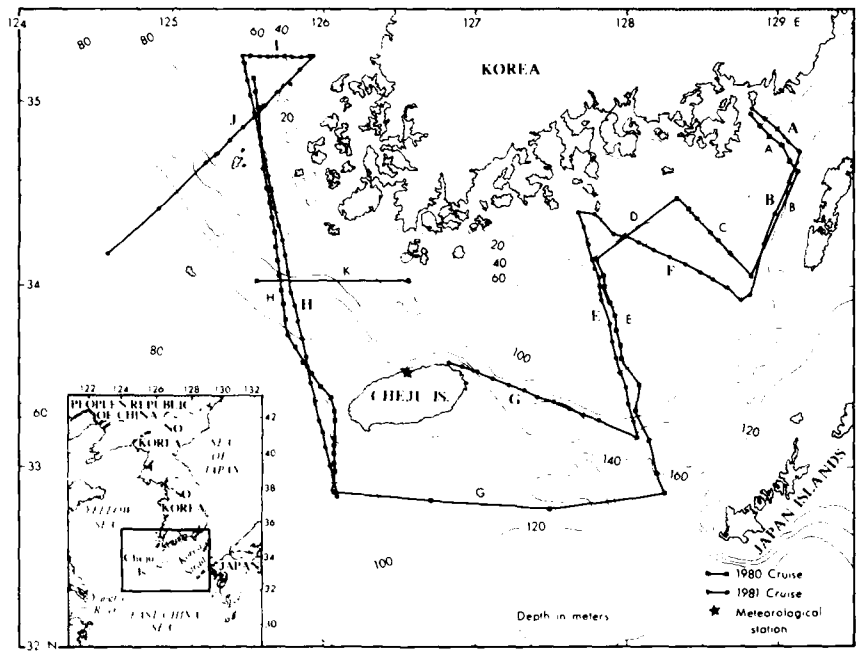

Fig. 1. Index map of southeastern Yellow Sea and Korea Strait showing transect lines and sampling stations.

Current speed and direction were determined from mid-depth moorings at two stations located approximately 60 km north of the study area (36°01'N, 126°02'E; 36°01'N, 126°14'E). Each mooring deployed during September and early October 1982 consisted of a neutrally buoyant Endeco 174 impellor-type current meter. Data were recorded on magnetic tape at 2-minute intervals, then averaged upon return to the laboratory to provide a reading once each hour. Selection of the mooring sites was made so that both stations would be located along an east-west line normal to the shoreline and to the southerly flow, which has been reported to occur at the onset of winter monsoons.

SUSPENDED SEDIMENT DISTRIBUTION

Suspended sediments are almost exclusively silt and clay sized, with sands comprising less than 1% of even the coarsest distributions. In fact, only 25% of the samples analyzed contained any sediment coarser than 40 μm and, on average, 90% of the sediment in each distribution was bracketed between 2 μm and 40 μm, the nominal sizing

range of the 100 μm aperture tube.

Figure 2 shows from four representative frequency curves that no systematic variation in size is apparent with distance above the bottom. Extremes in median size of individual samples are 4.2 μm and 17.5 μm, and average grain size along transect lines shows lines I and J to be the coarsest (11.1 μm and 11.7 μm, respectively), followed by lines H in 1981 (9.5 μm) and H in 1980 (7.1 μm). The intensity of storm waves and continuous tidal stirring suggest that the lack of sands in the water column reflects the fine-grained nature of the sediments on the bottom rather than an inability of currents to suspend coarse particles.

The patterns and levels of turbidity are remarkably similar in surface and bottom waters (Figs. 3, 4). The highest concentrations occur off the southwest tip of the Korean Peninsula in an area where bottom sediments are resuspended by storm waves of maximum possible fetch. Turbidity levels increase close to shore, exceeding 100 mg/l at both the surface and the bottom. A tongue of low-turbidity water appears to enter the strait from flow of the Tsushima Current north of Cheju Island. A tongue of high-turbidity water northeast of Cheju extends southeast more than halfway across the Korea Strait to latitude of nearly 33°N over an area of broad depth contours. The northeastern part of the strait is again characterized by concentrations on the order of 10-15 mg/l.

The distribution of clay minerals observed in water samples in this study is close to that reported from bottom samples by Chough and Kim (1981), Chen (1978), and Oinuma and and Kobayoshi (1966). Transect lines I and J and the northern part of line H show a predominance of illite (~70%) with lesser amounts of kaolinite (~10%) and chlorite (~13%). Montmorillonite is virtually absent. Several samples from the southern part of line H show a slight decrease in kaolinite and increase in illite, most likely a result of influence of the Tsushima Current. According to Chough and Kim (1981), the illite-rich waters in and just north of the study area are diluted by kaolinte and chlorite from local rivers; however, once within the main flow of the strait, mineralogy of sediments from the East China Sea shows greater influence. Although insufficient sediment was available for mineralogical analysis of water samples eastward through the Korea Strait, Han (1979) reports that illite from the East China Sea continues to predominate.

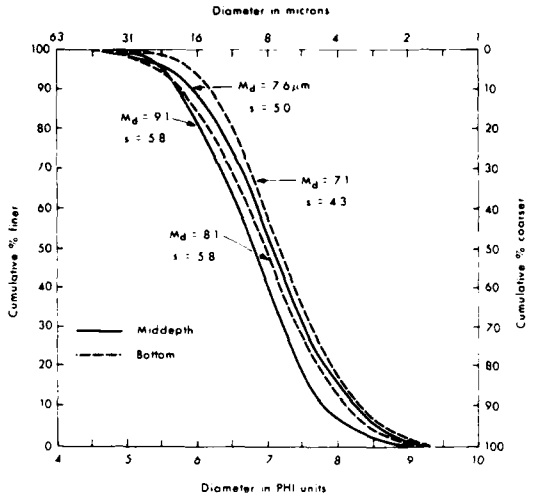

Fig. 2. Typical size distribution curves indicating median particle diameters and sorting values.

TURBIDITY FRONTS

The turbid waters along most of the south and west coasts of Korea end abruptly as turbidity fronts 25 to 50 km offshore in waters 20 to 80 m deep. As first observed in satellite imagery, turbidity fronts are well defined by the saturated, sediment-laden (white) returns in bands 4 and 5 of LANDSAT (Fig. 5). Whereas the turbidity front at the western end of the strait appears to follow bottom topography, ending offshore at the 40-m depth contour (Fig. 5), it loses lateral continuity midway through the strait at the eastern margin of the southeast-trending band of turbid water shown prominently in Figures 3 and 4 (longitude 128°E).

Although a turbidity front is present along the entire west coast of Korea, its width is variable, both spatially and temporally, and reflects gradient of the bottom, consistency of the bottom sediment, and, most importantly, intensity of wave and tide processes. Examination of 25 clear-sky LANDSAT scenes between September 1972 and October 1980 indicates that the front is best developed between September and November and weakest between January and March. Unfortunately, cloud cover after April prevents detection of a summer turbidity front. Intense mixing associated with cold-air outbreaks during winter may explain lack of definition in the fronts between January and March. Moreover, features such as eddies, wind rows, and

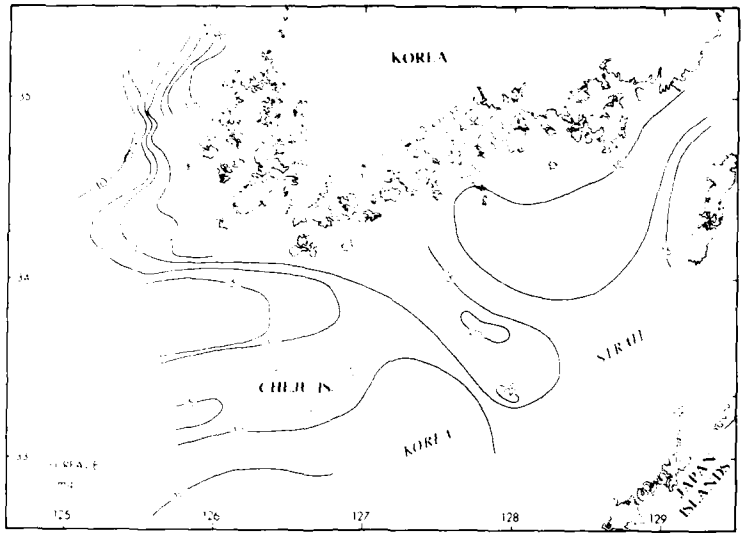

Fig. 3. Surface suspended-sediment concentrations in mid-November 1981.

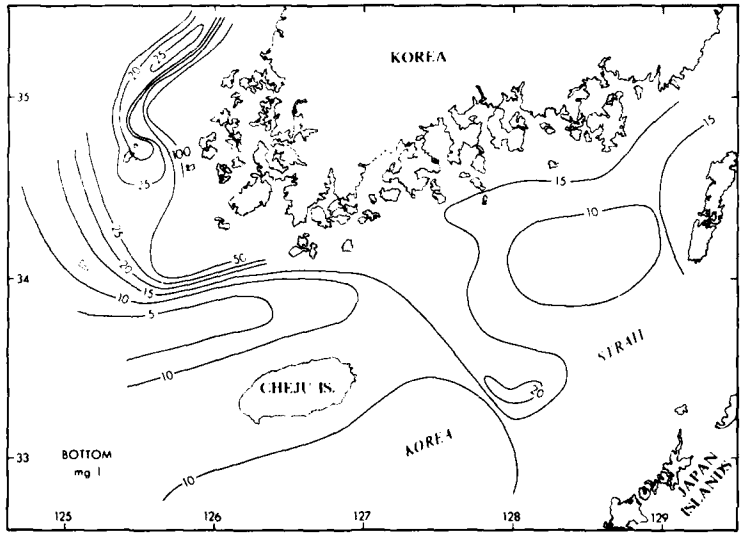

Fig. 4. Bottom suspended-sediment concentrations in mid-November 1981.

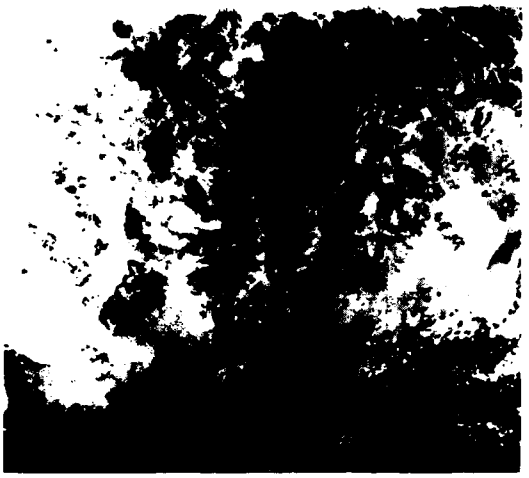

Fig. 5. LANDSAT band 4 image of the southwest part of the Korean Peninsula. Note zone of high turbidity (white) and its termination as a turbidity front at the 40-m depth contour.

breaking waves over subtidal sand ridges are typical winter-season occurrences that are able to obscure the turbidity fronts.

Figure 6 shows the structure of the south coast front in 1980 and at the same time (mid-November) in 1981, but under somewhat different conditions. Wind stress at Cheju Island was 12% higher during sampling and 17% higher during the month and a half preceding sampling in 1981 than in 1980. Suspended sediment contours in 1981 reflect this difference by showing a more nearly vertical structure as a result of resuspension of bottom sediment and destratification of the water column. Layers of turbid water near the bottom, such as that shown by the 250 mg/l contour in 1980, have been dispersed into the water column in 1981 (Fig. 6). The turbidity front itself is marked by a sharp decrease in suspended-sediment concentration from greater than 20 mg/l to less than 10 mg/l. Although satellite sensors cannot reliably be used to quantify suspended-sediment concentrations or to look below the surface waters, sediment sampling confirms that LANDSAT imagery consistently delineates as turbidity fronts suspended-sediment gradients of 10-20 mg/l and that thickness of the fronts is typically equal to the water depth.

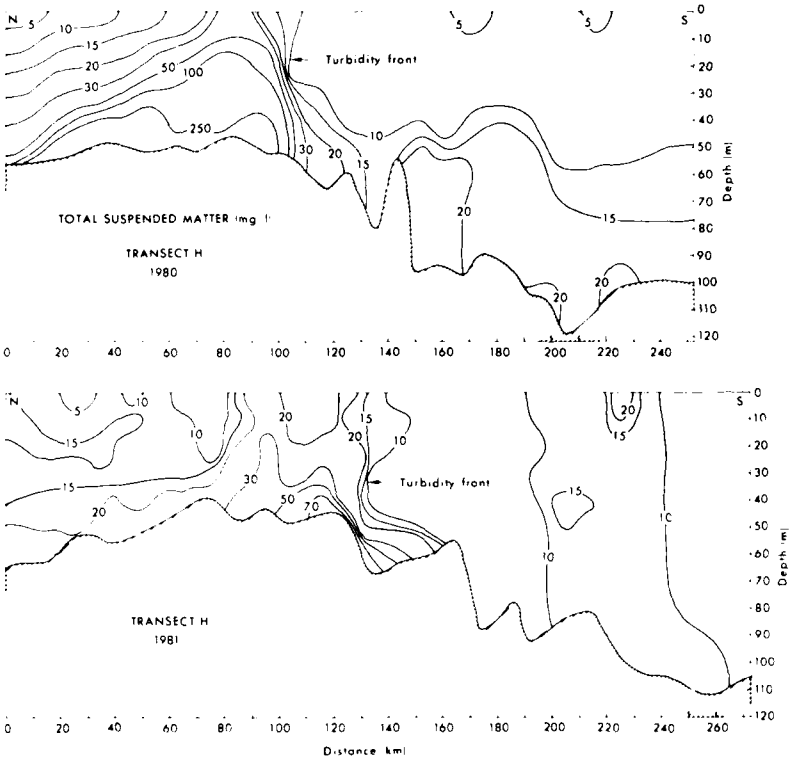

Fig. 6. Suspended-sediment concentrations and location of turbidity fronts along line H in 1980 and 1981.

MEAN FLOW AND SEDIMENT TRANSPORT

The west coast turbidity front marks the seaward boundary of a high-transport coastal mudstream within the South Korean Coastal Current. The fact that suspended-sediment concentrations are one to three orders of magnitude higher than in "typical" shelf waters indicates that sediment transport rates within this coastal mudstream may be enormous, even under relatively weak net currents. Several lines of evidence suggest that net flow is to the south during winter monsoons, and perhaps the year around. Uda (1966) reported residal currents of 15 cm/sec in the coastal current of the southeastern Yellow Sea. Lee (1968) indicated from drift bottle studies flows of 10 cm/sec in winter, and the U.S. Navy, in Summaries of Ship Drift Reports (1964), indicated weak flow to the south during all seasons. Further, observations of sea-surface temperature patterns from NOAA series satellites (Huh, 1982) follow closely those from

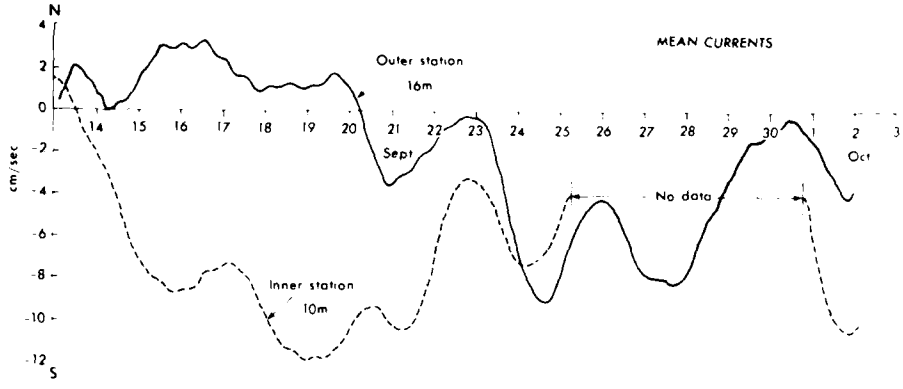

Fig. 7. Low-pass filter data (mean flow) from moorings off the Kum River entrance at latitude 36°N.

visible bands of LANDSAT.

Figure 7 shows average currents in September and early October from moorings deployed as part of this study. Average currents represent low-pass filter values run through a 75-hour Lanczos filter with a 50-hour half-power point. The inner station (25 km offshore) and the last half of the data record from the outer station (50 km offshore) show mean flow to be directed to the south at speeds of 7.8 and 3.8 cm/sec, respectively. Winds were light and variable for the duration of the moorings. It is reasonable to assume that this weak transitional-season current would become substantially stronger under the influence of strong northwest winds characteristic of the winter monsoon season that begins in late October (Wells et al., in press).

Flow of the South Korean Coastal Current provides a mechanism for transporting suspended sediment south into the Korea Strait. This is particularly significant in that flow may strengthen in the fall, precisely at a time when turbidities are increasing from the onset of monsoon winds. The fate of this suspended coastal sediment, transported south into the Korea Strait at rates estimated to be 25-250 x 10^6 m^3/yr, is not fully known. Fragmentary evidence from satellite and sea-floor sediment distribution data indicates that some of it may accumulate in shallow embayments along the south coast of the Korean Peninsula, whereas the remainder may be transported along the Chuo-Goto straths to the Goto submarine canyon or be transported into the western Sea of Japan.

CONCLUSIONS

1) Fall-season sampling shows that high levels of turbidity are maintained in the Korea Strait and southeastern Yellow Sea. Strong tidal currents throughout the year, together with storm waves in late fall and winter, keep turbidities consistently above 10 mg/l in waters up to 80 m deep. Destratification of the water column with the onset of winter monsoon winds results in nearly uniform suspended-sediment concentrations from the surface to the bottom.

2) Turbidity fronts, characterized by the abrupt decrease offshore in suspended-sediment concentrations from greater than 20 mg/l to less than 10 mg/l, occur along the Korean west coast and western half of the Korea Strait. Whereas bathymetry correlates reasonably well with turbidity fronts in the Korea Strait, definition of fronts in the southeastern Yellow Sea may be controlled mainly by sediment resuspension from storm waves.

3) The onset of winter monsoon winds (from the north) in late fall initiates a residual flow to the south that potentially carries large volumes of resuspended bottom sediments into the strait. A tongue of turbid water, most pronounced near the bottom, suggests that sediments enter the strait, then begin to move southeast across the strait at longitude 128°. Although the fate of fine-grained sediment that enters the strait is unknown, it is reasonable to assume that some of it accumulates in the south coast embayments and the remainder is transported to the Sea of Japan or accumulates in the deep strait.

REFERENCES

Chen, P.Y., 1978. Minerals in bottom sediments of the South China Sea. Bull. Geol. Soc. America, 89: 211-222.

Chough, S.K. and Kim, D.C., 1981. Dispersal of fine-grained sediments in the southeastern Yellow Sea: a steady-state model. Jour. Sed. Petrol., 51: 721-728.

Han, S.J., 1979. Clay minerals in recent sediments of the Korea Strait. Bull. KORDI, 1: 23-37.

Huh, O.K., 1982. Spring season flow of the Tsushima Current and its separation from the Kuroshio: satellite evidence. Jour. Geophys. Res., 87: 9687-9693.

Huh, O.K., Rouse, L.J., Jr., Hsu, S.A., Wells, J.T., and Shim, Taebo, 1981. Korea Strait-East China Sea-Yellow Sea remote-sensing experiment. Data Rept. to Office of Naval Research.

Lee, C.K., 1968. *The drift bottle experiment in the east of the* Yellow Sea (the west coast of Korea) during the year of the 1962-1966. Bull. Fisheries Res. and Devel. Agency, pp. 29-41.

Oinuma, K. and Kobayashi, K., 1966. Quantitative study of clay minerals in some Recent marine sediments and sedimentary rocks from Japan. In: A. Swineford and N.V. Plummer (Editors), Clays and Clay Minerals, Proc. 14th National Conf., Pergamon Press,

New York, pp. 209-219.
Uda, M., 1966. Yellow Sea. In: R.W. Fairbridge (Editor), Encyclopedia of Oceanography, Van Nostrand and Reinhold, New York, 1021 pp.
U.S. Naval Oceanographic Office, 1964. Ocean currents in the vicinity of the Japanese Islands and China coast. Publ. No. 237, 14 pp.
Wells, J.T., and Coleman, J.M., 1977. Nearshore suspended sediment variations, central Surinam coast. Mar. Geol., 24: M47-M54.
Wells, J.T., Huh, O.K., and Park, Y.A., in press, Dispersal of silts and clays by winter monsoon surges in the southeastern Yellow Sea. Proc., Sympos. Sediment. Cont. Shelf, Hangzhou, China.

UNCLASSIFIED

SECURITY CLASSIFICATION OF THIS PAGE

REPORT DOCUMENTATION PAGE

1a. REPORT SECURITY CLASSIFICATION Unclassified	1b. RESTRICTIVE MARKINGS
2a SECURITY CLASSIFICATION AUTHORITY	3. DISTRIBUTION / AVAILABILITY OF REPORT Approved for public release; distribution unlimited.
2b. DECLASSIFICATION / DOWNGRADING SCHEDULE	
4 PERFORMING ORGANIZATION REPORT NUMBER(S) Technical Report No. 400	5. MONITORING ORGANIZATION REPORT NUMBER(S)
6a. NAME OF PERFORMING ORGANIZATION Coastal Studies Institute 6b OFFICE SYMBOL (If applicable)	7a. NAME OF MONITORING ORGANIZATION
6c. ADDRESS (City, State, and ZIP Code) Louisiana State University Baton Rouge, LA 70803-7527	7b. ADDRESS (City, State, and ZIP Code)
8a. NAME OF FUNDING / SPONSORING ORGANIZATION Coastal Sciences Program/ONR 8b. OFFICE SYMBOL (If applicable)	9. PROCUREMENT INSTRUMENT IDENTIFICATION NUMBER N00014-83-C-0150
8c ADDRESS (City, State, and ZIP Code) Code 422CS 800 North Quincy Street Arlington, VA 22217	10. SOURCE OF FUNDING NUMBERS PROGRAM ELEMENT NO. / PROJECT NO. 388 002 / TASK NO. 7.A / WORK UNIT ACCESSION NO. 16

11 TITLE (Include Security Classification)

FALL-SEASON PATTERNS OF TURBIDITY AND SEDIMENT TRANSPORT IN THE KOREA STRAIT AND SOUTHEASTERN YELLOW SEA (Unclassified)

12. PERSONAL AUTHOR(S)
Wells, J. T. and Huh, O. K.

13a TYPE OF REPORT	13b. TIME COVERED	14. DATE OF REPORT (Year, Month, Day)	15. PAGE COUNT
	FROM 1/1/83 TO 12/31/83	1984	11

16 SUPPLEMENTARY NOTATION
Reprint from Ocean Hydrodynamics of the Japan and East China Seas, pp. 387-397, 1984.

17 COSATI CODES			18. SUBJECT TERMS (Continue on reverse if necessary and identify by block number)
FIELD	GROUP	SUB-GROUP	turbidity, sediment transport, Korea Strait, Yellow Sea, Sea of Japan
08	08		

19 ABSTRACT (Continue on reverse if necessary and identify by block number)

Suspended-sediment data collected in mid-November of 1980 and 1981 and current meter moorings deployed in September and early October of 1982 suggest an early-fall entrainment and subsequent transport of suspended sediment into the Korea Strait by the South Korean Coastal Current. During transition from summer to winter conditions, suspended-sediment concentrations in the southeastern Yellow Sea range from 5 to 100 mg/l at the surface and 15 to 250 mg/l at the bottom in waters that are 20-80 m deep. These concentrations, 1 to 3 orders of magnitude higher than "typical" shelf-depth waters in most other parts of the world, provide the opportunity for enormous sediment transport rates within this coastal mudstream, even under relatively weak currents. The abrupt termination of this inshore band of cold, turbid water as a turbidity front some 25-50 km offshore marks the seaward boundary of the high-transport zone. Landward of the turbidity front, surface waves associated with strong cold-air outbreaks every 7-10 days may destratify the coastal mudstream and entrain additional bottom sediment. Suspended sediments transported into the Korea Strait may accumulate in south-coast embayments, reside in the deep strait, or be carried into the Sea of Japan.

20 DISTRIBUTION / AVAILABILITY OF ABSTRACT	21. ABSTRACT SECURITY CLASSIFICATION
☒ UNCLASSIFIED/UNLIMITED ☐ SAME AS RPT. ☐ DTIC USERS	

22a NAME OF RESPONSIBLE INDIVIDUAL	22b. TELEPHONE (Include Area Code)	22c. OFFICE SYMBOL
Cheri Marquette	504-388-2395	

DD FORM 1473, 84 MAR 83 APR edition may be used until exhausted. All other editions are obsolete.

SECURITY CLASSIFICATION OF THIS PAGE
UNCLASSIFIED

Coastal Studies Institute
Louisiana State University
Baton Rouge, LA 70803-7527

Technical Report No. 401

A TEST OF THE GEOSTROPHIC APPROXIMATION IN THE WESTERN CHANNEL OF THE KOREA STRAIT

T. Shim, W. J. Wiseman, Jr., O. K. Huh, and W.-S. Chunag

1984

Reprint from Ocean Hydrodynamics of the Japan and East China Seas, pp. 263-272, 1984.

Office of Naval Research
Contract N00014-83-C-0150
Project NR 388 002

Reprinted from *Ocean Hydrodynamics of the Japan and East China Seas*, pp. 263–272
1984 Elsevier Science Publishers B.V., Amsterdam – Printed in The Netherlands

A TEST OF THE GEOSTROPHIC APPROXIMATION IN THE WESTERN CHANNEL OF THE KOREA STRAIT

T. SHIM, W. J. WISEMAN, JR., O. K. HUH, AND W.-S. CHUANG
Coastal Studies Institute, Louisiana State University, Baton Rouge, Louisiana 70803-7527 (USA)

ABSTRACT

Current meter measurements and lines of STD stations are analyzed to test the geostrophic method in the western channel of the Korea Strait. An array of three current meters was deployed in the deep central part of the channel. Meters were located near the surface, at mid-depth, and near the bottom in 203 m of water. They recorded approximately 550 hours of data between October 16 and November 2, 1972. Several cross-stream transects of physical properties with closely spaced (3-6 km) STD stations were acquired. The measured velocity differences between 25- and 80-m depths and between 80- and 195-m depths are approximately 0.24 m sec^{-1} and 0.42 m sec^{-1}, respectively. The corresponding geostrophic velocity differences vary from -0.05 to 0.10 m sec^{-1} and 0.35 to 0.61 m sec^{-1}, respectively. It would appear that geostrophic estimates of the total transport through the western channel may be in error and should be treated with caution.

INTRODUCTION

The Korea Strait is the major source of advected heat and salt for the Sea of Japan (Moriyasu, 1972; Yoon, 1982). Because of its importance, the transport through this strait has been monitored using indirect methods for many years. Bimonthly (and some monthly) hydrographic data have been collected, and geostrophic equilibrium in the cross-channel direction has been assumed. Thus, a seasonal cycle of transport through the strait has been defined (Hidaka and Suzuki, 1950; Yi, 1966, 1970). The classical geostrophic computation assumes a deep level of no motion (Sverdrup et al., 1942). The Korea Strait, though, is shallow, and the geostrophic calculations must be referenced to a certain depth (e.g., 125 m is used by Yi, 1966) or to the bottom. Furthermore, the important dynamical balances within the strait are not known. Toba et al. (1982) point out

the importance of the along-channel barotropic pressure gradient. Tidal currents are large (Ogura, 1933; Lee, 1970; Burns, 1975), and associated nonlinear terms in the mean momentum equation can be anticipated to be important. Frictional effects may also be significant. Furthermore, mesoscale eddies and frontal waves propagate through the strait, producing strong perturbations. In light of this, it seems reasonable to ask, "How good is the geostrophic approximation within the strait?"

The oceanographic data used for this study were acquired for a remote sensing experiment conducted in the Korea Strait from October 10 to November 10, 1972 (Huh, 1973a, b, 1976; MacDowell and Huh, 1973; Kern, 1974). Currents were measured with self-recording Geodyne A-101-1 current meters. They were taut moored in arrays of three positioned in the deep central parts of both western and eastern channels (Figs. 1, 2). Data were sampled every 10 minutes for 50 seconds; approximately 550 hours of data were recorded.

Measurements of physical properties were purposely made at much higher vertical resolution and horizontal spacing than the standard multi-year fisheries surveys. Measurements were made with a Bisset-Berman 9040 salinity-temperature-depth (STD) recording system with daily salinity checks against measurements of Nansen bottle samples laboratory analyzed to 0.001 $^{o}/_{oo}$. Vertical sampling rate was 0.5 m, with alongtrack station spacing of 3 to 6 km (Fig. 1). Because the STD lines covered only the western channel, in the following discussion we will focus attention on the flow in this channel.

WATER MASS STRUCTURE

Three closely spaced hydrographic sections were obtained across the western channel of the strait during the early part of the experiment (Fig. 1). While much structure was observed within the channel, the large-scale features consisted of the expected layering (Fig. 3). The deepest water was Korea Strait bottom water (Gong, 1971; Lim and Chang, 1969). This water mass appeared as a pycnostad (thermostad) at individual stations and was separated from overlying waters by a well-defined thermocline. Toward the Korean coast, to the northwest this water was somewhat warmer and fresher and the shallower overlying thermocline was weaker.

The mid-depth layer was also a pycnostad. In this case, though, we often found a haline-compensated thermal inversion. A salinity maximum occurred within this layer, which decreased in intensity as one approached the Korean coast. The data from this layer suggest

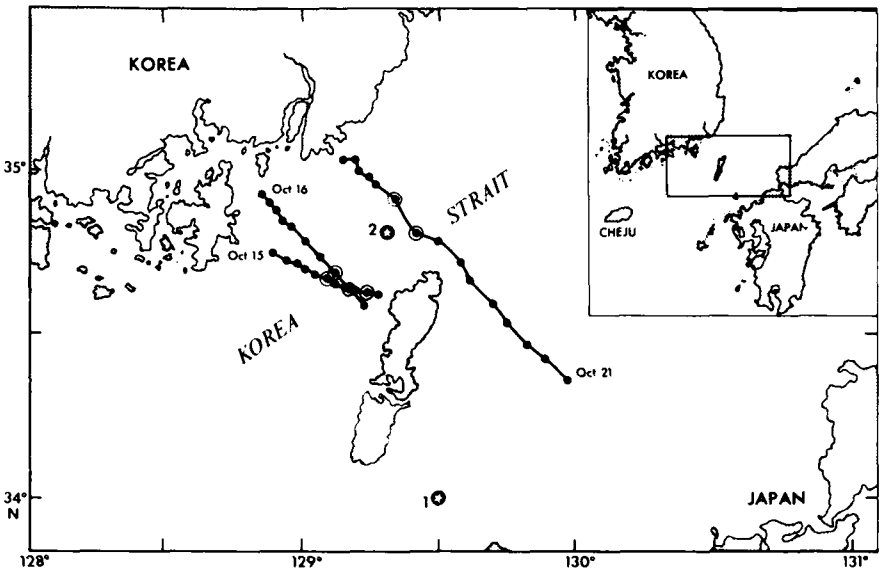

Fig. 1. Locations of current meter arrays (stars), lines of oceanographic stations, and the individual stations used for geostrophic calculations (circled dots).

the presence of isolated lenses of water within the strait.

The upper layer consisted of a broad pycnocline, both a thermocline and halocline, capped by a thin mixed layer less than 20 m thick. Again following Gong's analysis, this appears to be a mixture of Yellow Sea coastal water and Tsushima Warm Current water.

CURRENT MEASUREMENTS

The raw current data are dominated by the tidal currents, which reach amplitudes of 0.75 m sec^{-1} (Fig. 4a). The tidal currents from these moorings have been analyzed and described in detail by Burns (1975). In order to investigate the subtidal flows, the raw time series were rotated onto an along-channel/cross-channel coordinate system and filtered with a Lanczos filter having a 40-hour half-power point (Fig. 4b). The means of the along-channel subtidal current records are 0.64, 0.40, and -0.02 m sec^{-1} at 25-, 80-, and 195-m depth, respectively (a positive value indicates flow into the Sea of Japan). Thus the measured vertical shears of the along-channel flow are 0.24 m sec^{-1} between 25- and 80-m depths and 0.42 m sec^{-1} between 80- and 195-m depths. For comparison, mean vertical shear of along-channel flow in the east channel is 0.05 m sec^{-1} between

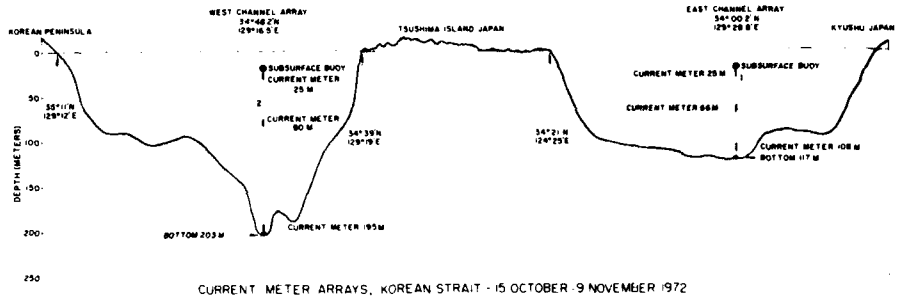

Fig. 2. Bathymetric profile across the entire strait showing locations of current meter arrays and their vertical spacing.

25 and 66 m and 0.15 m sec^{-1} between 66- and 108-m depths.

We wish to compare the west channel numbers with estimates of the geostrophic shears. Two difficulties occur. The current meters were placed near the deepest part of the channel, whereas the STD sections were taken across shoaler regions. Furthermore, the STD was kept well away from the bottom to protect the sensor head. Although this presents little problem for the calculation of geostrophic shear, we are forced to assume a level of no motion at 150 m when we estimate current velocity or geostrophic transport. Secondly, in order to avoid abnormally reducing the magnitude of the estimated currents by averaging over a wide region of the channel, where lateral shear may be important, we try to use STD stations that are closely spaced. On the other hand, the presence of mesoscale variability introduces bias in the geostrophic computations. Many years of fall-season satellite images of the sea-surface temperature field show evidence for propagation of mesoscale eddies and frontal meanders through the strait (Huh, 1976). We have subjectively selected the closest stations on either side of the mooring that best represent the mean slope of the isopycnals (for stations used, see Fig. 1). These are then projected on a cross-channel line oriented along 124°T, the direction normal to the isobaths at the location of the current meter mooring. The resultant density sections are then used to estimate the geostrophic shears between 80 m and 195 m and between 25 m and 80 m. The current profile computed from these estimates should closely approximate the absolute measurements, since the flow at 150-m depth is generally slow (Figs. 3, 4), lying within a well-mixed layer from which direct current measurements show minimal flow. Our best estimates

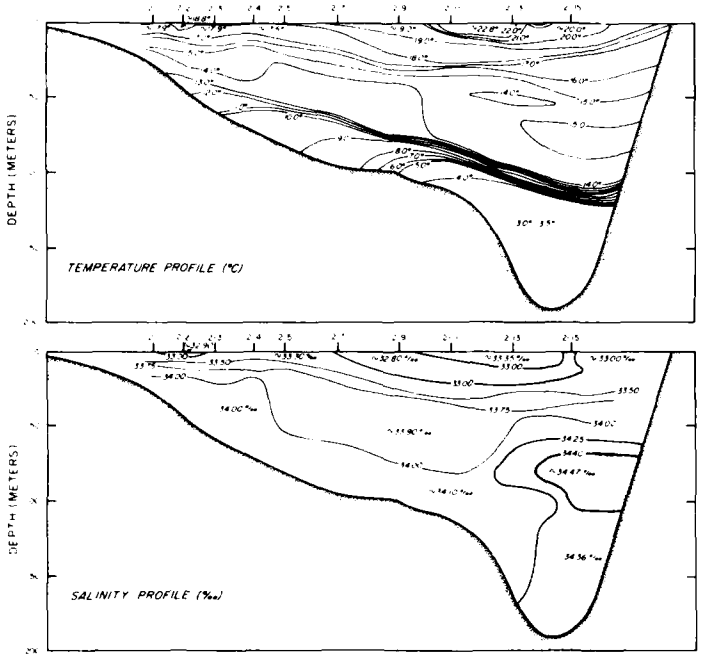

Fig. 3. The October 16, 1972, temperature and salinity profiles across the west channel of the strait. Note isolated lens at 50 m in temperature section near station 2-13.

of the geostrophic velocity profiles in the vicinity of the current meter array are presented in Figure 5, with the mean of the filtered data for the first 6 days, when the flow was very steady. Assuming the deep water to be nearly homogeneous, we have also plotted the bottom current measurement at 150 m rather than 195 m for comparison with the geostrophic estimates. Clearly, significant temporal variability occurs between the geostrophic estimates during a period when the current meters were reporting reasonably steady flow.

There are numerous ways in which the geostrophic shears could be compared. We could have matched all the profiles at the 80-m data point from the current meter and used the resultant profiles to estimate the level of no motion. This procedure, though, inherently assumes the validity of the geostrophic approximation for flow in the strait, an assumption that we are not prepared to accept as valid. We prefer to present the geostrophic velocities referenced

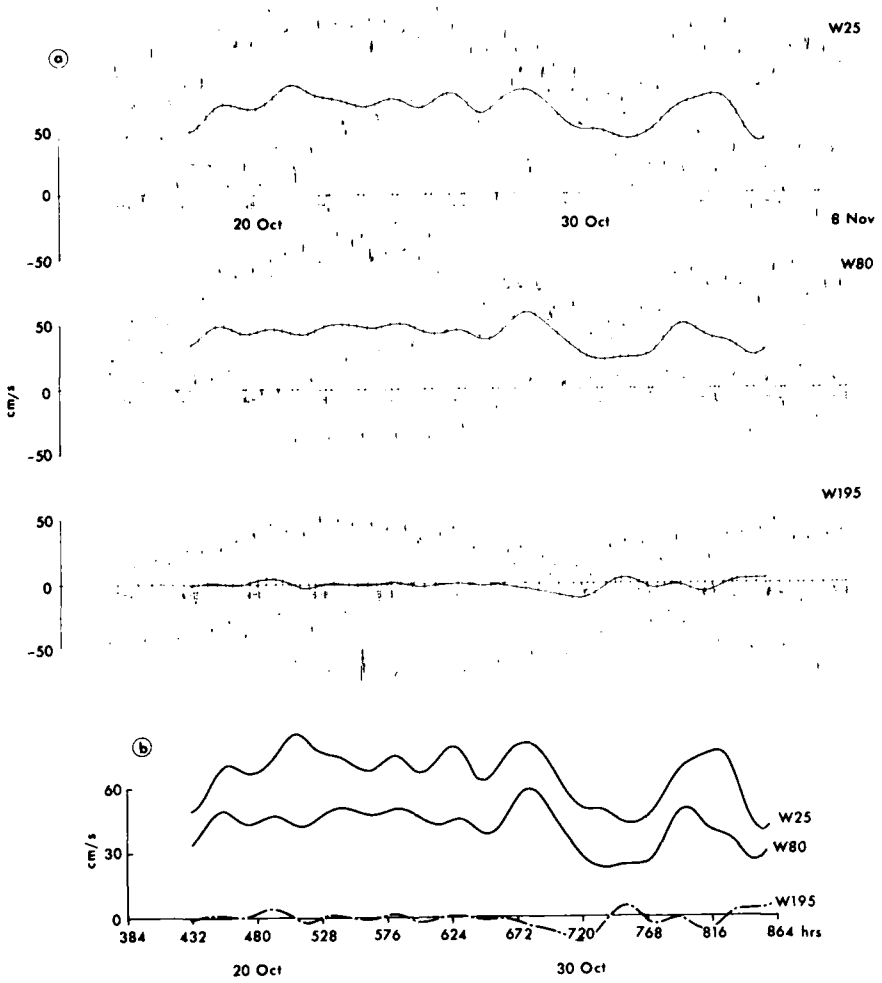

Fig. 4. (a) The along-channel component of current meter data, dominated by tidal currents. Vertical axis is velocity in centimeters per second, and horizontal axis is time in hours, with time 0 at 0000Z on 1 October 1972. The filtered mean is plotted for reference. Data from 25-, 80-, and 195-m depths in west channel. (b) Comparison of along-channel subtidal flows showing vertical shear of west channel data.

to 150 m and allow the reader to estimate the "goodness of fit" of the patterns. This approach has the added benefit of making the figure less "busy" near the 80-m depth.

It might be argued that the upper current meter is influenced by the wind. No evidence of local wind effects was seen when the cur-

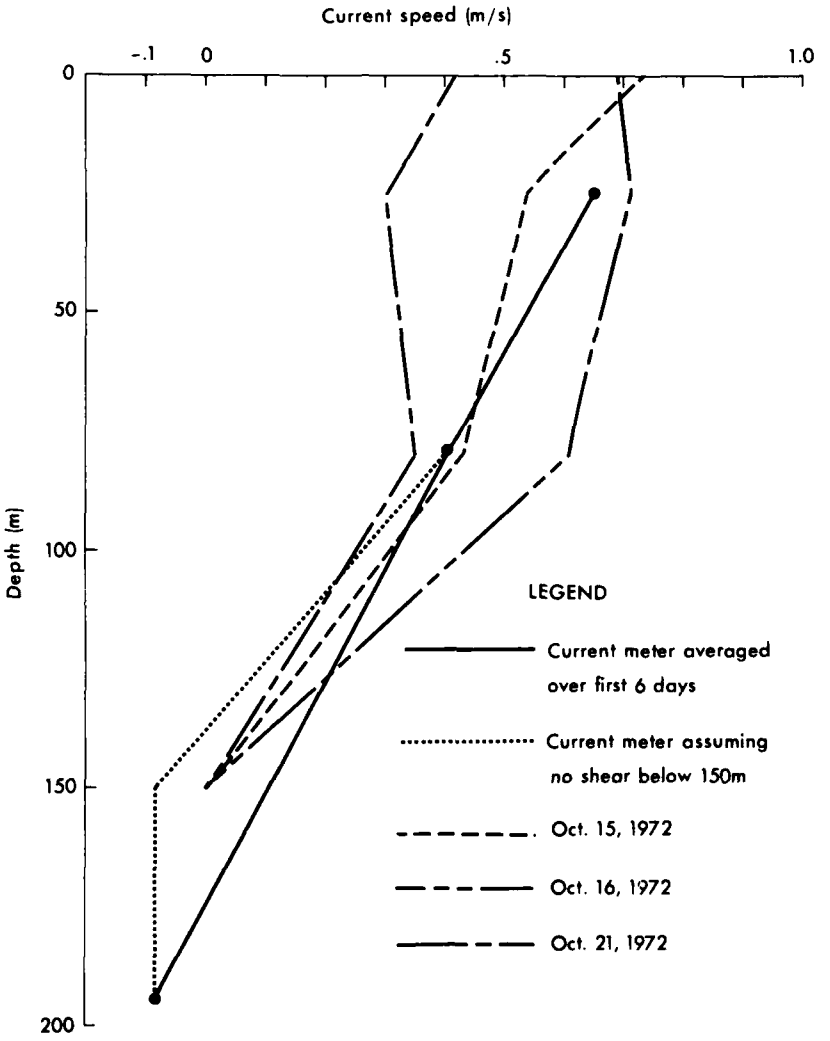

Fig. 5. Comparison of geostrophic and current meter measurements of vertical shear in west channel of the Korea Strait.

rents were compared with the along-channel and cross-channel winds as observed at Tsushima. Furthermore, the upper current meter was always within the upper pycnocline and not in the surface mixed layer, where wind effects may be expected to be most severe.

TRANSPORT ESTIMATES

The total geostrophic transport, assuming no deep flow, was estimated by integrating along the bottom. The geostrophic transports for the three STD sections taken on October 15, 16, and 21 were 0.89 x 10^6, 1.37 x10^6, and 1.6 x 10^6 m^3 sec^{-1}, respectively. Significant variations occur among the geostrophic estimates. How reliable are these geostrophic estimates, which vary by a factor of nearly 2 over a period of less than 1 week?

Warren and Volkmann (1968) suggest that careful geostrophic estimates of Gulf Stream transport may be in error by 20-30%. Because of different geometric constraints in the Korea Strait, the relative importance of their error sources is different from that in our case. Some of our variability must be attributed to eddies within the channel. These, however, appear confined to the central regions of the strait in our data and do not affect transport estimates significantly. They will, though, alter the velocity estimates. Internal tides may alter the density structure sufficiently to affect our calculations.

There is subtidal variation in the current meter records that may actually be reflected in the geostrophic estimates. Early in the record we see minor variations with a period of about 2 days, whereas later in the record a major event of approximately 4 days' duration occurs (Figs. 4a, b). These variations appear to be largely barotropic above the Korea Strait bottom water, while the variations in geostrophic shear do not appear uniform with respect to the deep water. In open-channel flow, transport is often approximated as a constant, α, times the cross-sectional area times the vertically averaged velocity at some mid-channel station. Clearly, for constant α, such an estimate would show less variability than the geostrophic estimates. It should be mentioned that Yoon (1982) has already questioned the validity of existing estimates of geostrophic transport through the strait both because of the lack of a good reference depth and because the presence of a potentially strong barotropic component is not resolved.

DISCUSSION

The data set available is insufficient to characterize definitively the utility of geostrophic transport estimates within the Korea Strait. A number of important points, though, are clear.

1. The depth of 125 m is a poor choice for a reference level for geostrophic computations within the strait.

2. Significant short-term variability occurs between careful geostrophic transport estimates.

3. Short-term flow variability is also seen in direct current measurements from the strait.

4. In the central part of the strait, where frictional forces may be expected to be least important and the geostrophic approximation most applicable, the correspondence between measured shear and estimated shear was poor, especially in the upper layers (0.24 m sec^{-1} versus -0.05 to 0.10 m sec^{-1}) (Fig. 5). It is not clear that the estimates will be even this good in shoal regions, where dissipation is important.

Forrester (1967) reports on a comparison of geostrophic velocity estimates with direct current measurements within the St. Lawrence estuary. He concludes that the geostrophic approximation is useful only when an average is taken over a large number of geostrophic estimates. The situation in the Korea Strait appears comparable. The density structure can change significantly on time scales of a few hours. The usefulness of a single hydrographic line for estimating the mean transport representative of a 1- or 2-month period must be considered suspect.

REFERENCES

Burns, D.A., 1975. Tidal frequency oscillations on the Tsushima current. U.S. Naval Oceanographic Office Tech. Note No. 1, 6110-4-75, 30 pp.

Forrester, W.D., 1967. Currents and geostrophic currents in the St. Lawrence Estuary. Rept. BIO 67-5, Bedford Inst. of Oceanogr., Dartmouth, N.S., Canada, 175 pp.

Gong, Y., 1971. A study on the South Korean Coastal Current. J. Oceanogr. Soc. Korea, 6: 25-36.

Hidaka, K., and Suzuki, T., 1950. Secular variations of the Tsushima Current. J. Oceanogr. Soc. Japan, 16: 28-31.

Huh, O.K., 1973a. Coastal oceanographic use of the Defense Meteorological Satellite Program (DMSP). Tech. Rept. 241, U.S. Naval Oceanogr. Office, ONR Contract NR 387-062, 52 pp.

Huh, O.K., 1973b. Mesoscale ocean circulation details from satellite infrared imagery, Sea of Japan and Yellow Sea (abst.). Trans. Amer. Geophys. Union, 54(11): 1112.

Huh, O.K., 1976. Detection of ocean thermal fronts off Korea with the Defense Meteorological Satellites. Remote Sensing of Environment, 5: 191-213.

Kern, J.J., 1974. Naval Oceanographic Office, real-time oceanography experiment in geodesy, mapping, and oceanography. The Military Engr., 66: 51-52.

Lee, Chang-ki, 1970. On the currents in the western channel of the Korea Strait. Bull. Fish. Res. Dev. Agency, 6: 175-201.

Lim, D.B., and Chang, S.D., 1969. On the cold water mass in the Korea Strait. J. Oceanol. Soc. Korea, 4: 71-82.

MacDowell, G.P., and Huh, O.K., 1973. Cold core cyclonic eddy detected off South Korea with space-borne infrared sensors. Trans. Amer. Geophys. Union, 54: 115.

Moriyasu, S., 1972. The Tsushima Current. In: H. Stommel and K. Yoshida (Editors), Kuroshio, Univ. Washington Press, Seattle and London, 517 pp.

Ogura, S., 1933. The tides in the sea adjacent to Japan. Bull. Hydrogr. Dept. Imperial Japanese Navy, vol. 7, 189 pp.

Sverdrup, H. U., Johnson, M.W., and Fleming, R.H., 1942. The oceans, their physics, chemistry and general biology. Prentice-Hall, New York, 1087 pp.

Toba, Y., Tomizawa, K., Kurasawa, Y, and Hanawa, K., 1982. Seasonal and year-to-year variability of the Tsushima-Tsugaru Warm Current System with its possible cause. La Mer, 20: 41-51.

Warren, B.A., and Volkmann, G.H., 1968. Measurement of volume transport of the Gulf Stream south of New England. J. Mar. Res., 26: 110-126.

Yi, S. U., 1966. Seasonal and secular variation of the water volume transport across the Korea Strait. J. Oceanol. Soc. Korea, 1: 7-13.

Yi, S. U., 1970. Variation of oceanic condition and mean sea level in the Korea Strait. In: J. Marr (Editor), The Kuroshio, East-West Center Press, Univ. Hawaii, pp. 125-142.

Yoon, J.H., 1982. Numerical experiment on the circulation in the Japan Sea, Part II, Influence of seasonal variations in atmospheric conditions on the Tsushima Current. J. Oceanogr. Soc. Japan, 38: 81-94.

UNCLASSIFIED
SECURITY CLASSIFICATION OF THIS PAGE

REPORT DOCUMENTATION PAGE

1a. REPORT SECURITY CLASSIFICATION Unclassified	1b. RESTRICTIVE MARKINGS
2a. SECURITY CLASSIFICATION AUTHORITY	3. DISTRIBUTION/AVAILABILITY OF REPORT Approved for public release; distribution unlimited
2b. DECLASSIFICATION/DOWNGRADING SCHEDULE	
4. PERFORMING ORGANIZATION REPORT NUMBER(S) Technical Report No. 401	5. MONITORING ORGANIZATION REPORT NUMBER(S)
6a. NAME OF PERFORMING ORGANIZATION Coastal Studies Institute 6b. OFFICE SYMBOL (If applicable)	7a. NAME OF MONITORING ORGANIZATION
6c. ADDRESS (City, State, and ZIP Code) Louisiana State University Baton Rouge, LA 70803-7527	7b. ADDRESS (City, State, and ZIP Code)
8a. NAME OF FUNDING/SPONSORING ORGANIZATION ONR/Coastal Sciences Program 8b. OFFICE SYMBOL (If applicable)	9. PROCUREMENT INSTRUMENT IDENTIFICATION NUMBER N00014-83-C-0150
8c. ADDRESS (City, State, and ZIP Code) Code 422 CS 800 North Quincy Street Arlington, VA 22217	10. SOURCE OF FUNDING NUMBERS PROGRAM ELEMENT NO. / PROJECT NO. NR 388 002 / TASK NO. 8 & 9 / WORK UNIT ACCESSION NO. 5

11. TITLE (Include Security Classification)
A TEST OF THE GEOSTROPHIC APPROXIMATION IN THE WESTERN CHANNEL OF THE KOREA STRAIT

12. PERSONAL AUTHOR(S)
Shim, T., Wiseman, W. J., Jr., Huh, O. K., and Chuang, W.-S.

13a. TYPE OF REPORT	13b. TIME COVERED FROM _____ TO _____	14. DATE OF REPORT (Year, Month, Day)	15. PAGE COUNT
		1984	10

16. SUPPLEMENTARY NOTATION
Reprint from Ocean Hydrodynamics of the Japan and East China Seas, pp. 263-272, 1984.

17. COSATI CODES			18. SUBJECT TERMS (Continue on reverse if necessary and identify by block number)
FIELD	GROUP	SUB-GROUP	geostrophic, Korea Strait, transport, current meter measurements, STD stations
08	10		

19. ABSTRACT (Continue on reverse if necessary and identify by block number)

Current meter measurements and lines of STD stations are analyzed to test the geostrophi method in the western channel of the Korea Strait. An array of three current meters was deployed in the deep central part of the channel. Meters were located near the surface, at mid-depth, and near the bottom in 203 m of water. They recorded approximately 550 hours of data between October 16 and November 2, 1972. Several cross-stream transects of physical properties with closely spaced (3-6 km) STD stations were acquired. The measured velocity differences between 25- and 80-m depths and between 80- and 195-m depths are approximately 0.24 m sec^{-1} and 0.42 m sec^{-1}, respectively. The corresponding geostrophic velocity differences vary from -0.05 to 0.10 m sec^{-1} and 0.35 to 0.61 m sec^{-1}, respectively. It would appear that geostrophic estimates of the total transport through the western channel may be in error and should be treated with caution.

20. DISTRIBUTION/AVAILABILITY OF ABSTRACT	21. ABSTRACT SECURITY CLASSIFICATION	
☒ UNCLASSIFIED/UNLIMITED ☐ SAME AS RPT. ☐ DTIC USERS	Unclassified	
22a. NAME OF RESPONSIBLE INDIVIDUAL Cheri Marquette	22b. TELEPHONE (Include Area Code) (504) 388-2395	22c. OFFICE SYMBOL

DD FORM 1473, 84 MAR 83 APR edition may be used until exhausted. All other editions are obsolete.

SECURITY CLASSIFICATION OF THIS PAGE
UNCLASSIFIED

Coastal Studies Institute
Louisiana State University
Baton Rouge, LA 70803-7527

Technical Report No. 402

SYNTHETIC APERTURE RADAR (SAR) IMAGERY OF STORM-INDUCED SEAS AROUND THE GOTO ISLANDS, JAPAN

O. K. Huh, G. A. Mastin, and J. N. Suhayda

1983

Reprint from Ocean Hydrodynamics
of the Japan and East China Seas,
pp. 347-360, 1984.

Office of Naval Research
Contract N00014-83-C-0150
Project NR 388 002

Reprinted from *Ocean Hydrodynamics of the Japan and East China Seas*, pp. 347–360
1984 Elsevier Science Publishers B.V., Amsterdam – Printed in The Netherlands

SYNTHETIC APERTURE RADAR (SAR) IMAGERY OF STORM-INDUCED SEAS AROUND THE GOTO ISLANDS, JAPAN

O.K. HUH,[1] G.A. MASTIN,[2] and J.N. SUHAYDA[3]

[1]Coastal Studies Inst., Louisiana State Univ., Baton Rouge, Louisiana (USA)

[2]Sandia National Laboratories, Albuquerque, New Mexico (USA)

[3]Civil Engineering Dept., Louisiana State University, Baton Rouge, Louisiana (USA)

ABSTRACT

High-quality, 3-m-resolution aircraft synthetic aperture radar (SAR) imagery of coastal seas around the Goto Islands was obtained on August 31, November 19, and November 27, 1982. The August data were taken during 10-17 m sec^{-1} (SE) winds associated with a typhoon that generated 200-m-long waves propagating toward 354°T. The November 19 data are from a calm period of winds less than 1.5 m sec^{-1} from the southwest; no sea returns were obtained with the exception of small oceanic fronts. The November 27 data are from a fall-season monsoonal surge of 9.5 m sec^{-1} winds from the northwest, generating 80-100-m-long waves propagating SSW (142-204°T). Sea and swell diffraction/refraction patterns are clearly discernible, as well as wave-current interactions, shallow-water fronts, and surface wind effects. A computer program has been developed that, using SAR-derived wavelength and surface wind data, estimates wave period, celerity, wave height, wind shear velocity, drag coefficient, and dynamic roughness length. SAR-derived wind directions agree closely with coastal station and ship of opportunity data. The quality of the radar sea return has been found to be critically dependent on antenna depression angle, wind speed, and surface roughness. The system used was the AN/UPD-4 radar mapping set operated on wavelengths of 3 cm (X band, 9.68 GHz).

INTRODUCTION

The objective of this paper is to report on the utility of a high-resolution X-band synthetic aperture radar system in making sea state/air-sea interaction observations in a complex coastal region. Surface roughness details in coastal regions (waters and land) hold large quantities of valuable environmental information.

Synoptic measurements of instantaneous sea-surface roughness can give important information on spatial variability of seas and swell, surface winds, circulation patterns, locations of oceanic fronts, and slicks. SAR systems are potentially able to measure surface roughness parameters in darkness, high humidity, or cloud cover. Thus, unaffected by weather conditions or solar illumination changes, data are obtained on each mission, without the limitations inherent in remote sensing using infrared and visible data.

The data were obtained by the Japan Self Defense Air Force using a Goodyear Aerospace Corporation AN/UPD-4 side-looking radar installed on an RF-4 Phantom aircraft. This is a synthetic aperture radar with a 3.1-cm wavelength (~9.68 GHz frequency), a constant 2-3-m slant range (cross-track) resolution, a 3-m along-track resolution, a 9.15-18.5-km swath width, and all-weather, day-night capabilities. Polarization of RF radiation is horizontal at the transmitter and horizontal at the receiver. A multichannel optical data recorder with four cathode ray tubes displays the incoming signal line by line on a continuously moving strip of 24.1-cm (9.5-inch) photographic film. Doppler phase histories of all surface features, fixed or moving, are created by backscattering of the transmitted radar beams. This film of stored phase histories is the data film, effectively a holograph of the imaged scene. The data film is converted to an image film on the ground, using the optical correlator-processor.

The images were recorrelated on the precision optical correlator at the Goodyear Aerospace Corporation facilities, Litchfield Park, Arizona, to obtain calibrated and optimized display of sea returns. The images were digitized to an 8-bit precision for computer analysis by scanning with a Hamamatsu C1000 vidicon camera system, interfaced with a Perkin-Elmer 3220 minicomputer. The resampled resolution was approximately 10 m per pixel, more than adequate to satisfy the Nyquist criterion for ocean waves in the imagery. Preprocessing included digitization shading correction, slant-range-to-ground-range correction, and map rectification (Mastin, 1981).

Mission parameters for the flights were as follows. Aircraft flew at speeds of approximately 270 m sec^{-1} at altitudes of 3660 and 3960 m. Angles of incidence of the radar beams ranged from 50° to 80° (antenna depression angles of 40-10°). Study of a large number of UPD-4 imagery over the seas has indicated that 35-45° incidence angles yield the best sea returns and that returns drop off at large incidence angles (Huh and Suhayda, 1978). Missions

were flown over the Goto and Tsushima islands on August 31, November 19, and November 27, 1981 (Fig. 1). This site was chosen for its deep waters near the coast, availability of wave/wind sensor data, convenience for aircraft, and readily detectable rocky coastline.

ANALYSIS AND INTERPRETATION OF THE SAR IMAGERY

The objective of this analysis is to obtain large-area, nearly instantaneous data on regional sea states. The analysis procedure is aimed at obtaining estimates of wavelength, period, direction, celerity, and height plus wind shear velocity, drag coefficient, and dynamic roughness length at any point or array of points in the scene. Wavelength and direction extraction from SAR imagery is well documented (Mattie et al., 1978; Meadows, 1980; Hayes and Shuchman, 1981; Shuchman et al., 1983). These parameters are normally extracted from two-dimensional digital or optical fourier transforms. Vesecky and Stewart (1982) report an average error between SEASAT-extracted wavelengths and in situ measurements of 12%. Shuchman et al. (1983) report RMS errors between aircraft SAR-extracted wavelengths and in situ measurements of 7.9% for X-band and 8.3% for L-band during the Marineland Experiment. RMS wave direction errors for the Marineland Experiment were 9.8% for X-band and 16.3% for L-band. The importance of these results is that wave direction and length are reasonably well extracted from SAR images, despite differences in radar wavelength, whether the SAR is airborne or spaceborne, or whether the data are digitally or optically processed. Wave period and celerity can be calculated using wavelength measurements and the deepwater dispersion equation, but wave height is not measurable on the imagery. There are, however, empirical models for estimating wave height and other parameters from wavelength, wind speed, and fetch (U.S. Army Coastal Engineering Research Center, 1977; Hasselmann et al., 1973).

Quantitative analysis of the imagery is based on direction and wavelength extraction using two-dimensional digital fast fourier transforms (2DFFT) and parameter estimation with previously established empirical formulas from the literature. Dominant components in the magnitude of the fast fourier transforms (mag. FFT) were determined after enhancement by special processing procedures (Mastin, 1983). Frequency components derived from the 2DFFT were converted to wavelengths by a computer program, which then calculated wave period and phase speed with the deepwater dispersion equation.

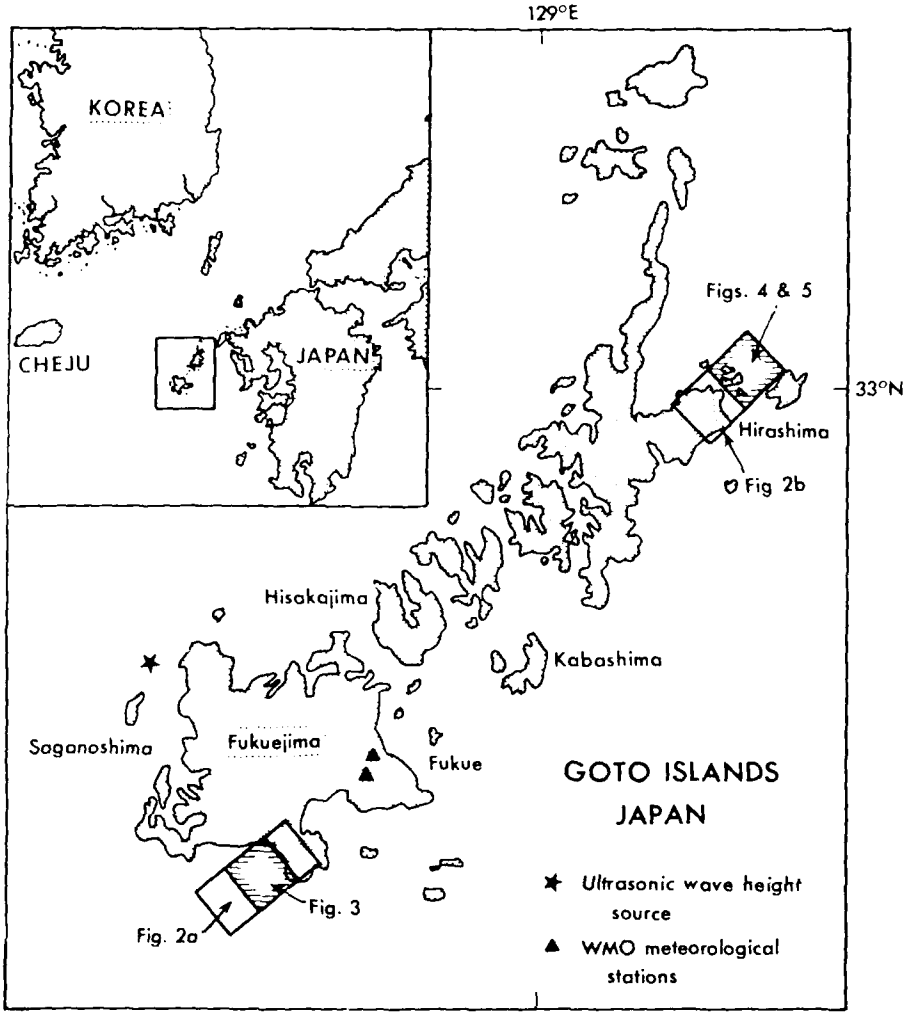

Fig. 1. Location chart showing the Goto Archipelago, location in the strait (inset), and subscenes analyzed here. (Note: Entire archipelago is covered with each aircraft pass.)

This deepwater assumption is usable with most data around the Goto Islands because of their pinnacle-like submerged form and deep water (>60 m) close to the coasts. Based on an in situ wind speed entered by the user, the program further estimates the wave height and air-sea interaction parameters, including wind shear velocity, drag coefficient, and dynamic roughness length, using the empirical

equations summarized below. These equations must be used with caution but are based on analyses of very large data sets, acquired globally.

Hasselmann et al. (1973) developed an empirical wave forecasting model as a function of fetch, wave frequency, and wind speed using laboratory and JONSWAP field experimental data. This model allows the significant wave height in a scene to be estimated, knowing only the significant wave period, T_w, and the wind speed, U_{10SEA}.

$$\sigma = \left(\frac{U_{10SEA}^2}{g}\right) 4 \times 10^{-4} \left(\frac{22\ g\ T_w}{2\pi\ U_{10SEA}}\right)^{3/2} \tag{1}$$

where g is the acceleration caused by gravity in meters per second per second and σ is the standard deviation of the surface displacement.

$$H \simeq 4\ \sigma \tag{2}$$

where H is the significant wave height. The key to using this relation is to verify that the dominant wavelength measured from the SAR mag FFT is coupled with the wind generating the wave field, whose speed is supplied by the analyst. In those cases where U_{10SEA}, the wind speed measured 10 m above the sea cannot be directly measured; corrections must be made. A wind speed from a land-based station is an example. First, the power wind profile relation (Hess, 1959) must be used to correct the wind speed from a station height, z m, to 10 m:

$$U_{10} = U_Z \left(\frac{10}{Z}\right)^{1/7}. \tag{3}$$

The power 1/7 has been suggested by Blackadar (1960) and is related to thermal stability. Correction from land wind speed to sea wind speed is given by Hsu (1980)

$$U_{10SEA} = 3U_{10}^{2/3} \tag{4}$$

Amorocho and DeVries (1980, 1981) have developed an empirical model for calculating the wind shear velocity U_*. The wird shear velocity is an indication of aerodynamic roughness at the boundary layer.

$$U_* = \left\{(0.00121 \pm 0.00029)\left[1 + \exp -\left(\frac{U_{10} - 12.5}{1.56}\right)\right]^{-1} + 0.00104\right\}^{1/2} U_{10SEA} \quad (5)$$

where

$U_* <= 0.23$ m sec^{-1} low roughness,
0.23 m sec^{-1} $< U_* <$ 0.98 m sec^{-1} transitional roughness,
$U_* <= 0.98$ m sec^{-1} high roughness.

The wind stress coefficient, C_{10}, can also be calculated.

$$C_{10} = (0.00121 \pm 0.00029)\left[1 + \exp\left(\frac{U_{10SEA} - 12.5}{1.56}\right)\right]^{-1} + 0.00104 \; . \quad (6)$$

Given H, U_*, and the wave phase speed, c, the dynamic roughness length, Z_0, can be calculated (Hsu, 1974):

$$Z_0 = \left[\frac{1}{2\pi}\frac{H}{(c/U_*)^2}\right] \; . \quad (7)$$

Images were acquired along the swaths indicated in Figure 1. Examples of the original undigitized 3-m-resolution data produced directly from the data film are shown in Figure 2a and b. These are slant plane versus ground plane images, meaning that the geographic information is projected on a plane connecting the imaged scene and the antenna directly. This is a somewhat compressed projection from the actual surface geometry that is corrected in computer processing. Interactive image processing software allows production of sea-state analyses from the corrected imagery using the 2DFFT and calculated parameters. The combination of visual display of the imagery and localized 2DFFT analyses helps resolve the 180° ambiguity of wave direction inherent in the fourier domain conjugate symmetry.

Quantitative information can now be extracted where needed from the imagery to interpret sea conditions. Results of analysis and examples of such sea state products are presented in Figures 3 and 5. On August 31, to windward (south) of Fukuejima, the seas from Typhoon Agnes have a prominent 200-m wavelength component propagating in a 354°T direction, with calculated period of 11.3 sec.

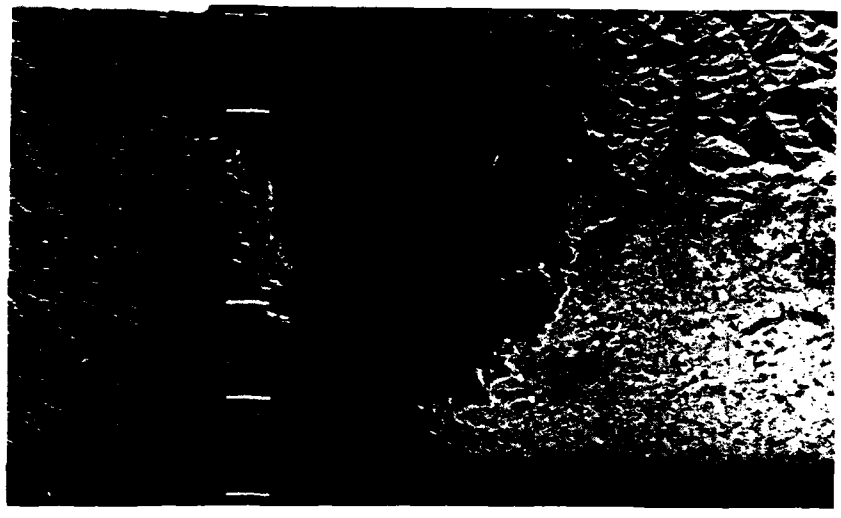

a

b

Fig. 2. Original 3-m resolution SAR imagery of coastal waters near the southern and northern Gotos. These were acquired under cloud-cover conditions. a. Tsutarashima, off the south coast of Fukuejima on 31 August, 1531 hr (JST), showing refraction patterns of long-fetched, low-wavelength waves from Typhoon Agnes. b. Adamashima (with airfield, northeastern Gotos) and the adjacent Aizaki Channel (to left) on 27 November, 1423 hr (JST), during the surge of the winter monsoon after cold-front passage.

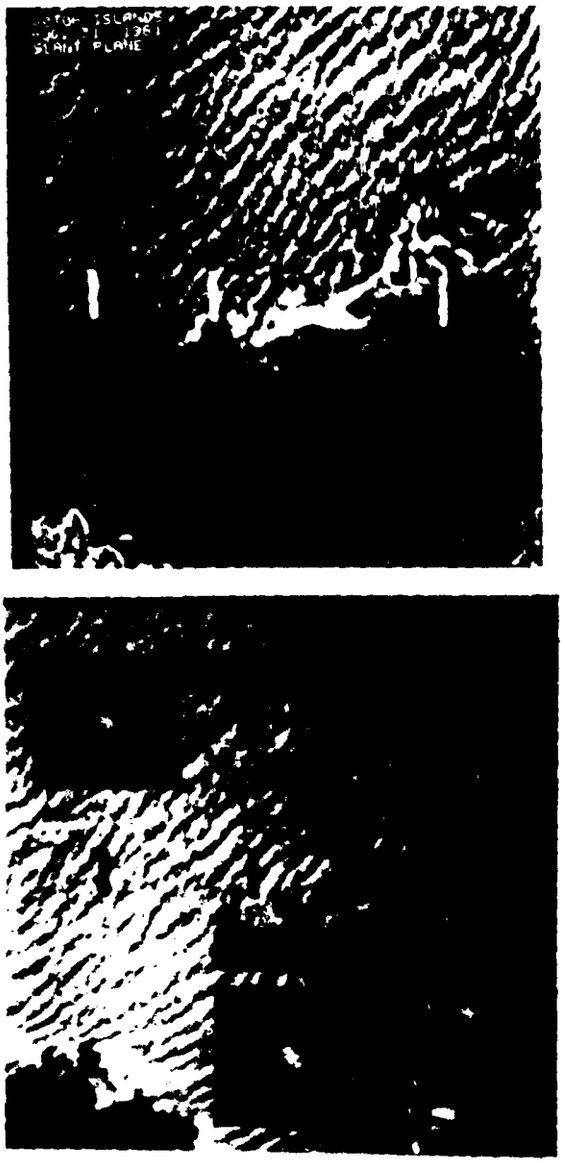

a

b

Fig. 3. SAR image of Typhoon Agnes driven seas incident on the south coast of Fukuejima and Tsutarashima. a. Digital slant plane image of incident waves in open sea and coastal waters. Offshore depth 100 m. b. Digital ground plane version of a, with 2DFFT and wavelength analyses.

a

b

Fig. 4. SAR-detected wind and wave patterns off Adamashima for the two storms, digital and slant plane imagery. a. 31 August image: winds and sea from the southwest, with windrows in lower part and "cats paws" in the upper part of the scene. b. 27 November: winds and seas from the northwest.

Fig. 5. Geometrically corrected (ground plane) SAR images shown in Figure 4, with 2DFFT spectra plots plus calculated wave parameters, an analyzed product. a. 31 August: waves from southeast propagating 342-349°T, lengths 81-95 m, with calculated periods of 7.2-7.8 sec. b. 27 November: winds from the northwest, waves propagating toward 145-205°T, winds from 350°T.

These seas, propagating northward along the Goto Islands and through the Aizaki Channel near Adamashima, have shorter wavelengths (80-90 m) and propagation direction of 342-349°T. Note the apparent wind streaking (or rows) on this same image in Figure 4a. The seas generated by the monsoonal surge are shown in the image of November 27 (Figs. 4b, 5b). Two intersecting wave patterns are observed with wavelengths of 76-105 m and propagation directions of 142-205°T. The sea state and air-sea interaction parameters calculated for these images are presented in Table 1. No ground truth is available for testing results of image analysis in these specific areas. However, an ultrasonic wave gage (maintained by Japan Meteorological Agency) off Tsutarashima (island) recorded significant wave period and height of 9.4 sec at 1.33 m on August 31, 5.3 sec at 0.32 m on November 19, and 5.7 sec at 1.6 m during northerly winds of November 27. Differences between measured and SAR-derived values are not presently understood but may be ascribed in part to the sheltered location of the in situ sensor.

CONCLUDING REMARKS

The quality of radar sea returns has been observed here to be a function of radar incidence angle (antenna depression angle) and strength of surface winds. Data from the innermost (closest to the aircraft) recorder channels with the steepest depression angles (circa 35-40°) showed good sea returns except on the calm days of November 19. The outer data channels, with lower depression angles of 10-20°, yielded no sea returns, even under the conditions of rough seas and high winds on August 31 and November 27. On November 19 no wave patterns were detected even at the highest depression angles, but numerous small oceanic fronts showed up clearly on the imagery in and around the Goto Islands and around the Tsushima Islands. The best image quality was obtained with steep antenna depression angles during the periods of wind speeds >10 m sec^{-1} with seas of 1-m height or better.

Interactive digital processing allows subjective scene analysis to be supplemented with quantitative data on wavelength, air-sea interaction parameters, and interpretation of wave propagation direction using refraction patterns. Airflow patterns over the sea surface are seen as windrows and random turbulence patterns among and offshore of the islands. Wind direction can be reasonably determined by reference to the synoptic meteorology in combination with the patterns over the entire scene.

TABLE 1
Data and calculated values from imagery and surface measurements.

Data Source	L (m)	T_{sig} (sec)	C (m/2)	H_{sig} (m)	θ_{Wave} (deg)	U_* (m/2)	C_{10}	Z_o (cm)	W (ppm)	θ_{Wind} (deg)	U_{10} (m/2)
A31A141	94.93	7.80	12.17	2.24	162	0.349	0.00126	0.029	8680	197	-
A31A142	81.37	7.22	11.27	1.99	162	0.349	0.00126	0.03	8680	202	-
A31A143	88.31	7.52	11.74	2.12	169	0.349	0.00126	0.03	8680	-	-
WMO Sta.	-	-	-	-	-	-	-	-	-	135	9.8+
Ultra-sonic Wave Sta.	-	9.4	-	1.33	-	-	-	-	-	-	-
Ship	-	3 (wave)	-	2 (wave)	30?	-	-	-	-	-	-
ZEOH	-	7 (swell)	-	3.5 (swell)	30?	-	-	-	-	140	12.4
N27A91	81.37	7.22	11.27	2.00	9	0.356	0.00128	0.032	9160	140	12.4
N27A92	83.62	7.32	11.42	2.05	12	0.356	0.00128	0.032	9160	359	-
N27A93	85.67	7.41	11.56	2.09	353	0.356	0.00128	0.031	9160	-	-
N27A94	104.69	8.19	12.78	2.43	25	0.356	0.00128	0.30	9160	350	-
WMO Sta.	-	-	-	-	-	-	-	-	-	-	-
Ultra-sonic Wave Sta.	-	5.7	-	1.55	-	-	-	-	-	360	9.94+
Ship UJAE	-	4.0?	-	4.0?	-	-	-	-	-	-	-

+Corrected for elevation of station and for location on land.
The ultrasonic wave station is on the lee side of the island.
?This report suspect.

Limited to ground truth available only through the existing network of wave, tidal, and meteorological stations, rigorous test of the wave parameter estimation capabilities of the SAR system and software developed here was not possible. The high quality of sea returns under storm winds with high antenna depression angles is demonstrated. In addition, wind direction determination from this kind of data is reported here for the first time.

ACKNOWLEDGMENTS

The authors wish to extend deepest appreciation to Lt. Col. Kenji Wakui and the reconnaissance squadron of the Japan Self Defense Air Force for a series of superbly conducted aircraft missions and outstanding data. We would like to acknowledge with appreciation the cooperation of Dr. Tsutomu Akiyama, Head, and Mr. K. Nagasaka, of the Oceanography Division, Marine Department, Japan Meteor logical Agency, for essential environmental data on a data exchange basis. Mr. Milton Hoover and Mr. Ralph Reid of the Goodyear Aerospace Arizona Division contributed greatly by providing access to and guidance with the precision optical correlator. Financial support was provided by the Coastal Sciences Program, Office of Naval Research (ONR Code 422CS).

REFERENCES

Amorocho, J., and DeVries, J.J., 1980. Wind stress over water. Jour. Geophys. Res., 85: 433-442.

Amorocho, J., and DeVries, J.J., 1981. Reply. Jour. Geophys. Res., 86: 4308.

Blackadar, A.K., 1960. A survey of wind characteristics below 1500 ft. Meteorol. Monogr., 4: 3-11.

Hasselmann, K., Barnett, T. P., Bouws, E., Carlson, H., Cartwright, D. E., Enke, K., Ewing, J. A., Gienapp, H., Hasselman, D. E., Kruseman, P., Marburg, A., Muller, P., Olbers, D. J., Richter, K., Sell, W., and Walden, H., 1973. Measurements of wind-wave growth and swell decay during the Joint North Sea Wave Project (JONSWAP). Dtsch. Hydrogr. Z., Erganzungsheft Reihe A, 12, 95 pp.

Hess, S., 1959. Introduction to theoretical meteorology. Holt, Rinehart and Winston, New York, 362 pp.

Hsu, S.A., 1974. A dynamic roughness equation and its application to wind stress determination at the air-sea interface. Jour. Geophys. Res., 4: 116-120.

Hsu, S.A., 1980. Models for estimating offshore winds from onshore meteorological measurements. Boun.-Layer Meteorol., 20: 341-351.

Huh, O.K., and Suhayda, J.N., 1978. Coastal oceanography use of the AN/UPD-4 synthetic aperture side-looking radar system. Unpubl. Trip Rept., Coastal Studies Inst., Louisiana State Univ., Baton Rouge, 32 pp.

Mastin, G.A., 1981. Digital interpolation of synthetic aperture radar data using digital filters. Software Documentation, Remote Sensing and Image Processing Laboratory, Louisiana State Univ., Baton Rouge.

Mastin, G.A., 1983. Computer analysis of coastal ocean features in synthetic aperture radar imagery. Ph.D. dissertation, Louisiana State Univ., Baton Rouge.

Mattie, M.G., Hsiao, S.V., Evans, D.D., 1978. Wave direction measured by four different systems. Jour. Oceanic Engr., IEEE, OE-6: 87-93.

Shuchman, R.A., Lyden, J.D., and Lyzenga, D.R., 1983. Estimates of ocean wavelength and detection from X0 and L-band synthetic aperture radar data collected during the Marineland Experiment. Jour. Oceanic Engr., IEEE, OE-9: 90-96.

U.S. Army Coastal Engineering Research Center, 1977. Shore protection manual, vol. 1. Dept. Army, Corps of Engineers, Section 3.51.

Vesecky, J.F., and Stewart, R.H., 1982. The observation of ocean surface phenomena using imagery from the SEASAT synthetic aperture radar: an assessment. Jour. Geophys. Res., 87: 3397-3430.

SECURITY CLASSIFICATION OF THIS PAGE

REPORT DOCUMENTATION PAGE

1a REPORT SECURITY CLASSIFICATION Unclassified	1b RESTRICTIVE MARKINGS
2a SECURITY CLASSIFICATION AUTHORITY	3 DISTRIBUTION/AVAILABILITY OF REPORT Approved for public release; distribution unlimited.
2b DECLASSIFICATION/DOWNGRADING SCHEDULE	
4 PERFORMING ORGANIZATION REPORT NUMBER(S) Technical Report No. 402	5 MONITORING ORGANIZATION REPORT NUMBER(S)
6a NAME OF PERFORMING ORGANIZATION Coastal Studies Institute 6b OFFICE SYMBOL (If applicable)	7a NAME OF MONITORING ORGANIZATION
6c ADDRESS (City, State, and ZIP Code) Louisiana State University Baton Rouge, LA 70803-7527	7b ADDRESS (City, State, and ZIP Code)
8a NAME OF FUNDING/SPONSORING ORGANIZATION ONR/Coastal Sciences Program 8b OFFICE SYMBOL (If applicable)	9 PROCUREMENT INSTRUMENT IDENTIFICATION NUMBER N00014-83-C-0150
8c ADDRESS (City, State, and ZIP Code) Code 422 CS 800 North Quincy Street Arlington, VA 22217	10 SOURCE OF FUNDING NUMBERS PROGRAM ELEMENT NO: / PROJECT NO: NR 388 002 / TASK NO: 8 & 9 / WORK UNIT ACCESSION NO: 5

11 TITLE (Include Security Classification)
SYNTHETIC APERTURE RADAR (SAR) IMAGERY OF STORM-INDUCED SEAS AROUND THE GOTO ISLANDS, JAPAN

12 PERSONAL AUTHOR(S)
Huh, O. K., Mastin, G. A., and Suhayda, J. N.

13a TYPE OF REPORT	13b TIME COVERED	14 DATE OF REPORT (Year, Month, Day)	15 PAGE COUNT
	FROM 1/1/83 TO 12/31/83	1983	14

16 SUPPLEMENTARY NOTATION
Reprint from Ocean Hydrodynamics of the Japan and East China Seas, pp. 347-360, 1984.

17 COSATI CODES			18 SUBJECT TERMS (Continue on reverse if necessary and identify by block number)
FIELD	GROUP	SUB-GROUP	Synthetic Aperture Radar (SAR), Goto Islands, Japan, storm,
08	08		

19 ABSTRACT (Continue on reverse if necessary and identify by block number)

High-quality, 3-m-resolution aircraft synthetic aperture radar (SAR) imagery of coastal seas around the Goto Islands was obtained on August 31, November 19, and November 27, 1982. The August data were taken during 10-17 m sec^{-1} (SE) winds associated with a typhoon that generated 200-m-long waves propagating toward 354°T. The November 19 data are from a calm period of winds less than 1.5 m sec^{-1} from the southwest; no sea returns were obtained with the exception of small oceanic fronts. The November 27 data are from a fall-season monsoonal surge of 9.5 m sec^{-1} winds from the northwest, generating 80-100-m-long waves propagating SSW (142-204°T). Sea and swell diffraction/refraction patterns are clearly discernible, as well as wave-current interactions, shallow-water fronts, and surface wind effects. A computer program has been developed that, using SAR-derived wavelength and surface wind data, estimates wave period, clelrity, wave height, wind shear velocity, drag coefficient, and dynamic roughness length. SAR-derived wind directions agree closely with coastal station and ship of

20 DISTRIBUTION/AVAILABILITY OF ABSTRACT	21 ABSTRACT SECURITY CLASSIFICATION
☒ UNCLASSIFIED/UNLIMITED ☐ SAME AS RPT ☐ DTIC USERS	Unclassified
22a NAME OF RESPONSIBLE INDIVIDUAL Cheri Marquette	22b TELEPHONE (Include Area Code) (504) 388-2395 / 22c OFFICE SYMBOL

DD FORM 1473, 84 MAR 83 APR edition may be used until exhausted
All other editions are obsolete

SECURITY CLASSIFICATION OF THIS PAGE

UNCLASSIFIED

IV International Symposium on Landslides, Toronto, 1984, Vol. 1. State-of-the- Art Lecture pp. 179-196.

Subaqueous Landslides

David B. Prior
Coastal Studies Institute,
Baton Rouge, Louisiana, U.S.A.

Recent geological research has revealed the presence of a wide variety of sea-floor features resulting from subaqueous slope instability. The methods of identification, including damage to offshore installations and high-resolution acoustic survey techniques, are reviewed and evaluated. Examples of both active and ancient subaqueous landslides are discussed, together with their diagnostic characteristics and various classification schemes. Many of the landslides are extremely large, and their magnitude far exceeds that of their terrestrial counterparts. Failure can occur on very low angle slopes and debris movement can continue for extremely long distances. Initiation of movement is difficult to quantify and appears to be associated with a wide range of geological and environmental factors.

INTRODUCTION

The geomorphology and geology of ocean floors can be subject to change by a variety of processes. Detailed studies of sea-floor morphology and near-surface structure are in progress which address problems of history, origin, and process mechanisms responsible for different submarine features.

Considerable impetus for these studies has been provided by the interests and needs of the offshore industry, specifically oil and gas, in terms of both hydrocarbon production in shallow-water areas and increased efforts at development of deeper water areas beyond the shelf break. For example, Shell Offshore Inc. has recently drilled a record-breaking exploration well in a water depth of 1,965 m off the U.S. Atlantic Coast. In the Gulf of Mexico, Getty Oil Company is conducting exploratory drilling in water 1,071 m deep. Such industrial activity requires detailed knowledge of sea-floor processes, particularly those that may affect the design, emplacement, and maintenance of engineering structures and pipelines (Prior and Doyle, 1984).

National government agencies such as the U.S. Geological Survey have undertaken detailed studies in particular locations around the U.S. continental margin. The "Mississippi Delta Project" is one example from a shallow-water area (Prior and Coleman, 1982), and others have been conducted in various deeper water localities (e.g., Robb et al., 1981; Carlson et al., 1982).

As such site-specific studies, together with more wide-ranging reconnaissance surveys, have progressed, both in the U.S. and elsewhere in the world's oceans, it has become clear that mass movement or landsliding on submarine slopes is and has been a very important sea-floor process, involving large areas and great volumes of sediments. Evidence is accumulating that indicates that many areas are actively experiencing slope instability or have been subject to mass movement in the relatively recent geologic past. Figure 1 shows the locations of landslide features offshore of North America that have been reported in the literature, including both shallow-water shelf and continental slope phenomena. In addition, some slope instabilities have been observed in lacustrine settings.

Various review articles and symposium publications are providing an increasingly global perspective on subaqueous landslide processes (Saxov and Nieuwenhuis, 1982; Schwarz, 1982; Geo-Marine Letters, vol. 2, 1982; Prior and Coleman, 1983). Indeed, on a worldwide basis it is becoming apparent that subaqueous slides can be found in a wide variety of geologic and environmental settings and on very low angle slopes. Moreover, Varnes' (1975) suggestion that "the largest of all slope movements on earth appear to have occurred on the bottom of the sea" can certainly be supported. Several individual subaqueous slide complexes have been identified that dwarf their terrestrial counterparts (Embley, 1976; Moore, 1977; Dingle, 1977; Bugge, 1983).

The study of these processes in remote underwater areas, often at great depths, is the focus of intensive interdisciplinary research. Geomorphologists, geologists, geophysicists, and oceanographers are combining efforts with specialists in marine geotechnology. Attempts are being made to document the subaqueous features resulting from slope instability and to determine their activity or geologic age.

METHODS OF LANDSLIDE IDENTIFICATION

Various diagnostic criteria can be used to identify active or formerly active subaqueous landslide areas. One immediate type of evidence of active landsliding is damage to coastal and offshore installations such as docks and harbors, sea-floor communication cables and pipelines, and bottom-supported platforms.

Coastal settlements, harbors, and docks have

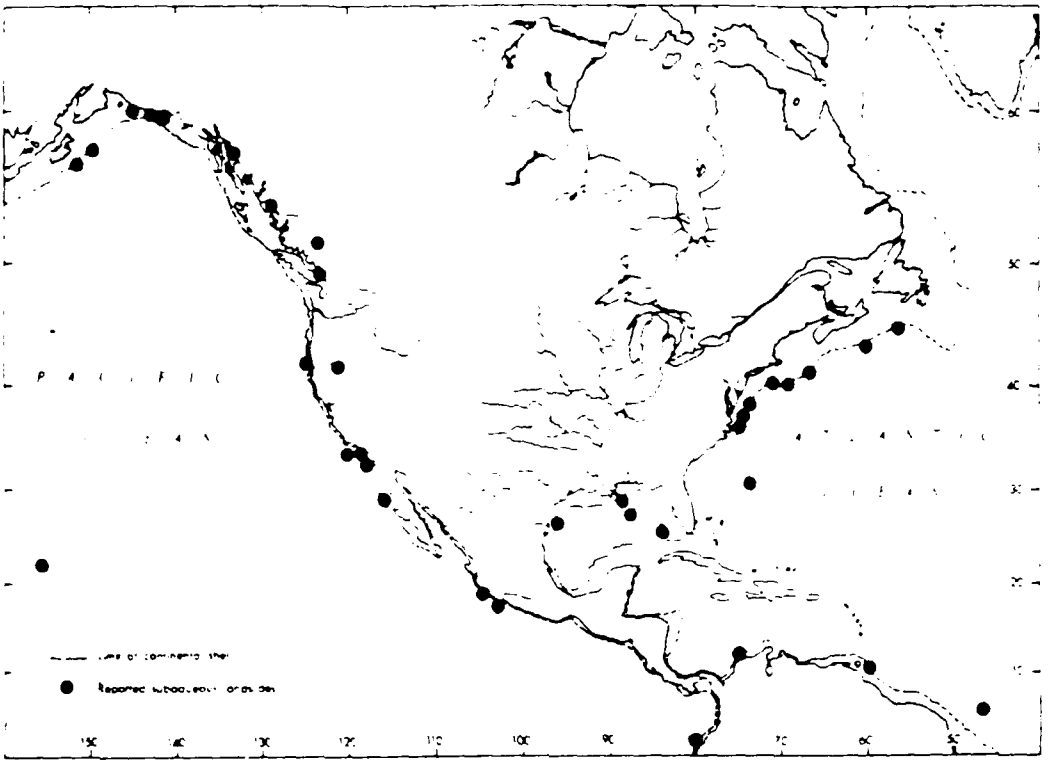

Figure 1. Map showing locations of subaqueous landslides reported in the literature on the continental margins around North America and the northern part of South America.

been adversely affected, either because of the landward extension of nearby subaqueous landslides or by inundation by local waves generated by movements of large volumes of sediment. An excellent example of this type of event is the Skredalsfjord slide, which took place in 1930 (Bjerrum, 1971). Coastal erosion, destruction of piers and harbor works, and severance of seafloor cables accompanied the subaqueous slide. Similarly, at Kitimat, British Columbia, a fjord-head slope failure in 1975, involving about 55 million m^3 of sediment, resulted in locally generated surface waves, which flooded adjacent lowlands (Murty, 1979; Prior et al., 1982).

Elsewhere along continental margins there have been numerous submarine cable breaks that cannot be attributed simply to hardware failures (e.g., Milne, 1897; Heezen, 1956; Terzaghi, 1956; Heezen and Drake, 1964). The most recent dramatic example occurred offshore of Hawaii in November 1982. Accompanying the passage of Hurricane Iwa over the Hawaiian archipelago, a series of underwater cables off Oahu were damaged or broken. In addition, current meters installed offshore in that area were displaced downslope during the same time period. From the observed data it was concluded that a "sedimentary or water sediment layer flowed downslope beginning in about the 115-m depth escarpment region and extending as far as 20 km offshore to a water depth of 2,740 m" (Noda, 1983).

Oil and gas pipelines and platforms have also suffered damage. For example, in the Mississippi Delta region, subaqueous mudslides and mudflows have caused considerable problems to offshore installations (Bea, 1971; Sterling and Strohbeck, 1973; Prior et al., 1979; Bea and Audibert, 1980). The best documented examples are from South Pass Blocks 61 and 70, in which three platforms were damaged by bottom mudslides and mudflows during Hurricane Camille in 1979 (Bea and Audibert, 1980).

More generally, however, the recognition of underwater landsliding, both active and relict, relies upon the interpretations of characteristic sea-floor morphology and subsurface sediment deformation features. Acoustic remote sensing methods are now available that allow acquisition of high-resolution data on sea-floor and subsurface features at a variety of scales, from nearshore areas to full ocean depths. Moreover, the high-resolution methods routinely applied in shallow-water areas are being used in deeply towed configurations, yielding unparalleled images of the sea floor to depths of 2,000-2,500 m (Prior and Doyle, 1984).

Subaqueous landslides have been detected with acoustic techniques such as echo-sounding profilers, side-scan sonar swaths and mosaics, and different types of subbottom profiling systems. The analyses of sediment samples from cores are used to support the interpretations of remotely acquired data.

1. Echo Sounding

Echo-sounding profiles and resulting bathymetric maps show the results of subaqueous landsliding, much in the manner that terrestrial contour maps can show large-scale slope instability features. Also, some active subaqueous landslide areas have been detected by anomalous depth changes noted on successive surveys. For example, in Sagami Bay, Japan, following an earthquake in 1923, substantial depth changes were interpreted by Shepard (1933) to be due to landsliding (Fig. 2). Similarly, changes in bathymetric profiles and contours in the Mississippi Delta region were considered by Shepard (1955) and more recently by Coleman et al. (1980) as the results of subaqueous mass transport of delta-front sediments. Also, the sudden appearance of water depth changes on the sea floor off the mouth of the Klamath River, northern California, in 1980 was the first indication of a subaqueous slope failure in that region (Field and Hall, 1982).

2. Side-Scan Sonar

Side-scan sonar systems provide images of the topography of the sea floor along swaths of predetermined widths. When adjacent swaths are combined, large-area mosaics can be constructed. These techniques are proving to be invaluable in the identification and definition of subaqueous landsliding, much in the manner that aerial photography has contributed to the understanding of terrestrial landslides.

A variety of different side-scan systems are now in use that provide data at various scales and

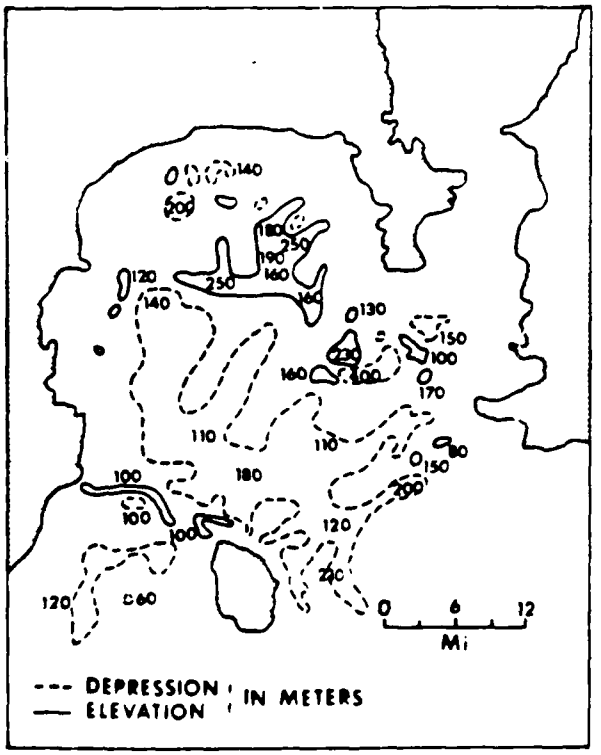

Figure 2. Depth changes in Sagami Bay, Japan, interpreted as the results of subaqueous landsliding (from Shepard, 1933).

resolutions. For the detection of landslides, each offers different capabilities in terms of resolution and area of coverage.

The GLORIA system, designed and operated primarily as a regional reconnaissance tool, is a long-range, 6.5-kHz sonar that can be tuned for a maximum range of 30 km, giving 60-km swaths. At such long range settings the resolution is insufficient to show details of local sea-floor topography, but the GLORIA system has proven effective in delineating the presence and outlines of very large scale slide complexes (e.g., Kenyon et al., 1978; Kidd, 1982). Recently, Bugge (1983) employed the GLORIA sonar to investigate the huge Storegga slide area off Norway, which has an upslope headwall length of 290 km.

The SEAMARC I side-scan sonar is a medium-range system operating at 27/30 kHz and capable of ranges of 500-2,500 m (1-5-km swaths). It has been used particularly to examine the geology and morphology along the U.S. Atlantic continental margin (e.g., Robb et al., 1981; McGregor et al., 1982). Also, from studies in this area, Pyle (1982) has interpreted SEAMARC I data in terms of subaqueous slope instability and has reported debris flow and sediment avalanche features.

An example of SEAMARC I data is provided in Figure 3, from the Atlantic continental slope off New Jersey. Surveys in this area were conducted to assess the potential for hazards to exploratory drilling (Coleman et al., 1982; Prior et al., 1984). Figure 3 (showing only one channel of data, or half the total swath) illustrates the morphology of an arcuate canyon head with large blocks of debris at the base of the headwall scarp, believed to be due to local subaqueous rockfall processes.

Shorter range, 100-kHz side-scan sonar systems allow mapping of sea-floor features in great detail. Operated at ranges of 100-250 m, most commercially available 100-kHz sonars claim individual target resolutions of approximately 1 400 range. Such short-range systems have proven to be extremely effective in the recognition of subaqueous landslides (Prior and Coleman, 1982; Field et al., 1982). A wide variety of characteristic bottom features have been identified, including hummocky topography, displaced blocks, crescentic and linear scarps, channels and chutes, and depositional lobes. Figure 4 is an example of a side-scan sonar mosaic composed of adjacent 100-kHz swaths for part of the mudslide/mudflow area off the Mississippi Delta. It shows chutes and displaced blocks, which are typical of active slope instability processes in that region.

3. Subbottom Seismic Profiles

Near-surface geologic structures are detected by various acoustic tools that penetrate beneath the sea floor to different depths and resolutions. Deep-penetration systems such as air guns, water guns, and sparkers can provide high-resolution data to depths of more than 1,000 m below the sea floor, depending upon local sediment characteristics and the manner in which the systems are employed. However, the capability to resolve subsurface features and their detail within the full depth range is highly variable, but may be improved by post-cruise processing. Such deep-penetration systems are most commonly

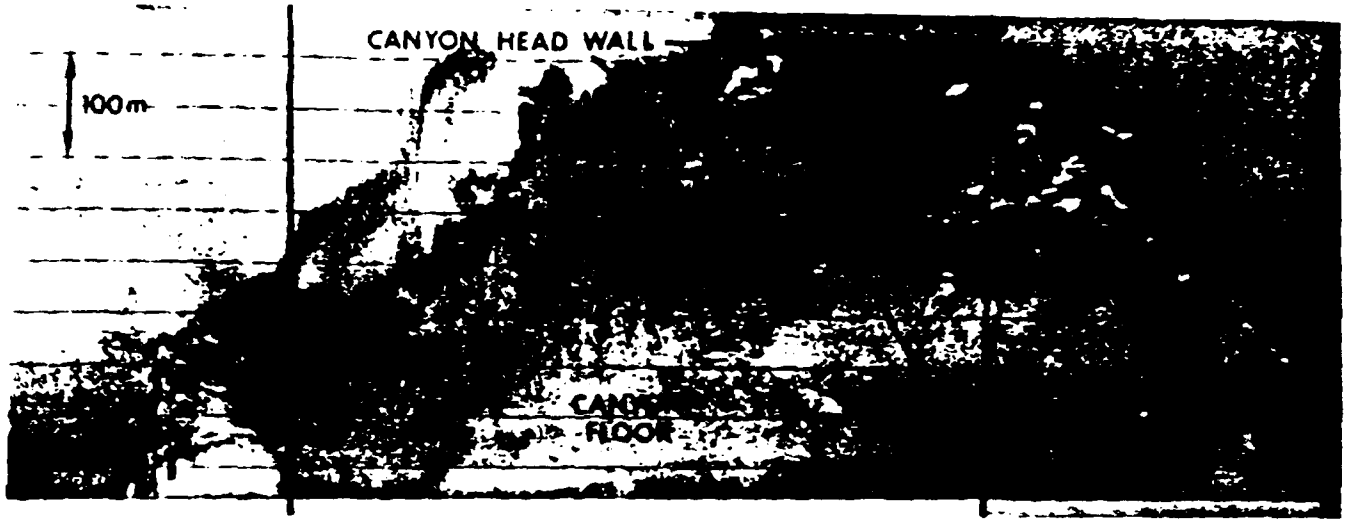

Figure 3. SEAMARC intermediate-range sonar swath (one channel) showing rockfall debris along the headwall slope of a submarine canyon.

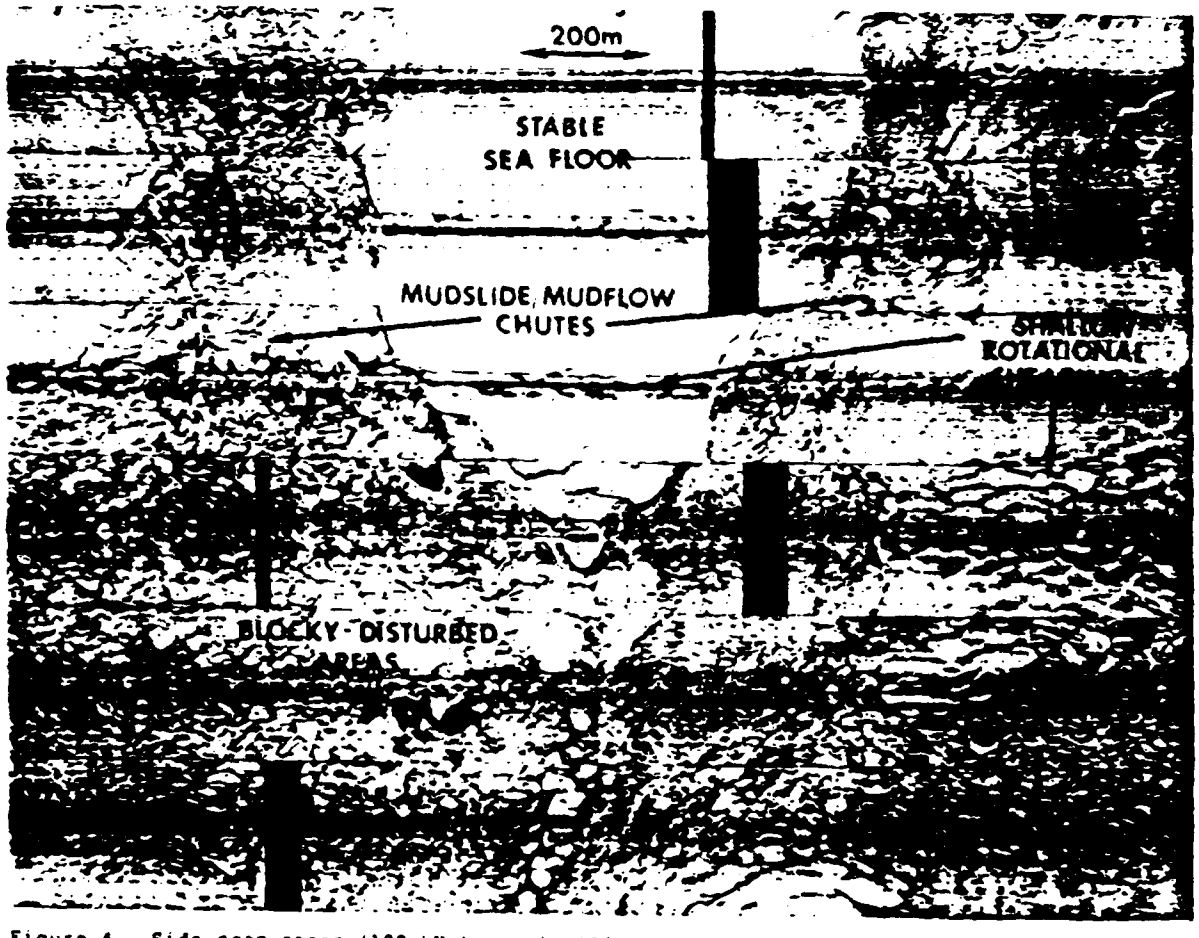

Figure 4. Side-scan sonar (100 kHz) mosaic illustrating subaqueous slope instability features off the Mississippi Delta.

used to interpret very large scale phenomena. For example, distorted seismic reflections, internally chaotic structures, and seismically amorphous units are often associated with cracks, faults, and discontinuities indicative of sediment shearing.

Figure 5 (A and B) shows examples of sparker profiles from the continental slope in the Gulf of Mexico. Large-scale subparallel fault/slide planes, bounding areas of backward-rotated sediment units, are found upslope of highly irregular topography over internally deformed sediment units. These deformational geometries can be interpreted as large-scale subaqueous landslides and are commonly found along the upper continental slope at the margins of former Pleistocene low-sea-level deltas or on the sides of uplifted diapirs.

High-resolution subbottom profiling systems, operating at frequencies of between 3.5 and 12

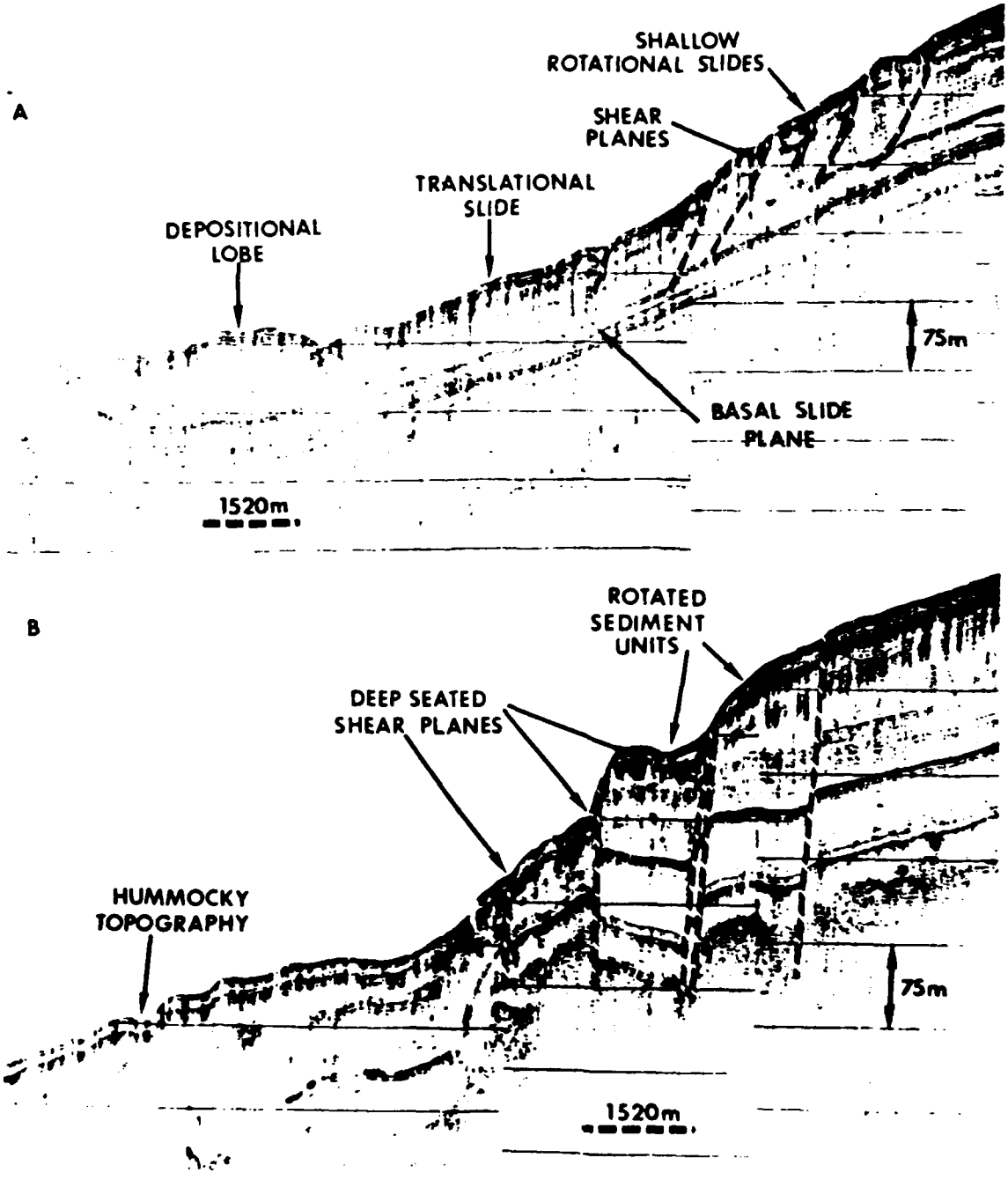

Figure 5. Sparker profiles across parts of the continental slope, Gulf of Mexico.

-Hz, are capable of showing details of subsurface geology to depths of 50-100 m, depending upon sediment acoustic properties. Such subbottom profiles have proven to be extremely useful in defining areas of relatively shallow subaqueous landsliding. Once more, distorted seismic reflections and chaotic structures, together with shearing and irregular surface topography, are diagnostic. In particular, 3.5-kHz profilers, used in combination with 100-kHz side-scan sonar systems, have yielded very precise information concerning the geometry and topography of subaqueous landslides.

Examples of high-resolution profiles across subaqueous landslide deposits are illustrated in Figure 6 (A and B). The complete absence of intact internal bedding and the presence of randomly distributed and oriented, "chaotic" internal acoustic reflectors, together with hummocky surface topography, are characteristic of reworking and partial remolding of marine sediments by landsliding processes (Fig. 6A). Also, such subbottom profiles can detect the presence of former instability events that have been buried by later marine sedimentation. For example, Figure 6B shows a profile across a depositional lense of acoustically transparent material, with a lobate profile and totally lacking coherent internal structure, sandwiched between laminated and bedded marine sequences.

Combined use of side-scan sonar and subbottom profiling to detect the effects of subaqueous landsliding is illustrated in Figure 7 (A and B). The sonar swath shows a lobate area of pressure ridges and blocky debris at the downslope margins of a subaqueous debris lobe, and there is a distinct contrast between the morphology of the lobe and the adjacent undisturbed sea floor, which is almost flat except for a thin, ill-defined surface debris splay. The accompanying subbottom profile also shows bedded and laminated seafloor sediments, the area that has been highly

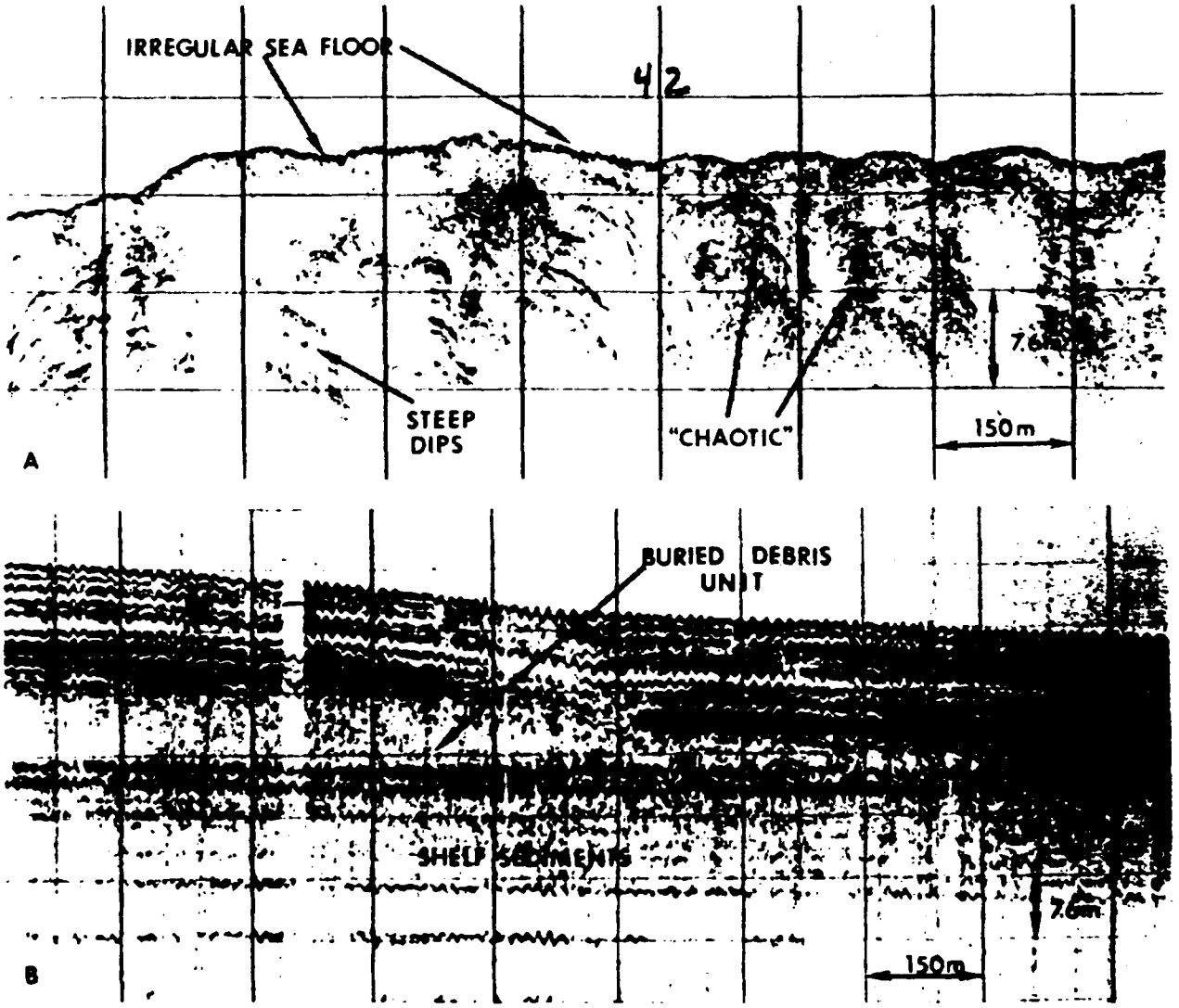

Figure 6. 3.5-kHz subbottom profiles across depositional areas associated with subaqueous landsliding. A, surface deposit; B, buried lobe beneath later stratified sediments.

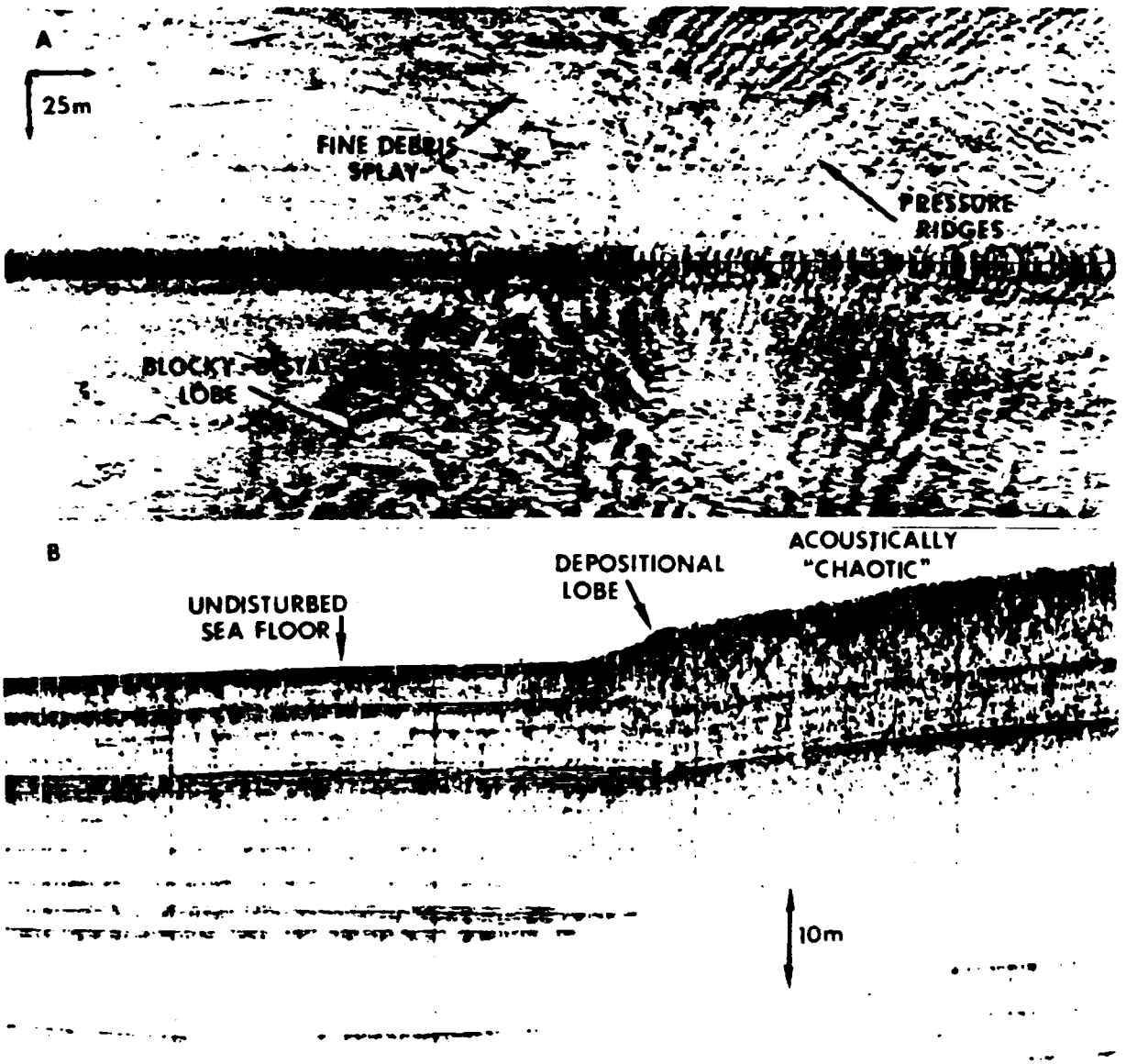

Figure 7. Combined side-scan sonar swath (100 kHz) and subbottom profile (3.5 kEz) across the margins of a depositional lobe. The profile corresponds to the center line of the sonograph.

disturbed by emplacement of the debris lobe (Fig. 7B), and the abrupt margin of the lobe. Once more, the debris lobe acoustic characteristics are acoustically "chaotic," indicating partial remolding and disturbance by the landsliding processes.

TYPES OF SUBAQUEOUS LANDSLIDES

Classification of subaqueous landslide phenomena is particularly difficult. Landslide movements have not been directly observed (apart from the remarkable incident off Toulon; Dugan, 1967), and thus deformational mechanisms and processes must be inferred from the resulting landslide geometry and depositional characteristics observed at some time after the particular event. During the actual downslope sediment movements, several different deformational mechanisms may be involved, the results of which are not necessarily preserved in the ultimate morphology and sediment properties of the slide.

Also, it is clear that some types of landslide are presently active in particular geologic settings and in response to modern environmental factors. By comparison, others are known to be ancient, inactive, and relict, and to owe their formation to geologic conditions different from those at present. However, a significant proportion of the features that have been identified by acoustic techniques have not been age dated, and their time of origin and present status are unknown. Embley (1982) perceives that "many au-

thors have either assumed or concluded on the basis of rather scanty data that most slumps and slides which occur on continental slopes are of Late-Wisconsin age." Moreover, he concluded that some large-scale features around the Atlantic continental margin show a relatively random distribution of age dates, from the present to 24,000 years B.P.

Notwithstanding differences in age and origin, various authors have proposed different classification schemes. For example, Dott (1963) suggested four main categories: submarine falls, slides or slumps, flows, and turbidity flows. Moore (1977) omitted turbidity flows and also subdivided the primary categories on the basis of type of material. Middleton and Hampton (1976) proposed the term "sediment gravity flows" and suggested that slides may evolve into different types of gravity flows. Slides and flows are regarded in this scheme as different parts of a process continuum.

In an unfortunate trend, marine geological literature overuses the term "slump," and it is often applied indiscriminately to widely different types of features. The term is much too generalized (Dott, 1963; Prior and Coleman, 1979), and its misapplication creates confusion.

Figure 8 attempts to provide a classification scheme in which the concept of process continuum of slides to flows is maintained but subdivisions of slide and flow phenomena are also indicated, following concepts and terminology developed from terrestrial landslides (Skempton and Hutchinson, 1969).

1. Slides

One of the most widespread types of subaqueous mass movements involves sliding over discrete basal shear planes, in many cases on slopes of less than 5°. Until recently, reservations were often expressed about slope instability under such low gravitational stresses, but it is now widely accepted that instability may begin on subaqueous slopes of 1° or less if sediment strength is sufficiently small. In a recent listing of slides, Bugge (1983) indicates a slope angle range of 0.2-10°. In the Mississippi Delta, mudslides and mudflows occur on slopes that have an average inclination of 0.5° (Prior and Coleman, 1982).

The volume of sediments involved in sliding is often extremely large, including more than 20,000 km^3 for the Agulhas slide, off South Africa (Dingle, 1977), and more than 5,500 km^3 for the Storegga slide, off Norway (Bugge, 1983). In addition, many much smaller slides have been identified from other localities, and it is likely that perceptions of smaller slides are limited more by the resolutions of survey systems and the amount of survey data than by slide mechanisms.

Two basic subdivisions of slides are possible on the basis of the geometry of basal shear surfaces: translational and rotational. Many slides appear to involve a basal failure plane that is inclined approximately parallel to the surface slope (e.g., Fig. 5A). Blocks of rock or shallow slabs of soft sediment are displaced downslope, and this translational process is consistent with low slope angles and the great length of many features. The Straits of Florida

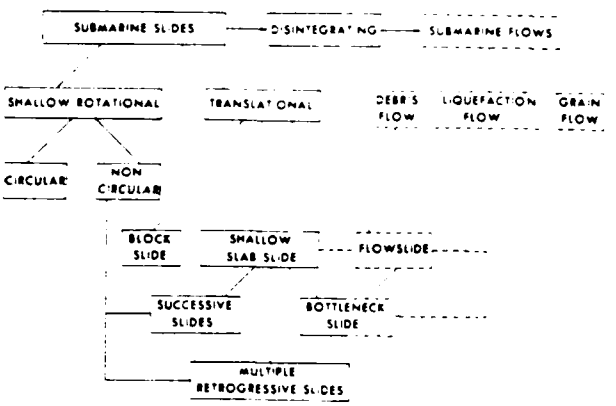

Figure 8. Suggested scheme illustrating the various types of submarine landslides, which comprise a continuum of slides and flows.

slide (Wilhelm and Ewing, 1972) is considered an example of block sliding, and many of the Mississippi Delta mudslides are examples of shallow slab sliding in which thin intact blocks of sediment are moved but stay right-way-up (Prior and Coleman, 1982). Successive slides are found where a large section of slope is subject to numerous adjacent translational and rotational failures, and a good example is provided from the Copper River delta (Alaska) by Reimnitz (1972) and from the Gulf of Alaska by Hampton et al. (1976). Multiple retrogressive slides occur where continued failure and interaction of adjacent slides produce multiple blocks and extension of instability upslope. Many submarine slides appear to fit this category (e.g., Moore, 1964; Stride et al., 1969; Dingle, 1977). Bottleneck slides can be considered intermediate between true slides and flows, possessing a very distinctive plan form (Fig. 9) in which debris moves downslope from an arcuate, depressed source region through a narrow neck to form a widespread depositional fan (Prior and Coleman, 1982).

Rotational slides are typified by displacement of relatively intact blocks over curved or spoon-shaped slip surfaces. Many subaqueous movements appear to fit this category, but it should be remembered that the curvature of failure planes and degree of rotation of blocks are emphasized by the vertical exaggeration inherent to most seismic records. Frequently the slides are shallow, relative to length, and both circular and noncircular failure surfaces can be identified. Dingle (1977) summarizes the diagnostic criteria, and a large number of rotational failures have been documented, particularly on relatively steep continental slope environments, where they may be responsible for very large-scale modification of the shelf edge and slope morphology.

The Norwegian continental margin provides some excellent examples of subaqueous slide phenomena, and they have been studied in some detail (Bugge et al., 1978; Bugge, 1983). There appears to have been extensive sliding of great antiquity beginning in Early or mid-Tertiary times, with the most recent events being associated with the Storegga slide. Figure 10 is a map of part of

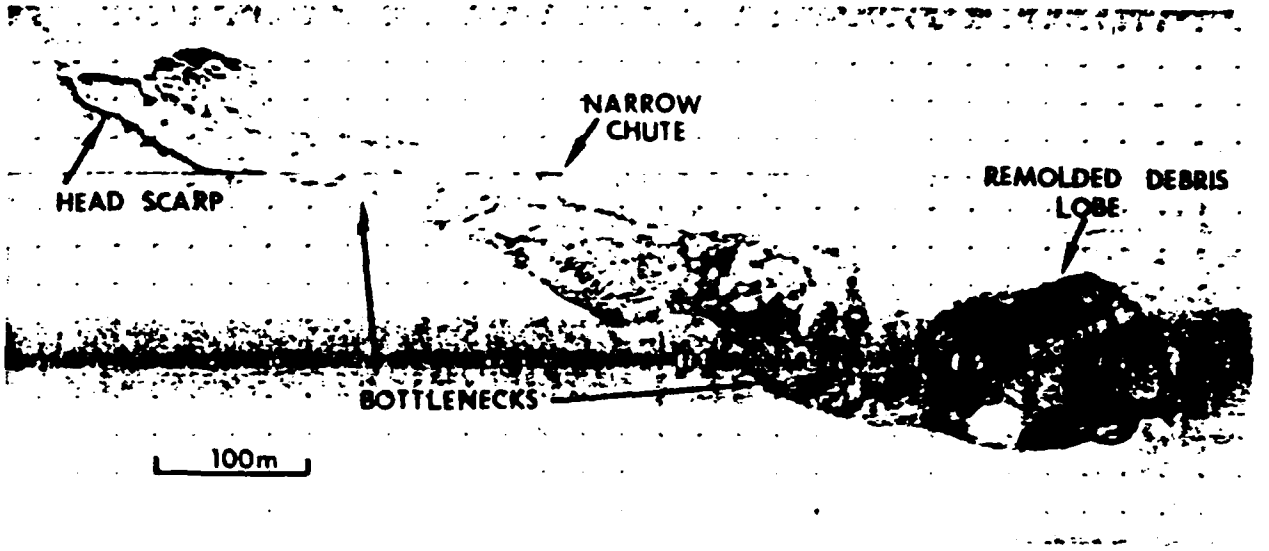

Figure 9. Side-scan sonar mosaic (100 kHz) of a bottleneck slide in the Mississippi Delta region.

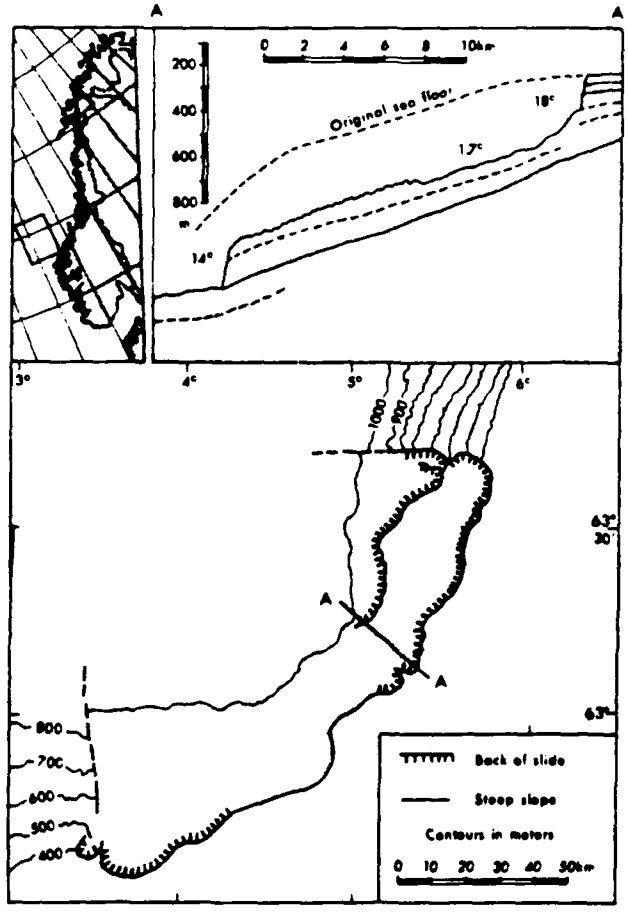

Figure 10. Map and profile of part of the Storegga slide (from Bugge et al., 1978). Recent work by Bugge (1983) has extended the boundaries of this slide and provides greater detail of its morphology.

the Storegga complex redrawn from Bugge et al. (1978). More recent work (Bugge, 1983) has extended the area of the Storegga slide and identified three separate episodes. The first event is believed to have occurred about 11-13,000 years B.P. and moved a volume of 3,880 km^3 of shelf-edge sediment 400 km from the headwall into a water depth of 3,000 m. The second event involved about 450 km^2 of the continental shelf and appears to date from 6,000-7,000 years ago. The last episode of sliding occurred shortly after the second, and together these events displaced a total volume of about 1,700 km^3 of sediment. The entire complex comprises large arcuate head scarps, indenting the shelf break and outer shelf, and extensive deposits of blocky, acoustically semi-transparent debris, which has been transported very considerable distances over very low slope angles.

Such slides (whether shallow of deep-seated) may also play a major role in the creation and evolution of some types of submarine canyons. For example, in the Gulf of Mexico Coleman et al. (1983) documented a large (14-km-wide, >30-km-long) canyonlike failure that involved a sediment thickness of more than 600 m. This retrogressive failure at the shelf edge occurred post 30,000 years B.P., and infilling of the entire canyon was completed by 15,000 years B.P. The rapid filling of the canyon has resulted in low sediment strengths within the fill, and presently large rotational slump faults (contemporaneous faults) are occurring within the area of previous failure. Movement along these present-day failure has created a topographic valley 5-6 km wide and 150 m deep.

Seismic evidence from the Mississippi Canyon (west of the modern Mississippi Delta) indicates that this large canyon (Fig. 11) was created by similar types of failures during the period of the last Pleistocene low sea level. C_{14} dating of the canyon sediments has revealed that it was formed between 25,000 and 20,000 years B.P., involving removal of 1,500-2,000 km^3 of shelf-

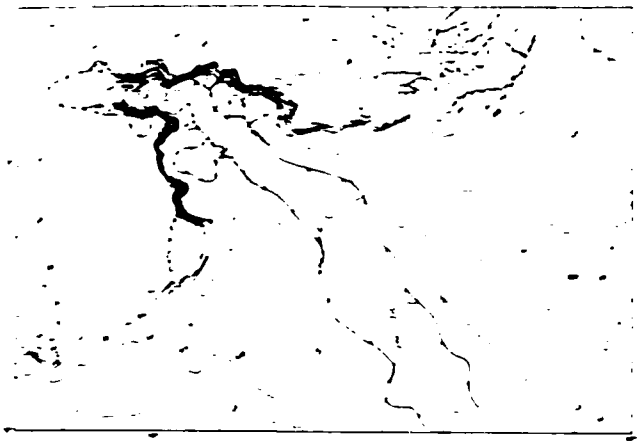

Figure 11. Map of the subsurface geometry of the base of the Mississippi Canyon, which apparently originated as a result of shelf-edge slope instability about 20-25,000 years B.P. Buried shelf-edge slide scar patterns are also shown northeast of the canyon.

edge and upper-slope sediments. The subsurface geometry of the base of the canyon is illustrated in Figure 11, showing the rather elongate trough traversing the upper slope beginning near the shelf break as a complex series of arcuate embayments. Correlation of seismic data, boreholes, and sediment analyses suggests that the canyon formed as a series of retrogressive rotational shelf-edge landslides. Some of the sediments within the base of the present canyon-fill sequence can be related directly back to the arcuate scars along the upper canyon headwall. It is believed that initiation of instability was related to rapid deltaic sedimentation and shelf-edge progradation during the last low sea level (Coleman et al., 1983). Moreover, the instability of the shelf edge and upper slope has resulted in deep-water sedimentation on the Mississippi Fan directly downslope from the canyon. Some of the fan sediments have characteristics consistent with debris flow deposition (Prior et al., 1983), and it is possible that the shelf-edge rotational slides that created the canyon evolved into debris flows as the sediment was displaced downslope into deeper water.

2. Flows

Subaqueous downslope flows of sediment are believed to involve four main processes: Debris flow, liquefaction flow, grain flow, and turbidity flow (Middleton and Hampton, 1976).

Debris flows comprise sediment movements in which clasts may be supported by a matrix that is a mixture of fluid and fine sediment that has a finite yield strength. It is believed that debris flows are significant, large-scale seafloor processes (Hampton, 1970, 1972; Embley, 1976; Jacobi, 1976; Flood et al., 1979).

For example, Embley (1976, 1982) has described the morphology and deposits of a debris flow off the Canary Islands that originated from a source area extending over 18,000 km^2 of sea floor and with a depositional area covering more than

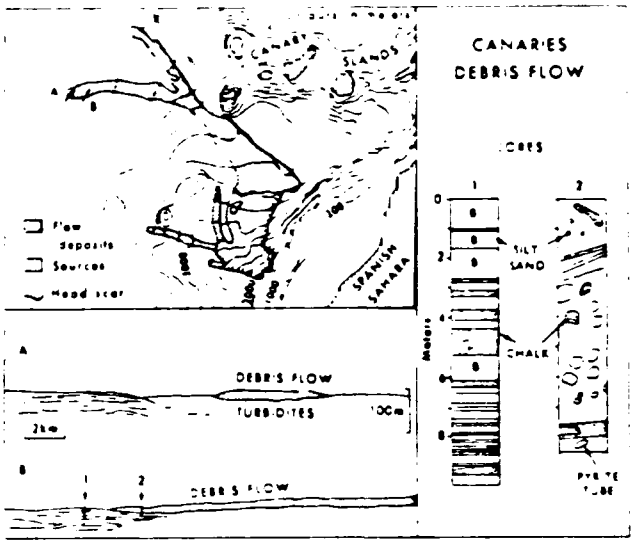

Figure 12. The Canary Island debris flow, morphology, cross-sectional profiles, and core characterisitcs (from Embley, 1976).

30,000 (km^2), with a total flow volume of more than 600 km^3 (Fig. 12). A depression on the sea floor, beginning at a water depth of 1,700 m, continues downslope for almost 200 km, averaging 125 km in width. The downslope deposits are acoustically unstratified and overlie deep-water sediments on the lower continental slope. The debris flow sediments form two elongate "finger-like" lobes that end at a depth of 4,600-4,800 m on slopes of about 0.1°. Cores from the debris flow lobes are distinctive and show irregularly shaped sediment inclusions, folds and angular contacts, and pebbles, described by Embley (1982) as "exotic," derived from shallow-water sources. Dating of the sediments overlying the debris flow indicates that it took place between 16,000 and 17,000 years B.P. However, there is also evidence that the debris flow was a multiphase event, with the latest sediment movements occurring as recently as 1,000-2,000 years ago.

Similar sediment flow phenomena have been documented off the Mississippi Delta, forming one component of a suite of slope instability features ranging from collapse depressions to bottleneck slides/flows, shallow translation and rotational slides, and elongate retrogressive mudslides and mudflows (Shepard, 1955; Terzaghi, 1956; Garrison, 1974; Coleman and Garrison, 1977; Prior and Coleman, 1978; Coleman et al., 1980; Prior and Coleman, 1982). Figure 13 illustrates part of the delta-front slope seaward of South Pass, where shallow-water areas are dominated by small collapse and bottleneck features and where large areas of the delta-front slope in 80- to 150-m water depths are dissected by elongate mudflow chutes and gullies. At the downslope (seaward) ends of the gullies there are extensive areas of irregular bottom topography composed of blocky debris discharged from the gullies. The deposits form complex systems of overlapping lobes or fans. Individual lobe thicknesses vary greatly, but locally the total thickness of superimposed lobes can achieve more

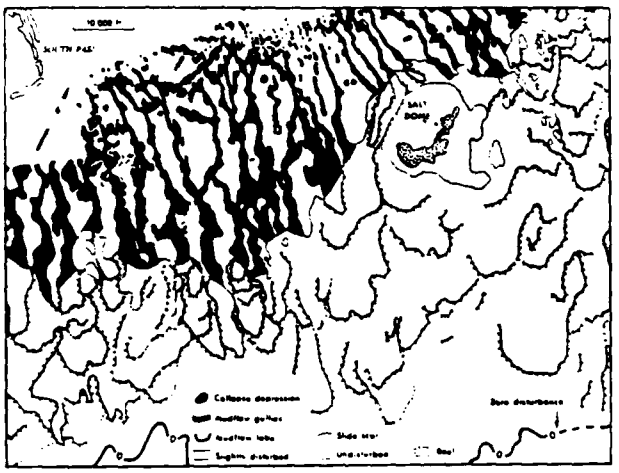

Above:
Figure 13. Map of part of the subaqueous slope off South Pass, Mississippi Delta, illustrating the profusion of collapse depressions, mudflow/mudslide gullies, and depositional lobes in the area.

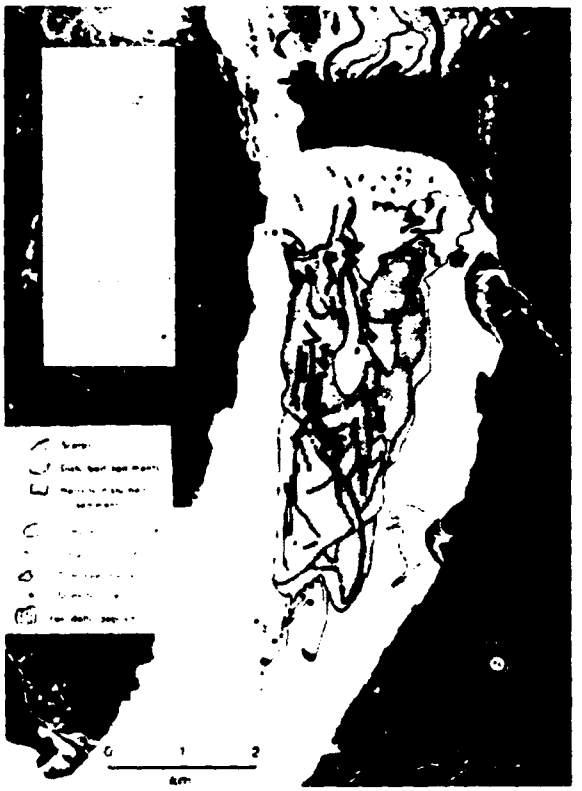

Right:
Figure 14. The morphology of the subaqueous landslide at Kitimat, British Columbia, an example of fjord-head slope instability processes.

than 40 m. The mudflow gullies and lobes are extremely active, and movement rates of several hundred metres/year have been recorded. Repeated sonar surveys have shown that individual debris lobes may prograde more than 1,000 m/yr into deeper water. Shorter term displacements have also been documented. For example, during winter storms in the delta region in January 1983, debris movement over distances of 150-250 m damaged sea-floor pipelines.

Other examples of active subaqueous slope instability have been found in fjord environments (e.g., Terzaghi, 1956; Karlsrud and Edgers, 1982), and in some cases these sediment movements appear to be complex combinations of sliding and debris flow processes (Prior et al., 1982a, b).

The Kitimat event (Fig. 14), which took place in a British Columbia fjord in 1975, involved failure of fjord-head delta sediments and mobilization of fjord bottom sediments for a distance of more than 5 km from the delta front. Deformational mechanisms include delta-front shallow rotational sliding, downslope shearing, and flowing, resulting in considerable remolding of the fjord bottom sediments and distal block gliding over weak high-water-content fjord sediments (Prior et al., 1982a, b; Prior et al., in preparation). Toward the outer margins of the debris flow, there are numerous closely spaced arcuate ridges and shallow troughs (Fig. 15A, B), which are arranged parallel and subparallel to one another. The ridges are believed to be the results of compressional forces as the debris flow prograded. Throughout the debris lobe, which moved downslope on a slope of 0.4°, there are elongate longitudinal shear planes arranged parallel to the direction of maximum movement. At the downslope outer margins of the debris lobe hummocky accumulations of large blocks of sediment are arranged in a broadly lobate form (Fig. 15C). In addition, quite large blocks of sediment are found beyond the downslope limits of the debris lobe. These blocks, which have individual volumes of 30-35,000 m^3, appear to have detached from the front of the lobe and continued to slide downfjord for distances of more than 1 km.

Liquefaction flows occur when loosely packed coarse-grained sediment collapses, the grains temporarily lose contact with each other, and the particle weight is transferred to the pore water. Liquefaction can occur as a result of disturbance by other slope instability processes or of application of stresses to loosely packed sediments. Terzaghi (1956) accounts for various subaqueous instabilities in terms of liquefaction, including the flowslides in sand off Zeeland described by Koppejan et al. (1948). Active liquefaction of sands and silts on the shelf near the Klamath Delta, northern California, was recently described by Field and Hall (1982) and Field et al. (1982). The mechanisms, interpreted from spectacular sonographs, include liquefaction, lateral spreading, and sediment collapse and flowage. Lateral spreading was inferred from a nearly continuous toe ridge bounding a failure terrace and from pressure ridges seaward of the failure zone. Liquefaction was indicated by the presence of sand boils and collapse features, and overlapping lobes suggested fluidization as part of the failure processes.

Grain flows comprising downslope sediment movement of loose individual sediment grains have been observed by Dill (1966) and Shepard and Dill (1966), particularly sand flows on the margins of

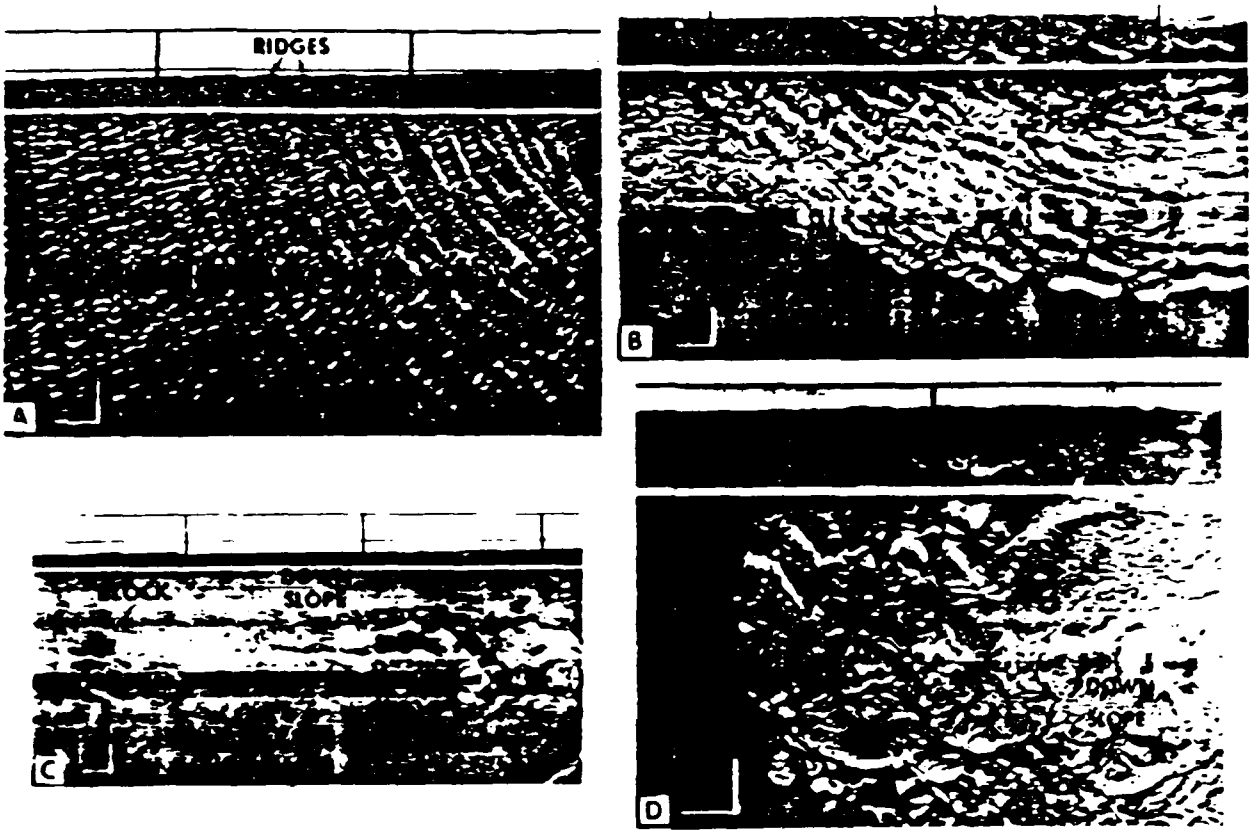

Figure 15. Side-scan sonar images of parts of the Kitimat landslide (from Prior et al., 1982a).

submarine canyons. In part, grain flows may be associated with weathering and local rockfall processes on subaqueous outcrops. For example, Dill (1966) recorded sand falls along canyon sidewalls. Many carbonate reefs and subaqueous outcrops have steep slopes and talus-like accumulations of debris, ranging in size from coarse sands to large boulders at their base, suggesting free-fall, rolling, or grain-flow processes.

FACTORS RESPONSIBLE FOR INITIATION OF LANDSLIDES

Subaqueous slope failure thresholds appear to be the result of a complex interaction of variables rather than any single factor. Moreover, the inaccessibility of subaqueous slopes and sediments means that measurement of parameters for stability analysis is technically demanding. New methods have been developed for the measurement of subaqueous sediment strength properties, and they are being increasingly applied. In situ tests down boreholes or using core penetrometers (e.g., Hampton et al., 1982) are being supplemented by a variety of tools mounted on manned submersibles (e.g., Lambert, 1982). In order to assess the strength properties of gassy subaqueous sediments, techniques have been developed to test samples maintained at their in situ subaqueous pressures (Johns et al., 1982). Also, piezometer probes have been employed to measure effective stress conditions in submarine sediments in order to assess stability (e.g., Bennett et al., 1982). However, Karlsrud and Edgers (1982) conclude that, while analytical methods for analysis of subaqueous slides are well developed, a major uncertainty is still the determination of the appropriate sediment parameters before and leading to failure. They conclude that very few slides are sufficiently well documented to be very instructive and that there is a great need for detailed case studies. Therefore, much of the information concerning the initiation of subaqueous slides is somewhat circumstantial, but it is also apparent that certain environmental/geologic conditions favor instability. Figure 16 illustrates some of the factors that appear to be associated with subaqueous slope instability and attempts to show how they may interact to increase stresses or to lower sediment strength.

1. Stresses

There are various ways in which stresses may become sufficient for failure even though gravitational stresses caused by the slope are relatively small. Stresses on sediments can be increased by the following processes.

Crustal Tectonics

In areas of active crustal tectonism, bottom slope angles can be increased by upwarping, diapirism, and faulting. Such areas are also characterized by active seismicity and large earthquakes. Large slides found in subduction zone

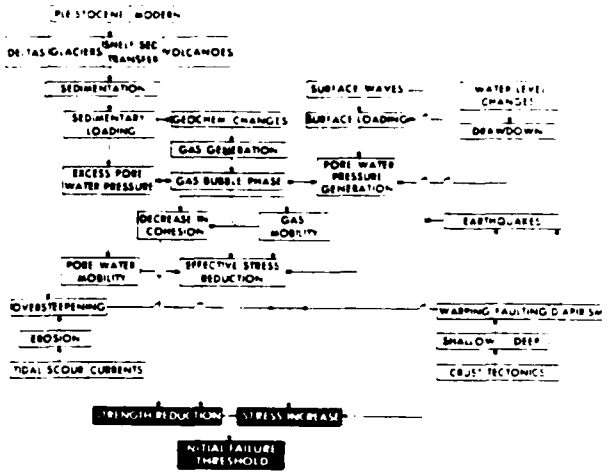

Figure 16. Factors that are associated with the initiation of subaqueous landslides.

margins are those described by Ross and Shor (1965), Moore et al. (1976), and Shepherd et al. (1973). Also, Almagor and Wiseman (1977), using stability analysis techniques and the limit equilibrium approach, cite tectonic warping as a factor in initiating slides in the eastern Mediterranean.

Earthquakes cause application of horizontal and vertical acceleration stresses. Pore water pressure changes can also occur within the sediments owing to intensive cyclic loading. A direct link between earthquakes and submarine slope instability is widely accepted, and there are several well-documented events (Heezen and Ewing, 1952, 1955; Houtz, 1962; Coulter and Migliaccio, 1966; Ryan and Heezen, 1965; Reimnitz, 1972). Morgenstern (1967) noted that many cases of failure accompanied earthquakes of >6.5 (Richter scale), and proposed a stability analysis model.

Hampton et al. (1978) used an effective stress approach to examine the combined effects of earthquake-related pore pressure changes and direct loading effects of acceleration. This procedure was used to explain slides in the Gulf of Alaska (Hampton et al., 1978).

Also, the features described by Field et al. (1982) and Field and Hall (1982) off the Klamath Delta, northern California, appear to have been caused by a major offshore earthquake in the region in 1980. The earthquake was of large magnitude (6.5 M_L-7.2 M_S) and induced liquefaction on slopes of 0.25°. Local fishermen noticed ridges and scarps on the normally flat sea floor immediately after the earthquake.

Current Scour

Localized sea-floor erosion by current action, particularly in shallow water, is a well-known process. Also, currents in canyons are capable of significant sea-floor scour and sediment transport (Shepard et al., 1974; Inman et al., 1976). Slope oversteepening undoubtedly accompanies these processes, but their undermining effects on local slope stability have yet to be determined.

Surface Water Waves

In shallow-water nearshore and shallow shelf regions the passage of large surface water waves applies hydraulic forces to the sea floor. Watkins and Kraft (1978) cite large storm waves inducing pressures of up to 70 kN/m^2 in water depths of 60 m and suggest that surface waves may affect bottom stability in water depths to 150 m. Henkel (1970) determined theoretically that waves impose oscillatory motion on loose sediments sufficient to cause downslope movement. Hampton et al. (1978) used Henkel's methods to explain submarine sliding off the Malaspina Glacier, Alaska. In a series of experiments in the Mississippi Delta region (SEASWAB), bottom-mounted accelerometers and pressure sensors were used to measure wave effects directly (Suhayda et al., 1976; Dunlap et al., 1979). Both bottom sediment perturbation and cyclic loading pore pressure increases were detected.

Sedimentation

Rapid sedimentation in offshore delta areas and canyon heads causes slope oversteepening. Sands deposited in canyon heads accumulate until the angle of repose is exceeded and failure takes place (Shepard, 1932, 1933; Heezen, 1956). Instability in the Mississippi Delta region may be related in part to oversteepening of bar-front slopes during progradation (Coleman et al., 1974). Also, on the slopes of many basins, sediment loading has resulted in diapirism. Diapiric structures are often several square kilometres in area and 300-500 m high. Continued vertical movement of diapirs causes oversteeping of adjacent slopes and recently deposited sediments and contributes to their failure. The slide feature illustrated in Figure 5A is situated on the flanks of a diapir on the continental slope of the Gulf of Mexico.

2. Sediment Strength

Following the principle of effective stress, sediment strength can be reduced by generation of interstitial pore water and pore gas pressures.

Sedimentary Loading

Many marine environments are (or have been) subject to rapid rates of sedimentation. Prograding deltas, glacier margins, slopes of active volcanoes, and site-specific shelf locations where sediment is concentrated all may be situations where excess pore pressures can develop. Terzaghi (1956) described the principle in which excess hydrostatic pressures can be developed by rapid sedimentation and used the concept to explain various submarine failures. Prior and Suhayda (1979) used infinite slope analysis to calculate pore pressures needed for failure of Mississippi Delta sediments. While large pore pressures are necessary, the calculated values are consistent with the results of in situ piezometer measurements (Dunlap et al., 1979).

Cyclic Loading by Waves

The SEASWAB experiment measured the effects of winter storms and hurricanes on pore pressures (Suhayda et al., 1976; Suhayda, 1977; Dunlap et al., 1979). Significant ambient pore pressures were measured, and sharp increases accompanied storm passage.

Pore Gas Generation

Many marine sediment/water systems are influenced by internal geochemical and bacteriological processes, which lead to the generation of pore gases, particularly methane. When gas amounts are sufficiently large at a particular pore water pressure, the dissolved gas will change to the bubble phase (Whelan et al., 1975, 1976, 1978). The exact effects of gas bubble formation on interparticle cohesion and friction are not known, but are believed to reduce sediment strength substantially. Certainly the association between gassy sediments and subaqueous instability is striking.

Tidal Water Level Changes

Some nearshore and intertidal areas experience sediment slope failure that is apparently related to water level fluctuations. A number of authors have noted that failures accompany extremely low tides (Koppejan et al., 1948; Terzaghi, 1956; Wells et al., 1980; Karlsrud and Edgers, 1982). The concept is that seepage pressures and elevated pore water pressures develop with ebbing tide in a manner similar to drawdown, which causes river bank instability.

In particular, Karlsrud and Edgers (1982) show that many fjord slope failures occurred at times of low tide and also often accompanied the emplacement of manmade fills along the coastline. The Kitimat, British Columbia, event also took place in similar circumstances. The failure of the delta-front slope occurred about one hour after an unusually low tide, and there had been construction activity along the coast in the previous few months (Prior et al., 1982a, b).

Figure 16 attempts to depict the way in which the critical strength/stress disequilibrium can be achieved. It is apparent that individual failure thresholds can be achieved by quite different combinations of factors. Clearly, the worst conditions are where two or more factors combine. Areas in which large excess pore water pressures, caused by sedimentation and wave effects, combine with bubble gas in the sediments and active seismic shocks are likely to be extremely unstable. This description applies almost exactly to areas of the Gulf of Alaska, where many submarine instabilities have been recorded (Reimnitz, 1972; Carlson and Molnia, 1977; Hampton et al., 1978).

STATE OF THE ART SUMMARY

Some aspects of the present state of knowledge concerning subaqueous landslides can be summarized as follows:

1. A very large number of localities (worldwide) have been identified, using various criteria, that appear to have been affected by subaqueous landsliding. Schwarz (1982) provides a listing of some 286 examples from both marine and lacustrine environments.

2. Modern high-resolution geophysical techniques are proving extremely effective in defining locations and characteristic geometries of landslide features, although different acoustic systems provide different degrees of detail.

3. The interpretation of acoustic data must be approached with care, and its successful use depends upon the amount of data coverage and line orientations with respect to feature geometry. Process inferences from remote sensing data are also dependent upon the end products of complex instability and deformational mechanisms.

4. Landsliding, on both continental shelves and slopes, is responsible for a wide range of distinctive erosional morphology, including some types of canyons. Long-distance downslope sediment transport results in deposition of shallow-water sediments in deep-water settings.

5. The magnitude of individual subaqueous landslides is remarkable; the volumes of sediment mobilized by slope instability events matches or exceeds that of many terrestrial landslides. For example, the largest known (prehistoric) slide on land, at Saidmerreh, Iran, has a volume of 20 km^3, considerably smaller than the Storegga slide. Also, the Sherman Glacier landslide, Alaska, is about half the volume of the Kitimat landslide.

6. Subaqueous landslides occur on much lower slope angles than most terrestrial types. Slope instability under water appears to be common on slope angles of 5° or less, and many examples are known on slopes of less than 1°. Moreover, once initiated, sediment movement can continue for very long distances over areas that are virtually flat.

7. Some landslides are of ancient origin, and some appear to date from periods of Pleistocene lower sea levels, when shelf-edge progradation was occurring. However, the age of many relict landslide systems has not been determined, and this comprises a significant gap in knowledge.

8. Active landsliding is known from various geologic environments, for example off modern deltas, in fjords, and in earthquake-prone regions. Initiation of instability is associated with a variety of factors, including rapid deposition of low-strength sediments; sediments with large accumulations of pore gases; oversteepening owing to sedimentation/scour/crustal tectonism, diapirism, and faulting; earthquake shocks; storm-generated surface waves; tidally induced drawdown; or coastal construction.

9. The quantification of precise cause/effect relationships is difficult owing to problems of defining appropriate sediment strength parameters, assessing original sea-floor geometries, and the immense scale and remoteness of the processes.

10. Classification of subaqueous landslide types is based primarily on feature geometry and sediment properties from cores. It is widely recognized that there is a continuum of processes from various types of slides to flows of different viscosities, often within the same event. However, precise modes of deformation and downslope transport are largely inferred, and information is generally lacking on velocities and geometries of moving debris. The velocities of a few subaqueous failures have been calculated (e.g., Orkdalsfjord, 25 km/hr, Bjerrum, 1971).

11. Subaqueous landsliding is significant eco-

nomically. Increased use of offshore environments for hydrocarbon production, mining, waste disposal, communication, and defense surveillance systems means that sea-floor installations can be at risk from active landsliding and must be located and designed to minimize damage. Repair of damage or replacement can be extremely costly. Preventative engineering is requiring improved geological and geotechnical perspectives on underwater landsliding processes for prediction of magnitudes, frequencies, mechanisms, and applied stresses.

REFERENCES

Almagor, G., and Wiseman, G. (1977). Analysis of submarine slumping in the continental slope off the southern coast of Israel: Marine Geotechnology (2), 349-388.

Bea, R.G. (1971). How sea floor slides affect offshore structures: Oil and Gas Journal (November), 88-92.

Bea, R.G., and Audibert, J.M.E. (1980). Offshore platforms and pipelines in Mississippi River delta: Journal of Geotechnical Engineering Division (106), GT8, 853-869.

Bennett, R.H., Burns, J.T., Clarke, T.L., Faris, J.R., Forde, E.B., and Richards, A.F. (1982). Piezometer probes for assessing effective stress and stability in submarine sediments, in (Saxov, S., and Nieuwenhius, J.K., eds.) Marine Slides and Other Mass Movements: Plenum Press, New York and London (6), 129-162.

Bjerrum, L. (1971). Subaqueous slope failures in Norwegian fjords: Norwegian Geotechnical Institute Bulletin (88), 8 pp.

Bugge, T., Reidar, L.L., and Rokoengen (1978). Quaternary deposits off More and Trondlag, Norway: seismic profiling: Continental Shelf Inst., Trondheim, Norway, Pub. 99, 55 pp.

Bugge, T. (1983). Submarine slides on the Norwegian continental margin, with special emphasis on the Storegga area: Continental Shelf Inst., Norway, Pub. 10, 152 pp.

Carlson, P.R., and Molnia, B.F. (1977). Submarine faults and slides on the continental shelf, northern Gulf of Alaska: Marine Geotechnology (2), 275-290.

Carlson, P.R., Karl, H.A., and B.D. Edwards (1982). Puzzling mass movement features in the Navarinsky Canyon Head, Bering Sea: Geo-Marine Letters (2), 3/4, 123-127.

Coleman, J.M., and Garrison, L.E. (1977). Geological aspects of marine slope stability, northwestern Gulf of Mexico: Marine Geotechnology (2), 9-44.

Coleman, J.M., and Prior, D.B. (1983). Deltaic environments of deposition: American Association of Petroleum Geologists Memoirs, No. 31, pp. 139-178.

Coleman, J.M., Prior, D.B., and Garrison, L.E. (1980). Subaqueous sediment instabilities in the offshore Mississippi River delta--explanation of maps: Bureau of Land Management Report 80-01, New Orleans, La., 60 pp.

Coleman, J.M., Suhayda, J.N., Whelan, T., and Wright, L.D. (1974). Mass movement of Mississippi River delta sediments: Transactions Gulf Coast Association of Geological Societies (24), 49-68.

Coleman, J.M., Doyle, E.H., and Prior, D.B. (1982). East Coast Hazards Observation (ECHO) Program - Deep-water geologic surveying for platform siting: Proc. Offshore Technology Conference, Paper 4171, 61-72, Houston, Texas.

Coulter, H.W., and Migliaccio, R.R. (1966). Effects of the earthquake of March 27, 1964, at Valdez, Alaska: U.S. Geological Survey Professional Paper 542-C.

Dill, R. F. (1966). Sand flows and sand falls, in (Fairbridge, R.W., ed.) Encyclopedia of Oceanography: Reinhold, New York, pp. 763-765.

Dingle, R.V. (1977). The anatomy of a large submarine slump on a sheared continental margin (southeast Africa): Journal of the Geological Society (134), 3, 293-310.

Dott, R.H. (1963). Dynamics of subaqueous gravity depositional processes: Bulletin American Association of Petroleum Geologists (47), 104-128.

Dugan, J. (1967). Taxis to the deep, in (Dugan, J., Cowen, R.C., Barada, B., Marden, L., and Crum, R. M.) World Beneath the Sea: National Geographic Society, 143-163.

Dunlap, W.A., Bryant, W.R., Williams, G.N., and Suhayda, J.N. (1979). Storm wave effects on deltaic sediments--results of SEASWAB I and II: Proc. POAC (2), 899-920.

Embley, R.W. (1976). New evidence for occurrence of debris flow deposits in the deep sea. Geology (4), 371-374.

Embley, R.W. (1982). Anatomy of some Atlantic margin sediment slides and some comments on ages and mechanisms, in (Saxov, S., and Nieuwenhuis, J.K., eds.) Marine Slides and Other Mass Movements: Plenum Press, New York and London (6), 189-213.

Field, M.E., and Hall, R.K. (1982). Sonographs of submarine sediment failure caused by the 1980 earthquake off northern California: Geo-Marine Letters (2), 3/4, 135-141.

Field, M.E., Gardner, J.V., Jennings, A.E., and Edwards, B.D. (1982). Earthquake induced sediment failures on a 0.25° slope, Klamath River delta, California: Geology (10), 542-546.

Flood, R.D., Hollister, C.D., and Lonsdale, P. (1979). Description of the Feni sediment drift by debris flows from Rockall Bank: Marine Geology (32), 3/4, 311-335.

Garrison, L.E. (1974). The instability of surface sediments on parts of the Mississippi delta front: U.S. Geological Survey Open File Report 74-4, 18 pp., 3 maps.

Geo-Marine Letters (2), 3/4, 111-292, September-December 1982.

Hampton, M.A. (1970). Subaqueous debris flow and generation of turbidity currents: Unpublished Ph.D. dissertation, Stanford University, Stanford, California.

Hampton, M.A. (1972). The role of subaqueous debris flow in generating turbidity currents: Journal of Sedimentary Petrology (42), 775-793.

Hampton, M.A., Bouma, A.H., Sangrey, D.A., Carlson, P.R., Molnia, B.M., and Clukey, E.C. (1978). Quantitative study of slope instability in the Gulf of Alaska: Proc. Offshore Technology Conference, Paper 3314, 2307-2318, Houston, Texas.

Hampton, M.A., Lee, H.J., and Beard, R.M. (1982). Geological interpretation of cone penetrometer tests in Norton Sound, Alaska: Geo-Marine Letters (2), 3/4, 223-230.

Heezen, B.C. (1956). Corrientes de turbidez del Rio Magdalena: Bol. Soc. Geog. Colombia (51-52), 135-143.

Heezen, B.C., and Drake, C.L. (1964). Grand Banks slump: Bulletin American Association of Petroleum Geologists (48), 2, 221-233.

Heezen, B.C., and Ewing, M. (1952). Turbidity currents and submarine slumps and the 1929 Grand Banks earthquake: American Journal of Science (250), 849-873.

Heezen, B.C., and Ewing, M. (1955). Orleansville earthquake and turbidity currents: Bulletin American Association of Petroleum Geologists (39), 2505-2514.

Henkel, D.J. (1970). The role of waves in causing submarine landslides: Geotechnique (20), 75-80.

Houtz, R.E. (1962). The 1953 Suva earthquake and tsunami: Bulletin Seismic Society of America (52), 1-12.

Inman, D.L., Nordstrom, C.E., and Flick, R.E. (1976). Currents in submarine canyons, an air-sea-land interaction, in (Van Dyke, M., Vincenti, W.G., and Wehausen, J. V., eds.) Annual Reviews of Fluid Mechanics (8), 275-310.

Jacobi, R.D. (1976). Sediment slides on the northwestern continental margin of Africa: Marine Geology (22), 3, 157-173.

Johns, M.W., Taylor, E., and Bryant, W. R. (1982). Geotechnical sampling and testing of gas-charged marine sediments at in situ pressures: Geo-Marine Letters (2), 3/4, 231-236.

Kenyon, N.H., Belderson, R.H., and Stride, A.H. (1978). Channels, canyons and slump folds on the continental slope between south-west Ireland and Spain: Oceanologica Acta (1), 3, 369-380.

Kidd, R.B. (1982). Long-range sidescan sonar studies of sediment slides and the effects of slope mass sediment movement on abyssal plain sedimentation, in (Saxov, S., and Nieuwenhuis, J.K., eds.) Marine Slides and Other Mass Movements: Plenum Press, New York and London (6), 269-303.

Karlsrud, K., and Edgers, L. (1982). Some aspects of submarine slope stability, in (Saxov, S., and Nieuwenhius, J.K., eds.) Marine Slides and Other Mass Movements: Plenum Press, New York and London (6), 61-81.

Koppejan, A.W., van Wamelan, B.M., and Weinberg, L.J.H. (1948). Coastal flow slides in the Dutch province of Zeeland: Proc. Conference on Soil Mechanics and Foundation Engineering (5), 89-96, Rotterdam.

Lambert, D. N. (1982). Submersible mounted in situ geotechnical instrumentation: Geo-Marine Letters (2), 3/4, 209-214.

McGregor, B.A., Twichell, D.C., and Ryan, W.B.F. (1981). Side-scan sonar images of the continental slope around Wilmington Canyon off the eastern United States (abst.): American Association of Petroleum Geologists.

Middleton, G.V., and Hampton, M.A. (1976). Subaqueous sediment transport and deposition of sediment gravity flows, in (Stanley, D.J., and Swift, D.J.P., eds.) Marine Sediment Transport and Environmental Management: John Wiley, New York, 197-218.

Milne, J. (1897). Suboceanic changes: Geographical Journal (10), 129-146, 259-289.

Moore, D.G. (1977). Submarine slides, in (Voight, B., ed.) Rockslides and Avalanches, vol. 1, Natural Phenomena: Developments in Geotechnical Engineering (14A), 563-604.

Moore, D.G., Curray, J. R., and Emmel, F.J. (1976). Large submarine slide (Olistostrome) associated with Sunda arc subduction zone, northeast Indian Ocean: Marine Geology (21), 211-226.

Moore, J. G. (1964). Giant submarine landslides on the Hawaiian ridge: U.S. Geological Survey Professional Paper 501D, 95-98.

Morgenstern, R.N. (1967). Submarine slumping and the initiation of turbidity currents, in (Richards, A., ed.) Marine Geotechnique: University of Illinois Press, Urbana, Ill., 189-220.

Murty, T.S. (1979). Submarine slide-generated water waves in Kitimat Inlet, British Columbia: Journal of Geophysical Research (84), C12, 7777-7779.

Noda, E.K. (1983). Effects of Hurricane Iwa, November 23, 1982, offshore of Kahe Point, Oahu: Special report prepared by Noda, E.K., and Associates, Honolulu, Hawaii.

Prior, D.B., and Coleman, J.M. (1978). Submarine landslides on the Mississippi River delta-front slope: Geoscience and Man, Louisiana State University, Baton Rouge (19), 41-53.

Prior, D.B., and Coleman, J.M. (1979). Submarine landslides - geometry and nomenclature: Zeitschrift fur Geomorphologie (23), 4, 415-426.

Prior, D.E., and Coleman, J.M. (1982). Active slides and flows in underconsolidated marine sediments on the slopes of the Mississippi Delta, in (Saxov, S., and Nieuwenhuis, J.K., eds.) Marine Slides and Other Mass Movements: Plenum Press, New York and London (6), 21-49.

Prior, D.E., and Coleman, J.M. (1983). Lateral movements of sediments: Ocean Science and Engineering (6), 2, 113-155.

Prior, D.E., and Doyle, E.H. (1984). Geological hazard surveying for exploratory drilling in water depths of 2000 meters: Proc. Offshore Technology Conference, Paper 4747, Houston, Texas.

Prior, D.E., and Suhayda, J.N. (1979). Application of infinite slope analysis to submarine sediment instabilities, Mississippi Delta: Engineering Geology (14), 1-10.

Prior, D.E., Coleman, J.M., and Carey, P.L. (1979). Sea floor mapping using microcomputer assisted side-scan sonar: 13th Remote Sensing Symposium, Ann Arbor, Michigan.

Prior, D.E., Bornhold, B.D., Coleman, J.M., and Bryant, W.R. (1982a). Morphology of a submarine slide, Kitimat Arm, British Columbia: Geology (10), 588-592.

Prior, D.E., Coleman, J.M., and Bornhold, B.D. (1982b). Results of a known seafloor instability event: Geo-Marine Letters (2), 3/4, 117-122.

Prior, D.E., Coleman, J.M., and Doyle, E.H. (1984). Antiquity of the continental slope, U.S. middle-Atlantic margin: Science (223), 926-928.

Prior, D.E., Adams, C.E., and Coleman, J.M. (1983). Characteristics of a deep-sea channel on the middle Mississippi Fan as revealed by a high-resolution survey: Trans. Gulf Coast Assoc. Geological Societies (33), 389-394.

Prior, D.E., Bornhold, B.E., and Johns, M.W. (in preparation). Depositional characteristics of a submarine debris flow.

Reimnitz, E. (1972). Effects of the Copper River delta: the Great Alaska Earthquake of 1964, in Oceanography and Coastal Engineering: National Academy of Sciences, Washington, D.C. (ISBN 0-309-1605-3), 290-302.

Rott, J., Hampson, J., Hampson, J., Jr., and Twichell, D. (1981). Geomorphology and sediment stability of a segment of the U.S. continental slope off New Jersey: Science (211), 935-937.

Ross, D. A., and Shor, G. G. (1965). Reflection profiles across the Middle America trench: Journal of Geophysical Research (70), 5551-5571.

Ryan, W.B.F., and Heezen, B.C. (1965). Ionian Sea submarine canyons and the 1908 Messina turbidity current: Bulletin Geological Society of America (76), 915-932.

Ryan, W.B.F. (1982). Imaging of submarine landslides with wide-swath sonar, in (Svend, S., and Nieuwenhuis, J. K., eds.) Marine Slides and Other Mass Movements: Plenum Press, New York and London (6), 175-186.

Saxov, S., and Nieuwenhuis, J.K. (1982). Marine slides and other mass movements: Plenum Press, New York and London (6), 353 pp.

Schwarz, H.-U. (1982). Subaqueous slope failures - experiments and modern occurrences, in (Fuchtbauer, H., Lisitzyn, A.P., Milliman, J.D., and Seibold, E., eds.) Contributions to Sedimentology: E. Schweizerbart'sche Verlags buchandlung, Stuttgart, 116 pp.

Shepard, F.F. (1932). Landslide modifications of submarine valleys: Transactions American Geophysical Union (13), 226-230.

Shepard, F.F. (1933). Depth changes in Sagami Bay during the great Japanese earthquake: Journal of Geology (41), 527-536.

Shepard, F.F. (1955). Delta front valleys bordering the Mississippi distributaries: Bulletin Geological Society of America (66), 1489-1498.

Shepard, F.F., and Dill, R.F. (1966). Submarine canyons and other sea valleys: Rand McNally, Chicago, 381 pp.

Shepard, F.F., Marshall, N.G., and McLoughlin, P.A. (1974). Currents in submarine canyons: Deep-Sea Research (21), 691-706.

Shepherd, G.L., Kipperman, L.K., and Moberly, R. (1973). Shallow crustal structure of the Peruvian continental margin: Geological Society of America, Abstracts with Programs (5), 103.

Skempton, A.W., and Hutchinson, J.N. (1969). Stability of natural slopes and embankment foundations: Proc. 7th Conference on Soil Mechanics and Foundation Engineering, State-of-the-Art Volume, 291-340, Mexico City.

Sterling, G.H., and Strohbeck, E.E. (1973). The failure of the South Pass 70 "B" platform in Hurricane Camille: Proc. Offshore Technology Conference, Paper 1898, 719-730, Houston, Texas.

Stride, A.H., Curray, J.R., Moore, D.G., and Belderson, R.H. (1969). Marine geology of the Atlantic margin of Europe: Philosophical Transactions, Royal Society of London (A264), 31-75.

Suhayda, J. N. (1977). Surface waves and bottom sediment response: Marine Geotechnology (2), 135-146.

Suhayda, J. N., Whelan, T., Coleman, J.M., Booth, J.S., and Garrison, L.E. (1976). Marine sediment instability: interaction of hydrodynamic forces and bottom sediments: Proc. Offshore Technology Conference, Paper 2426, 29-40, Houston, Texas.

Terzaghi, K. (1956). Varieties of submarine slope failures: Proc. 8th Texas Soil Mechanics and Engineering Conference, 1-41.

Varnes, D.J. (1975). Slope movements in the western United States, in (Yatsu, E., Ward,

A.J., and Adams, F., eds., Mass Wasting: 4th Guelph Symposium on Geomorphology, 1-17.

Watkins, D.J., and Kraft, L.M. (1978). Stability of continental shelf and slope off Louisiana and Texas: geotechnical aspects, in Bouma, A.D., Moore, G.T., and Coleman, J.M., eds.) Framework, Facies, and Oil Trapping Characteristics of the Upper Continental Margin: American Association of Petroleum Geologists (7), 267-286.

Wells, J.T., Prior, D.B., and Coleman, J.M. (1980). Flowslides in muds on extremely low angle tidal flats, northeastern South America: Geology (8), 272-275.

Whelan, T., Coleman, J. M., Suhayda, J. N., and Garrison, L.E. (1975). The geochemistry of Recent Mississippi River delta sediment: gas concentration and sediment stability: Proc. Offshore Technology Conference (3), 71-84, Houston, Texas.

Whelan, T., Coleman, J.M., Roberts, H.H., and Suhayda, J.N. (1976). The occurrence of methane in Recent deltaic sediments and its effect on soil stability: International Association of Engineering Geologists Bulletin (14), 55-64.

Whelan, T., Ishmael, J.T., and Rainey, G.B. (1978). Gas-sediment interaction in Mississippi Delta sediments: Proc. Offshore Technology Conference, Paper 3166, 1029-1033, Houston, Texas.

Wilhelm, O., and Ewing, M. (1972). Geology and history of the Gulf of Mexico: Bulletin Geological Society of America 83), 575-600.

Coastal Studies Institute
Louisiana State University
Baton Rouge, LA 70803-7527

Technical Report No. 404

EFFECT OF COLD-AIR ADVECTION ON INTERNAL BOUNDARY-LAYER DEVELOPMENT OVER WARM OCEANIC CURRENTS

S. A. Hsu

Dynamics of Atmospheres and
Oceans, 8 (1984) 307-319.

Office of Naval Research
Contract No. N00014-83-C-0150
Project No. NR 388 002

Dynamics of Atmospheres and Oceans, 8 (1984) 307–319
Elsevier Science Publishers B.V., Amsterdam – Printed in The Netherlands

EFFECT OF COLD-AIR ADVECTION ON INTERNAL BOUNDARY-LAYER DEVELOPMENT OVER WARM OCEANIC CURRENTS

S.A. HSU

Coastal Studies Institute, Louisiana State University, Baton Rouge, LA 70803-7527 (U.S.A.)

ABSTRACT

Hsu, S.A., 1984. Effect of cold-air advection on internal boundary-layer development over warm ocean currents. Dyn. Atmos. Oceans, 8: 307–319.

Field experiments have shown that an internal boundary layer (IBL) can develop when the wind blows perpendicularly from the cold-water side of a warm oceanic current to the warmer side. The height of this IBL downwind from the thermal front as computed by an equation originally developed by Venkatram is in excellent agreement with observations.

1. INTRODUCTION

Significant atmospheric and oceanographic differences have often been observed in the region lying on either side of an oceanic front with a sharp

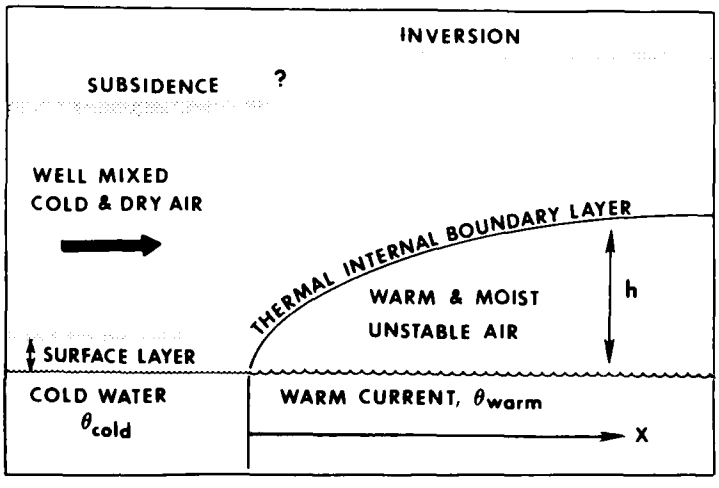

Fig. 1. Schematic diagram of the thermally modified boundary layer, or the internal boundary layer, over a warm oceanic current caused by advection of cold air (for explanation of symbols, see text).

0377-0265/84/$03.00

temperature gradient such as the Gulf Stream (Sweet et al., 1981; LaViolette, 1982) or the Kuroshio Current (Mahrt and Paumier, 1982). Of the many geophysical aspects associated with these differences, one is the development of a so-called internal boundary layer (IBL) over the warm-water side when the wind blows at right angles from the cold-water side (Fig. 1).

It is the purpose of this paper to provide observational evidence of such a development. The Korea Strait region, which for the most part is influenced by monsoon conditions, was thus selected as the field site. We also employ measurements made in the Alboran Sea region, where light-wind conditions or winds that are parallel to the oceanic front prevail, to show that some conditions are not favorable to the development of an IBL.

2. THEORETICAL CONSIDERATIONS

The oceanic thermal front may be considered a transitional zone in which the air flow adjusts to a new set of boundary conditions when it crosses the front. In the process, air adjacent to the sea surface becomes modified. This modified layer is often called the internal boundary layer (Fig. 1). A general description of the IBL may be found in Oke (1978). Formulae to estimate the height of the IBL and a general review of the subject for coastal regions are provided in Hsu (1983a).

Venkatram (1977) has derived a theoretical formula from the first principles that states that

$$h = \frac{U_*}{U_m}\left[\frac{2(\theta_{warm} - \theta_{cold})X}{\gamma(1-2F)}\right]^{1/2} \tag{1}$$

where h is the height of the IBL, U_* and U_m are the friction velocity and mean wind speeds, respectively, inside the IBL, γ is the lapse rate above the boundary layer or upwind condition, F is an entrainment coefficient, which ranges from 0 to 0.22, θ_{warm} and θ_{cold} are the potential temperatures over the warm- and cold-water sides, respectively, and X is the distance or fetch downwind from the front.

Equation 1 may be simplified by employing the drag coefficient, which is defined as $(U_*/U_m)^2$. Thus

$$h = \left[\frac{2C_d(\theta_{warm} - \theta_{cold})X}{\gamma(1-2F)}\right]^{1/2} \tag{2}$$

Equation 2 will be shown to be verified by observations.

3. EXPERIMENTAL RESULTS

Because of the monsoonal effect, the prevailing wind direction during fall and winter over the Korea Strait is northwesterly. The speed varies from 5 to

15 m s^{-1}. The winds are approximately perpendicular to the oceanic thermal front associated with the Tsushima current, a branch of the Kuroshio.

The warm oceanic current in the Korea Strait is readily seen in satellite imagery (Fig. 2). Dry-bulb (T_{dry}) and dew-point (T_{dew}) temperatures over the cold-water side are shown in the left panel in Fig. 3, and those over the warm side are given on the right. The measurements were made by radiosondings from ship track line E. There is an ~ 30% increase in relative humidity and mixing ratio from the cold side to the warmer side ~ 15 km downwind from the ocean front. As expected, the modification occurred in the lower atmosphere.

The height of the mixed layer is lower over the cold side than over the warm side, where the effect of surface heat flux is larger (Fig. 4). The mixing height increases from ~ 250 m on the upwind (cold-water) side to > 550 m

Fig. 2. Warm oceanic current (dark area) in the Korea Strait. Ship track is outlined. NOAA-6 meteorological satellite image (November 17, 1980). Channel 4, calibrated to 0.25 °C resolution, was used. For detailed satellite data processing see Huh and DiRosa, 1981.

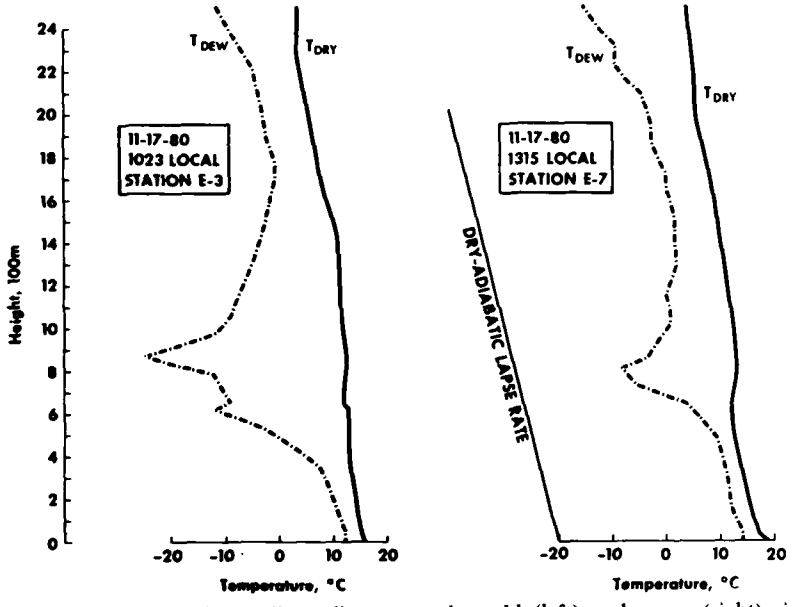

Fig. 3. High-resolution radiosondings over the cold (left) and warm (right) sides of the oceanic current in the Korea Strait (cf. Fig. 2). Note that station E7 is located (in Fig. 2) near the lower left corner of letter E on line E, which was ~15 km downwind from the oceanic front. The location of this station was 33°38'N and 128°00'E.

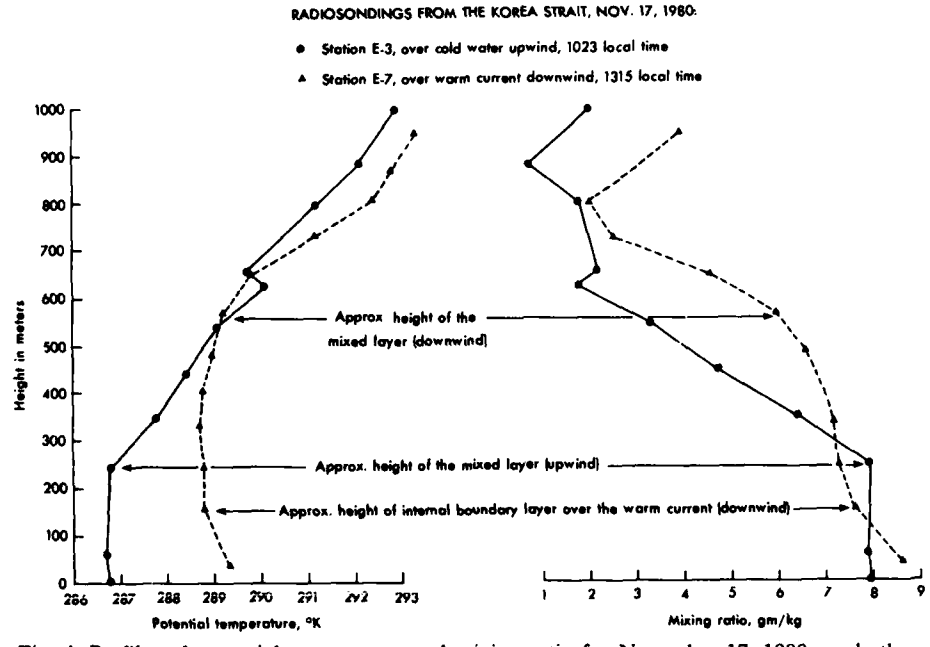

Fig. 4. Profiles of potential temperature and mixing ratio for November 17, 1980, on both upwind and downwind sides of the thermal front (cf. Fig. 2) (see text for explanation).

on the warm-water side. The corresponding water temperature was 11.5 °C on the cold side and 18.0 °C on the warm side. Note that the determination of the mixing height is based on both profiles of the potential temperature and the mixing ratio. Since the data points or sampling rates are not dense enough, these determinations are not absolute. More detailed high-resolution radiosondings were obtained in a followup experiment. Figure 5 shows an example. Comparison of Fig. 5 with results obtained by Wyngaard et al. (1978) indicates that, except for the atmospheric structure at ~ 250 m, this figure is about the same as theirs.

Figures 4 and 5 show that the precision of determination of the IBL height is dependent upon the sampling rate. However, the accuracy of the IBL height (see, e.g., 150 m in Fig. 4) is related mainly to the pressure measurement near the surface. Since the pressure accuracy in the surface layer is < 1 mbar, the variation is therefore $< \pm 10$ m at 150 m. This is based on application of the standard hypsometric equation.

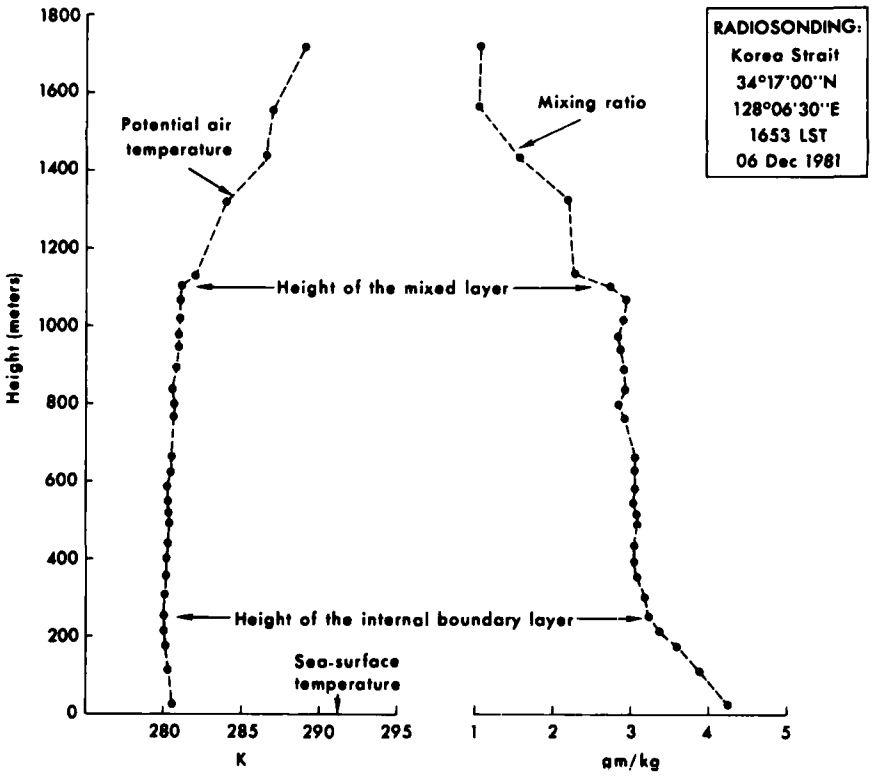

Fig. 5. Profiles of potential temperature and mixing ratio for December 6, 1981, over the warm side of the Tsushima current in the Korea Strait.

The increase in mixing height over the warm-water side has also been observed by Sweet et al. (1981). They showed that a 320-m increase occurs when the air crosses an 8°C front and a 400-m increase occurs when it crosses a 12°C oceanic thermal front.

To show this mixed layer further, pertinent data from a recent experiment over the Alboran Sea as part of Project "Donde Va" (Kinder, 1982) are presented. Figure 6 shows the warm gyre in the Alboran Sea. Figure 7 provides a detailed plot of sea-surface temperature (SST) and winds at 300 m. A series of high-resolution radiosondings were made over both sides of

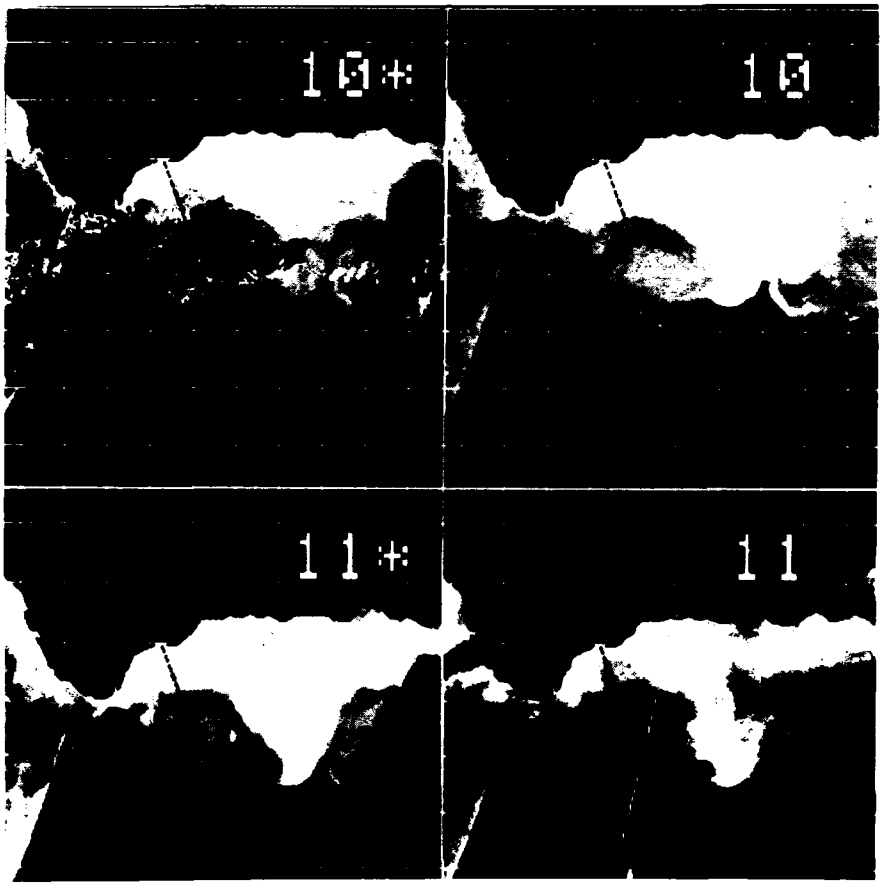

Fig. 6. A satellite detection of the warm waters in the Alboran Sea on October 10 and 11, 1982 (courtesy of Paul LaViolette). The dotted black line is the Marbella Line, which began at Marbella, Spain (see Fig. 7) at 36°27'N and 4°47'W and ended at 35°45'N and 4°30'W. The squares are bounded by longitude and latitude half a degree apart (for reference see Fig. 7. For satellite data processing and related topics, see LaViolette, 1984).

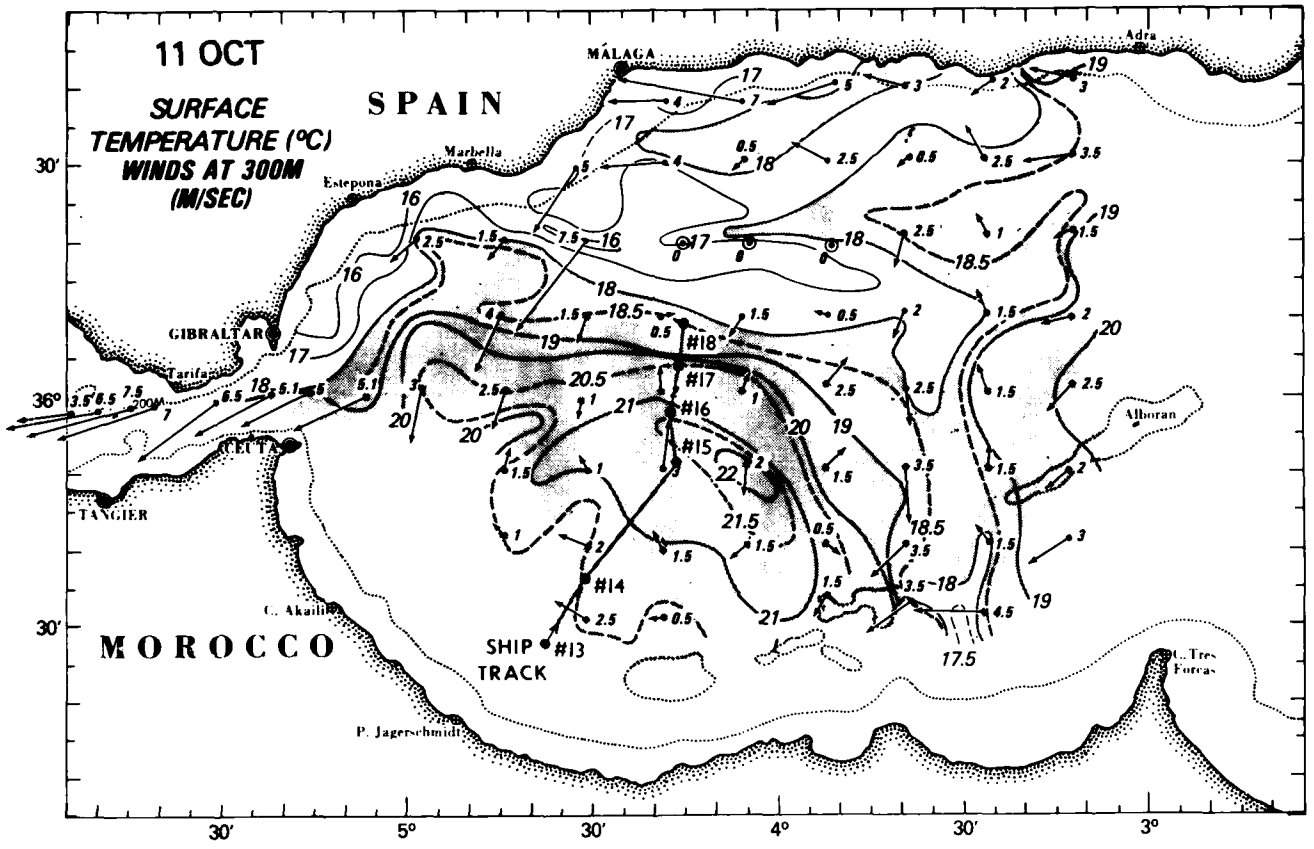

Fig. 7. Sea-surface temperature and winds at 300 m on October 11, 1982, for the Alboran Sea (courtesy Paul LaViolette). Numbers #13 through #18 represent the radiosonde stations on this day (see Fig. 8).

cold and warm waters. Figure 8 presents examples of the profiles of potential temperature (θ) and mixing ratio (q). On October 11, 1982, the USNS *Bartlett* made a survey track from the southwest toward the northeast, then northward (Fig. 7). A dry and cold air mass prevailed over the cold-water

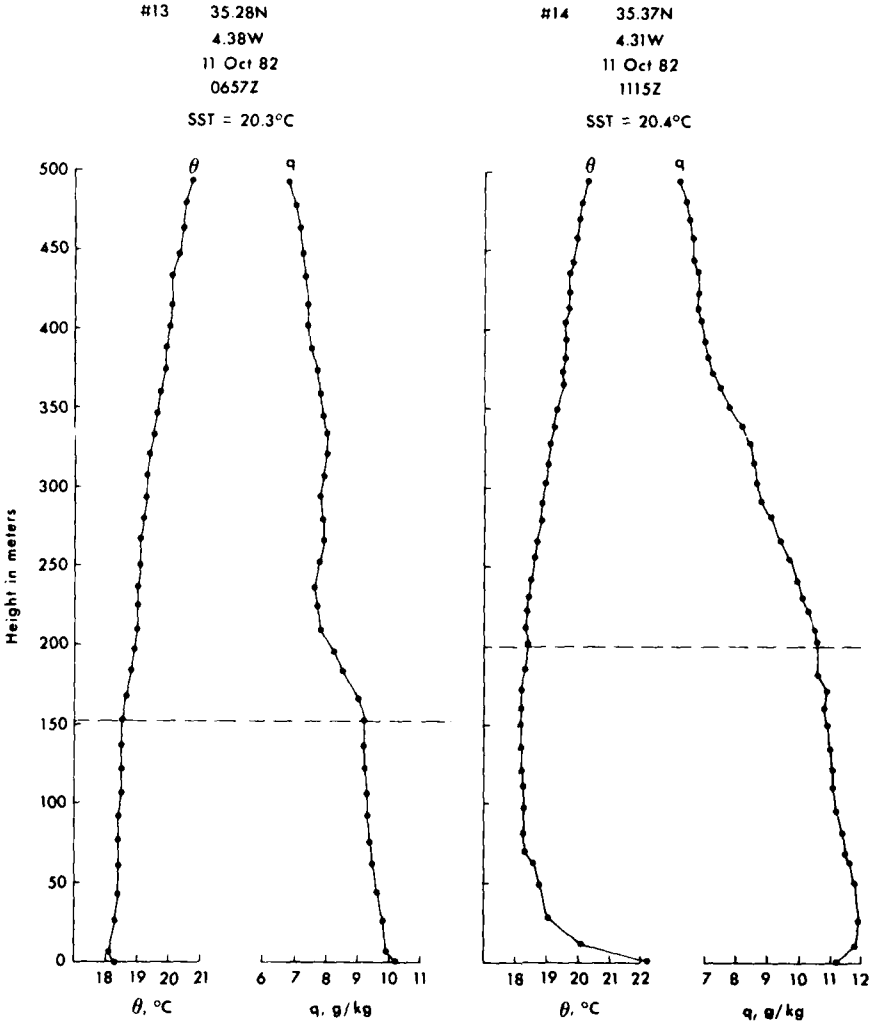

Fig. 8. High-resolution radiosondings over the Alboran Sea. Dashed lines are the approximate heights of the mixed layer. The symbol θ represents the potential temperature and q is the mixing ratio.

side (see Fig. 8, radiosonde launch #13). However, over the warm water the air mass was warm and moist (Fig. 8). Note that the average height of the mixed layer was ~ 150 m over the cold side (from #13) and 200 m over the warm side (Fig. 8). This average is obtained by using 200 m from #14, 158 m from #15, 170 m from #16, 270 m from #17, and 214 m from #18; the mean is 202 m and the standard deviation is 44 m. Note also that on this day there were no clouds in the area (Fig. 6) and the winds were light and variable over the warm water (Fig. 7).

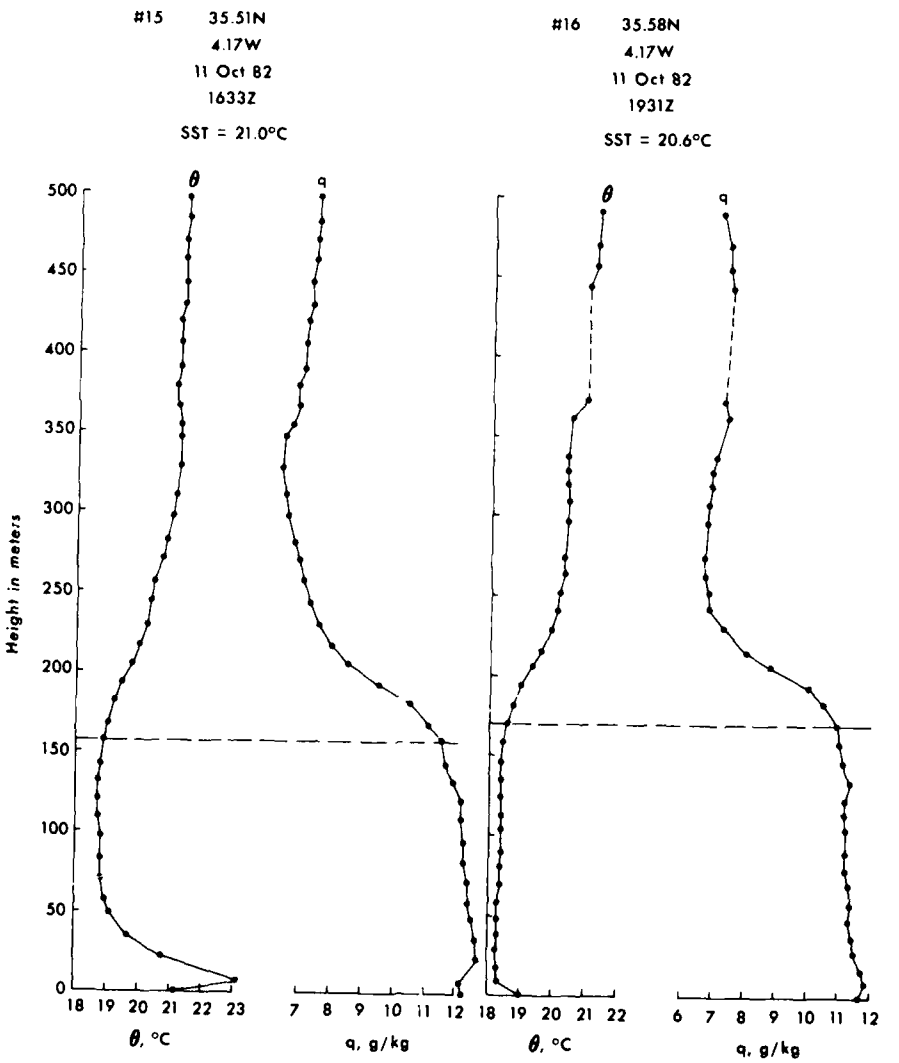

Fig. 8. (continued).

Figure 9 shows a detailed comparison between the boundary-layer structure on either side of the Alboran gyre. The high-resolution radiosonding over the cold side was taken from the R/V *Naucrates* near the Spanish coast. The soundings over the warm side are based on #14, as shown in Fig. 8. Over the cold-water side an inversion layer existed from 30 to 70 m (Fig. 9). However, there was no stable layer over the warm water. Figure 9 also shows

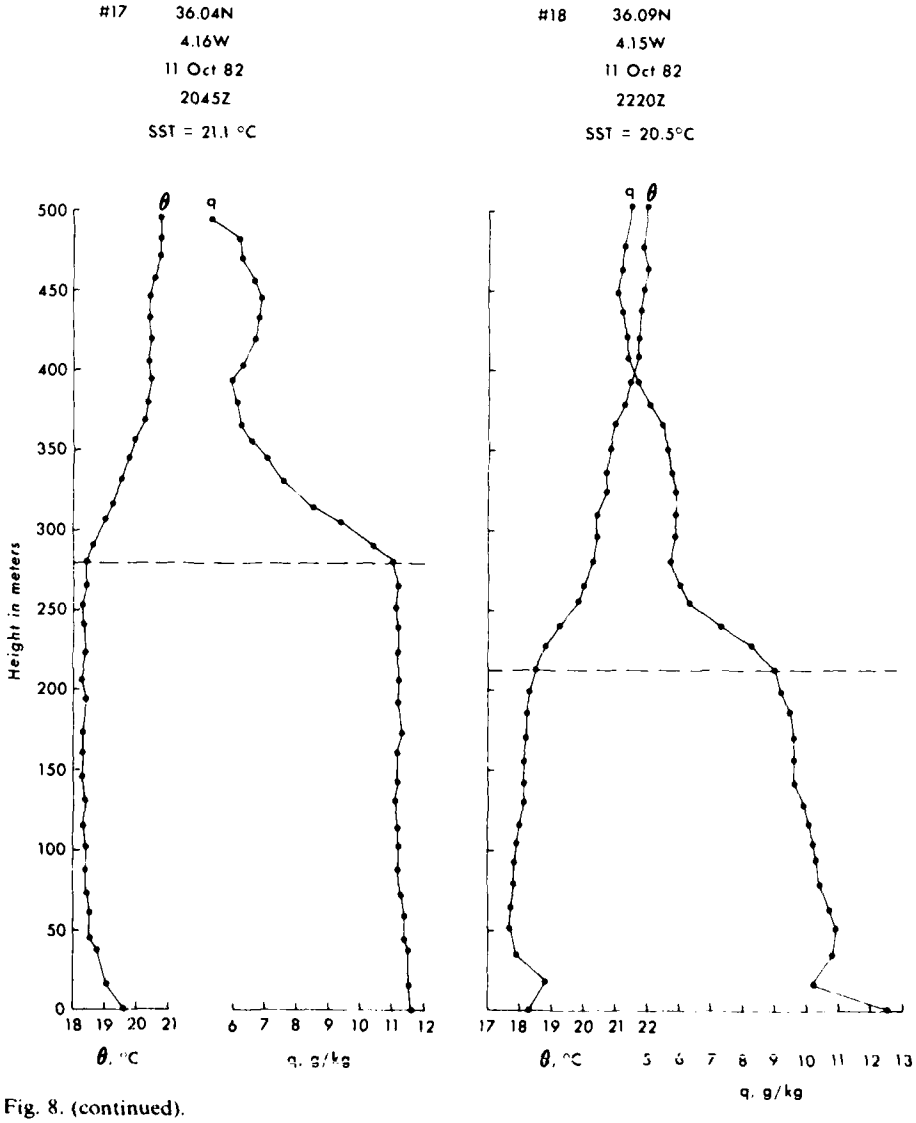

Fig. 8. (continued).

that the standard radiosonde measurement over land even from a small peninsula such as Gibraltar cannot be used to represent detailed marine boundary-layer structures.

The justification for the choice of soundings compared in Fig. 9 (i.e., #14 versus Spanish coast) is that the sondes were launched within 1 h of each other and that #14 has the mixed-layer height of 200 m, which is nearly the same as the mean height over the warm water as discussed previously.

Since there were no systematic winds that blew from the cold-water to the warm-water side, the variation of θ and q from the sea surface to ~ 50 m cannot be attributed to the development of the so-called "internal boundary layer." On the other hand, the slope changes around 150 m, shown in Fig. 4, and 250 m, in Fig. 5, cannot be explained by the physics of the surface layer

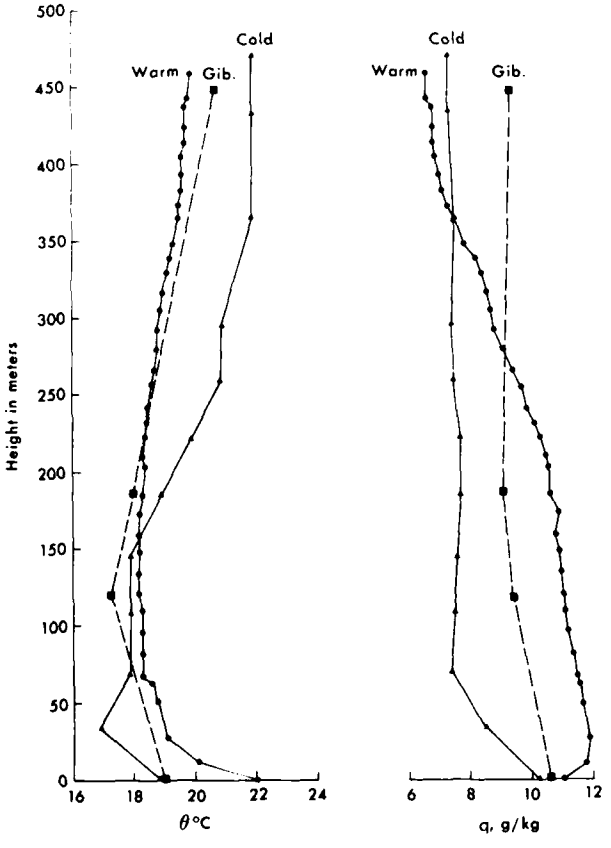

Fig. 9. Comparison of radiosondings on October 11, 1982, over warm water (SST = 20.4°C) at 1115Z and cold water (SST = 16.9°C) at 1013Z of the Alboran Sea as well as from Gibraltar (Gib.) at 1100Z. The symbol θ is the potential temperature and q is the mixing ratio.

or constant flux layer, which is normally of the order of 10 m over the water (see, e.g., Danard, 1981). Note also that under superadiabatic or free convection conditions in a desert environment the convective surface boundary layer over land can reach only ~ 100 m, as discussed by Danard (1981) and measured by Hsu (1983b).

On the basis of observations discussed above, eq. 2 may be applied. Since the Kuroshio is a warm oceanic current originating in the tropics, we adopt $C_d = 0.0015$ (Pond et al., 1971). Figure 4 shows that $(\theta_{warm} - \theta_{cold}) = 2.7\,^{\circ}C$. A common value of F is 0.2 (e.g., Driedonks, 1982). From the ship's log and Fig. 4, we have $X = 15$ km or 15 000 m and $\gamma = 1\,^{\circ}C\ 100\ m^{-1}$.

Substituting these values into eq. 2, we obtain $h = 142$ m. This computed value is in excellent agreement with the measured value of 150 m, as shown in Fig. 4 (the accuracy of this measured value of 150 m has been discussed previously). Note that the height to fetch ratio, i.e., h/X, is ~ 1/100, which is consistent with values discussed in the literature (Oke, 1978).

4. CONCLUSIONS

When the wind blows approximately perpendicular to an oceanic thermal front such as the Kuroshio, an internal boundary layer can develop. An equation based on theoretical considerations can be used to compute successfully the height of the IBL downwind from the front. The height to fetch ratio is found to be 1/100, which is consistent with similar thermal contrast situations over land.

Data obtained from an experiment in the Alboran Sea indicate that an IBL is not formed when the wind is calm or blows parallel to a thermal front. Certainly more field experiments should be conducted to further substantiate the results.

ACKNOWLEDGMENTS

This study was sponsored by the Coastal Sciences Program, U.S. Office of Naval Research, Arlington, Virginia 22217. The field experiment was supported in part by the U.S. Naval Environmental Prediction Research Facility, Monterey, California 93943.

REFERENCES

Danard, M., 1981. A note on estimating the height of the constant flux layer. Boundary Layer Meteorol., 20: 397–398.

Driedonks, A.G.M., 1982. Sensitivity analysis of the equations for a convective mixed layer. Boundary-Layer Meteorol., 22: 475–480.

AD-A174 470 A COLLECTION OF REPRINTS(U) LOUISIANA STATE UNIV BATON ROUGE COASTAL STUDIES INST W J WISEMAN ET AL. JAN 86 TR-398 N00014-83-C-0150 3/3

UNCLASSIFIED F/G 8/10 NL

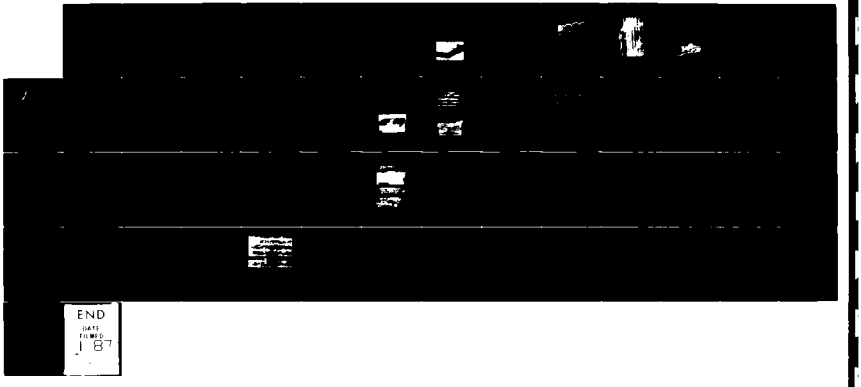

END

DATE FILMED

1 87

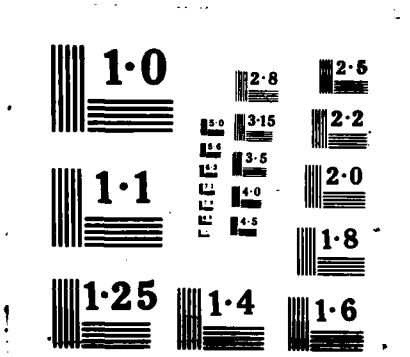
1·0
1·1
1·25
1·4
1·6
1·8
2·0
2·2
2·5
2·8
3·15
3·5
4·0
4·5

Huh, O.K. and DiRosa, D., 1981. Analysis and interpretation of TIROS-N AVHRR infrared imagery, western Gulf of Mexico. Remote Sensing of Enrivon., 11: 371–383.

Hsu, S.A., 1983a. On the growth of a thermally modified boundary layer by advection of warm air over a cooler sea. J. Geophys. Res., 88: 771–774.

Hsu, S.A., 1983b. Measurements of the height of the convective surface boundary layer over an arid coast on the Red Sea. Boundary Layer Meteorol., 26: 391–396.

Kinder, T.H., 1982. Project Donde Va, Operation plan, Alboran Sea, October, 1982. Available through Naval Ocean Research and Development Activity Code 331, NSTL Station, Ms. 39529.

LaViolette, P.E., 1982. The Grand Banks Experiment: a satellite/aircraft/ship experiment to explore the ability of specialized radars to define ocean fronts. Report 49, Naval Ocean Research and Development Activity, NSTL Station, Ms. 39529.

LaViolette, P.E., 1984. The advection of submesoscale thermal features in the Alboran Sea gyre. J. Phys. Oceanogr., 14: 550–565.

Mahrt, L. and Paumier, J., 1982. Cloud-top entrainment instability observed in AMTEX. J. Atmos. Sci., 39: 622–634.

Oke, T.R., 1978. Boundary Layer Climates. Methuen, London, 372 pp.

Pond, S., Phelps, G.T., Paquin, J.E., McBean, G. and Stewart, R.W., 1971. Measurements of the turbulent fluxes of momentum, moisture, and sensible heat over the ocean. J. Atmos. Sci., 28: 901–917.

Sweet, W., Fett, R., Kerling, J. and LaViolette, P., 1981. Air–sea interaction effects in the lower troposphere across the north wall of the Gulf Stream. Mon. Weather Rev., 109: 1042–1052.

Venkatram, A., 1977. A model of internal boundary-layer development. Boundary Layer Meteorol., 11: 419–437.

Wyngaard, J.C., Pennell, W.T., Lenschow, D.H. and LeMone, M.A., 1978. The temperature–humidity covariance budget in the convective boundary layer. J. Atmos. Sci., 35: 153–164.

1a REPORT SECURITY CLASSIFICATION Unclassified	1b RESTRICTIVE MARKINGS
2a SECURITY CLASSIFICATION AUTHORITY	3 DISTRIBUTION/AVAILABILITY OF REPORT Approved for public release; distribution unlimited
2b DECLASSIFICATION/DOWNGRADING SCHEDULE	
4 PERFORMING ORGANIZATION REPORT NUMBER(S) Technical Report No. 404	5 MONITORING ORGANIZATION REPORT NUMBER(S)
6a NAME OF PERFORMING ORGANIZATION Coastal Studies Institute 6b OFFICE SYMBOL (If applicable)	7a NAME OF MONITORING ORGANIZATION
6c ADDRESS (City, State, and ZIP Code) Louisiana State University Baton Rouge, LA 70803-7527	7b ADDRESS (City, State, and ZIP Code)
8a NAME OF FUNDING/SPONSORING ORGANIZATION ONR 8b OFFICE SYMBOL (If applicable)	9 PROCUREMENT INSTRUMENT IDENTIFICATION NUMBER
8c ADDRESS (City, State, and ZIP Code) Code 422 CS 800 North Quincy Street Arlington, VA 22217	10 SOURCE OF FUNDING NUMBERS PROGRAM ELEMENT NO: PROJECT NO: NR 388 002 TASK NO: 3.B WORK UNIT ACCESSION NO: 14

11 TITLE (Include Security Classification)

Effect of Cold-Air Advection on Internal Boundary-Layer Development over Warm Oceanic Currents

12 PERSONAL AUTHOR(S)
S. A. Hsu

13a TYPE OF REPORT	13b TIME COVERED	14 DATE OF REPORT (Year, Month, Day)	15 PAGE COUNT
Research	FROM 1/1/84 TO 12/31/85	1984	13

16 SUPPLEMENTARY NOTATION

Dynamics of Atmospheres and Oceans, 8 (1984) 307-319; Elsevier Science Publishers, Amsterdam

17 COSATI CODES			18 SUBJECT TERMS (Continue on reverse if necessary and identify by block number)
FIELD	GROUP	SUB-GROUP	
04	02		internal boundary layer, oceanic current, thermal front

19 ABSTRACT (Continue on reverse if necessary and identify by block number)

Field expericments have shown that an internal boundary layer (IBL) can develop when the wind blows perpendicularly from the cold-water side of a warm oceanic current to the warmer side. The height of this IBL downwind from the termal front as computed by an equation originally developed by Venkatram is in excellent agreement with observations.

20 DISTRIBUTION/AVAILABILITY OF ABSTRACT ☒ UNCLASSIFIED/UNLIMITED ☐ SAME AS RPT ☐ DTIC USERS	21 ABSTRACT SECURITY CLASSIFICATION Unclassified
22a NAME OF RESPONSIBLE INDIVIDUAL Arlene C. Smith	22b TELEPHONE (Include Area Code) 504-388-2396 22c OFFICE SYMBOL

DD FORM 1473, 84 MAR 83 APR edition may be used until exhausted
All other editions are obsolete

SECURITY CLASSIFICATION OF THIS PAGE
UNCLASSIFIED

Coastal Studies Institute
Louisiana State University
Baton Rouge, LA 70803-7527

Technical Report No. 405

SUBMARINE SLOPE INSTABILITY

David B. Prior and James M. Coleman

1984

Reprint from Slope Instability
John Wiley & Sons, 1984, 419-455.
D. Brunsden and D. B. Prior, eds.

Office of Naval Research
Contract No. N00014-75C-0192
Project NR 388 002

Slope Instability
Edited by D. Brunsden and D. B. Prior

CHAPTER 10

Submarine slope instability

David B. Prior and James M. Coleman

Coastal Studies Institute,
Louisiana State University

'It is well to remember that the largest of all slope movements on earth appear to have occurred on the bottom of the sea...' (Varnes, 1975)

10.1 INTRODUCTION

The economic significance of submarine environments is increasing. Offshore oil and gas, mineral exploration and waste disposal projects have meant the proliferation of bottom-mounted engineering structures, pipelines, and communication cables. The use of continental shelves and deeper water shelf slope regions is growing and diversifying with technological developments. It is already apparent that the active geologic processes of erosion, sedimentation, faulting, diapirism, and volcanism provide considerable challenges to offshore engineering. Geologists and engineers are also beginning to appreciate that submarine slope instability is a common, widespread phenomenon that imposes many constraints on engineering projects. Active landsliding and areas of former instability are being identified by modern sophisticated geophysical survey techniques.

There is evidence of submarine slope instability in a wide variety of offshore environments, from shallow water, near-shore zones, continental slopes, and beyond to the deep ocean floors. Some of the concepts of submarine slope instability need revision. Specifically, offshore surveys are showing that sea floor instability can occur in extremely small low angle slopes ($< 1^{\circ}$). Sediment strengths can be extremely small, and various levels of underconsolidation are common. Pore water and pore gas pressures can be extremely large, approaching geostatic values in particular locations. Moreover, in some areas instability is so active that offshore engineering structures have been damaged and destroyed.

The significance of submarine mass movement processes to geological sedimentation models has been underestimated. Slope instability is responsible

for various deformation structures, bed thickness inconsistencies, faunal and textural anomalies, and in some places it may be the dominant method of sediment transport from shallow to deeper water. Geologic interpretation of former marine sediment sequences is showing that ancient marine slopes were often sites of extensive large-scale submarine mass transport processes.

The present chapter examines early concepts and reviews some of the modern survey methods used to identify submarine slope features. The main types of features and inferred mechanisms are discussed in relation to causative factors and methods of stability analysis, with specific examples.

10.2 EARLY CONCEPTS

In the nineteenth century submarine communication networks were laid in shallow coastal areas, over the continental shelves, and across the ocean floors connecting the continents. Subsequent damage to these cables was the subject of numerous reports (e.g., Milne, 1897; Benest, 1899; deSmitt, 1932). In most cases the breaks were attributed to submarine earthquakes, but Milne (1897) drew particular attention to the probability that earthquakes were likely to cause submarine slope instability, which in turn could cause cable damage. Also, discussing submarine deltaic slopes, Milne (1897) stated that they might be

> 'subject to sudden modification due to the sliding of masses of material on their faces...by a facial shear by overloading or an increase in the angles of stability by the wearing actions of currents'.

Among numerous examples of cable breaks Milne (1897) reported that landsliding appeared responsible for breaks off Newfoundland bank in 1884—a prophetic observation, considering the great Grand Banks slide event in 1929.

Heim (1908), perhaps better known for research on sturtzstroms, considered the evidence for recent and fossil submarine instabilities and proposed the terms 'subsolifluction or subaqueous solifluction.' Heim's theories were cited by two later authors, who in different ways drew attention to evidence for submarine mass movements. Archanguelsky (1930) studied cores from the submarine slopes of the Black Sea. On 2–3° slopes stripping of recent sediments from the upper slopes exposed older deposits 'in the form of long continuous stripes'. Intense deformation was observed on the lower slopes. Archanguelsky concluded that the evidence for 'slips may be looked upon as definitely proved'.

Hadding (1931) discussed a variety of evidence from ancient rocks, including 'folding and creasing', oversliding structure or flow structure; and 'rolling up of strata'. Subaqueous slope instabilities were considered responsible for 'supernumery strata' (thickened bedding), 'subnumerary strata'

(stripped horizons), superposition of older over younger beds, rearrangement of abnormal failure sequences, and deformation of strata.

In 1938 Stetson and Smith conducted a series of tank experiments, addressing the problems of the origins of submarine valleys. They convincingly caused 'slumping' on an artificial shelf edge, and attributed the slumping to seepage pressures.

In view of the technology available and the lack of actual sea floor data, the conclusions reached by Milne, Heim, Hadding, Stetson and Smith (and others) are quite remarkable. Since the 1930s various remote sensing acoustic tools have been applied which provide data validating many of these earlier concepts.

10.3 MODERN SEA FLOOR SURVEY METHODS

The detection and recognition of submarine slope instability relies on the identification of sea floor morphology and sediment deformation analogous to better known terrestrial landslide geometry. Improvement in offshore remote exploration technology, particularly acoustic sensors such as precision depth recording, high-resolution seismic profiling, and side-scan sonar, provide accurate sea floor and sub-bottom data. Side-scan sonar and seismic data can be linked directly to sediment properties and distribution by bottom sampling, borehole logging, and core analysis. These techniques, combined with computerized ship navigation, allow mapping of sea floor instability. Figure 10.1

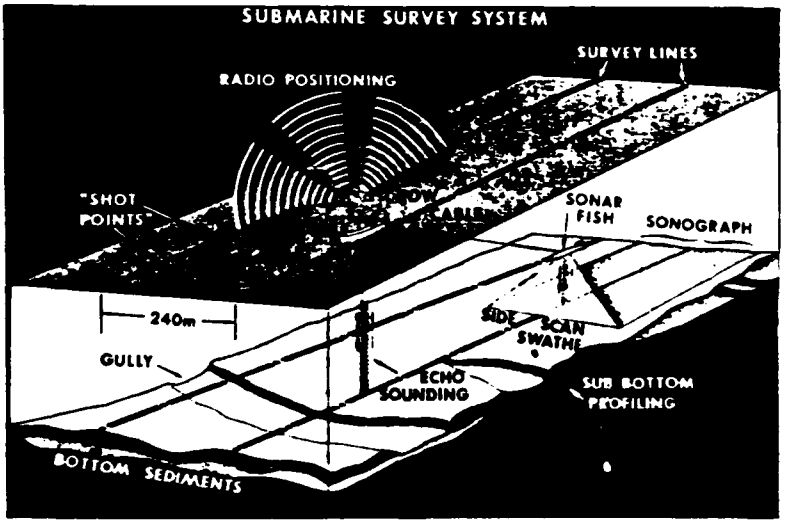

Figure 10.1. Schematic of modern submarine survey system used to map submarine slope instabilities in the Gulf of Mexico (Prior *et al.*, 1979b)

depicts schematically the submarine survey system used to map sea floor geology and geomorphology in the Gulf of Mexico.

10.3.1 Navigation

Accurate navigation is essential for establishing correct spatial relationships of sea floor features and for the construction of scale-true maps. Various methods are available which provide different degrees of accuracy, including radio position fixing from shore and satellite stations. Also, sea bed acoustic transponders provide high precision over small areas. Reconnaissance regional surveys of shelf and shelf edge regions commonly use medium-range systems such as Loran C or specific survey systems such as Decca High Fix. They can be used to achieve grid line coverage, permitting high-density data acquisition. In some areas, for example in the offshore oil and gas lease block assessments in the Gulf of Mexico, grids composed of survey lines spaced at 240 m intervals have been constructed. Recently the entire submarine portion of the Mississippi Delta (almost 2000 km^2) has been surveyed in this manner (Coleman *et al.*, 1983), by more than 17,500 km of survey lines controlled by Loran C or autotape navigation. Such modern position fixing methods are now routinely available, permitting return to designated areas and precise comparative resurveys, essential for the evaluation of bottom process dynamics (Prior *et al.*, 1979a; Prior and Suhayda, 1979a,b).

10.3.2 Echo-sounding

Sea floor profiles are constructed along survey lines by emitted sound pulses and their return echos from the bottom, calibrated for the velocity of sound in water. Navigation fix marks are automatically displayed on the depth profiles. Grid surveys can be used to construct contoured bathymetric charts. Identification of submarine instability from bathymetry and bathymetric profiles alone (such as those shown in Figure 10.2) is difficult and speculative (Shepard, 1955). However, time comparisons of bathymetric surveys of the same area have proved useful in detecting active sea floor slope instability (Shepard, 1933, 1955; Coleman *et al.*, 1974; Prior and Suhayda, 1979b; Coleman *et al.*, 1983).

10.3.3 Side-scan sonar

This technique represents the most significant development in mapping sea floor topography and has proved particularly invaluable in the recognition of submarine landslides. The principle is similar to that of the echo sounder (Belderson *et al.*, 1972; Fleming, 1976). A transducer fish is towed behind the exploration vessel on a transmission cable to a multi-channel recorder on the

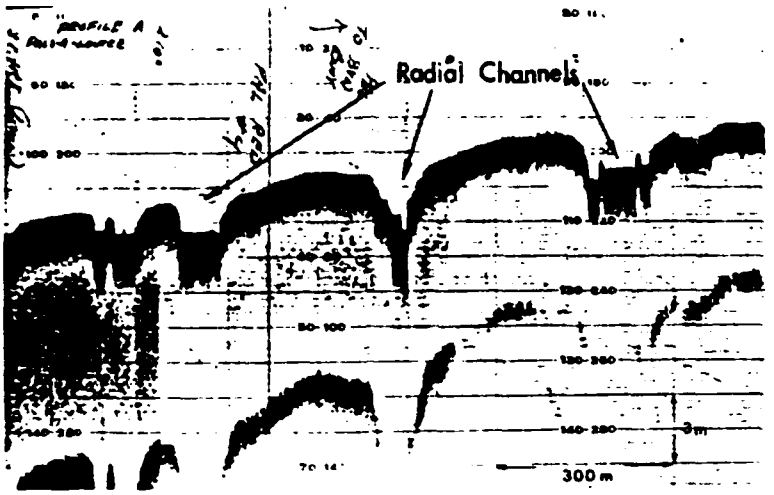

Figure 10.2. Example of fathometer trace across submarine delta-front channels, interpreted by Shepard (1955) to be of mass movement origin (Coleman *et al.*, 1974)

vessel. High-frequency sound pulses (100 ± 15 kHz) are transmitted from the fish at regular intervals in a narrow beam. As the sound waves touch the bottom and encounter different bottom roughness features or various slopes, the sound is scattered or reflected. The reflected energy is received by the transducer, transmitted back to the vessel, and the relative intensities of sound versus elapsed time recorded graphically. Thus, as the vessel and transducer move along, a grey-toned picture of the bottom, referred to as a sonograph, is constructed. In effect, the record can be considered analogous to an aerial photograph made when the sun is low and behind the camera, except that a camera records reflected light, whereas the sonar records reflected sound waves. In a sonograph steep slopes or scarps facing the transducer will appear darker. Large objects such as ridges are good reflectors, but may also produce acoustic shadows behind them, indicated by white patches. In addition to plan views of sea floor morphology (to selected ranges on either side of the ship's track), sonographs include depth profile data along the ship's track.

Until recently all conventional sonographs possessed several inherent scale distortions, and hence bottom features were not depicted in true dimensional perspective. Consequently, interpretation and mapping of submarine landslides were difficult and tedious. Fleming (1976) discusses the cause of scale variations. In 1978 a new digital side-scan system (SMS 960) was developed by EG & G which uses microprocessors to correct automatically for angular slant range and ship's speed (Clifford *et al.*, 1979). The resulting sonographs are scale correct and give true plan views of sea floor morphology. The system is

Figure 10.3. Side-scan sonar mosaic image (scale true) showing collapsed blocky sea floor feeding narrow debris flow chutes. Mississipi Delta (Prior *et al.*, 1979a)

particularly useful for mapping since adjacent survey lines can be combined to produce true-scale mosaics (Figure 10.3) of large areas of sea floor (Prior *et al.*, 1979a). The SMS 960 has proved particularly valuable in mapping submarine instabilities in the Gulf of Mexico (Prior *et al.*, 1979a,b).

10.3.4 Continuous seismic profiling

A variety of seismic techniques are available which detect variations in sediment properties to great depths below the sea bed. The basic principle involves detection of sediment stratigraphy and structure, indicated by variations in acoustic reflection characteristics. Several different types of acoustic source are available (e.g., pinger, sparker, boomer) which provide different resolutions at different energy frequencies. The suitability of each system is a function of the bottom materials, resolution and depth of penetration required. Sediment instability studies have found high-resolution methods particularly useful for the definition of sub-bottom landslide geometry (e.g., Garrison, 1974; Coleman *et al.*, 1974; Moore, 1977; and Figure 10.4–10.13). Digital acquisition and rapid signal sampling have allowed a variety of signal processing methods to be applied, which enhance resolution, remove multiples, and allow migration of data. True-scale subsurface sediment structures and details of sediment acoustic properties are thus obtained. Moore (1977) evaluates the advantages and limitations of seismic profiling and provides examples of its application

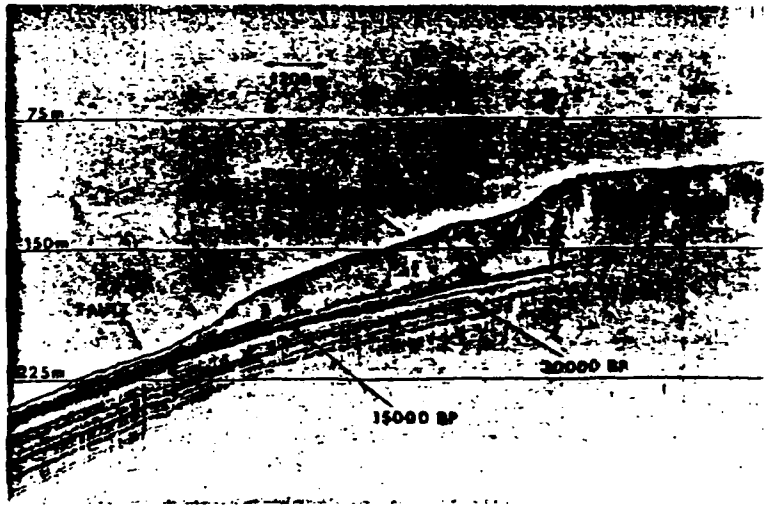

Figure 10.4. High-resolution seismic profile across depositional lobes associated with submarine debris flows, Mississippi Delta (Coleman and Garrison, 1977)

to landslide studies in the Indian Ocean, the Grand Banks area, Gulf of Alaska, Northwest Peru, Bay of Biscay, Florida, and California. In many cases seismic profiling defines clearly the geometry of subsurface failure planes, essential for stability analyses. However, where sediments contain large quantities of *in situ* gas, the acoustic returns are poor and the technique has severe limitations (Coleman and Garrison, 1977).

As oceanographic surveying has progressed, these remote sensing techniques have detected a variety of different types of sea floor instabilities, in diverse submarine environments. Detailed mapping has commenced in selected areas of the Gulf of Mexico, Gulf of Alaska, Pacific and Atlantic coasts of North America, and very substantial amounts of new data have been acquired. But for other offshore regions the evidence for submarine slope failure is available only from widely spaced preliminary reconnaissance survey lines.

10.4 TYPES OF INSTABILITY

The evidence for submarine mass movements on slopes from geological and geophysical surveys is supported by numerous telegraph cable breaks attributed to submarine slope movements (e.g., Milne, 1897; Heezen and Ewing, 1952, 1955; Heezen, 1956; Terzaghi, 1956; Houtz, 1960; Heezen and Drake,

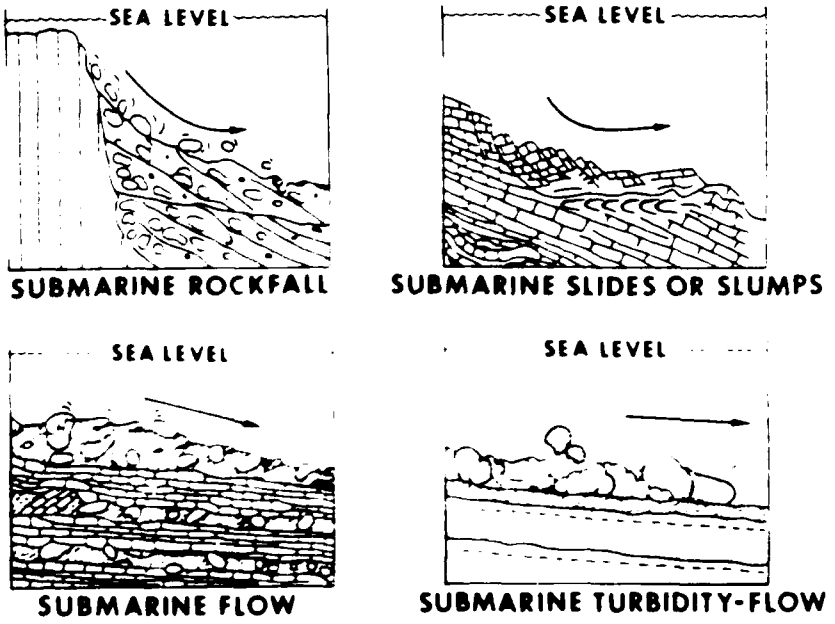

Figure 10.5 Main types of submarine slope instability (Dott, 1963)

1964). There have also been cases of substantial damage to offshore oil and gas structures (Bea, 1971; Sterling and Strohbeck, 1973; Prior *et al.*, 1979c).

From the available evidence it is possible to suggest several different types of instability processes. Dott (1963) identified four main categories (Figure 10.5): submarine falls; slides, or slumps; flows; and turbidity flows. Recently Moore (1977) suggested a modification of Varnes' (1958) classification scheme for terrestrial landslides. Moore's (1977) classification does not include turbidity currents but subdivides the primary categories (falls, slides, and flows) on the basis of material type.

10.4.1 Submarine falls

The free fall of rock, mud, or sand-sized particles is restricted to localized steep, near-vertical slopes. Dill (1966) has recorded sand falls along the walls of submarine canyons. Other localities where sand and rock falls take place are trench walls and flanks of sea mounts. Also, many carbonate reefs possess steep outer slopes and talus-like accumulations of blocks of coral at anomalous depths suggest that detached blocks fall freely or roll downslope.

10.4.2 Slides

The most widespread type of submarine slope instability involves sliding of both rock and soft sediments. Some individual slides and slide complexes are extremely large and cover very extensive areas of sea floor. Table 10.1 lists some examples, and the volumes of displaced rock are often much larger than most terrestrial slides. The Agulhas slide, off South Africa (Dingle, 1977), is

Table 10.1. Characteristics of large submarine slides

Location	Length (km)	Width (km)	Area (km^2)	Volume (km^3)	Slope
Agulhas, S. Africa	750	106	79,488	20,331	
Bassein, Bay of Bengal	108	37	4,000	900	6–1 [c]
Grand Banks, Nfld.	240	140	27,500	760	4–3 [c]
Rockall, N.E. Atlantic	160	13.8	2,200	300	2 [c]
Ranger, Baja Calif.	35	8.6	300	20	3 [c]
Kidnappers, New Zealand	45	5.6	250	8	4–1 [c]

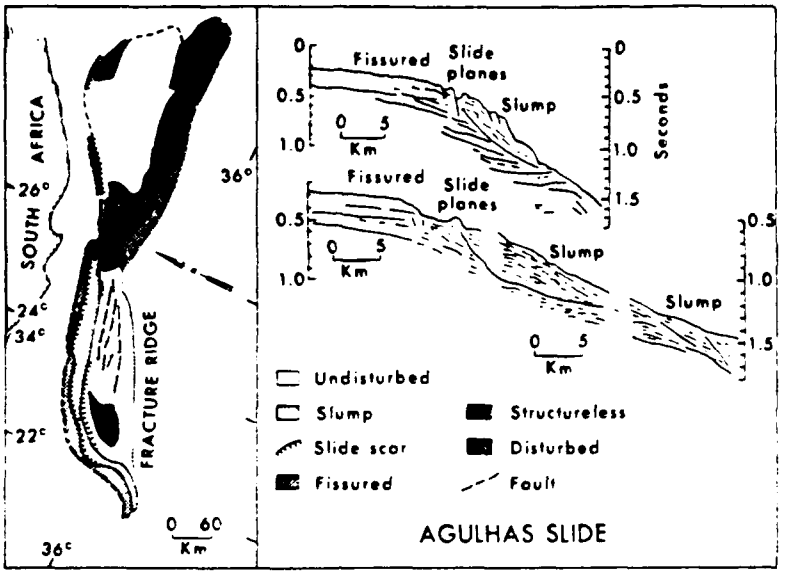

Figure 10.6. Characteristics of the Agulhas slide, South Africa (Dingle, 1977)

a gigantic failure complex estimated to involve more than 20,000 km^3 of displaced rock (Figure 10.6).

Dingle (1977) summarizes some of the diagnostic characteristics of large submarine slides as follows:

1. upslope fissured zones, with numerous tensional, stepped faults;
2. slide plane scar—the outcrop of the main shear surface;
3. tensional depression— a bathymetric hollow between the slide plane and the reverse slope of the slumped block;
4. slumped mass; detached, rotated material bounded at its base by concave-upward shear surfaces. The outer edge may show compressional folding or thrusting. Where the slipped masses have not remained intact, multiple blocks, subsidiary shear planes, and distorted debris flow structures may be found.

A large number of features with some or all of these characteristics have been recognized, in addition to those listed in Table 10.1 (Moore, 1977). They typically occur along continental shelf edge slopes, particularly along the Atlantic and Pacific coasts of North America in inter-canyon areas (Uchupi, 1967; Knebel and Carson, 1979; Stanley and Silverman, 1969). Other locations include the Gulf of Mexico (Walker and Massingill, 1970; Wilhelm and Ewing, 1972; Bryant *et al.*, 1968); the Gulf of Alaska (Carlson and Molnia, 1977; Hampton *et al.*, 1978); off the coasts of Africa (Embley and Hayes, 1974);

Europe (Roberts and Stride, 1968; Stride *et al.*, 1969); New Zealand (Lewis, 1971); Hawaii (Moore, 1964); Indian Ocean (Moore *et al.*, 1976); the Mediterranean (Almagor and Wiseman, 1977). Moore (1977) provides a systematic review and cites numerous examples. Slides appear to be extremely common where submarine slopes are subject to crustal tectonics and earthquake shocks (Table 10.2). Similarly, slide processes appear to be associated with areas of rapid sedimentation, such as deltas. For example, slides have been documented in the Mississippi Delta region (Shepard, 1955; Terzaghi, 1956; Coleman *et al.*, 1974; Prior and Coleman, 1978a,b; Prior *et al.*, 1979a,b,c); the Magdalena and Esmeraldas deltas in South America (Shepard, 1932; Heezen, 1956); the Copper River delta of Alaska (Reimnitz, 1972; Hampton *et al.*, 1978); the Fraser River delta of Canada (Mathews and Shepard, 1962).

Most of the slides are located on very low-angle slopes ($< 5^{\circ}$)(Tables 10.1 and 10.2). Until recently reservations were often expressed about slope instability under such low gravitational stresses. But Lewis (1971) provided convincing seismic evidence of slides on $1-4^{\circ}$ (Kidnappers Slide, Figure 10.7), and acceptance is growing of the potential for submarine instability on slopes of 1° or less. For example, the Mississippi delta-front slides occur on submarine slopes that have an average inclination of 0.5° (Prior and Coleman, 1978a,b).

Submarine slides are often referred to in the literature as 'slumps'. Dingle (1977) specifically refers to 'slumped' and rotated blocks of sediment. This term is considered to be too generalized and often misused (Dott, 1963; Prior and Coleman, 1982). Specifically, seismic data usually possess severe distortion due to vertical exaggeration (Figure 10.4); curvature of failure planes is visually enhanced, and the apparent rotational component of displacement is often ascribed undue significance. In reality, the real curvature of the bound-

Table 10.2. Submarine slope instability and earthquakes (Morgenstern, 1967)

Location and date	Slope (degrees)	Magnitude (Richter)	Focal depth (km)	Within epicentral region
Grand Banks, 1929	3.5	7.2	Shallow	Yes
Orleansville, 1954	4–20	6.7	7	No
Strait of Messina, 1908	4	7.5	8	Yes
Suva, 1953	3	6.75	60	Yes
Chile, 1922	6	8.3	Shallow	No
Valdez, 1964	6	8.5	Shallow	Yes
Aegean Archipelago, 1956	10	7.5	15	No

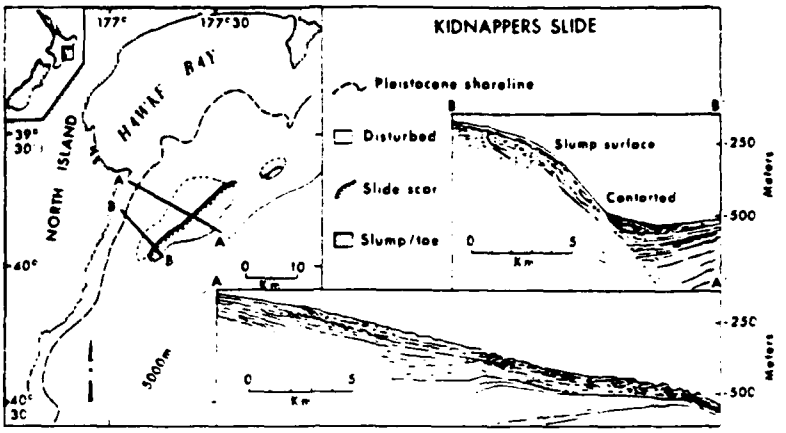

Figure 10.7. Characteristics of the Kidnappers Slide, NZ (Lewis, 1971)

ing shear planes is extremely small and is most pronounced (if present at all) toward the upslope margins of individual slides. As such, the degree of rotation of the displaced mass of rock or sediment is very much subordinate to longitudinal downslope movement. Also, rather than there being a single displaced and rotated block, the slides often disintegrate downslope into chaotic and hummocky topography. A reconsideration of the profile form of most major submarine slides shows that depth/length ratios are extremely small (Prior and Coleman, 1982).

Alternatively, submarine slides can be specifically described by true-scale

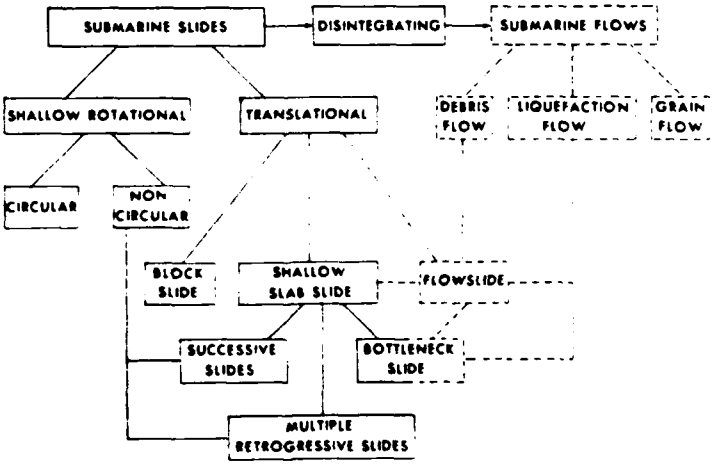

Figure 10.8. Suggested subdivision of submarine slides and flows (omitting turbidity flows)(Prior and Coleman, 1983)

horizontal and vertical geometry, and a first approximation of a scheme for the classification of submarine slides is suggested in Figure 10.8. This scheme uses some of the nomenclature and concepts in common usage with respect to subaerial slope failures suggested by Skempton and Hutchinson (1969).

Submarine slides are broadly separated from various types of submarine flows, but it is also clear that many slides can become flows with continued downslope movement as the debris progressively disintegrates. Slides are subdivided primarily into shallow rotational and translational types.

Many submarine slides are shallow rotational types with either circular slip surfaces or non-circular failures deviating from the true circular arc form in the downslope direction. The Bassein slide (Moore *et al.*, 1976) is an example of the latter, with obvious non-circularity of the basal shear surface extending horizontally more than 30 km and to an average depth of 360 m below the sea floor (Figure 10.9).

Translational slides, in which the basal failure surface is planar and inclined approximately parallel to the surface slope, appear to be the most common form of submarine instability. This is consistent with the low slope inclinations and the great length of most features. Systematic rotation of individual displaced blocks is usually confined only to the extreme upslope margins of the features. The amount of rotation is very small, magnified in appearance by vertical exaggeration in most survey records, and constitutes only a very small part of the total geometry of each source area and a relatively insignificant portion of each entire slide. Most of the large slides cited in Table 10.1 appear

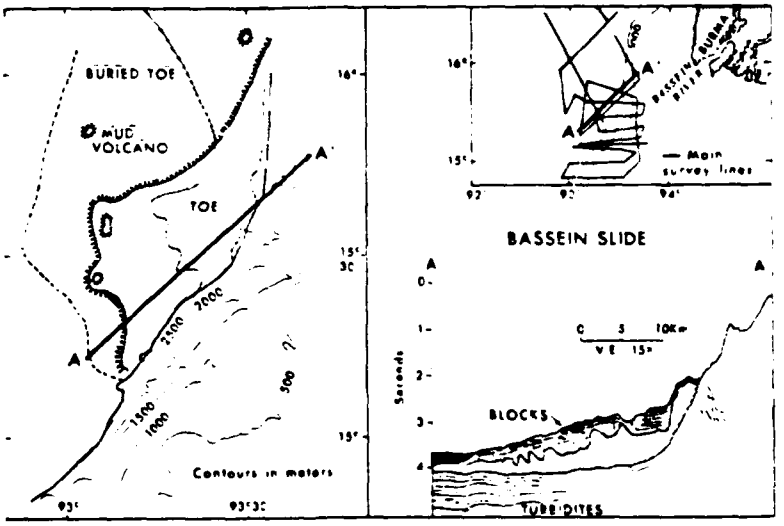

Figure 10.9. Characteristics of the Bassein slide, Burma (Moore *et al.*, 1976)

to possess these attributes. Heezen and Drake's (1964) seismic profiles of the famous Grand Banks 'slump' can be interpreted in this way, notwithstanding Moore's (1977) reservations. Where translational slides involve upper superficial layers of sediment only, they may be characterized as 'shallow slab slides'. Many of the Mississippi delta-front failures are in this category, with thin intact blocks of sediment moving downslope but staying the right way up (Prior and Coleman, 1978a). Block slides differ from slab slides in that the former usually involve downslope translation of massive bedrock units. The Straits of Florida slide (Wilhelm and Ewing, 1972) is considered by Moore (1977) to exemplify this type.

Both shallow rotational and shallow slab failures may be arranged in groups on a slope, in which adjacent failures ultimately form a related *en echelon* series in a downslope direction. This more complex form, in which a large section of slope is subject to numerous adjacent failures, can best be described as successive slides, and good examples are provided by Hampton *et al.* (1978) from the Copper River delta (Reimnitz, 1972) and the Malaspina Glacier slide area. Successive slides may evolve into multiple retrogressive types in which continued failure and interaction of adjacent slides produce multiple blocks and an extension of the limit of instability upslope. Many submarine slides appear to fit this category: the Agulhas slide complex (Dingle, 1977); the Hawaiian slide (Moore, 1964); and some of those described by Stride *et al.* (1969) from the European shelf edge.

Bottleneck slides are those with a very distinctive plan form in which debris moves downslope from an arcuate, depressed source region through a narrow neck to form a widespread depositional fan. In cross-section the source area may show some slab-slide or multiple retrogessive features, and the initial failure mechanism is shear failure followed by extensive loss of sediment strength and remoulding. Bottleneck slides have been identified in association with underconsolidated, methane-gas-rich sediments on very low-angle (0.3–0.4°) slopes in inter-distributary bays in the Mississippi Delta region (Prior and Coleman, 1978a,b). As indicated in Figure 10.8(a), bottleneck slides (and flow-slides) are difficult to classify since they may involve both sliding and flowing. They can best be considered to be intermediate between true slides and flows.

10.4.3 Flows

Submarine downslope flows of sediment are believed to involve four main processes: debris flow; liquefaction flow; grain flow; and turbidity flow. Alternatively the categories are suggested as

> 'conceptual end members, whereas real flows exist throughout a continuum between these end members' (Middleton and Hampton, 1976) (Figure 10.8(b))

Debris flows

These are defined as flows of sediment in which larger clasts are supported by a matrix, i.e. a mixture of interstitial fluid and fine sediment that has a finite yield strength. Middleton and Hampton (1976) also described debris flows as

> 'sluggish downslope movement of mixtures of granular solids, clay minerals, and water in response to gravity'.

They are sometimes regarded as transitional between slides and turbidity currents (Hampton, 1972).

It is becoming increasingly apparent that submarine debris flows are very important processes. Hampton (1970, 1972, 1975), Fisher (1971), and Embley (1976) have discussed the morphology, mechanics of movement, and resulting sediments. Embley (1976) describes debris flows off the Canary Islands which originate on slopes of 1.5° (Figure 10.10). Beginning as slide scars, they possess very elongate channels and chutes with natural levées leading to finger-like lobes of deposited material. The deposited sediments possess a unique

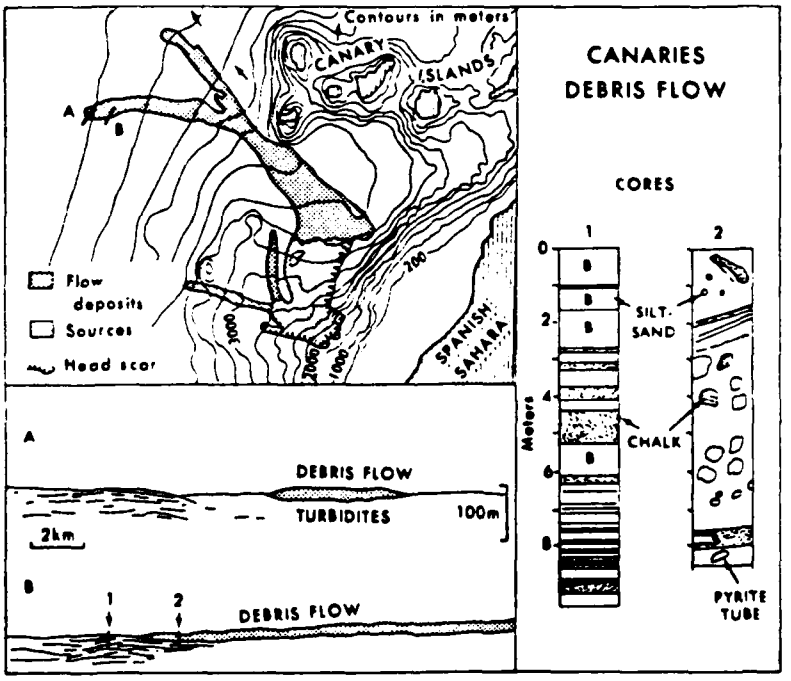

Figure 10.10. Characteristics of the Canaries debris flow (Embley, 1976)

fabric of large clasts within a finer matrix. The flows originate from a source area extending over 18,000 km^2 of sea floor, and the deposits cover more than 30,000 km^2 with an estimated volume of 600 km^3.

Jacobi (1976) identifies similar features near the Senegal coast. A total volume of 649 km^3 of material was deposited from four flows downslope of source area slides covering 14,214 km^2 of sea floor. The Canaries and Senegal debris flows are considered to be of the Pleistocene age, but the volumes of sediment and areas of disturbed sea floor rival some of the larger slides in Table 10.1. Flood *et al.* (1979) examine the distribution and characteristics of sediments, covering more than 11,000 km^2 of the Rockall Bank, which they attribute to debris flow processes operating on slopes of 0.2–1.5°. These debris flows were probably associated with submarine slides dating from 15–16,000 years B.P.

Active debris flows and mudflows associated with bottleneck slides and slab slides have been identified on the Mississippi delta-front slope (Figure 10.11). Elongate mudslide and debris flow systems extend radially from the main distributaries of the Mississippi River down the delta-front slope (inclination 0.5°) to water depths of 150 m. The features, often achieving lengths of 8–10 km, typically possess three distinct components: a subsidence source bowl area; an elongate transport chute (Figure 10.3 and 10.12); and downslope depositional lobes (Figure 10.13). The subsidence bowls occur on the upper slopes in water depths of 15–40 m and comprise extensive areas of disturbed sea floor that have been displaced vertically below the surrounding intact

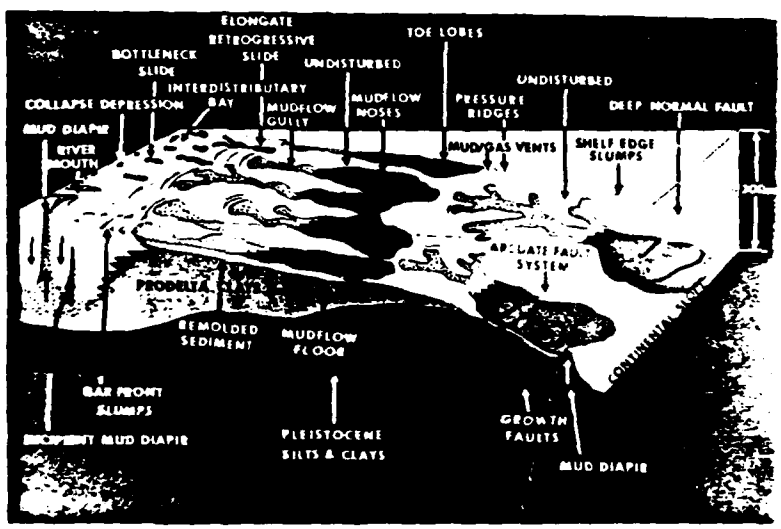

Figure 10.11. Schematic distribution of submarine slope instabilities, Mississippi Delta (Roberts *et al.*, 1983)

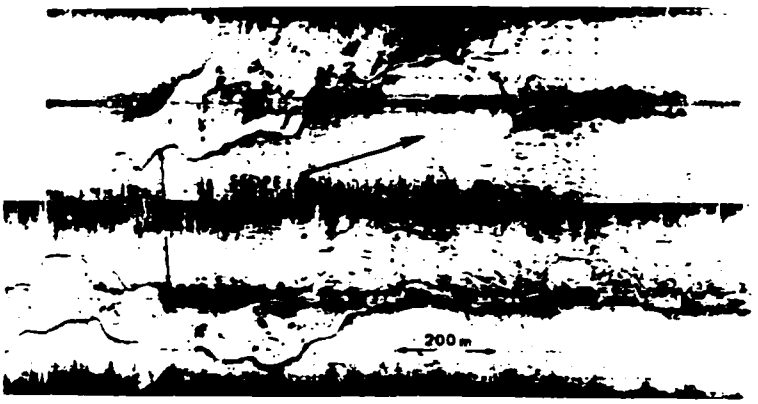

Figure 10.12. Side-scan sonar mosaic of instability chutes, Mississipi Delta

sediments. Typical subsidence areas are full of large displaced blocks, and they supply debris to elongate incised transport chutes which extend downslope. A range of chute morphology has been identified. At one extreme chutes are broad and linear, full of blocks, and movement appears to be the result of 'plug flow' within marginal and basal shears. Alternatively, many chutes are extremely narrow, elongate and sinuous, with widths ranging from 25 m to 200 m; often narrow, steep sections alternate with wider, low-angle segments. These narrow chutes appear to transport debris downslope as a viscous remoulded flow capable of supporting large individual blocks. Both types of chute are affected by sidewall instability. At the downslope ends of the

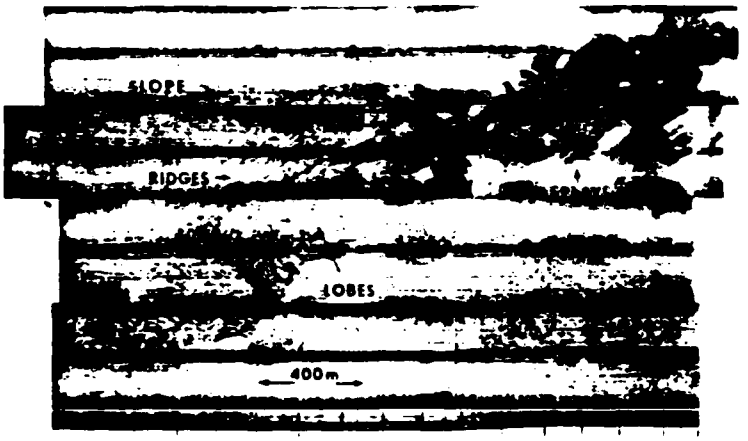

Figure 10.13. Side-scan sonar mosaic of depositional lobes from debris flows, Mississippi Delta (Coleman *et al.*, 1983)

elongate chutes there is distinctive overlapping of depositional lobes consisting of debris discharged from the chutes (Figure 10.4).

Bottom topography on the lobes is characterized by crenulated, blocky debris and often by abundant mud vents and mud volcanoes. The lobes terminate abruptly and vary in height from a few metres to greater than 30 m, with angles up to 3°. Adjacent lobes often coalesce, forming an almost continuous but complex frontal scarp that may extend to distances of 20–25 km around the base of the delta-front slope. The thickness of the lobes is often difficult to determine precisely, but is of the order of 15–20 m. Overlapping sequences of lobes can total a thickness of 50–60 m of deposited sediment from an individual transport chute. These features on the Mississippi delta-front slope have been the subject of several publications (Shepard, 1955; Terzaghi, 1956; Bea, 1971; Garrison, 1974; Coleman *et al.*, 1974; Coleman and Garrison, 1977; Prior and Coleman, 1978a,b; Prior and Suhayda, 1978a,b; Prior *et al.*, 1979a,b,c). A map series showing the distribution of bottom instabilities, comparisons of bathymetric data from 1874, 1940 and 1979, near-surface geology, and isopach maps of disturbed sediments for the entire delta, has been compiled (Coleman and Prior, 1983), together with an explanatory report (Coleman et al., 1983).

Liquefaction flows

Liquefaction sediment transport occurs when a loosely packed, coarse-grained sediment collapses, the grains temporarily losing contact with each other and the particle weight is transferred to the pore water (Terzaghi, 1956). Temporary excess pore water pressures are induced and downslope gravitational stresses cause sediment to flow. Liquefaction can occur as a result of disturbance by other slope instability processes, or spontaneously. In spontaneous liquefaction, collapse is related to other factors that disturb the sediment fabric, such as earthquakes. Fluidized sediment flows are those in which the sediment is supported by the upward flow of fluid escaping from between the grains as the grains are settled out by gravity. Middleton and Hampton (1976) indicate that fluidization and liquefaction processes are essentially similar, but Lowe (1976) makes a clear distinction between the two. Lowe (1976) claims that fluidization is unlikely to be as significant as liquefaction; and further, that since liquefaction flows are likely to be turbulent, there may be a continuous gradation between liquefaction flows and turbidity currents.

Terzaghi (1956) accounts for various submarine instabilities in terms of liquefaction, including 'flowslides' in sand off Zeeland, Holland (Koppejan *et al.*, 1948), and various submarine failures in fine sands in Norwegian fjords. Andresen and Bjerrum (1967), considering these failures, conclude that it is useful to subdivide into 'flowslides' and 'liquefaction slides'. Flowslides typically retrogress, slice by slice, owing to shear failure accompanied by

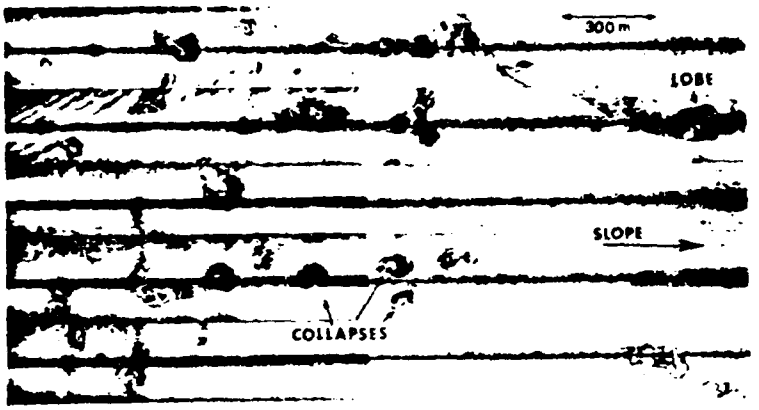

Figure 10.14. Side-scan sonar mosaic of collapse depression, bottleneck slides, and elongate slides, Mississippi Delta (Coleman *et al.*, 1983)

subsequent liquefaction, whereas liquefaction slides are the result of spontaneous liquefaction and 'propagate in all directions' (Andresen and Bjerrum, 1967).

A liquefaction type of process seems to be significant in fine silts and clays in the Mississippi Delta region (Prior and Suhayda, 1979a; Dunlap *et al.*, 1979), particularly in the formation of 'collapse depressions' and elongate flows. In these sediments pore water pressures are extremely large, approaching geostatic, and the voids also contain large amounts of biogenic methane gas, both soluble and in the bubble phase (Whelan *et al.*, 1975, 1976, 1978; Prior and Suhayda, 1979b). Following initial shear failure, strain softening of the highly pressured clay/water/gas system causes remoulding and strength loss similar to a type of 'liquefaction' or 'quick' behaviour, which accounts for *in situ* collapse and observed instances of sinking of pipelines and sea floor monitoring equipment vertically into the sediment. Dunlap *et al.* (1979) recorded equipment loss during storm conditions when pore water pressures were elevated. Increased pore pressures during storms caused bottom movement, collapse, and indications that the sediment was active as a viscous fluid. On very low angle slopes (0.1–0.2°) distinct 'collapse depressions' (Figure 10.14) are formed, whereas on slightly steeper slopes (0.3–0.4°) more elongate flows result.

Grain flows

Downslope sediment movement may involve direct grain-to-grain interaction. This process applies specifically to the movement of loose sand grains, without fine silt or clay. Submarine sand flows, resulting from this process, have been visually observed by Dill (1966) and Shepard and Dill (1966) on steep slopes

in submarine canyons. Sand derived from nearshore areas is carried into canyons by currents and

> 'flow continues as long as the material is added at the head of the flow and the accumulation slope exceeds the angle of repose (Shepard and Dill, 1966).

Middleton (1970) suggests that grain flows are possible only on relatively steep submarine slopes, and therefore that their effects are localized.

Turbidity currents (flows)

This process is widely used in the interpretation of ancient marine sediment sequences (e.g., Bouma, 1962). Turbidity flows involve the downslope transport of sediment which is supported by the upward component of fluid turbulence within the current. They are believed to occur off the mouths of major rivers where high-density water-sediment plumes move downslope into deeper water (Heezen *et al.*, 1964). In this sense they cannot be considered true slope instability processes. However, turbidity currents are also considered to occur in association with submarine slides and debris flows. Heezen *et al.* (1954) related the high-velocity sediment transfer from the Grand Banks slide to turbidity currents triggered by the slide. A similar explanation has been advanced for other sea floor disturbances, such as the Orleansville earthquake event (Heezen and Ewing, 1955). Similarly, Holtedahl (1965) has identified turbidites associated with slides in fjord environments. Menard (1964), Morgenstern (1967), and Hampton (1972) have discussed the conditions whereby slope instability can evolve into turbidity flows. Hampton (1972) cites boundary shear between advancing debris flow lobes and the water column as a mechanism for the production of turbulent dense suspensions, and requires slides to evolve and pass through a debris flow stage before turbidity flows result. Turbidity currents are apparently very widespread and significant processes, whether of fluvial or slope instability origin, responsible for submarine cable breaks, levéed submarine channels, the construction of submarine fans, and extensive deep-sea turbidite beds.

While distinctions are possible between the main types of submarine slope instability—falls, slides, and flows—a rigid, comprehensive classification scheme is not possible. Dott (1963) emphasized that, in reality, submarine instabilities involve a suite of interrelated mechanisms. The process interactions can be both causal and evolutionary.

Firstly, one type of instability may cause another. For example, a translational slide can cause retrogressive rotational failure at its upslope margins owing to oversteepening and unloading. Rotational slides may initiate other types

of failure farther downslope owing to undrained loading and load-induced pore water pressures.

Secondly, slides and flows can evolve during displacement. Unstable sediment often radically alters its rheological properties as it moves downslope. For example, slides often progressively disintegrate, the degree of breakup reflecting original sediment strengths and behaviour under shear. Debris flows may evolve from some slides, perhaps by incorporation of water (Hampton, 1972).

It must be borne in mind that the present explanations of the mechanics of submarine slope instability are generally inferred from morphology and sediment structure after the fact. Further, the morphological and sedimentological end results of a particular instability event do not necessarily exhibit all the features indicative of the true, entire process sequence. Thus, precise origins for particular submarine features (and subsequent classifications) are particularly problematical because of the largely remote, inaccessible submarine environment.

10.5 FACTORS RESPONSIBLE FOR SUBMARINE SLOPE INSTABILITY

Analysis of the conditions that cause submarine slope instability is a difficult task. Many of the examples cited are of undetermined age. Some shelf-edge slope movements appear to date from Pleistocene times, when sea floor conditions were substantially different from the present ones. Even where active, or recent, instability has been documented, it is clear that the slope failure thresholds are the result of a complex interaction of variables, rather than any single factor.

The inaccessibility of submarine slopes means that measurement of all the factors needed for precise stability analyses is technically demanding. For example, sediment strength data (whether from *in situ* tests or from core samples) are often poor owing to low sediment strengths and susceptibility to sample disturbance. In particular, depressurization due to borehole drilling and core extraction commonly leads to pore water and pore gas pressure reduction and changes of effective cohesion and friction parameters. Also, remote, retrospective surveying cannot always provide the true post-failure geometry, and the original slope characteristics are almost always unknown.

Nevertheless, there are factors that appear to influence submarine slope stability (Figure 10.15), and attempts have been made to construct conceptual and quantitative models. The basic conditions for any slope failure exist when stresses exerted on the sediment are sufficient to exceed its strength. This can be the result of stress increases, strength reduction, or a combination of the two.

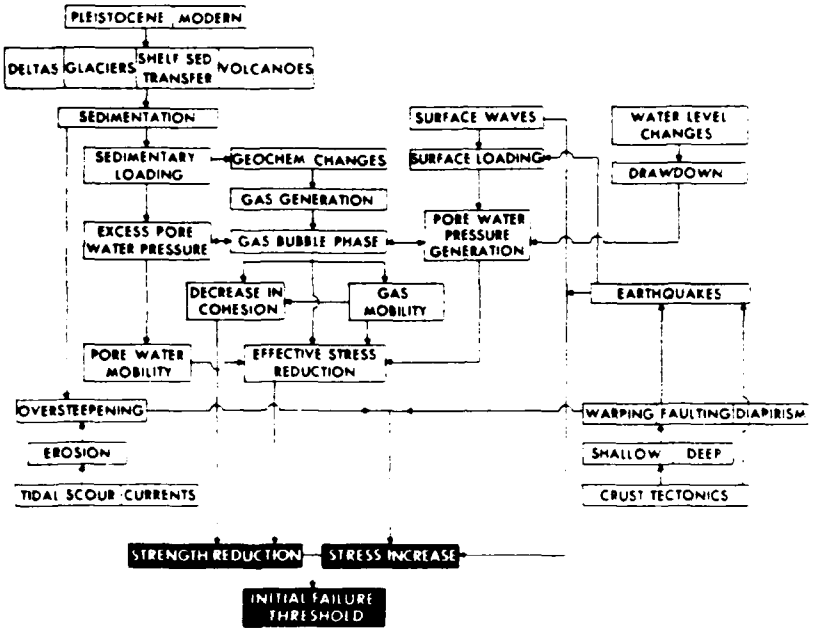

Figure 10.15. Factors and process interrelationships responsible for initiation of submarine slope instability (Prior and Coleman, 1983)

10.5.1 Stresses

Submarine slope angles and associated gravitational stresses are generally small, but they may be sufficient for failure where sediment strengths are extremely low. Gravitational stresses can be increased by localized slope angle steepening, over various time and space scales, owing to the following processes.

Crustal tectonics

In continental margins where the oceanic lithosphere is underthrusting the continental lithosphere (subduction zones), tectonic activity can lead to slope angle increases owing to warping and faulting. Similarly, such areas are characterized by active seismicity and large earthquakes. Moore (1977) refers to large slides that have been recorded from subduction zone margins by Ross and Shor (1965), Seely *et al.* (1974), Beck (1972), Moore *et al.* (1976), Shepherd *et al.* (1973). Moore (1977) identifies particularly large slides on submarine trench walls in which accretion of deep-ocean sediments are affected by 'oversteepening of slopes as part of tectonic off-scraping'. Almagor

and Wiseman (1977) use tectonic warping as a factor in initiating slides in the eastern Mediterranean.

In such active crustal zones earthquakes have significant effects on submarine slope stability. Earthquakes cause application of horizontal and vertical acceleration stresses. Pore water pressure changes also occur within the sediments owing to intensive cyclic loading, and sediment strengths are altered (Figure 10.16). A direct link between earthquakes and submarine slope instability is widely accepted, and there are several well-documented events (Heezen and Ewing, 1952, 1955; Houtz, 1962; Coulter and Miglaccio, 1966; Ryan and Heezen, 1965; Reimnitz, 1972).

Morgenstern (1967) considers the mechanism of earthquake-induced slope instability in terms of undrained failure and derives the equation:

$$\frac{C_u}{\gamma' h} = \frac{1}{2}\sin 2\beta + K'\left(\frac{\gamma}{\gamma'}\right)\cos^2\beta \tag{10.1}$$

where C_u is undrained strength and K' is a horizontal body force (σ_0 gravity). For undrained failure, this equation relates the critical slope angle β to undrained strength, the density of the sediment γ, submerged density γ', the height of the slope h, and the horizontal earthquake acceleration. From this,

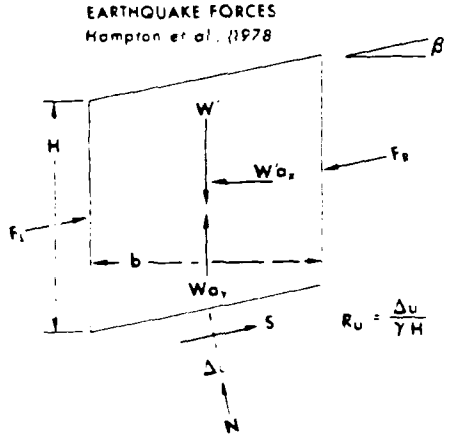

$$F = \left[\frac{1 - \frac{\gamma}{\gamma'}a_y - \frac{\gamma}{\gamma'}a_x\tan\beta - \frac{R_u}{\cos^2\beta}}{1 - \frac{\gamma}{\gamma'}a_y + \frac{\gamma}{\gamma'}\frac{a_x}{\tan\beta}}\right]\frac{\tan\phi'}{\tan\beta}$$

Figure 10.16. Model for earthquake effects on submarine slope instability (Hampton *et al.*, 1978)

Morgenstern (1967) concludes that even small earthquake-induced stresses are likely to be detrimental to the stability of submarine slopes. Further, it was noted that many documented cases of failure accompanied earthquakes of greater than 6.5 on the Richter scale.

Hampton *et al.* (1978) concede that modelling of the total effects of earthquakes (stresses and strength reductions) is extremely difficult and that

> 'defining the exact loading function and incorporating it into the analysis is extremely complex and beyond the present state of practice'.

Nevertheless, with certain limitations they attempt to evaluate the combined effects of earthquake-related pore pressure changes and direct loading effects of acceleration. Hampton *et al.* (1978) propose a model (Figure 10.16) in which horizontal acceleration a_x and vertical acceleration a_y are considered with γ (total unit weight), γ' (buoyant unit weight), β (slope angle), ϕ' (effective friction angle), and R_u (pore water pressure ratio). In effective stress terms (Figure 10.16):

$$F = \left[\frac{1 - \gamma\gamma' a_y - \gamma\gamma' a_x \tan\beta - R_u \cos^2\beta}{1 - \gamma\gamma' a_y + \gamma\gamma' a_x \tan\beta}\right]\frac{\tan\phi'}{\tan\beta} \qquad (10.2)$$

This analysis procedure was used to explain slides on the Albatross Bank, Gulf of Alaska, using measured strength properties and slide geometry from seismic data (Hampton *et al.*, 1978).

Current scour

Localized sea floor erosion, particularly in shallow water, by current action is a well-known process (Sternberg, 1972). Also, currents in canyons are capable of significant sea floor scour and sediment transport (Shepard *et al.*, 1974; Inman *et al.*, 1976). Slope oversteepening undoubtedly accompanies these processes, but their effects on local slope stability have yet to be determined.

Surface water waves

In shallow water near shore and in shelf environments, the passage of large surface water waves applies hydraulic forces to the sea floor. Watkins and Kraft (1978) cite large storm waves inducing pressure anomalies with 300 m wavelengths and amplitudes of 70 kN/m^2 in water depths of 60 m. Wiegel (1964) illustrates that pressure amplitudes decrease with increasing water depths, and Watkins and Kraft (1978) conclude that surface wave effects are unlikely to affect sea floor stability in water depths greater than 150 m. Henkel (1970) considered oil rig damage due to sliding in the Gulf of Mexico associated with Hurricane Camille and determined theoretically that waves im-

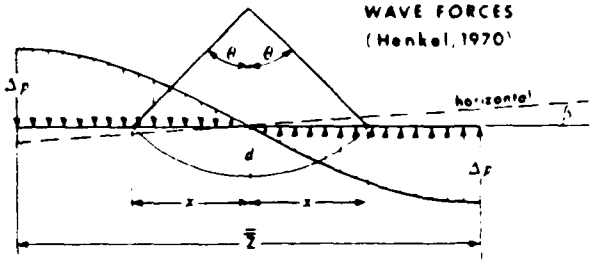

$$M_d = \frac{2}{3}\chi^3\beta\gamma' + \frac{L^2\Delta p}{2\pi^2}(\sin\alpha - \alpha\cos\alpha)$$

$$M_r = 2\chi^3\left(\frac{C_u}{\gamma' z}\right)\gamma'\left(\frac{\sin\theta - \theta\cos\theta}{\sin^3\theta}\right)$$

Figure 10.17. Model for wave loading of submarine sediments (Henkel, 1970)

pose oscillatory motion on loose sediments, sufficient to cause downslope movement (Figure 10.17). The magnitude of disturbing M_d and the resisting moments M_r can be calculated (Figure 10.17) using the equations:

$$M_d = \frac{2}{3}\chi^3\beta\gamma' + \frac{L^2\Delta P}{2\pi^2}(\sin\alpha - \alpha\cos\alpha) \tag{10.3}$$

$$M_r = 2\chi^3\frac{C_u}{\gamma' z}\gamma'\left(\frac{\sin\theta - \theta\cos\theta}{\sin^3\theta}\right) \tag{10.4}$$

where χ is the half length of the slide, d is the depth, 2θ is the angle of arc sliding, and α is the angular portion of the sinusoidal load on the slide length. When $M_d > M_r$ failure will take place, and Henkel (1970) suggests that Mississippi delta-front instability can be explained by hurricane-generated downslope stresses.

Hampton *et al.* (1978) use Henkel's approach to explain submarine sliding of the Malaspina Glacier, Alaska. Their calculations show that in water depths greater than 150 m pressure fluctuations are sufficient to cause instability.

In a series of experiments in the Gulf of Mexico (SEASWAB), bottom-mounted accelerometers and wave pressure sensors were used to monitor surface wave effects (Suhayda *et al.*, 1976; Dunlap *et al.*, 1979). The field data show wave pressure/bottom response relationships that are complex. While there are indications of linear relationships at low wave amplitudes, the bottom sediments also show non-linear responses to high wave pressures, perhaps due to viscoelastic properties of the sedimen.s. Nevertheless, these experiments have shown that increased downslope stresses are produced by surface waves and that they contribute to slope instability.

Sedimentation

Rapid sedimentation in offshore delta areas and canyon heads experience slope oversteepening and gravitational stress increases. Sands deposited at canyon heads accumulate until the angle of repose is exceeded and failure takes place (Shepard, 1932, 1933; Heezen, 1956). Also, slides on the upper Mississippi delta-front slope have been explained by Coleman *et al.* (1974) by the oversteepening of the distributary-mouth bars as a direct result of bar progradation processes. Coleman *et al.* (1974) report that

> 'by the time several floods have passed the bar front has prograded significantly seaward and the slope has steepened and become unstable'.

This implies that the slope angle progressively increases until a critical angle is exceeded, and that this is rarely achieved within a single phase of bar sedimentation and seaward growth. Similar effects seem to be prevalent off other major delta regions, such as the Esmeraldas (Shepard, 1932) and Magdalena deltas (Heezen, 1956), and the Fraser River delta (Mathews and Shepard, 1962).

On the continental slopes of many basins, sediment loading during Cenozoic times has resulted in the formation of a large number of diapiric structures that vary widely in scale and in intensity of movement. These diapiric structures are often several square kilometres in area and display heights of 300–500 m. Continued vertical movement of the diapiric mass causes local oversteepening of sediments and leads to widespread sediment instability. Often the diapiric masses form adjacent deep localized basins into which the disturbed debris accumulates to considerable thicknesses (Bouma *et al.*, 1978).

10.5.2 Sediment strength

The sediment strength at a potential failure surface is a function of cohesive and frictional forces, and these are influenced by the weight of sediment (or normal force) over the slip surface. Strength may be reduced in a number of ways (Figure 10.15), mainly by the production of internal pressures within the sediment voids. These pore water and pore gas pressures affect sediment strength by reduction of the normal forces, following the principle of effective stress.

Sedimentary loading

Many marine environments are (or have been) suoject to rapid rates of sedimentation. Prograding deltas have already been mentioned, but other localities include the peripheral margins of glaciers, the submarine slopes of

active volcanic islands, and site-specific shelf locations where shelf sediment transfer processes concentrate deposition.

Where sedimentation rates exceed the capacity for drainage of pore water from within progressively buried sediment layers, the sediment becomes underconsolidated and excess pore pressures are developed. Terzaghi (1956) discusses the concept of excess hydrostatic pressures caused exclusively by the lag between accumulation and consolidation, in relation to specific submarine failures, including the Mississippi delta-front features, first identified by Shepard (1955). Terzaghi suggests that these instabilities are the result of the low shear strength of the delta sediments because of excess pore water pressures. Excess pressures, substantially exceeding hydrostatic, are necessary to explain the failure of such low-angle slopes (average 0.5°). Prior and Suhayda (1979b) applied infinite slope analysis to the delta-front slides and derived the pore water pressure necessary for failure using the equation:

$$u = \frac{c' - F(\gamma' z \sin\beta \cos\beta)}{\tan\phi'} + \gamma' z \cos^2\beta \qquad (10.5)$$

where c' is cohesion, ϕ' is friction angle, γ' is unit weight, z is the depth to the slip surface, β is the slope slip surface angle, and $F = 1$. Calculated values, based on three sets of effective strength parameters and for two depths to failure, are in close agreement with measured pore water pressure data from *in situ* piezometers. The analysis suggests that reduction in effective stress may be sufficient to explain failure.

Cyclic loading by waves

In addition to the downslope stresses discussed earlier, surface waves are believed to generate pore water pressures in submarine sediments by cyclic loading. Recent experiments in the Gulf of Mexico (SEASWAB) using *in situ* piezometers measured the effects of winter storms and hurricanes (Suhayda *et al.*, 1978; Suhayda, 1977; Dunlap *et al.*, 1978, 1979). Significant ambient excess pore pressure were measured, approaching and even exceeding the overburden pressure. The latter case represents a case of zero effective stress. Sharp increases of pore water pressure accompanied the passage of storms (Dunlap *et al.*, 1978, 1979). Moreover, during storms (and accompanying large excess pore pressures), bottom displacements and subsidence were monitored, believed to be due to a liquefaction type of collapse, as predicted by Prior and Suhayda (1979a). Clearly cylic wave loading and related pore pressure fluctuations are limited to relatively shallow water depths (< 150 m) but they play a major role in failure of weak, underconsolidated sediments in deltaic regions. Cyclic loading by earthquakes is believed to affect sediment strength in a similar manner (Hampton *et al.*, 1978).

Pore gas generation

Many marine sediment/water systems are influenced by internal geochemical and bacteriological processes which lead to the generation of pore gases, particularly methane. When gas amounts are sufficiently large, at a particular pore water pressure, the dissolved gas in the pore water will change to the bubble phase (Whelan *et al.*, 1975, 1976, 1978). The presence of bubble gas in marine sediments is often detected indirectly by poor acoustic seismic returns (Coleman and Garrison, 1977).

The exact effects of gas bubble formation on sediment interparticle cohesion and friction are as yet unknown. It is likely that gas bubbles combine with pore water pressure in the sediment voids to reduce soil strength, as the total gas and water pressures increase. Also, it must be acknowledged that methane gas bubbles and pore water can be mobile from one part of the sediment sequence to another, giving rise to very localized high gas/water pressures and low sediment strength.

Geochemical and engineering tests are in progress, using a pressurized core barrel developed by Texas A and M University. Sediment strength parameters are being determined on sediment/water/gas samples maintained at their original sub-bottom pressures (Dunlap, 1979, personal communication). It is hoped that this work will help to clarify the influence of pore gas on sediment strength.

Tidal water level changes

Some nearshore and intertidal areas experience sediment slope failure, apparently related to tidal water level fluctuations. For example, Koppejan *et al.* (1949) observed intertidal flowslides in loose fine sand in Zeeland, Holland, occurring during excessive tide differences (springs) and during ebb tide between half tide and low water. The Orkdalsfjord failure in silty sand in 1930 was associated with an exceptionally low tide, although there were other contributory factors (Terzaghi, 1956). Recently Wells *et al.* (1981) documented numerous small subaqueous flowslides on intertidal mudflats in Surinam. Movements commenced in the last part of the ebb tide cycle. Pore pressures were apparently superelevated owing to partial removal of the component of normal load related to the tidal head. Terzaghi (1956) commented that the Zeeland failures were probably due to seepage pressures of groundwater returning to the ocean during the receding tide. Such seepage pressures, together with temporarily elevated pore pressures, may be similar to drawdown processes which cause failure in river banks after floods. In

macrotidal nearshore areas local slope instabilities may be more significant components of sediment transfer systems than has hitherto been realized.

Figure 10.15 attempts to summarize some of the major factors contributing to submarine slope instability. It is apparent that there are several different ways in which the critical strength/stress disequilibrium can be achieved. There are also many factor interrelationships and interdependencies. Individual failure thresholds at a specific location can be achieved by quite different combinations of the same basic factors. For example, large wave-generated bottom pressures associated with a hurricane (or earthquake stresses) will have greater effects if sediments are very underconsolidated owing to rapid sedimentation. At the same location, instability may occur owing to excess pore pressures and localized oversteepening, without wave earthquake perturbation. Clearly the worst possible conditions are likely to occur in areas where two or more factors combine. For example, gas charged, underconsolidated delta sediments in an active seismic area with high-energy surface waves are likely to be extremely unstable. This description applies almost exactly to areas of the Gulf of Alaska where many submarine instabilities have been recorded (Reimnitz, 1972; Carlson and Molnia, 1977; Hampton *et al.*, 1978). Similarly, arctic fjord environments are areas that provide a classic combination of circumstances. Bottom slopes in fjords, especially at proglacial delta margins, are frequently very steeply inclined. Rapid progradation of the delta-front slopes during the spring melt causes temporary oversteepening and increases in gravitational stresses. Furthermore, prograding arctic deltas commonly build out aprons of coarse gravels, cobbles and sands over previously deposited distal fjord bottom clays. Such a sedimentary loading condition is frequently subject to instability owing to underdrained loading of low-strength, incompetent basal sediments. There is increasing evidence of instability in arctic fjords—or former Pleistocene fjords environments (Terzaghi, 1956; Holtedahl, 1956; Bjerrum, 1971; Lewis *et al.*, 1977; Gilbert, 1978).

10.6 MAGNITUDE AND FREQUENCY CONSIDERATIONS

The magnitude and frequency of submarine instability in particular areas is difficult to assess. At present only generalizations are possible.

Firstly, the magnitude of individual slope failures is indicated by the areas of disturbed sea floor and volumes of displaced sediment (Table 10.1). Extremely large areas and volumes appear to have been involved in these processes. For example, about 40 per cent of the submarine slopes (water depth 10–200 m) of the Mississippi Delta show instability features in a survey conducted in 1978/79.

Also, it must be borne in mind that large areas of continental shelves and slopes have not yet been surveyed by modern techniques. New examples of

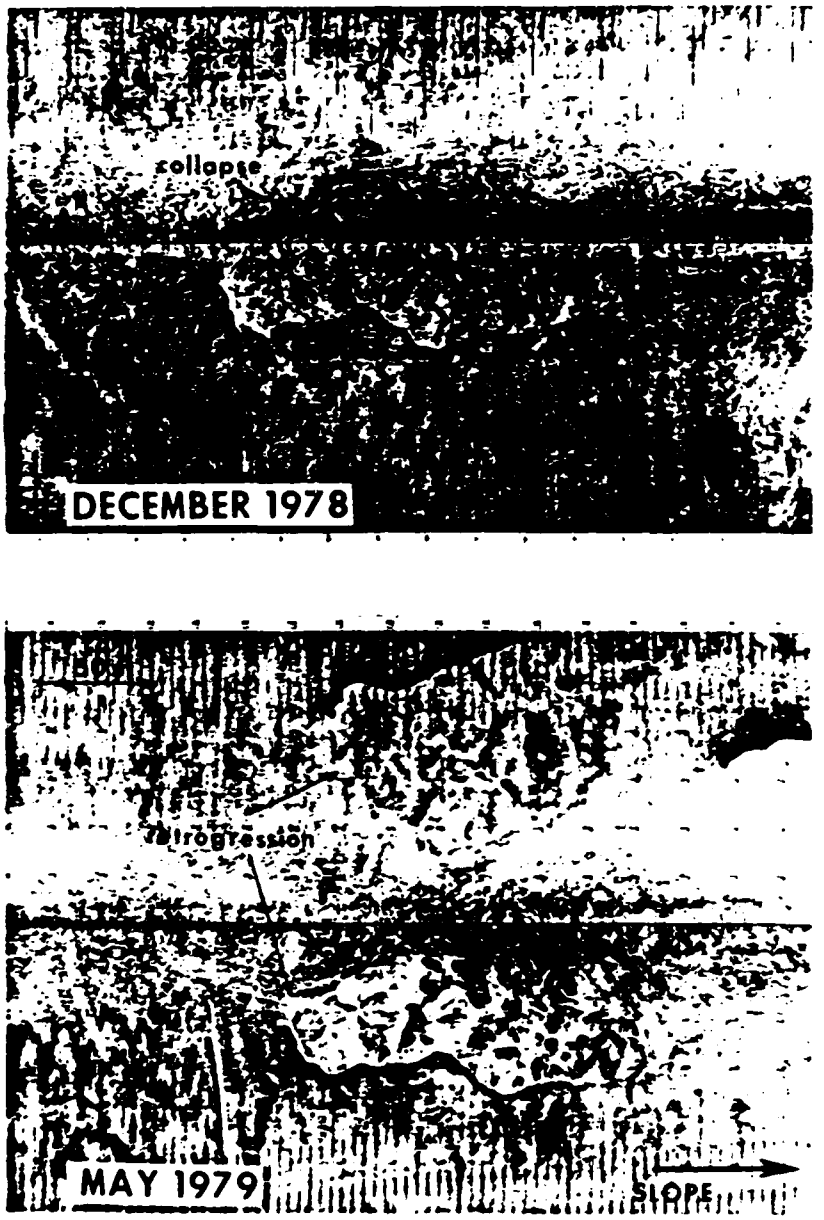

Figure 10.18. Time-lapse comparative side-scan sonar images of part of the Mississippi Delta sea floor showing instability development

submarine slope failures are frequently being discovered as surveying proceeds. Moreover, instability can be recognized only where sea floor and sediment disturbance is within the resolution of sensing techniques. Sea floor creep is predicted by stability modelling, especially on shallow-water slopes; but as yet no evidence is available for what may be a widespread and significant sediment transport process.

The age of individual slope failures is extremely variable, and ages of known features in particular areas vary from Tertiary, Pleistocene, late Pleistocene to contemporary. Broadly, modern active instabilities appear to be confined to active seismic regions or areas of continued rapid sedimentation. In many areas features of different ages are juxtaposed (e.g., Almagor and Wiseman, 1977; Coleman and Garrison, 1977). Precise dating and assessment of modern slope activity are critical questions for offshore engineering. For example, many shelf edge and intercanyon instabilities along the Atlantic coast of North America are generally believed to be of the Pleistocene age. They are attributed to rapid sedimentary loading near the shelf edge during low sea level stands, and are therefore not capable of present or future development. Projected oil and gas developments in the Baltimore Canyon region cannot rely on surmises but need definitive statements on age and activity potential.

The periodicity of instability in known active areas varies with the time base of the major causative factors. Earthquake frequency, magnitude, and epicentre location are major controls on the periodicity of failures in seismically active areas, such as the Gulf of Alaska and Pacific shelf edges of North America. Similarly, the hydrologic regimes of delta-forming rivers are significant since they control the magnitude and frequency of sedimentary loading and slope oversteepening. Heezen (1956) noted that cable breaks due to slope movements off the Magdalena Delta accompanied river floods. Also, comparisons of repeated bathymetric surveys off the Mississippi Delta have shown new slides and debris flow gullies after major floods. For example, 15 new features followed the 1922 flood, 7 in 1927, and 10 after the 1945 flood (Prior *et al.*, 1979c). Superimposed on this pattern are movements related to the frequency of hurricane incidence (Bea, 1971; Sterling and Strohbeck, 1973; Dunlap *et al.*, 1979). Recent resurveys using side-scan sonar show feature reactivation, development and enlargement of existing features, often without major triggering events. Figure 10.18 shows two sonar passes over the same section of Mississippi Delta sea floor, five months apart. An existing small collapse has enlarged, and the head of a debris flow gully retrogressed into the area, during that time.

Magnitude/frequency relationships of submarine slope failures are clearly extremely complex and as yet poorly understood. Repeated sea floor surveys, with bathymetric and sonar comparisons, such as those shown in Figure 10.18, will help to clarify movement characteristics in known active areas.

10.7 CONCLUSIONS

Mass-movement processes on submarine slopes are extremely significant to both offshore engineering and stratigraphic geology. Geologists exploring ancient marine sediment sequences, particularly for hydrocarbon resources, are now fully aware that former continental slopes and deltas have been subject to such processes on both large and small scales (e.g., Cook and Enos, 1977; Cook and Taylor, 1977). Cook (1979) reports an excellent series of exposures in Paleozoic sediments in which large-scale sliding, debris flows, and turbidity flows can be recognized. An ancient example of the progression and transformation from translational sliding to debris and turbidity flows is described. Also, stratigraphic evidence from Pleistocene deposits suggests that subaqueous fjord mass movement has been a significant process. Shaw (1977) postulates sliding accompanied by density flows/turbidity flows to account for anomalous deltaic and fjord bottom beds. Similarly, certain Pleisocene proglacial lake sequences can be fully explained only when subaqueous landsliding is invoked (Orombelli and Gnacolini, 1978). Evenson *et al.* (1977) have suggested an elegant model involving subaqueous debris flows to explain the origin of some laminated till deposits. Such 'flow tills' are common components of Pleistocene ice marginal lacustrine sediments. Such research on the record from ancient sedimentary process analogues is truly complementary to offshore process and engineering studies.

Watkins and Kraft (1978) have indicated the main research themes essential for the assessment of modern offshore slopes, including the compilation and interpretation of geologic and geophysical data from bathymetric, seismic and sonar sources; specific subsurface investigations at particular sites by drilling, coring and dating; laboratory investigations of sediment properties; and engineering analyses based on sediment properties, slope geometries and measured parameters such as pore pressures.

The two-way interaction between such offshore studies and the interpretation of the geologic results of these processes will continue to provide a better understanding of submarine slope instability mechanics and dynamics.

ACKNOWLEDGEMENTS

This research was conducted under the sponsorship of the Geography Programs and Arctic Program of the Office of Naval Research, Arlington, Virginia 22217, and of the United States Geological Survey, Marine Geology Branch, Corpus Christi, Texas.

REFERENCES

Almagor, G., and Wiseman G. (1977). Analysis of submarine slumping in the continental slope off the southern coast of Israel. *Marine Geotechnology*, 2, Marine slope instability, 349–388.

Andresen, A., and Bjerrum L. (1967). Slides in sub-aqueous slopes in loose sand and silt. *Marine Geotechnique*, 221–229.

Archanguelsky, A. D. (1930). Slides of sediments on the Black Sea bottom and the importance of this phenomenon for geology. *Bull. Soc. Nat.*, Moscow (Sci. Geol.), **38**, 38–80.

Bea, R. G. (1971). How sea floor slides affect offshore structures. *Oil and Gas J.*, 88–92.

Beck, R. H., (1972). The oceans, new frontiers in exploration. *Bull. Amer. Petrol. Explor. Assoc.*, **12**, 5–28.

Belderson, R. H., Kenyon, N. H., Stride, A. H., and Stubbs, A. R., (1972). *Sonographs of the Sea Floor: a Picture Atlas*, Elsevier Amsterdam.

Benest, H. (1899). Submarine gullies, river outlets and fresh water escapes beneath the sea level. *Geogr. J.*, **14**, 394–413.

Bjerrum, L. (1971). Subaqueous slope failures in Norwegian fjords. *Proc. 8th Conf. on Port and Ocean Engineering under Arctic Conditions*, Trondheim, Norway.

Bouma, A. H. (1962). *Sedimentology of Some Flysch Deposits*, Elsevier Amsterdam, 168pp.

Bouma, A. H., Smith, L. B., Sidner, B. R., and McKee, T. R. (1978). Intraslope basin in northwest Gulf of Mexico. In: *Framework, Facies and Oil Trapping Characteristics of the Upper Continental Margin* (A. H. Bouma, G. T. Moore, and J. M. Coleman, Eds.), Amer. Assoc. Petrol. Geologists, Studies in Geology, No. 7, 289–302.

Bryant, W. R., Antoine, J., Ewing, M., and Jones, B. (1968). Stuctures of Mexican shelf and slope, Gulf of Mexico. *Bull. Amer. Assoc. Petrol. Geologists*, **52**, 1204–1228.

Carlson, P. R., and Molnia, B. F. (1977). Submarine faults and slides on the continental shelf, northern Gulf of Alaska. *Marine Geotechnology*, **2**, Marine slope instability, 275–290.

Clifford, P. J., Germain, F. R., and Caron, R. L. (1979). A totally new approach to sea floor mapping. *Proc. Offshore Technology Conf.*, Houston, Texas, Paper 3548, 1681–1690.

Coleman, J. M., and Garrison, L. E. (1977). Geological aspects of marine slope stability, northwestern Gulf of Mexico. *Marine Geotechnology*, **2**, Marine slope instability, 9–44.

Coleman, J. M., and Prior, D. B. (1983). *Maps of the Offshore Geology of the Mississippi River Delta*, US Geol. Surv. Open File Report, Corpus Christi, Texas.

Coleman, J. M., Prior, D. B, and Garrison, L. E. (1983). Subaqueous sediment instabilities in the offshore Missisippi River delta—explanation of maps, US Geol. Surv. Open File Report, Corpus Christi, Texas.

Coleman, J. M., Suhayda, J. N., Whelan, T., and Wright, L. D. (1974). Mass movement of Mississippi River delta sediments. *Trans. Gulf Coast Assoc. Geol. Soc.*, **24**, 49–68.

Cook, H. E. (1979). Ancient continental slope sequences and their values in understanding modern slope development. In: *Geology of Continental Slopes* (L. J. Doyle and O. H. Pilkey, Eds.), Soc. Econ. Paleontologists and Mineralogists Spec. Publ. 27, Tulsa, Okla, 287–305.

Cook, H. E., and Enos, P. (Eds.) (1977). *Deep Water Carbonate Environments*, Soc. Econ. Paleontologists and Mineralogists Spec. Publ. 19, Tulsa, Okla, 174–192.

Cook, H. E., and Taylor, M. E. (1975). Early Paleozoic continental margin sedimentation, trilobite biofacies and the thermocline, western Unite! States. *Geology*, **3**, 559–562.

Coulter, H. W., and Migliaccio, R. R. (1966). *Effects of the Earthquake of 27 March 1964, at Valdez, Alaska*, US Geol. Surv. Prof. Paper 542–C.

deSmitt, V. P. (1932). Earthquakes in the North Atlantic as related to submarine cables (abstract), *Amer. Geophys. Union Trans.*, pp. 103–109 (unpublished mimeographed Western Union Co. report, 1932, revised 1936).

Dill, R. F. (1966). Sand flows and sand falls. In *Encyclopedia of Oceanography* (R. W. Fairbridge, Ed.), Reinhold, New York, 763–765.

Dingle, R. V. (1977). The anatomy of a large submarine slump on a sheared continental margin (S. E. Africa). *J. Geol. Soc.*, **134**, 293–310.

Dott, R. H. (1963). Dynamics of subaqueous gravity depositional processes. *Bull. Amer. Assoc. Petrol. Geologists*, **47**, 104–128.

Dunlap, W. A., Bryant, W. R., Bennet, R., and Richards, A. (1978). Pore pressure measurements in underconsolidated sediments. *Proc. 10th Offshore Technology Conf.*, Paper 3168, 1049–1056.

Dunlap, W. A., Bryant, W. R., Williams, G. N., and Suhayda, J. N. (1979). Storm wave effects on deltaic sediments—results of SEASWAB I and II. *Proc. Conf. on Port and Ocean Engineering under Arctic Conditions*, **2**, 899–920.

Embley, R. W., and Hayes, D. E. (1974). Giant submarine slump south of the Canaries. *Geol. Soc. Amer.* Abstracts with Program, **6**, 721.

Evenson, E. B., Dreimanis, A., and Newsome, J. W. (1977). Subaquatic flow tills: a new interpretation for the genesis of some laminated till deposits. *Boreas*, **6**, 115–133.

Fisher, R. V., (1971). Features of coarse-grained high concentration fluids and their deposits. *J. Sediment. Petrology*, **41**, 916–927.

Fleming, B. W. (1976). Side-scan sonar, a practical guide. *Internat. Hydrographic Rev.*, **LIII**, no. 1.

Flood, R. D., Hollister, C. D., and Lonsdale, P. (1979). Disruption of the Feni sediment drift by debris flows from Rockall Bank. *Mar. Geol.*, **32**, 311–335.

Garrison, L. E. (1974). The Instability of Surface Sediments on Parts of the Mississippi Delta Front. US Geol. Surv. Open File Report 74–4, 18pp.

Gilbert, R. (1978). Observations on oceanography and sedimentation at Pangnirtung Fjord, Baffin Island. *Maritime Sediments*, **14**, 1–9.

Hadding, A. (1931). *On Subaqueous Slides*, Meddelanden fran Lunds Geologisk-Mineralogiska Institution No. 47, 377–393 (reprinted from *Geologiska Foreningens, Stockholm Forhandlingar*).

Hampton, M. A. (1970). Subaqueous debris flow and generation of turbidity currents. Unpublished Ph.D. dissertation, Stanford Univ., Stanford, Calif.

Hampton, M. A. (1972). The role of subaqueous debris flow in generating turbidity currents. *J. Sedimentary Petrol.*, **42**, 775–793.

Hampton, M. A., Bouma, A. H., Sangrey, D. A., Carlson, P. R., Molnia, B. M., and Clukey, E. C. (1978). Quantitative study of slope instability in the Gulf of Alaska. *Proc. Offshore Technology Conf.*, Houston, Texas, Paper 3314, 2307–2318.

Heezen, B. C. (1956). Corrientes de turbidez del Rio Magdalena. *Bol. Soc. Geog. Colombia*, **51–52**, 135–143.

Heezen, B. C., and Drake, C. L. (1964). Grand Banks slump. *Bull. Amer. Assoc. Petrol. Geologists*, **48**, 221–233.

Heezen, B. C., and Ewing, M. (1952). Turbidity currents and submarine slumps and the 1929 Grand Banks earthquake. *Amer. J. Sci.*, **250**, 849–873.

Heezen, B. C., and Ewing, M. (1955). Orleansville earthquake and turbidity currents. *Bull. Amer. Assoc. Petrol. Geologists*, **39**, 2505–2514.

Heezen, B. C., *et al.* (1964). Congo submarine canyon. *Bull. Amer. Assoc. Petrol. Geologists*, **48**, 1126–1149.

Heim, A. (1908). Weer rezente und fossile subaquatische Rutschungen und deren lithologische Bedentung. *Neues Jahrbuch fur Mineralogie, Geologie und Paleontologie*, Bd. TI, Stuttgart, 136–157.

Henkel, D. J. (1970). The role of waves in causing submarine landslides. *Geotechnique*, **20**, 75–80.

Holtedahl, H. (1965). Recent turbidites in the Hardangerfjord, Norway. In: *Submarine Geology and Geophysics* (W. F. Whittard and R. Bradshaw, Eds.), 17th Symposium of Colston Research Society, Butterworths, London, 107–141.

Houtz, R. E. (1960). The 1953 Suva earthquake and tsunami. *Geol. Surv. Dept. Fiji, Ref. Geol. Ser.*, **61**, 13pp.

Houtz, R. E. (1962). The 1953 Suva earthquake and tsunami. *Bull. Seism. Soc. Amer*, **52**, 1–12.

Inman, D. L., Nordstrom, C. E., and Flick, R. E. (1976). Currents in submarine canyons: an air–sea–land interaction. *Ann. Rev. Fluid Mech.*, **8**, 275–310.

Jacobi, R. D. (1976). Sediment slides on the northwestern continental margin of Africa. *Mar. Geol.*, **22**, 157–173.

Knebel, H. J., and Carson, B. (1983). Small-scale slump deposits, Middle Atlantic continental slope, off eastern United States. *Mar. Geol.* (in press)

Koppejan, A. W., van Wamelan, B. M., and Weinberg, L. J. H. (1948). Coastal flow slides in the Dutch province of Zeeland. *Proc. 2nd Internat. Conf. Soil Mech. and Foundation Engng*, Rotterdam, **5**, 89–96.

Lewis, K. B. (1971). Slumping on a continental slope inclined at 1–4°. *Sedimentology*, **1**, 97–110.

Lewis, C. F. M., Blasco, S. M., Bornhold, B. D., Hunter, J. A. M., Judge, A. S., Kerr, J. W. M., McLaren, P., and Pelletier, B. R. (1977). *Marine Geological and Geophysical Activities in Lancaster Sound and Adjacent Fjords*. Geol. Surv. Canada, Paper 77–1A, 495–506.

Lowe, D. R. (1976). Subaqueous liquefied and fluidized sediment flows and their deposits. *Sedimentology*, **23**, 285–308.

Mathews, W. H., and Shepard, F. P. (1962). Sedimentation of the Fraser River delta, B. C. *Bull. Amer. Assoc. Petrol. Geologists*, **46**, 1416–1437.

Menard, H. W. (1964). *Marine geology of the Pacific*, McGraw Hill, New York, 271pp.

Middleton, G. V. (1970). Experimental studies related to problems of flysch sedimentation. In: *Flysch Sedimentology in North America* (J. Lajoie, Ed.), Geol. Assoc. Canada Spec. Paper 7, 253–272.

Middleton, G. V., and Hampton, M. A. (1976). Subaqueous sediment transport and deposition by sediment gravity flows. In: *Marine Sediment Transport and Environmental Management* (D. J. Stanley and D. J. P. Swift, Eds.), New York.

Milne, J. (1897). Suboceanic changes. *Geog. J.*, **10**, 129–146 and 259–289.

Moore, D. G. (1977). *Submarine Slides*. In: *Rockslides and Avalanches, 1: natural phenomena* (B. Voight, Ed.), Developments in Geotechnical Engineering, 14A, 563–604.

Moore, D. G., Curray, J. R., and Emmel, F. J. (1976). Large submarine slide (olistostrome) associated with Sunda arc subduction zone, northeast Indian Ocean. *Mar. Geol.*, **21**, 211–226.

Moore, J. G. (1964). *Giant Submarine Landslide on the Hawaiian Ridge*. US Geol. Surv. Res. Paper 501D, 95–98.

Morgenstern, R. N. (1967). Submarine slumping and the initiation of turbidity currents. In: *Marine Geotechnique* (A. Richards, Ed.), Univ. of Illinois Press, Urbana, 189–220.

Orombelli, G., and Gnaccolini, M. (1978). Sedimentation in pro-glacial lakes: A Wurmian example. *Zeitschrift fur Geomorphologie*, **22**, 417–425.

Prior, D. B., and Coleman, J. M. (1978a). Submarine landslides on the Mississippi delta-front slope. *Geoscience and Man*, **XIX**, 41–53, School of Geosciences, Louisiana State Univ., Baton Rouge, La.

Prior, D. B., and Coleman, J. M. (1978b). Disintegrating, retrogressive landslides on very low angle subaqueous slopes, Mississippi Delta. *Marine Geotechnology*, **3**, 37–60.

Prior, D. B., and Coleman, J. M. (1982). Submarine landslides--geometry and nomenclature. *Zeitschrift fur Geomorphologie*, **4**, 21–33.

Prior, D. B., and Suhayda, J. N. (1979a). Submarine mudslide morphology and development mechanisms. *Proc. Offshore Technology Conf.*, Houston, Texas, Paper 3482, 1055–1061.

Prior, D. B., and Suhayda, J. N. (1979b). Application of infinite slope analysis to submarine sediment instabilities, Mississippi Delta. *Engng Geol.*, **14**, 1–10.

Prior, D. B., Coleman, J. M., and Garrison, L. E. (1979a). Digitally acquired undistorted side scan sonar images of submarine landslides, Mississippi Delta. *Geology*, **7**, 423–425.

Prior, D. B., Coleman, J. M., and Caron, R. L. (1979b). Sea floor mapping using micro-computer assisted side-scan sonar. *Proc. 13th Internat. Remote Sensing Symposium*, Ann Arbor, Mich.

Prior, D. B., Coleman, J. M., Suhayda, J. N., and Garrison, L. E. (1979c). Subaqueous landslides as they affect bottom structures. *Proc. Conf. on Port and Ocean Engineering under Arctic Conditions*, Trondheim, Norway.

Reimnitz, E. (1972). Effects in the Copper River delta: the Great Alaska earthquake of 1964. In: *Oceanography and Coastal Engineering*, National Acad. Sciences, Washington, DC, 290–302.

Roberts, D. G., and Stride, A. H. (1968). Late Tertiary slumping on the continental slope of southern Portugal. *Nature*, **217**, 48–50.

Ross, D. A., and Shor, G. G. (1965). Reflection profiles across the Middle America Trench. *J. Geophys. Res.*, **70**, 5551–5571.

Ryan, W. B. F., and Heezen, B. C. (1965). Ionian Sea submarine canyons and the 1908 Messina turbidity current. *Bull. Geol. Soc. Amer.*, **76**, 915–932.

Saxov, S., and Nieuwenhuir, J. K. (Eds.) (1980). *Marine Slides and Other Mass Movements*, Plenum Press, New York.

Seely, D. R., Vail, P. R., and Walton, G. G. (1974). Trench slope model. In: *The Geology of Continental Margins* (C. A. Burk and C. L. Drake, Eds.), Springer, New York, 249–260.

Shaw, J. (1977). Sedimentation in an alpine lake during deglaciation, Okanagan Valley, British Columbia, Canada. *Geografiska Annaler*, **59(A)**, 221–240.

Shepard, F. P. (1932). Landslide modifications of submarine valleys. *Trans. Amer. Geophys. Union*, **13**, 226–230.

Shepard, F. P. (1933). Depth changes in Sagami Bay during the great Japanese earthquake. *J. Geol.*, **41**, 527–536.

Shepard, F. P. (1955). Delta front valleys bordering the Mississippi distributaries. *Bull. Geol. Soc. Amer.*, **66**, 1489–1498.

Shepard, F. P., and Dill, R. F. (1966). *Submarine Canyons and Other Sea Valleys*, Rand McNally, Chicago, 381pp.

Shepard, F. P., Marshall, N. G., and McLoughlin, P. A. (1974). Currents in submarine canyons. *Deep Sea Research*, **21**, 691–706.

Shepherd, G. L., Wipperman, L. K., and Moberly, R. (1973). Shallow crustal structure of the Peruvian continental margin. *Geol. Soc. Amer., Abstracts with Programs*, **5**, 103.

Skempton, A. W., and Hutchinson, J. N. (1969). Stability of natural slopes and embankment foundation. *Proc. 7th Int. Conf. on Soil Mechanics and Foundation Engng*, Mexico, State-of-the-Art volume, 291-340.

Stanley, D. J., and Silverberg, N. (1969). Recent slumping on the continental slope off Sable Island Bank, south-east Canada. *Earth and Planetary Science Letters*, **6**, 123–133.

Sterling, G. H., and Strohbeck E. E. (1973). The failure of the South Pass 70 'B' platform in Hurricane Camille. *Proc. 6th Offshore Technology Conf.*, Houston, Texas, Paper 1898, 719–730.

Sternberg, R. W. (1972). Predictive initial motion and bedload transport of sediment particles in the shallow marine environment. In: *Shelf Sediment Transport* (D. J. P. Swift, D. B. Duane, and O. H. Pilkey, Eds), Dowden, Hutchinson and Ross, Stroudsburg, Pa., 61–82.

Stetson, H. C., and Smith, J. F. (1938). Behavior of suspension currents and mud slides on the continental slope. *Amer. J. Sci.*, **35**, 1–13.

Suhayda, J. N. (1977). Surface waves and bottom sediment response. *Marine Geotechnology*, **2**, 135–146.

Suhayda, J. N., Whelan, T., Coleman, J. M., Booth, J. S., and Garrison, L. E. (1976). Marine sediment instability: interaction of hydrodynamic forces and bottom sediments. *Proc. 8th Offshore Technology Conf.*, Houston, Texas, Paper 2426, 29–40.

Stride, A. H., Curray, J. R., Moore, D. G., and Belderson, R. H. (1969). Marine geology of the Atlantic margin of Europe. *Phil. Trans. Roy. Soc. London, Ser. A*, **264**, 31–75.

Terzaghi, K. (1956). Varieties of submarine slope failures. *Proc. 8th Texas Oil Mech. and Engng Conf.*, 1–41.

Uchupi, E. (1967). Slumping on the continental margin south-east of Long Island, New York. *Deep Sea Research*, **14**, 635–639.

Varnes, D. J. (1958). Landslide types and processes. In: *Landslides and Engineering Practice* (E. B. Eckel, Ed.), Highway Research Board Special Report 29.

Varnes, D. J. (1975). Slope movement in the western United States. In: *Mass Wasting*, 4th Guelph Symposium on Geomorphology (E. Yatsu, A. D. Ward and F. Adams, Eds.), Geo Abstracts Ltd., Univ. of East Anglia, England, 1–18.

Walker, J. R., and Massingill, J. V. (1970). Slump features on the Mississippi fan—northeastern Gulf of Mexico. *Bull. Geol. Soc. Amer.*, **81**, 3101–3108.

Watkins, D. J., and Kraft L. M. (1976). Stability of continental shelf and slope off Louisiana and Texas—geotechnical aspects. In: *Beyond the Shelf Break* (A. H. Bouma, G. T. Moore and J. M. Coleman, Eds.), Amer. Assoc. Petrol. Geologists Short Course, New Orleans, II: B1–B34.

Wells, J. T., Prior, D. B., and Coleman, J. M. (1981). Flowslides in extremely low angle tidal flat muds, northeastern South America. *Geology*.

Whelan, T., Coleman, J. M., Suhayda, J. N., and Garrison, L. E. (1975). The geochemistry of recent Mississippi River delta sediment: gas concentration and sediment stability. *Proc. 7th Offshore Technology Conf.*, **3**, 71–84.

Whelan, T., Coleman, J. M., Roberts, H. H., and Suhayda, J. N. (1976). The occurrence of methane in recent deltaic sediments and its effects on soil stability. *Int. Assoc. Engr. Geol. Bull.*, **14**, 55–64.

Whelan, T., Ishmael, J. T., and Rainey, G. B. (1978). Gas-sediment interactions in Mississippi Delta sediments. *Proc. 10th Offshore Technology Conf.*, Houston, Texas, Paper 3166, 1029–1033.

Wiegel, R. L. (1964). *Oceanographic Engineering*, Prentice Hall, Englewood Cliffs, New Jersey.

Wilhelm, O., and Ewing, M. (1972) Geology and history of the Gulf of Mexico. *Bull. Geol. Soc. Amer.*, **83**, 575–600.

SECURITY CLASSIFICATION OF THIS PAGE

REPORT DOCUMENTATION PAGE

1a REPORT SECURITY CLASSIFICATION Unclassified	1b RESTRICTIVE MARKINGS
2a SECURITY CLASSIFICATION AUTHORITY	3 DISTRIBUTION/AVAILABILITY OF REPORT Approved for public release; distribution unlimited.
2b DECLASSIFICATION/DOWNGRADING SCHEDULE	
4 PERFORMING ORGANIZATION REPORT NUMBER(S) Technical Report No. 405	5 MONITORING ORGANIZATION REPORT NUMBER(S)
6a NAME OF PERFORMING ORGANIZATION Coastal Studies Institute 6b OFFICE SYMBOL (If applicable)	7a. NAME OF MONITORING ORGANIZATION
6c ADDRESS (City, State, and ZIP Code) Louisiana State University Baton Rouge, LA 70803-7527	7b. ADDRESS (City, State, and ZIP Code)
8a NAME OF FUNDING/SPONSORING ORGANIZATION ONR/Geography/Arctic Programs 8b OFFICE SYMBOL (If applicable)	9 PROCUREMENT INSTRUMENT IDENTIFICATION NUMBER N00014-75C-0192
8c ADDRESS (City, State, and ZIP Code) Code 425 800 North Quincy Street Arlington, VA 22217	10 SOURCE OF FUNDING NUMBERS PROGRAM ELEMENT NO. / PROJECT NO. NR 388 002 / TASK NO. 10 / WORK UNIT ACCESSION NO. 16
11 TITLE (Include Security Classification) SUBMARINE SLOPE INSTABILITY	
12 PERSONAL AUTHOR(S) Prior, David B. and Coleman, James M.	
13a TYPE OF REPORT research 13b TIME COVERED FROM 1/1/83 TO 12/31/85	14 DATE OF REPORT (Year, Month, Day) December 16, 1985 15. PAGE COUNT 37
16 SUPPLEMENTARY NOTATION In Slope Instability (D. Brunsden and D. B. Prior, eds.), pp. 419-455, 1984.	

17 COSATI CODES			18. SUBJECT TERMS (Continue on reverse if necessary and identify by block number)
FIELD	GROUP	SUB-GROUP	Submarine environment, slope instability
08	08		
08	10		

19 ABSTRACT (Continue on reverse if necessary and identify by block number)

20 DISTRIBUTION/AVAILABILITY OF ABSTRACT ☒ UNCLASSIFIED/UNLIMITED ☐ SAME AS RPT ☐ DTIC USERS	21. ABSTRACT SECURITY CLASSIFICATION
22a NAME OF RESPONSIBLE INDIVIDUAL Arlene C. Smith	22b. TELEPHONE (Include Area Code) 504-388-2395 22c. OFFICE SYMBOL

DD FORM 1473, 84 MAR 83 APR edition may be used until exhausted
All other editions are obsolete.

SECURITY CLASSIFICATION OF THIS PAGE
Unclassified

TECHNICAL REPORT NO. 406

The American Association of Petroleum Geologists
V. 68, No. 11 (November 1984), P. 1732-1743, 15 Figs., 1 Table

Distributary-Mouth Bar Development and Role of Submarine Landslides in Delta Growth, South Pass, Mississippi Delta[1]

JOHN F. LINDSAY[2], DAVID B. PRIOR[3], and JAMES M. COLEMAN[3]

ABSTRACT

Submarine landslides play a major role in the development of distributary-mouth bars and are of major importance in transporting sediment from the bar front to deeper water along the Mississippi delta front. Historic maps of the South Pass of the Mississippi delta show that the bar advanced seaward more than 1 mi (1.6 km) between 1867 and 1953. Details of the growth of the bar have been elucidated using an elaborate computer modeling program to analyze these historic maps.

The analysis has shown that the geometry of the bar was controlled by the dynamics of the freshwater plume of river water as it mixed with saline Gulf water. Approximately half the sediment deposited on the bar was moved into deeper water by submarine landslides. The underlying causes of bar failure were established during major floods with the deposition of thick blankets of unstable, water-saturated sediments on the bar front. Failure occurred one to four years later in response to a variety of triggering mechanisms, which either changed the shear strength of the sediment or modified local bottom slope. The triggering mechanisms include: major storms and hurricanes, mudlump activity, and possibly, increased pore pressures resulting from generation of biogenic gas. Bar growth and basinward movement of sediment thus represent a multivariate problem that can be approached by means of a computer analysis of bathymetric data.

INTRODUCTION

The Mississippi delta is a highly complex area sedimentologically. During the last 40-50 years it has been studied intensely, and large volumes of geologic, geophysical, and geochemical data are the result. These data show that sediment dispersal on the delta is highly variable both temporally and spatially (Fisk et al, 1954). Sediment is transported to the delta by three main distributary channels and dispersed by a variety of mechanisms (Figure 1). Deposition is rapid on the prograding bars that form at the distributary mouths, but slow in the interdistributary bays. Despite intensive study there is still much to be learned about sedimentary processes in the deeper water beyond the distributary channels.

[1]Manuscript received, August 17, 1983; accepted, February 7, 1984.

[2]Exxon Production Research Co., Houston, Texas. Current address: Bureau of Mineral Resources, GPO Box 378, Canberra, ACT, 2601, Australia.

[3]Coastal Studies Institute, Louisiana State University, Baton Rouge, Louisiana.

Evidence now available from a variety of sources suggests that the deltaic sediment dispersal system is vastly complicated by underwater landsliding or mass movements of unconsolidated materials. The occurrence of submarine slides on the Mississippi delta in water depths from 15 to 300 ft (4.6 to 91 m) is well documented (Prior and Coleman, 1978; Coleman and Prior, 1978). These slides and the damage caused by them are significant. For example, slides destroyed a platform in South Pass Block 70 and damaged two other platforms at the time of Hurricane Camille (Sterling and Strohbeck, 1973; Garrison, 1974; Bryant and Hall, 1979; Bea et al, 1975). An understanding of the mechanisms responsible for these submarine landslides is important in offshore petroleum production.

One possible approach to the study of sediment dispersal patterns and of landslide activity on the Mississippi delta is through a comparison of historic bathymetric maps. Shepherd (1955) was the first to use this technique. More recently, Coleman et al (1980) used the large-scale maps of 1874, 1940, and 1977-79 to show the regional effects of deltaic progradation and sediment redistribution caused by landslide activity.

Near the South Pass of the Mississippi delta, detailed bathymetric data covering much shorter time periods than have been studied previously are available. From 1867 to 1953 the distributary mouth area was mapped on almost an annual basis by the United States Army Corps of Engineers. The data were gathered as an aid to navigation across the approaches to the bar and the river channel at South Pass (Figure 1).

In this investigation, we analyzed this extensive data set for the first time using modern computer-processing techniques. The primary objectives of this report are to (1) analyze the temporal and spatial evolution of the distributary-mouth bar of the South Pass, (2) evaluate quantitative data on rates of sedimentation and the redistribution of the accumulated sediments, and (3) provide insights into the mechanisms controlling the historic growth and mass failure of the distributary-mouth bar.

GEOLOGIC COMPONENTS OF MISSISSIPPI DELTA SYSTEM

The modern Mississippi delta is characterized by three distinct distributaries separated by broad, shallow, interdistributary bays. Figure 1 shows these passes and the location of the study area.

General patterns of sedimentation can be defined for the delta by studying changes in the regional bathymetric maps of 1874 and 1979 (Coleman et al, 1980) (Figure 1).

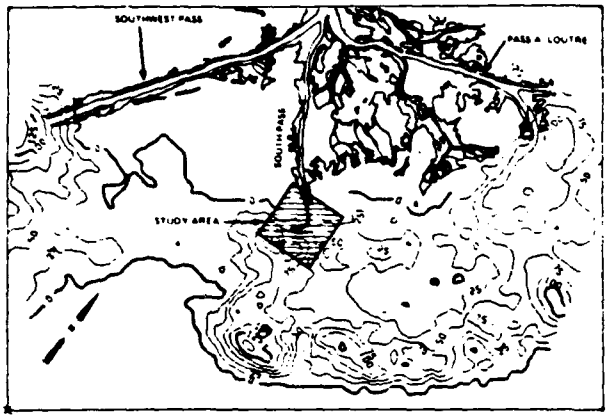

Figure 1—Map of modern distributary channels of Mississippi delta, showing contours with gross sediment accumulation from 1874 to 1979 superimposed. Study area at mouth of South Pass is outlined. Contour interval = 25 ft (7.6 m).

The data reflect the effects of both regional and local subsidence as well as those of sedimentation. The resulting map of net bathymetric change displays several different spatial components of the deltaic complex. Between South Pass and Southwest Pass is a broad, shallow, interdistributary bay where sedimentation rates are very low. Immediately seaward of each of the main distributaries, however, there is a well-defined locus of rapid sedimentation. For example, more than 100 ft (30 m) of sediment was deposited off the mouth of South Pass during the period (1867-1953). Seaward of the interdistributary bays and the passes is a U-shaped zone of intermediate sedimentation. Even farther seaward is a zone in which more than 125 ft (38 m) of sediment has been deposited over large areas. This outer sedimentary zone, which forms an apron encompassing the delta front, is particularly well developed between South Pass and Pass a'Loutre.

Such high rates of deposition cannot be explained by sedimentation from suspension. Rather, it is now recognized that the deeper water accumulations resulted from the seaward transportation and redistribution of sediments by landslides. The slopes between the distributaries and the deeper water constitute, essentially, an area of sediment bypass. Figure 1 provides for the first time a quantified regional perspective demonstrating the importance of landslide redistribution processes.

Using this regional framework, it is possible to study in detail the upper delta-front deposits in the vicinity of one of the distributaries. In particular, we will address the manner in which its development contributes to the landslide processes feeding the deeper water deposits.

Distributary Channel—South Pass

South Pass forms one of the major distributary channels of the Mississippi River (Figure 1). The earliest measurement of its discharge in 1838 suggests that the pass carried about 9% of the Mississippi River flow reaching Head of Passes. Since 1915, when more comprehensive data became available, the discharge had increased to about 16% of the total (Morgan, 1977).

In 1867, at the beginning of the period analyzed in this study, South Pass was in its natural state. Only 19% of the water entering the South Pass system at Head of Passes flowed into the open Gulf of Mexico through the main channel. The remainder was lost to the interdistributary bays, most of it through Grand Bayou (71%) and a lesser amount (10%) through smaller bayous located along the banks of the pass. The mouth of the main channel was outlined by two spits or levees formed by the dominance of marine forces over fluvial processes (Morgan, 1977).

In 1875, construction began on concrete jetties at the entrance to the pass. The jetties paralleled the original levees, but were built on their inner margins, thus slightly constricting the channel. In the following year (1876), a dam was constructed across Grand Bayou in an attempt to increase flow through the main channel. It was not, however, until 1879 that the bayou was closed more or less completely.

Thus, by 1879, the channel of South Pass was "fixed" so that most of the water entering the head of the pass flowed through a channel of known dimensions with minimum overbank loss. The present channel, which averages about 720 ft (220 m) in width, ranges somewhat in depth from around 30 ft (9 m) to slightly more than 60 ft (18 m). These variations in depth are periodic, with deeper zones about 2,000 ft (610 m) apart. A slightly deeper scour pool about 200 ft (61 m) in diameter is present at the mouth of the channel. The pool is generally asymmetric and tends to develop at the entrance end of the east jetty.

Distributary-Mouth Bar

Seaward of the scour pool at the mouth of the pass, the sea floor rises abruptly to the crest of the distributary mouth bar, which has formed since the 1875 construction of the jetties. By 1953 the bar had grown to more than 1 mi (1.6 km) in width (Figure 2).

Mudlumps, distinctive components of the bar-front area, have been described in detail at South Pass by Morgan et al (1963). These lumps are diapiric structures that result from rapid loading of fine, less dense prodelta and marine-shelf clays with the coarser, denser prograding bar and sediments. The zone of mudlump development parallels the growth of the bar front.

On the outer bar and upper delta-front slope, distinct gully systems are present and radiate outward from the bar front. The gullies emerge from disturbed or slumped topography high on the delta front. Each has a recognizable area of rotational instability, or slumping, at its upslope margin. Similarly, each feature has a long, narrow chute or channel that links a depressed hummocky source area at the upslope end to a complex of depositional lobes at the downslope end. Prior and Coleman (1978) have described in detail these elongate submarine slides, which occur all around the Mississippi delta on the delta-front slope (Figure 3). Many of these sediment failures originate on the bar front.

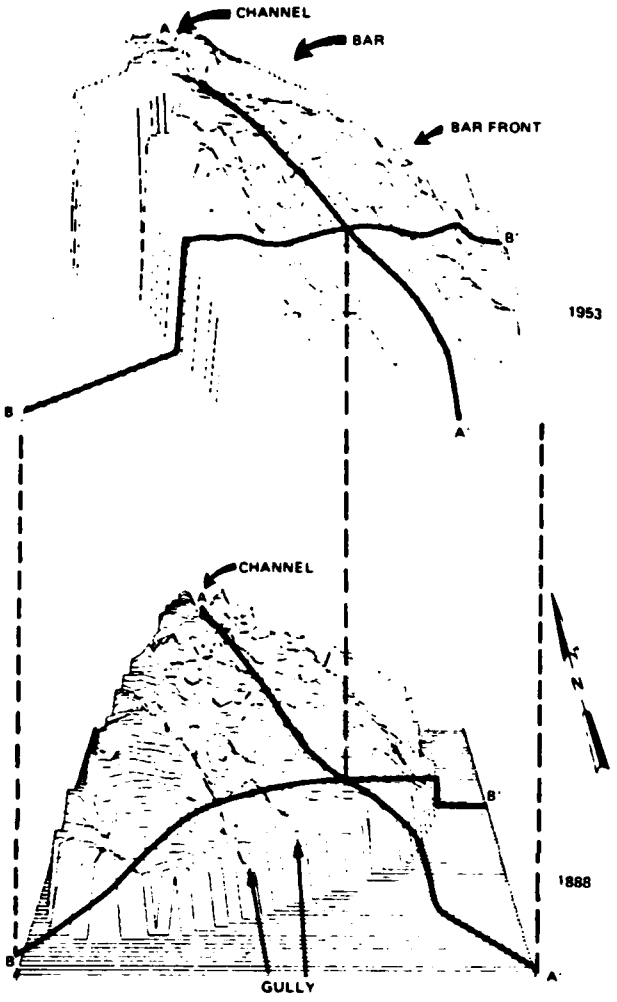

Figure 2—Perspective view of South Pass from south as it appeared in 1888 and 1953, showing section lines used throughout report. Vertical exaggeration 40:1. Note growth of bar and appearance of spit at distributary mouth. Gullies extending down bar front in 1888 acted as conduits for small mudflows. AA′, BB′ = lines of sections shown in Figures 5-13.

Many variables influence sedimentation patterns and progradation rates of the distributary-mouth bar. The bar's growth involves annual cyclical episodes of deposition: spring floods bring a net accretion and net progradation of the bar, which contrast with periods of erosion and redistribution caused by wave and current action. Computer models developed for this study allow the changing patterns of deposition over the bar to be studied in detail over a long period.

DATA ANALYSIS PROCEDURE

More than 300 bathymetric maps covering the South Pass of the Mississippi River were reviewed for the present study. Although most were published by the United States Army Corps of Engineers or its predecessor, they vary considerably in quality, scale, coverage, and temporal frequency. Few were published before 1867, and those after 1953 include only the dredged portion of the ship channel and therefore provide no information on the delta front. Ultimately, 61 maps from the period 1867 to 1953 were selected for analysis. In this period, the distributary mouth was generally mapped at least once annually, but data are missing for the following years: 1868-74, 1877-78, 1881-82, 1886, 1889, 1892-94, 1898-1901, 1906, 1946-47, 1949, 1951-53. Maps used in this study are referenced in Morgan et al (1963, Appendix A).

In general, the maps were selected to obtain the best areal coverage on a 1-yr sampling interval. If more than one map was available for a particular year, those showing original sounding data were selected over those that showed only interpreted isobaths. If there was a choice, surveys were selected from the June-July period to introduce a temporal standardization.

The analysis of this extensive data set could be accomplished only by the use of sophisticated computer techniques. A simplified flow chart of the computer analysis appears in Figure 4. In preparation for the computer analysis, it was necessary to digitize each map. However, before digitizing, the 61 maps were standardized using the following procedure. The local datum on maps published earlier than 1927 was readjusted to the North American datum. Programs were then written to generate transparent overlays individually tailored to each map. The overlays consisted of an outline marked in standardized universal transverse-Mercator coordinates. Within the map boundary, a series of fixed survey points were plotted along with the boundaries of the South Pass jetties and the lease block boundaries. It was thus possible to register the transparent overlay accurately with each individual map, regardless of scale or any other variable. Once each map had been registered with its overlay, it was digitized. Where original soundings were plotted on the map, each point was digitized and the interpreted contours were disregarded. When interpreted contours were the only data available, they were digitized at 10 points/in., regardless of map scale.

Phase I, Two-Dimensional Modeling

Once all the data were assembled in machine-useable form, the maps were gridded to produce two-dimensional square matrices of points with a standard grid interval. Each matrix consisted of 76 rows and 76 columns, with each grid point separated from the next by 200 ft (61 m). We estimated the Z-value at each grid point by selecting the nearest data point in each of 16 segments surrounding the grid point and fitting a third-order polynomial surface to the data. The Z-values at any grid point lying more than 500 ft (152 m) beyond the nearest data point were not estimated.

The resulting grids allowed the historic surfaces at each time interval to be compared directly. Standardized contour maps, perspective views of the surfaces, profiles to show surface changes, and isopach maps were then generated.

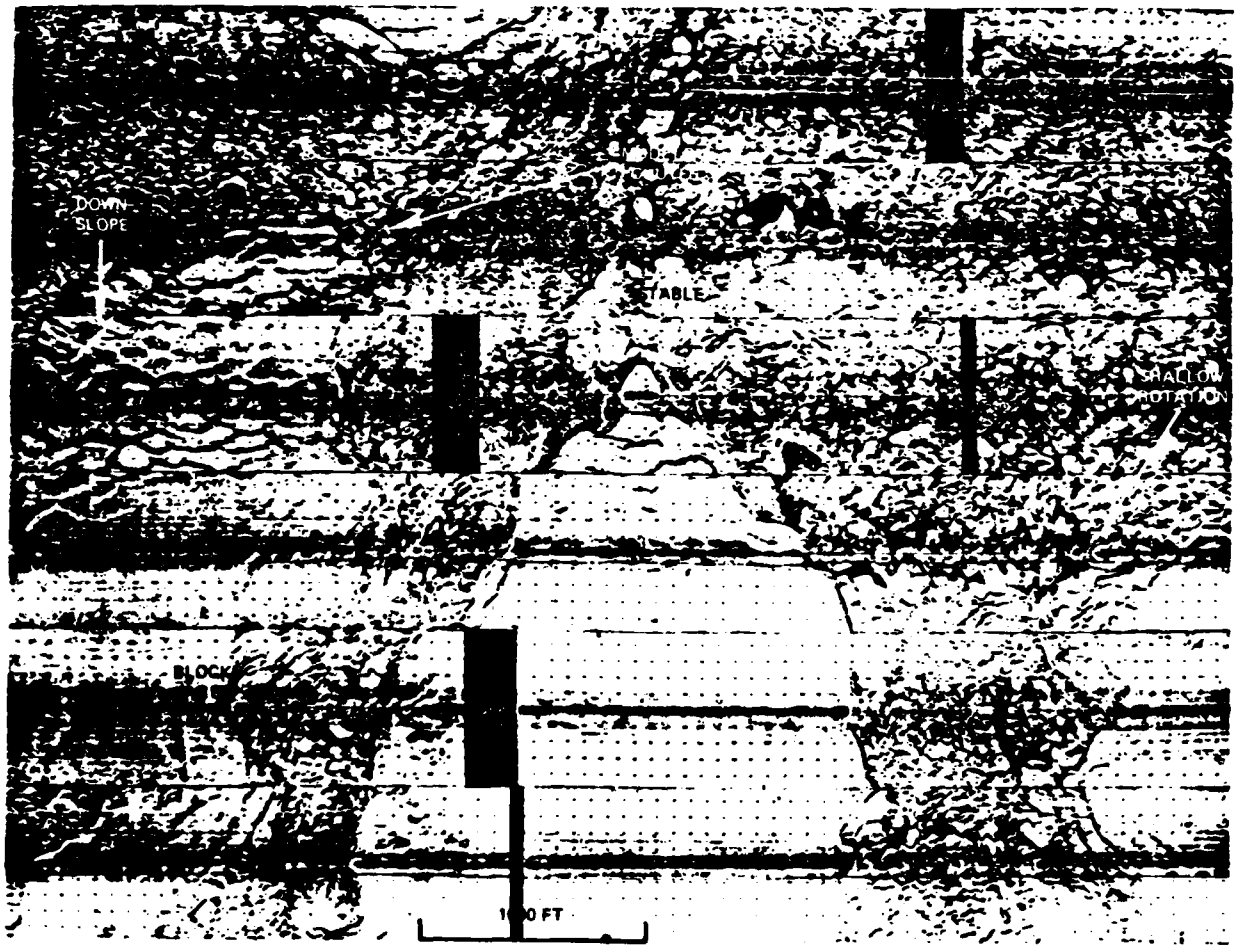

Figure 3—Sidescan sonar image of part of delta front, illustrating mudflow chutes that transport blocky sediment downslope to deeper water.

Phase II, Three-Dimensional Modeling

The standardized matrices were combined (Figure 4) in a second program to produce a three-dimensional matrix. The X- and Y-coordinates were maintained as the original map coordinates with a resolution of 200 ft (61 m), whereas the Z-coordinate became the time axis with an incremental resolution of one year. Water depth, as before, remained the independent variable. Where surveys were missing for a particular year, a dummy matrix with blank characters was inserted. The blanks were later filled by vertical, linear interpolation through each column of the matrix.

To obtain a three-dimensional model of deposition rates, the first matrix was simply duplicated on magnetic disk and the Z-axis was shifted by one unit—i.e., one year. A third matrix was created by subtracting the original matrix from the duplicate to produce annual deposition rates.

RESULTS

The three-dimensional models of bathymetry and depositional rate allow us to (1) view the evolution of the bar in the long-term perspective by studying its overall growth patterns; and (2) dissect the models and study the short-term components of the longer term growth patterns.

Long-Term Bar Progradation

Using the sedimentation rates determined from bathymetry (available in the form of a three-dimensional matrix), the gross accumulation, gross erosion, and net accumulation were determined (Figures 5, 6, 7). This assessment was made by summing positive and negative sedimentation rates separately through each vertical column of the matrix. Figure 5 shows the apparent gross accumulation of sediment over the bar between 1867 and 1953. The word apparent is used because bathymetric changes do not take account of the consolidation history of particular sediment inputs and because the effects of mudlump growth cannot be isolated easily from those of deposition. The mean gross deposition over the bar during the study period is approximately 100 ft (30 m), or an average accumulation rate of 1.2 ft/yr (37 cm/yr).

Maximum gross accumulation occurred at the bar proper and declined sharply in a seaward direction. The

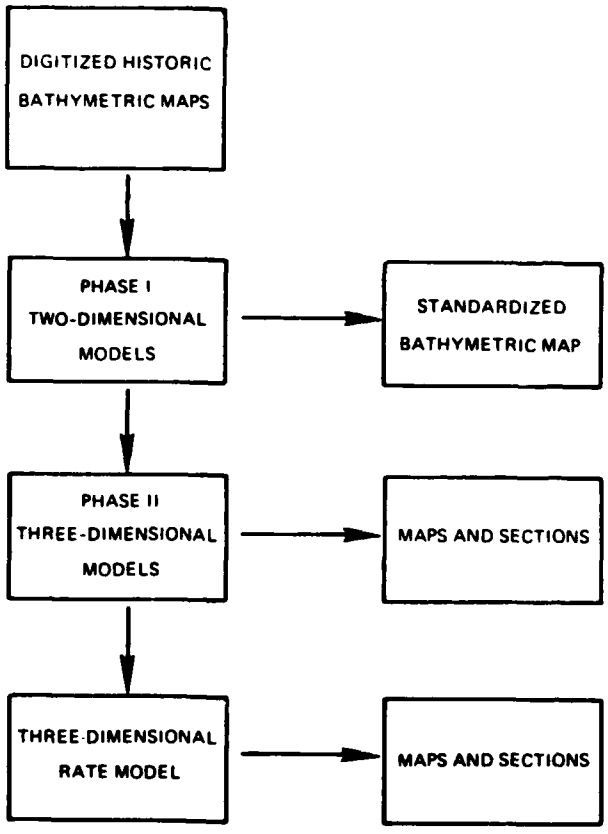

Figure 4—Flow chart outlining steps followed in data reduction.

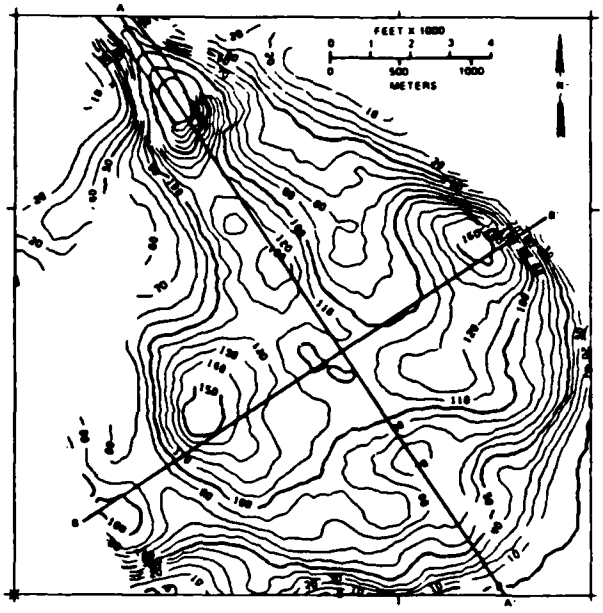

Figure 5—Map of South Pass showing gross accumulation of sediment from 1867 to 1953. Note symmetrical bimodal distribution of sediments on bar. Contour interval = 10 ft (3 m).

sediment was not deposited in a single symmetric mound immediately seaward of the distributary mouth; rather, the distribution is bimodal. The two modes lie approximately 8,000 ft (2,440 m) seaward of the distributary mouth and about 4,000 ft (1,220 m) lateral to the bar's axis of symmetry. Each mode represents slightly more than 150 ft (46 m) of gross accumulation. On this long time base, the bar growth thus appears extremely symmetric and regular, a fact that masks the less regular short-term growth patterns.

Gross erosion in the same time period shows a strongly similar, though less symmetric, inverse distribution (Figure 6). That is, sediment is lost from areas where deposition has been most rapid. Gross erosion equals approximately 50% of the gross sedimentation, meaning that about half of the sediments deposited on the bar are eventually moved on into deeper water.

As a result of this inverse relationship between gross sedimentation and accumulation, the net accumulation (Figure 7) was relatively unimodal. Fifty to 80 ft (15 to 24 m) of sediment has been added to the bar front in the form of an elongate lobe that thins sharply both landward and seaward. Laterally, the sediment lobe extends about 1.5 mi (2.4 km) on either side of the bar's axis of symmetry.

The symmetrical bimodal distribution of sediments about the distributary mouth (Figure 5) is not easy to explain. However, the fact that the symmetry of the gross accumulation pattern is so ideal suggests that it relates to the mechanics of flow of the river-water plume entering the ocean rather than to some other less regular, stochastic process such as mudlump growth.

Waldrop and Farmer (1974) performed a numerical simulation of the stream flow at South Pass. They found that a buoyant plume was created as the fresh water of the river flowed out over the surface of the denser, saline Gulf waters. Under such circumstances, two almost symmetrical vortices develop in the plume. The vortices aid in mixing salt and fresh water by convecting higher density bottom water to the surface. Dye experiments and salinity measurements in the field suggest that such mixing patterns are present at South Pass (Waldrop and Farmer, 1974; Wright and Coleman, 1971). Thus, sedimentation patterns are controlled by the symmetry of the plume, as its vortices carry sediment outward from the center. At the same time, the plume is decreasing in velocity laterally and away from the distributary mouth.

The less-regular bimodal symmetry of the gross erosion is a direct function of the distribution of accumulating sediments. As discussed in a following section, much sediment loss is due to bar-front failures that occur in recently deposited sediments. The overall temporal and spatial relationships between deposition and slope failure control the shape of the bar.

Short-Term Bar Progradation

Although it is instructive to view the evolution of the bar from a long-term perspective, such an approach provides only a limited insight into the local mechanisms involved in the overall pattern of growth. For example, short-term changes in flood patterns combined with periods of localized and severe erosion, or bar-front slope instability, can

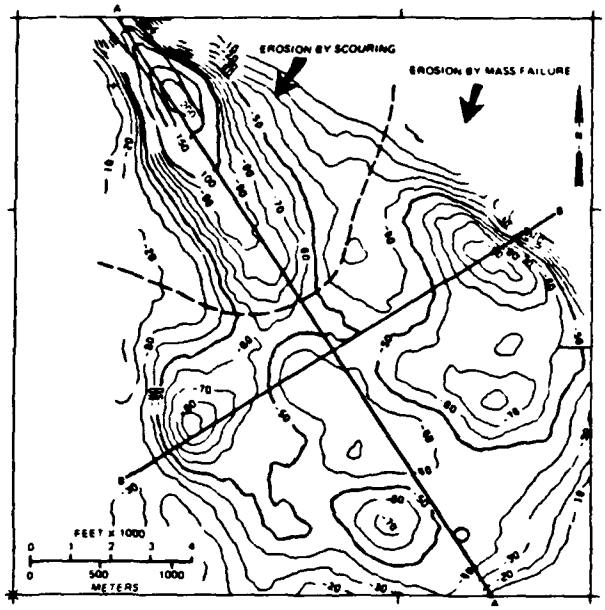

Figure 6—Map of South Pass showing gross erosion of sediment during 1867 to 1953 period. Contour interval = 10 ft (3 m). Note bimodal nature of distribution.

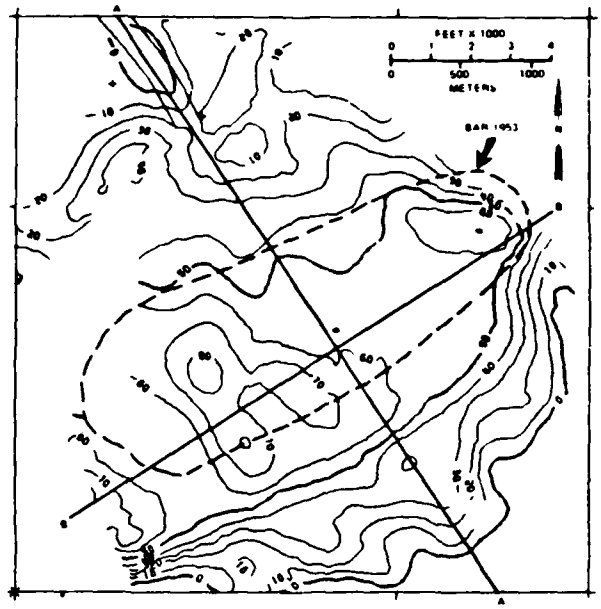

Figure 7—Net accumulation of South Pass distributary-mouth bar between 1867 and 1953. This map is sum of maps in Figures 5 and 6. Contour interval = 10 ft (3 m).

radically influence the short-term growth patterns. These significant events may occur in a short period of time, but are masked in the long term by other factors.

The results of these shorter term effects are evident in Figure 8, which is a longitudinal section through the three-dimensional model of bathymetry and time. The section (Figure 2, section AA') extends down the distributary channel and out to sea across the distributary-mouth bar in the direction of maximum progradation. Because the time axis is expressed in increments of one year, the historic development of the bar can be viewed directly.

If, for convenience, the edge of the distributary-mouth bar is defined as the 30-ft (9-m) isobath, one can see that the bar has widened considerably since the jetties were built in the mid to late 1870s. In 1875 the bar did not exist, but by 1953 it was approximately 1.1 mi (1.8 km) wide. It is clear, however, that although there is an overall increase in the bar's width, its growth has been irregular. During the period between 1910 and 1940, for example, the top of the bar had been scoured and rebuilt regularly. This scouring also coincides with a deepening of the distributary channel close to its mouth, although the scour pool described earlier, just at the channel mouth, appears to be a fairly stable feature. In some places, the scouring of both the channel and the bar can be related to major flood episodes. For example, at least 20 ft (6 m) of sediment was removed from part of the bar during the severe flood of 1927 (Figure 9). Some scouring of the bar likewise occurred during the large floods of 1922 and 1937.

The growth patterns along the bar front are also complex (Figures 8, 9). The overall pattern is one of seaward shallowing with time; i.e., the bar front is advancing into deeper water. The advance of the bar front was not always continuous or regular. At times it advanced rapidly, whereas at other times it apparently retreated for short periods. Almost all periods of sudden retreat were preceded by periods of rapid advance (Figure 8).

In all cases, the rapid advance of the bar was associated with major floods. Generally, during these periods, both the river channel and the bar crest were scoured while large volumes of sediment were being added to the bar front.

A sudden retreat of the bar generally occurred 1-4 yr after a flood. The retreat was rapid, and in each case was apparently caused by a large-scale failure of the bar front. Such well-defined cycles involving flood-related growth of the bar followed by slope failure a short time later can be associated with the major floods (Table 1).

Sections through the three-dimensional rate model show clearly the relationship between the bar and the bar front (Figures 10, 11). The data portrayed on these sections have been reduced to their simplest binary form—deposition vs. erosion. In Figure 10, an axial section, growth of the bar proper was erratic. Random alternations from erosion to deposition occurred with little net change. Along the bar front the pattern is more predictable, with landslides appearing as clearly defined horizontal erosional stripes. Rapid sedimentation on the bar front during major floods was followed by loss of sediment caused by the subsequent slope failure. In the larger events in 1927 and 1939, the zone of sediment loss extends beyond the seaward limit of the data. For some of the smaller events, however—in 1891, 1922, and 1945, for example—the zone of sediment loss simply pinches out laterally.

In Figure 11, which is a section at right angles to the axial section of Figure 10, the reason for this geometry is clear. The erosional landslides became mudflows that were channeled in a seaward direction down gullies or chutes on the delta front (Figure 2). The gullies or chutes were probably parts of the elongate slides described by Prior and Coleman (1978). This suggests that bar-front erosion related

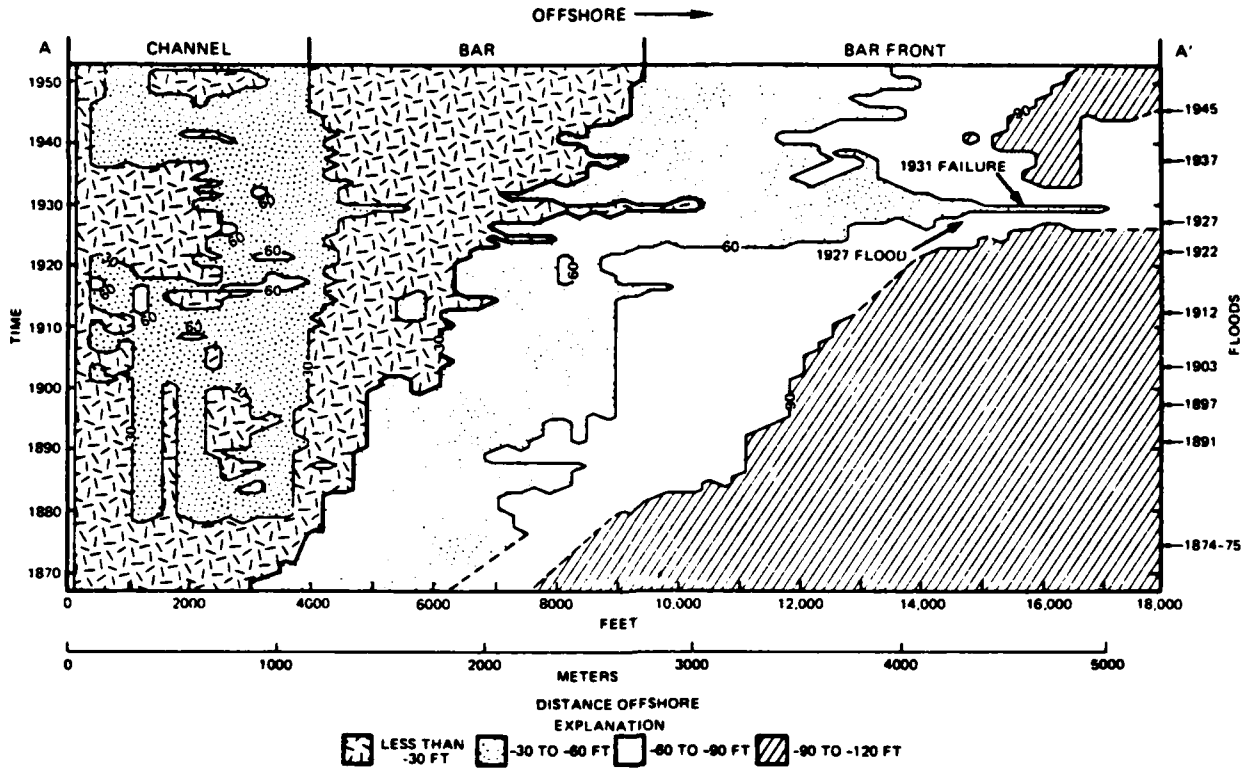

Figure 8—Section AA′ (Figure 2) through three-dimensional bathymetric model. Figure shows changes in position of bathymetric contours through time. Arrows along right margin of diagram indicate occurrence of extreme flooding conditions. Note rapid growth during 1927 flood and retreat owing to 1931 bar-front failure.

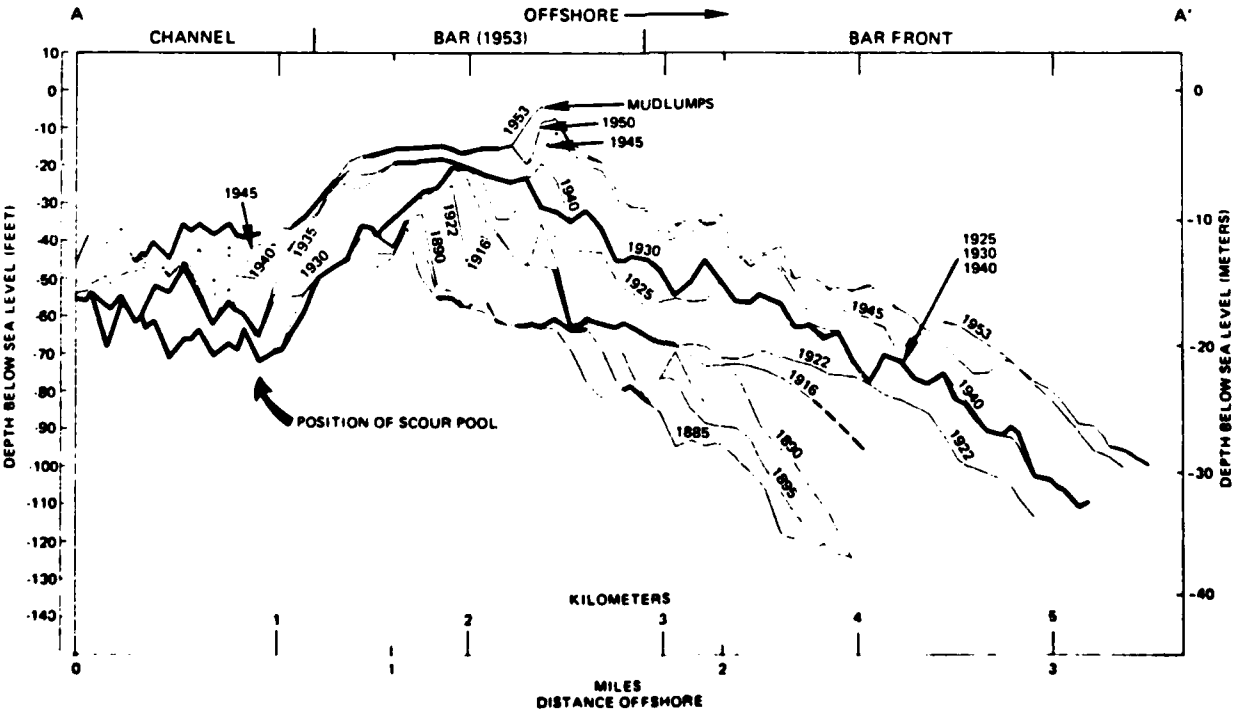

Figure 9—Section AA′ (Figure 2) across distributary-mouth bar at South Pass showing depositional surfaces. Erosion surfaces are indicated by heavy lines. Major erosional surface reflects 1927 flood and subsequent failure of 1931. Note backfill behind bar following 1927-31 events.

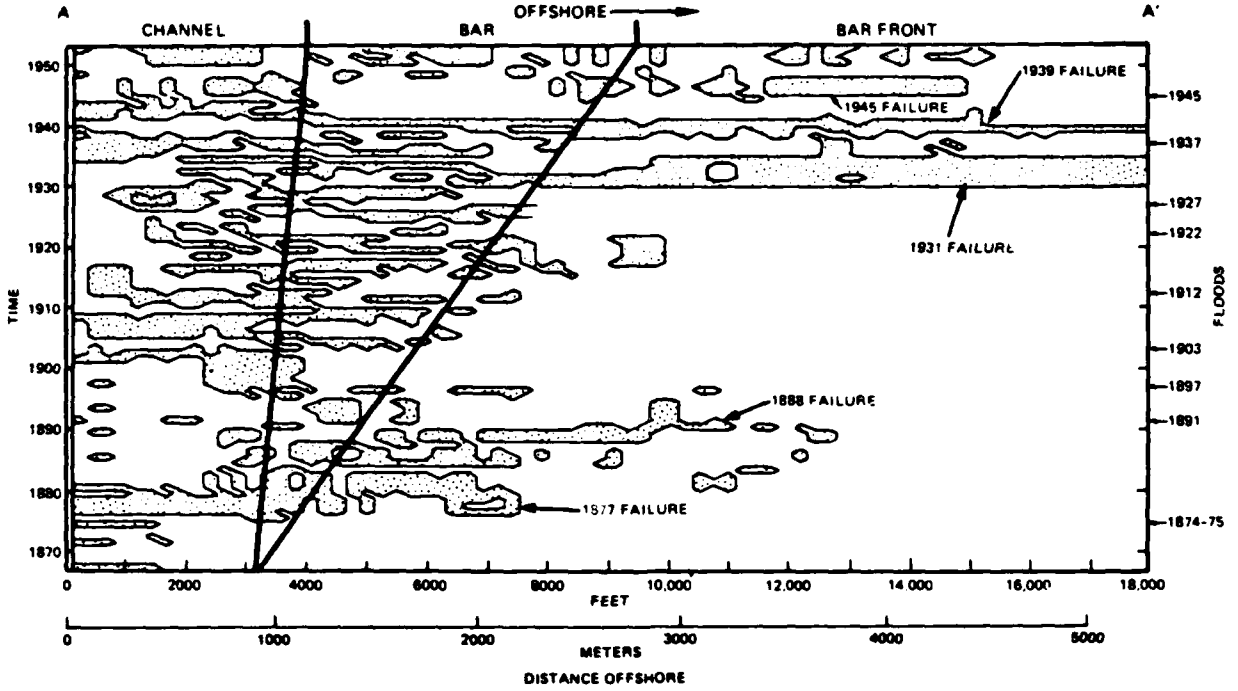

Figure 10—Section AA′ (Figure 2) across distributary-mouth bar through three-dimensional depositional-rate model. Stippled areas are periods of erosion; unpatterned area represents periods of accumulation, or no change. Broadening of erosional bands is artifact of computational method. Amount of broadening is determined by frequency and areal extent of historic maps.

to slope failure may have far-reaching consequences on the delta front, because one slump triggers the next, causing sediment to cascade basinward down these gullies.

Effects of the 1927 Flood

Periods of rapid progradation of the bar and subsequent loss of sediment from slope failure can be linked with major floods. Of all the events documented between 1867 and 1953, the flood of 1927 is by far the most significant. Not only was the flood discharge the largest on record for the Mississippi River, but it also resulted in the greatest recorded progradation of the bar and, subsequently, the largest recorded bar-front retreat caused by the slope failure processes.

The discharge of the 1927 flood was 2.05×10^6 ft^3/sec (5.80×10^4 m^3/sec)—20% greater than in any other major flood during the period of study. The flood removed as much as 30 ft (9 m) of sediment from the back of the bar in the scour pool, and it spread a blanket of sediment from 25 to 55 ft (8 to 17 m) thick across the whole bar front and beyond the mapped area (Figure 12).

Viewed in the long term, the slope of the bar front was surprisingly constant. Typically, the slope ranged from 0.6° to 2.3°, with slopes of 1.2° being most common. Only around active mudlumps and in the vicinity of the sandspit extending to the southwest from the distributary mouth were these values exceeded. Slope changes after the 1927 flood were likewise minimal if viewed in a broad context (Figures 12, 13). The slope increased in the confined area along the bar front by as much as 2°. This local oversteepening was probably of critical importance to slope stability.

Table 1. Discharge of Mississippi River During Major Floods

Year	Ft^3/Sec	M^3/Sec
1874-75	?	?
1891	1.69×10^6	4.79×10^4
1897	1.70×10^6	4.81×10^4
1903	1.59×10^6	4.50×10^4
1912	1.70×10^6	4.81×10^4
1922	1.69×10^6	4.79×10^4
1927	2.05×10^6	5.81×10^4
1937	1.47×10^6	4.16×10^4
1945	1.52×10^6	4.30×10^4

The bar-front retreat appears to have occurred in early 1931; the bar was partially mapped in August of that year, and by that time, erosional removal by slope failure had occurred. As is evident on Figure 12, the thickness of the failed sediments closely followed the patterns of deposition during the 1927 flood. In general, 50 to 90% of the thickness of sediments that accumulated during the flood was lost in the failure. In only a few exceptional areas were pre-flood sediments removed by the failure. The failure was generally confined to the areas that had undergone recent rapid deposition.

Slope changes resulting from the failure are almost the exact inverse of those caused by the 1927 flood (Figure 13). The slope increased significantly (up to 2°) over the

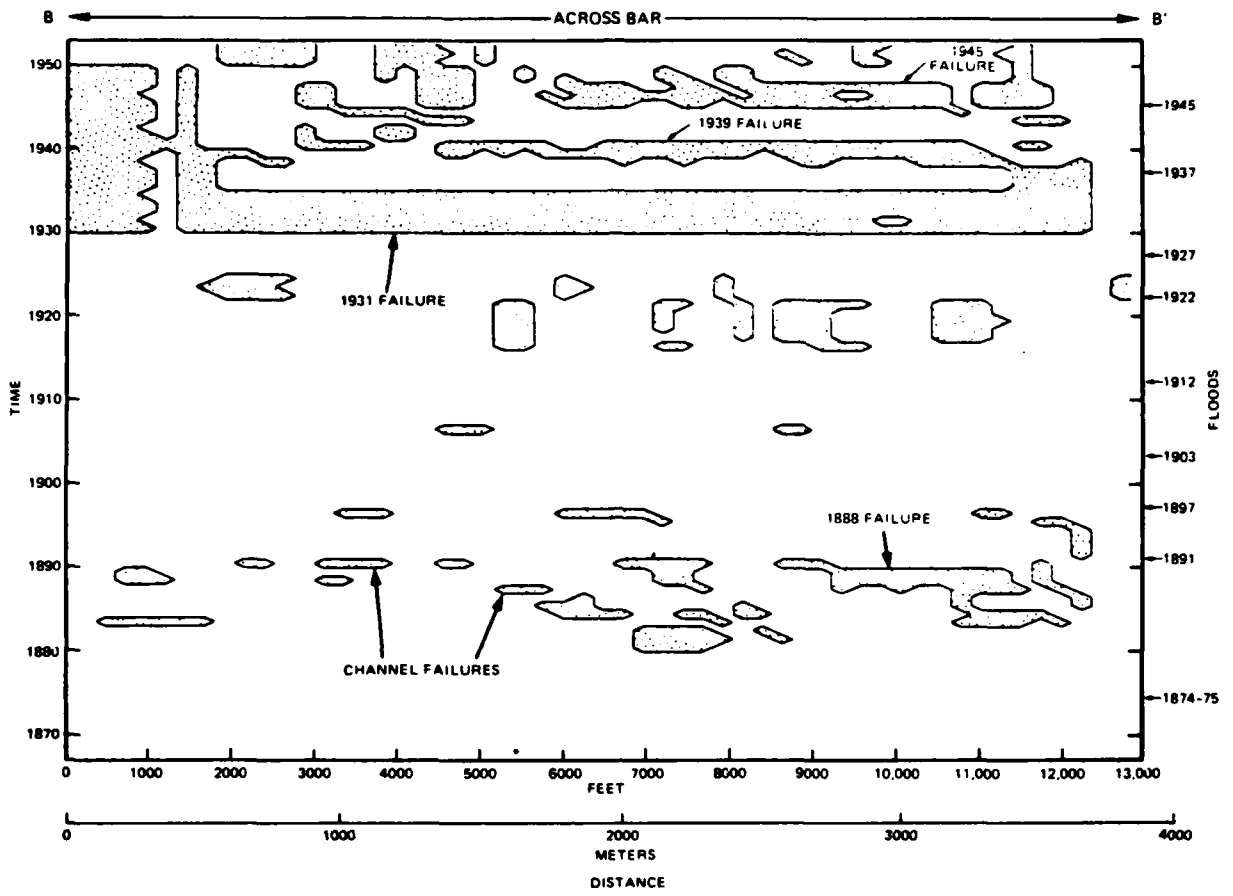

Figure 11—Section BB′ (Figure 2) through three-dimensional depositional-rate model. Arrows indicate major floods. Stippling indicates periods of erosion, as on Figure 10. Note that major failures extend across width of diagram, whereas lesser failures in 1880s and 1890s were confined to channels.

bar crest and to a lesser extent over the bar front. A noticeable decrease in slope occurred at the bar front following failure. Slope instability thus appears to have returned the bar to an equilibrium state by reducing the slope angles in the area that had been oversteepened during the previous flood event. It appears that oversteepening of the bar front because of rapid deposition during major floods is an important cause of bar-front instability.

Triggering Mechanisms

The data suggest that some of the basic conditions leading to slope failure on the bar front were established by large floods. The sediments deposited during these floods were water-saturated and, at least locally, the bar front became oversteepened. However, other variables appear to be contributing to slope failure. If rapid deposition was the only factor, failure might be expected to occur immediately after deposition. However, the sediments did not slide immediately but, rather, remained in place from 1 to 4 yr before becoming unstable. For example, a 4-yr lag occurred between the deposition of the 1927 flood sediments and the subsequent failure. The evidence clearly suggests that for slope failure to occur, a large flood must first establish conditions conducive to failure; however, an additional triggering mechanism must also be involved.

Two sets of variables determine sediment stability on the bar front—those that induce failure and those that resist it. The forces inducing failure are, primarily, gravity controlled, and the two most important factors are slope and sediment density. The forces resisting failure are essentially determined by sediment shear strength in which pore-fluid pressure plays a major role. For a slump to be triggered, one of these two general sets of variables must be affected.

Slope angle can increase in many ways. As previously noted, sediments deposited during major floods locally oversteepened the bar at the time of deposition. It also seems likely that deposition during lesser flood stages and reworking of the bar crest by waves could contribute to oversteepening as well. However, one direct cause of local slope-oversteepening is mudlump growth, and this phenomenon appears to be a significant factor.

As observed earlier, mudlump formation is an inherent part of a bar's growth. Mudlumps are diapiric structures that, once generated, may significantly alter a bar's stability. They push rapidly to the surface, causing sudden oversteepening of the bar-front sediments.

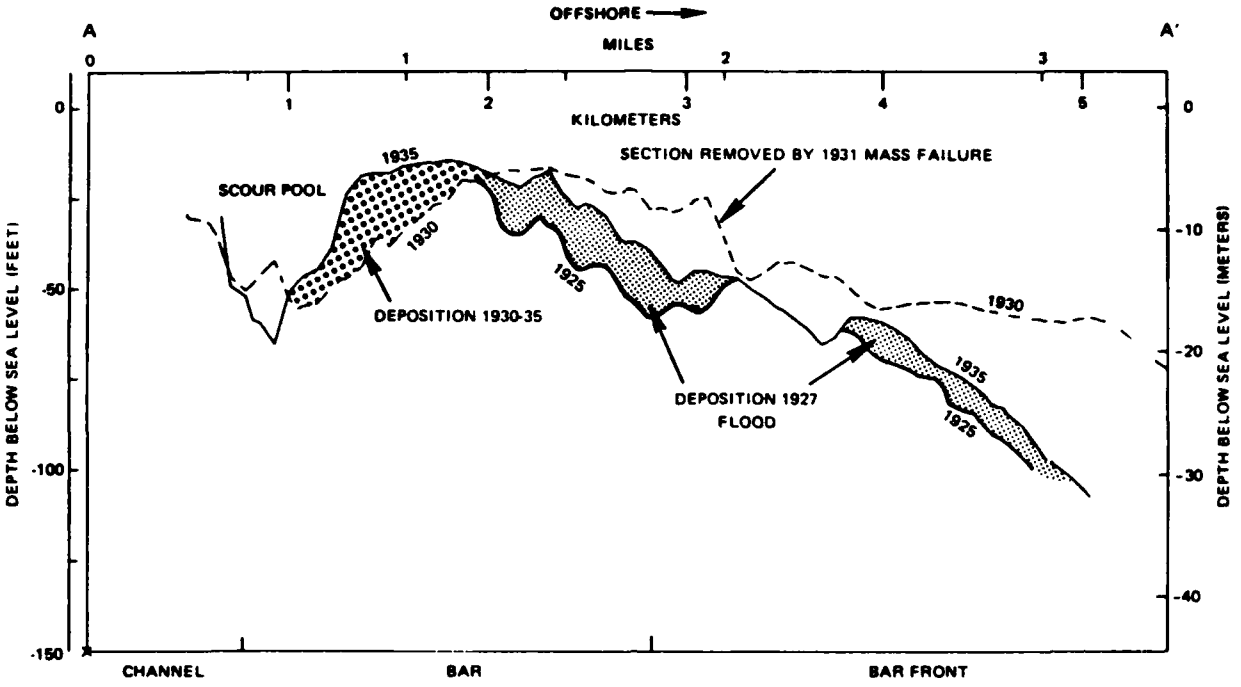

Figure 12—Longitudinal section (AA′) (Figure 2) across distributary-mouth bar showing sediments accumulated during 1927 flood and then subsequently lost owing to 1927 bar-front failure. Note that failed sediments were mostly deposited during 1927 flood.

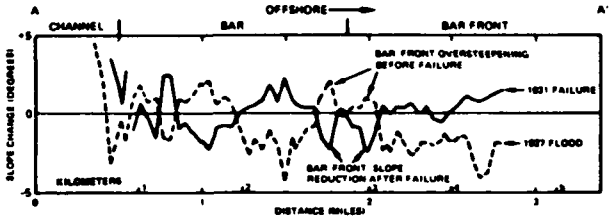

Figure 13—Section AA′ (Figure 2) across distributary-mouth bar showing slope changes brought about by 1927 flood and 1931 failure. Note that two curves are generally antipathetic.

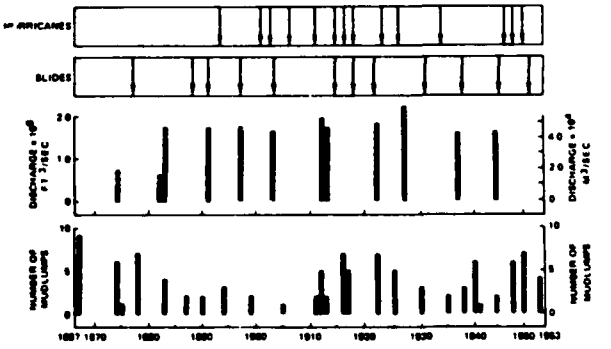

Figure 14—Temporal relationship among major variables influencing bar growth at South Pass. Vertical bars show discharge (middle graph) through South Pass during periods of major flooding and number of mudlumps (lower graph) appearing for first time during any one year. Arrows indicate passage of hurricanes within 100 mi (160 km) of site and occurrence of major bar-front failures. Such failures tend to occur 1-4 yr after major floods.

During the 1867-1953 study period, the appearance of mudlumps at South Pass has varied considerably. As many as nine mudlumps appeared in some years, whereas in other years there was no activity. Overall, there is a rough cyclicity in the timing of mudlump activity. The cycles appear to be about 30 to 40 yr long, with major periods of activity around 1878, 1917, and 1950 (Figure 14). Mudlump formation could, therefore, act as a trigger in any single event. However, mudlumps cannot be the sole trigger mechanism, for there were long periods when activity was negligible, yet failures still occurred.

The conditions governing variations in sediment strengths in this environment are difficult to determine precisely; moreover, the role of pore-fluid pressure in the failure of underconsolidated marine sediments is difficult to assess. Suhayda and Prior (1978) suggest that pore pressures in the delta region approach geostatic values and may be an important cause of failure on these low-angle slopes. However, if pore-fluid effects are included as part of sediment strength, the factor of safety (F) is simply the ratio of the forces resisting failure (sediment strength) to those tending to cause failure (gravitational). Thus,

$$F = 2\,Cu/\rho' h \sin 2\beta, \qquad (1)$$

where Cu is the average undrained shear strength of the sediment, ρ' is the submerged density of the sediment, h is the thickness of the failed slab, and β is the slope of the depositional surface.

With the mechanisms controlling failure reduced to these simple terms, the computer could be used to carry

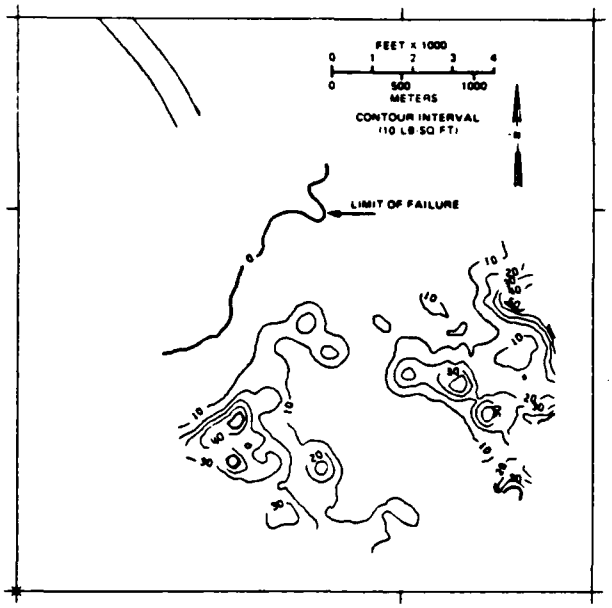

Figure 15—Map showing undrained shear strength of soil at South Pass at instant that bar front failed in 1931. Strengths (lb/ft^2) were calculated on assumption that pore-fluid pressure was insignificant. Entrance to South Pass channel appears at upper left. Contour interval = 10 lb/ft^2 (0.5 kPa).

out a series of matrix operations on the gridded map data to provide a complete areal analysis of the 1931 failure following the 1927 flood. At the instant of failure, the safety factor F, by definition, should have been 1.0. The local submerged sediment density (ρ') is relatively constant at 31 lb/ft^2 (1.48 kPa), and β, the slope, can be calculated directly from the surface as mapped immediately before the failure. It is here assumed that the subsurface failure plane was roughly parallel to the surface slope. The thickness of the failed slab can be determined from the bathymetric surfaces mapped before and after the event if we assume that all the failed material was carried beyond the study area. By using these parameters, it becomes possible to calculate Cu, the shear strength of the sediment, at the instant of failure.

The results of such an analysis, plotted spatially across the bar-front area, appear in Figure 15. The map shows the distribution of soil strengths that are conducive to failure (for F = 1), given local values of slope geometry. The map shows that in a large part of the area, sediment shear strengths must be as low as 10 lb/ft^2 (0.5 kPa) for F = 1. That value is almost an order of magnitude lower than measured soil strengths from this part of the Gulf of Mexico. Locally, in gullies where the thickness of failed material is greater, sediment shear strengths of 60-70 lb/ft^2 (2.9-3.4 kPa) would result in failure. A similar analysis was made of the 1939 failure, following the 1937 flood, with almost identical results. Calculated sediment strengths at failure were, if anything, lower in 1939 than in 1931.

At least two possible interpretations of this analysis are evident. (1) Local slope angles are actually greater than envisioned in our analysis. Such steep slopes may exist below the limit of bathymetric resolution, or they may be induced by mudlump uplift; or (2) sediment shear strengths at failure are, indeed, much lower than the strengths normally measured, perhaps the result of very high excess pore-fluid pressures.

Possible explanations for the high pore-fluid pressures are relatively few. An external mechanism might be the passage of large storm waves—in particular, those generated by hurricanes—causing an elevation in fluid pressure because of cyclic loading. Internal mechanisms possibly include fluid migrations from deeper sediment sources or increases owing to the in-situ generation of organic gases.

Major hurricanes are common occurrences along the northern coast of the Gulf of Mexico, particularly in the vicinity of the Mississippi delta. Waves generated by the passages of these storms may, under certain conditions, trigger submarine landslides by a combination of cyclic loading and heightened pore-fluid pressures, and from stress generated by wave-sea-floor interaction. The failures that occurred during Hurricane Camille in 1969 are well documented (Sterling and Strohbeck, 1973; Bea et al, 1975; Garrison, 1974; Bryant and Hall, 1979). Dunlap et al (1978) found that during storms, sediment pore-fluid pressures responded cyclically to wave-induced bottom pressures and, thus raised, could induce sediment failure.

To assess these relationships in a longer term, data were assembled for all hurricanes passing within 100 mi (160 km) of South Pass during the historic period. The results are shown in Figure 15. Only two well-defined failures can be associated with these hurricanes. All other events, including the major failure of 1931, occurred in years when there were no hurricanes. It would thus seem that although such storms are capable of causing failures of the bar front, they are not the only triggering mechanism. Lesser storms such as winter storms are not as well documented. However, movements of the bottom do occur in association with winter storms. For example, numerous pipeline breaks attributed to sediment movement in the delta region were associated with the winter storms of January 1983. The data base for correlating winter storms with bottom movements has not yet been synthesized.

Finally, an additional (but little understood) mode by which soil strength is weakened involves the generation of methane gas within the sediments. Certainly, gas-charged sediments are seen commonly on high-resolution profiler records over large areas of the Mississippi delta front, suggesting that they are an important constituent of the delta sediments. Whelan et al (1978) has suggested that biogenic methane gas might be a significant factor in the reduction of sediment shear strength. If biogenic gas generation is involved in weakening sediment, it may well account for the lag of up to 4 yr between the deposition of flood sediments and their subsequent failure.

CONCLUSION

The growth of the South Pass distributary-mouth bar is governed by a composite system of variables with a complex feedback mechanism. Primary sedimentation over the bar is controlled by the annual flood cycle. The sediments deposited during floods are generally underconsoli-

dated and have a high water content and high pore-water pressures. Sediment influxes to the bar front during floods cause oversteepening in critical areas, which in turn loads the underlying sediments. When flood conditions are extreme and sedimentation rapid, the blanket of newly deposited sediment is susceptible to failure, so that even a small change in prevailing conditions (gas content, wave perturbations) may trigger a landslide.

Triggering mechanisms are associated with two variables: slope of the bar front and pore-fluid pressure. The most likely cause of local oversteepening, apart from the sedimentation process itself, is mudlump growth, a feedback mechanism caused by the loading of the underlying prodelta sediments. Pore-fluid pressure may be increased by the passage of large storm waves, particularly during hurricanes. Increased pore-fluid pressure resulting from the internal generation of organic gasses is a possible, but as yet unproven, mechanism.

Two- and three-dimensional modeling of the South Pass of the Mississippi delta has led to several conclusions concerning the development of a distributary-mouth bar and the generation of submarine landslides at the bar front. The most important of these conclusions can be briefly stated.

1. The South Pass distributary-mouth bar has prograded more than 1.1 mi (1.8 km) during the period from 1867 to 1953, with a mean net sedimentation rate of 1.2 ft/yr (37 cm/yr).

2. Sediments accumulate in a symmetrical, bimodal pattern over the bar. The unexpected bimodal distribution is probably a direct function of river plume dynamics.

3. Approximately 50% of the sediment deposited on the bar is ultimately transported to deeper water by landslides.

4. Growth of the bar in the short term is erratic, responding to deposition by major floods and later failure of the bar front.

5. Bar-front failures occur one to four years after the major flood event and involve only the sediments deposited during the last major flood. These sediments are underconsolidated and potentially unstable, and movement may be initiated by several of the variables contained in Equation 1.

6. The use of computer techniques in analyzing complex data with both temporal and spatial variables is essential in resolving the multivariate problems involved in delta growth.

REFERENCES CITED

Bea, R. G., H. A. Bernard, P. Arnold, and E. H. Doyle, 1975, Soil movements and forces developed by wave-induced slides in the Mississippi delta: Journal of Petroleum Technology, v. 7, p. 500-514.

Bryant, L. M., and R. A. Hall, 1979, Design for complex foundation configurations and submarine mudslide conditions: OTC-3403, Annual Offshore Technology Conference, Houston, Texas, p. 405-409.

Coleman, J. M., and D. B. Prior, 1978, Submarine landslides in the Mississippi delta: OTC-3170, Annual Offshore Technology Conference, Houston, Texas, p. 1067-1071.

——— ——— and L. E. Garrison, 1980, Subaqueous sediment instabilities in the offshore Mississippi River delta: Bureau of Land Management Open File Report 80-01, 60 p.

Dunlap, W. A., W. R. Bryant, R. A. Bennett, and A. F. Richards, 1978, Pore pressure measurements in underconsolidated sediments: OTC-3168, Annual Offshore Technology Conference, Houston, Texas, p. 1049-1055.

Fisk, H. N., C. R. Kolb, and L. G. Wilbert, 1954, Sedimentary framework of the modern Mississippi delta: Journal of Sedimentary Petrology, v. 24, p. 76-99.

Garrison, L. E., 1974, The instability of surface sediments on parts of the Mississippi delta front: U.S. Geological Survey Open File Report 74-4, 9 p.

Morgan, D. J., 1977, The Mississippi River delta legal geomorphologic evaluation of historic shoreline changes: Geoscience and Man, v. 16, 196 p.

Morgan, J. P., J. M. Coleman, and S. M. Gagliano, 1963, Mudlumps at the mouth of the South Pass, Mississippi River; sedimentology, paleontology, structure, origin, and relation to deltaic processes: Louisiana State University Studies, Coastal Studies Series 10, 190 p.

Prior, D. B., and J. M. Coleman, 1978, Submarine landslides on the Mississippi River delta-front slope: Geoscience and Man, v. 19, p. 41-53.

——— and J. N. Suhayda, 1979, Submarine mudslide morphology and development mechanisms, Mississippi delta: OTC-3482, Annual Offshore Technology Conference, Houston, Texas, p. 1055-1058.

Shepherd, F. P., 1955, Delta front valleys bordering the Mississippi distributaries: GSA Bulletin, v. 66, p. 1489-1498.

Sterling, G. H., and E. E. Strohbeck, 1973, The failure of the South Pass 70 "B" Platform in Hurricane Camille: OTC-1898, Annual Offshore Technology Conference, Houston, Texas, p. 11720-11724.

Suhayda, J. N., and D. B. Prior, 1978, Explanation of submarine landslide morphology by stability analysis and rheological models: OTC-3171, Annual Offshore Technology Conference, Houston, Texas, p. 1075-1080.

Waldrop, W. R., and R. C. Farmer, 1974, Three-dimensional computation of buoyant plumes: Journal of Geophysical Research, v. 79, p. 1269-1276.

Whelan, T., J. T. Ishmael, and G. B. Rainey, 1978, Gas-sediment interactions in Mississippi delta sediments: OTC-3166, Annual Offshore Technology Conference, Houston, Texas, p. 1029-1032.

Wright, L. D., and J. M. Coleman, 1971, Effluent expansion and interfacial mixing in the presence of a salt wedge, Mississippi River delta: Journal of Geophysical Research, v. 76, p. 8649-8661.

Unclassified Distribution List
Reports of Contract N00014-83-C-0150
Project NR 388 002

Office of Naval Research
Coastal Sciences Program
Code 422CS
Arlington, VA 22217

Defense Documentation Center
Cameron Station
Alexandria, VA 22314

Director, Naval Research Lab
Attn: Technical Information Officer
Washington, DC 20375

Director
Office of Naval Research Branch Office
1030 East Green Street
Pasadena, CA 91101

Director, Code 100
Office of Naval Research Branch Office
536 South Clark Street
Chicago, IL 60605

Director
Office of Naval Research Branch Office
495 Summer Street
Boston, MA 02210

Commanding Officer
Office of Naval Research Branch Office
Box 39
FPO NY 09510

Chief of Naval Research
Asst. for Marine Corps Matters
Code 100M
Office of Naval Research
Arlington, VA 22217

Office of Naval Research
Code 480
National Space Technology Lab
Bay St. Louis, MS 39520

Office of Naval Research
Operational Applications Division
Code 200
Arlington, VA 22217

Office of Naval Research
Scientific Liaison Officer
Scripps Inst. of Oceanography
La Jolla, CA 92038

Director, Naval Research Lab
Attn: Library, Code 2628
Washington, DC 20375

ONR Scientific Liaison Group
American Embassy, Room A-407
APO San Francisco 96503

Commander
Attn: Library
NSTL Station
Bay St. Louis, MS 39520

Chief of Naval Operations
OP 987P1
Department of the Navy
Washington, DC 20350

Naval Academy Library
U.S. Naval Academy
Annapolis, MD 21402

Commandant Officer
Naval Coastal Systems Laboratory
Panama City, FL 32401

Librarian
Naval Intelligence Support Center
4301 Suitland Road
Washington, DC 20390

Commanding Officer
Naval Air Development Center
Warminster
Johnsville, PA 18974

Naval Ordnance Lab
White Oak
Silver Spring, MD 20910

Commanding Officer
Naval Civil Engineering Lab
Port Hueneme, CA 93041

Officer in Charge
Environmental Prediction Research Facility
Naval Postgraduate School
Monterey, CA 93940

Dr. Warren C. Thompson
Dept. of Meteorology and Oceanography
U.S. Naval Postgraduate School
Monterey, CA 93940

Commander, Amphibious Force
U.S. Pacific Fleet
Force Meteorologist
COMPHIBPAC Code 23 5
San Diego, CA 92155

Commanding General
Marine Corps Development and Educational Command
Quantico, VA 22134

Dr. A. L. Slafkosky
Scientific Advisor
Commandant of the Marine Corps
Code RD-1
Washington, DC 20380

Defense Intelligence Agency
Central Reference Division
Code RDS-3
Washington, DC 20301

Director
Defense Mapping Topographic Center
Attn: Code 50200
Washington, DC 20315

Commanding Officer
U.S. Army Engineering Topographic Lab
Attn: ETL-ST
Fort Belvoir, VA 22060

Director
Coastal Engineering Research Center
U.S. Army Corps of Engineers
Kingman Building
Fort Belvoir, VA 22060

Chief, Wave Dynamics Division
USAE-WES
P. O. Box 631
Vicksburg, MS 39180

Commandant
U.S. Coast Guard
Attn: GECV/61
Washington, DC 20591

Library
U.S. Coast Guard Academy
New London, CT 06320

National Oceanographic Data Center
c/o D764
Environmental Data Services
NOAA
Washington, DC 20233

Assistant Director
Research and Development
National Ocean Survey
6001 Executive Boulevard
Rockville, MD 20852

Central Intelligence Agency
Attn: OCR/DD-Publications
Washington, DC 20205

Dr. Donald Swift
PRC-G130
ARCO Oil & Gas Company
Box 2819
Dallas, TX 75080

Ministerialdirektor
Dr. F. Wever
Rue/FO
Bundesministerium der Verteidigung
Hardthoehe
D-5300 Bonn, WEST GERMANY

Oberregierungsrat
Dr. Ullrich
Rue/FO
Bundesministerium der Verteidigung
Hardthoehe
D-5300 Bonn, WEST GERMANY

Mr. Tage Staerup
Defence Research Establishment
Osterbrogades Kaserne
DK-2100 Kobenhavn O, DENMARK

Dr. Yoshimi Goda
Director, Wave Research Division
Port and Harbor Research Inst.
Ministry of Transportation
1-1 Nagase, 3 Chome
Yokosuka, 239 JAPAN

Prof. Dr. Rer. Nat. H. G. Gierloff-Emden
Institut f. Geographie
Universitaet Muenchen
Luisenstrasse 37/111
D-800 Muenchen 2
WEST GERMANY

Prof. Dr. Eugen Seibold
Geol.-Palaeontolog. Institut
Universitaet Kiel
Olshausenstrasse 40-60
D-2300 Kiel, WEST GERMANY

Dr. R. Koester
Geol.-Palaeontolog. Institut
Universitaet Kiel
Olshausenstrasse 40-60
D-2300 Kiel, WEST GERMANY

Prof. Dr. Fuehrboeter
Lehrstuhl F. Hydromechanik U. Kuestenwasserbau
Technische Hochschule
Braunschweig
Beethovenstrasse 51A
D-3300 Braunschweig
WEST GERMANY

Prof. Dr. Walter Hansen
Direktor D. Institute f. Meereskunde
Universitaet Hamburg
Heimhuderstrasse 71
D-2000 Hamburg 13
WEST GERMANY

Prof. Dr. Klaus Hasselmann
Institut F. Geophysik
Universitaet Hamburg
Schluterstrasse 22
D-2000 Hamburg 13
WEST GERMANY

Prof. Dr. Nils Jerlov
Institute for Physical Oceanography
Kobenhavns Universitet
Haraldsgade 6
DK-2200 Kobenhavn, DENMARK

Prof. Kiyoshi Horikawa
Coastal Engineering Laboratory
Dept. of Civil Engineering
University of Tokyo
Bunkyo-ku
Tokyo, JAPAN

Prof. Yuji Iwagaki
Civil Engineering Department
Kyoto University
9 Shimogamo Zenbucho
Sakyo-ku
Kyoto, JAPAN

Delft Hydraulics Laboratory
P. O. Box 177
2600 MH
Delft, THE NETHERLANDS

Ir. M. W. Van Betenberg
Physisch Laboratorium TNO
Oude Waalsdorper Weg 63
Den Haag, THE NETHERLANDS

Prof. Toshiyuki Shigemura
Civil Engineering Department
National Defense Academy
1-10-20 Hashirimizu
Yokosuka 239, JAPAN

Mr. William T. Whelan
Telecommunication Enterprises Inc.
2630 Industrial Drive
Panama City, FL 32405

Director
Institute of Marine Research
University of California
A-028
La Jolla, CA 92093

Dr. G. D. Hickman
Applied Science Technology, Inc.
19212 Plummer Drive
Germantown, MD 20767

Dr. Bernd M. Brennenkmeyer, SJ
Department of Geology and Geophysics
Boston College
Chestnut Hill, MA 02167

Dr. Choule J. Sonu
Tek Marine, Inc.
37 Auburn Avenue
Sierra Madre, CA 91024

Dr. Richard A. Davis, Jr.
Department of Geology
University of South Florida
Tampa, FL 33620

Dr. William T. Fox
Department of Geology
Williams College
Williamstown, MA 01267

Dr. Hsiang Wang
Department of Civil Engineering
Dupont Hall
University of Delaware
Newark, DE 19711

Dr. John T. Kuo
Henry Krumb School of Mines
Seeley W. Mudd Building
Columbia University
New York, NY 10027

Dr. Edward B. Thornton
Department of Oceanography
Naval Postgraduate School
Monterey, CA 93940

Prof. C. A. M. King
Department of Geography
University of Nottingham
Nottingham, ENGLAND

Dr. Douglas L. Inman
Scripps Inst. of Oceanography
La Jolla, CA 92037

Dr. Omar Shemdin
Jet Propulsion Lab 183-301
4800 Oak Grove Drive
Pasadena, CA 91103

Dr. William W. Wood
Department of Geosciences
Purdue University
Lafayette, IN 47907

Dr. John B. Southard
Department of Earth and Planetary Sciences
Massachusetts Inst. of Technology
Cambridge, MA 02139

Dr. J. Ernest Breeding, Jr.
Department of Oceanography and Ocean Engineering
Florida Institute of Technology
Melbourne, FL 32901

Dr. John C. Kraft
Department of Geology
University of Delaware
Newark, DE 19711

Dr. Dag Nummedal
Department of Geology
LSU

Mr. Fred Thomson
Environmental Research Institute
P. O. Box 618
Ann Arbor, MI 48107

Dr. Thomas K. Peucker
Simon Fraser University
Department of Geography
Burnaby 2, B. C., CANADA

Dr. Robert Dolan
Department of Environmental Sciences
University of Virginia
Charlottesville, VA 22903

Revised 12/84


DATE
ILMED
-8